MASTERARBEIT / MASTER'S THESIS

Titel der Masterarbeit / Title of the Master's Thesis

The Corona Australis star-forming region

A complete sample of young stellar members selected with VISIONS, WISE, 2MASS, Spitzer, and Gaia.

verfasst von / submitted by

David Hernandez, BSc

angestrebter akademischer Grad / in partial fulfillment of the requirements for the degree of

Master of Science (MSc)

Wien, 2022 / Vienna 2022

Studienkennzahl lt. Studienblatt / degree programme code as it appears on the student record sheet:	UA 066 861
Studienrichtung lt. Studienblatt / degree programme as it appears on the student record sheet:	Astronomie
Betreut von / Supervisor:	Mag. Dr. Josefa Großschedl, Bakk

Contents

Abstract

In the constellation *Corona Australis* (CrA) we find a molecular cloud of the same name, which is one of the closest star-forming regions to our Sun ($d \approx 150\,\mathrm{pc}$). Projected in the plane of the sky, CrA appears to be relatively isolated just below the center of the Milky Way. In combination with its vicinity and its peculiar cometary shape this makes it an excellent candidate for star formation studies.

My thesis aims at revisiting the evolutionary status and the number of young stellar object (YSO) candidates in CrA as selected from their infrared-excess. To achieve this, I made use of the new ESO *VISIONS* public survey in combination with existing public infrared survey data from *WISE*, *2MASS*, and *Spitzer*. The *VISIONS* survey covers all star forming regions visible from the southern hemisphere and will provide near-infrared (NIR) photometry and multi epoch astrometry. This enables us, for the first time, to determine proper motions for a significant number of stars that suffer from strong extinction, such as young embedded protostars.

The ESA *Gaia* satellite enables a complementary method to select stellar members associated with CrA. The unprecedented quality of *Gaia* parallaxes makes it possible to pre-select objects in a distance interval centered on CrA. This facilitates a YSO search based on infrared colors, since this approach naturally reduces extragalactic contamination (star-forming galaxies, AGNs), which often exhibit similar infrared colors compared to YSOs. However, this method relies on the optical *Gaia* observations, which leads to incompleteness especially concerning the youngest or highly embedded sources. Thus, in order to compile the most complete YSO catalog for CrA, I will utilize observations from the visible to the infrared range, and apply careful selections in various color-color and color-magnitude diagrams.

By selecting sources within a 625 square degree science field from all-sky surveys (*WISE*, *2MASS*, *Gaia*) around the CrA molecular cloud combined with the smaller ($38.5\,\mathrm{deg}^2$) *VISIONS* wide field, I selected with my methods 73 YSO candidates with infrared-excess. I can thereby confirm 20 previously known IR selected candidates. By combining my selection with literature catalogs of the young stellar population in Corona Australis, I compiled a most complete set of 557 young stellar members associated with the CrA SFR, including 17 new previously unknown YSO candidates.

The sources in this catalog were assigned membership to one of three sub-clusters in the CrA region and the disk-fraction for these sub-clusters were computed. I found a decreasing disk-fraction for the sub-clusters from South to North, indicating an age gradient with the youngest component coinciding with the Coronet cluster in the South, associated with the molecular cloud. This Age gradient confirms previous literature results who independently found a similar gradient based on other methods.

This most complete sample of young stellar members in the CrA region, as presented in this thesis, opens a gateway to a number of science cases. For example a detailed analysis of the evolutionary status of the CrA star-forming region, by studying the star-formation history in greater detail. Moreover, statistics like the initial mass function or the star formation rate and efficiency can be investigated in more detail. Finally, by combining optical *Gaia* proper motions with infrared *VISIONS* proper motions, in the future, it will be possible to analyze the 3D space motion of the young stellar population, especially when combined with auxiliary radial velocity surveys. This study, which improves upon previous studies about CrA, will add another puzzle piece to the greater picture; this means it will enable us to get a more complete picture of the star formation history in the solar neighborhood.

Zusammenfassung

Im Sternbild *Corona Australis* (CrA) befindet sich eine gleichnamige Molekülwolke, die in einer mittleren Entfernung von zirka 150 pc liegt, und somit eine der der Erde am nächst gelegenen Sternentstehungsregionen darstellt. Auf die Himmelskugel projiziert erscheint CrA knapp unterhalb des Zentrums der Milchstraße in einer relativ isolierten Region. In Kombination mit der unmittelbaren Nähe und dem einzigartigen kometenähnlichen Aussehen, daher stellt CrA eine hervorragenden Wahl für detailiertere Untersuchungen dar.

Diese Arbeit zielt darauf ab, den evolutionären Status der Sternentstehungsregion und die Anzahl junger stellarer Objekte (YSO) in CrA zu ermitteln, indem sie anhand ihrers Überschusses an Infrarotstrahlung selektiert und klassifiziert werden. Um dies zu erreichen, nutzte ich vorläufige Daten des ESO *VISIONS* Public Survey in Kombination mit bestehenden öffentlichen Infrarot-Survey-Daten von *WISE*, *2MASS* und *Spitzer*. Die *VISIONS*-Survey deckt alle Sternentstehungsregionen ab, die von der Südhalbkuel zugänglich sind, und wird Nahinfrarot-Photometrie und Multi-Epochen-Astrometrie bieten. Dies wird es erstmals ermöglichen, Eigenbewegungen (proper motions) für eine signifikante Anzahl von YSOs zu bestimmen, welche noch in die Wolke eingebettet sind, wie z. B. junge Protosterne die tief in der Molekülwoke liegen oder noch von Gas und Staub umhüllt sind.

Das *Gaia* Weltraumobservatorium der Europäischen Raumfahrtbehörde (ESA) ermöglicht weitere Methoden zur Selektion von Objekten, die mit CrA in Verbindung gebracht werden können. Die beispiellose Qualität von *Gaia*-Parallaxen macht es möglich, Objekte in einem auf CrA zentrierten Entfernungsintervall vorab auszuwählen. Dies erleichtert eine YSO-Suche auf der Grundlage von Infrarotfarben, da dieser Ansatz auf natürliche Weise extragalaktische Kontaminationen (Galaxien mit aktiver Sternetstehung, aktive Galaxienkerne) reduziert, die im Vergleich zu YSOs häufig ähnliche Farbindizes aufweisen. Allerdings ist diese Methode auf die optischen *Gaia*-Beobachtungen angewiesen, was insbesondere bei den jüngsten oder stark geröteteten Quellen dazu führt, dass diese nicht detektiert werden können. Um einen YSO-Katalog für CrA zusammenzustellen, der auf beste Vollständigkeit orientiert ist, werde ich Beobachtungsdaten vom sichtbaren bis zum infraroten Wellenlängenbereich des elektromagnetischen Spektrums verwenden und sorgfältige Auswahlkriterien in verschiedenen Farb-Farb und Farben-Helligkeitsdiagrammen treffen. Durch die Auswahl von Quellen aus in-

frarot All-Sky Surveys (*WISE*, *2MASS*, *Gaia*), innerhalb eines 625 Quadratgrad grossen Bereiches um Corona Australis, in Kombination mit der 38.5 deg^2 abdeckenden *VISIONS* Beobachtungskampagne, konnte ich 73 YSO-Kandidaten mit Infrarot-Exzess identifizieren. Indem ich meine Auswahl mit Literaturkatalogen junger Sterne in Corona Australis kombinierte, erstellte ich einen Gesamtkatalog für CrA der 557 YSOs und potentielle YSOs in Corona Australis enthält, darunter 17 neue, bisher unbekannte YSO-Kandidaten.

Weiters wurden die Quellen in meinem Katalog einem von drei Subclustern in CrA zugeordnet, und die relative Anzahl junger stellarer Objekte mit zirkuumstellarer Scheiben für diese Subcluster bestimmt. Daraus resultierend fand ich eine relative Scheibenanzahl, welche für die weiter vom Coronet entfernten Subcluster abnimmt, was auf einen Altersgradienten hinweist, wobei der älteste Subcluster am weitesten von der nördlichen Spitze der CrA-Molekülwolke entfernt ist.

Mein YSO Katalog ebnet den Weg zu einer Reihe von weiterführenden Forschungsthemen, wie zum Beispiel einer detaillierten Analyse des evolutionären Status der CrA-Sternentstehungsregion, indem die Sternentstehungsgeschichte dieser Region genauer untersucht wird. Außerdem können Statistiken wie die Initial Mass Function oder die Sternentstehungsrate und -effizienz genauer untersucht werden. Durch die Kombination optischer *Gaia*-Eigenbewegungen mit infrarot *VISIONS*-Eigenbewegungen ist es nun möglich, die 3D-Raumbewegung der jungen Sternpopulation zu analysieren, insbesondere in Kombination mit zusätzlichen Messungen von Radialgeschwindigkeit. Diese Arbeit, welche frühere Studien über CrA ergänzen, wird dem Gesamtbild ein weiteres Puzzleteil hinzufügen, das ermöglichen wird, ein vollständigeres Bild der Sternentstehungsgeschichte in der Nachbarschaft der Sonne zu bekommen.

List of Tables

List of Figures

Chapter 1

Introduction

1.1 Motivation

Our understanding of how stars form in the Milky Way, and in particular in the solar neighborhood, has improved significantly over the last few decades (Bok 1948; Shu et al. 1987; Evans 1999; Larson 2003; Lada 2005; Kennicutt & Evans 2012). However, there are still many blind spots in our knowledge on how stars are born. For instance, our current understanding of the star formation process points to stars forming through gravitational collapse of clouds composed mostly of molecular hydrogen (Spitzer et al. 1974; McKee & Ostriker 2007; André et al. 2014). However, it is not yet completely understood how these molecular clouds form, or how the conditions within the cloud influence the formation process.

In order to better understand the processes that are leading to, and determine the formation of a new star, we characterize star-forming regions (SFRs) and assess their evolutionary status. The focus of this thesis lies on the star forming region associated with the Corona Australis molecular cloud (Reynolds 1916; Forbrich & Preibisch 2007; Neuhäuser & Forbrich 2008). An updated census and analysis of the young stellar population in the Corona Australis (CrA) star-forming region (SF (SFR)R) will provide a new puzzle piece and help to complete our picture of star formation. With the data from the ESO public survey *VISIONS*, a near-infrared observation campaign (see Section 1.3.1.4), I have the opportunity to employ early survey data from high resolution images with high photometric sensitivity. Moreover, my thesis is an important quality control step for the *VISIONS* survey to, which will help to improve the quality of the data.

This thesis is structured into three chapters, where Chapter 1 will give a basic introduction into star formation in general, to the data used in this study, and the Corona Australis (CrA) star-forming region. In Chapter 2 I describe the science and control fields, as well as the methods to select and classify young stellar objects (YSOs). Chapter 3 presents the results of my thesis, with Chapter 4 discussing them, as well as giving a brief conclusion. Finally, in Chapter 5 I give a short outlook on possible future research options building on the insights gained from this study.

1.2 How stars form

In order to analyze the evolutionary state of any star-forming region it is important to understand where stars come from and how they form. We want to understand the intermediate steps when starting from the large scale structures, traversing several orders of magnitude in size, density, and temperature, to finally arrive at an object, which fuses hydrogen to helium at its center (Shu et al. 1987; van Dishoeck 2004; McKee & Ostriker 2007; Kennicutt & Evans 2012).

1.2.1 Molecular clouds and cores

To our current understanding, the formation of stars takes place within giant molecular clouds (GMCs) (see e.g. Blitz 1993; Lada & Lada 2003; McKee & Ostriker 2007). These structures can be found all throughout our Galaxy, and provide the fuel reservoir from which the gas is drawn in the star formation process (Genzel & Stutzki 1989; Lada et al. 1993; Bergin & Tafalla 2007; Heyer & Dame 2015). Since these clouds consist mainly of molecular hydrogen (Spitzer et al. 1974), their observation is challenging. The conditions in a molecular cloud which make it possible for molecular hydrogen to exists and not disassociate into atomic hydrogen are the main reason why molecular hydrogen is so hard to observe. The low temperatures in molecular clouds create an environment in which molecular hydrogen is mostly in its ground state, with insufficient thermal energy in the cloud to excite the hydrogen molecules. Luckily, molecular clouds also contain traces of other molecules and dust, which we use as a tracer to probe gas properties (Wilson et al. 1970; Mathis 1990; Pendleton 1997; Williams 2005). We can further draw conclusions about the inner structure and the physical processes taking place in molecular clouds from these tracer observations (Bergin et al. 1994; Heyer & Dame 2015; Hacar et al. 2020a).

It is yet not entirely known how the formation of a star takes off. Molecular clouds are internally complex structures, highly filamentary (Schneider & Elmegreen 1979; Heyer & Dame 2015; Hacar et al. 2018) and fractal (Stutzki et al. 1998), with a multitude of properties (Hacar et al. 2013; André et al. 2014). It is still debated what role certain properties such as turbulence (Elmegreen & Scalo 2004; Scalo & Elmegreen 2004) and magnetic fields (Mestel & Spitzer 1956; Krumholz & Federrath 2019) play in the star formation process. The star formation process can be initiated and influenced by a number of mechanisms, such as external triggers like galactic merger events (Hopkins et al. 2013; Pearson et al. 2019), or by massive stellar feedback (e.g., by supernovae or stellar winds, Mac Low & Klessen 2004; Hopkins 2014; Rey-Raposo et al. 2017), which can excavate the molecular clouds and trigger star formation at the edge of the expanding bubble (Zucker et al. 2022). These triggers can lead to a compression of the gas within the cloud, which can further lead into gravitational collapse of sub regions in the GMC (Larson 2003), if they are powerful enough to overcome the stabilizing mechanisms (Evans 1999). However, recent studies also take into account that Molecular clouds are not closed systems, tying star formation to the gas inflow, rather than to the cloud mass (Burkert 2017). These collapsing sub regions are also known as clumps. Over time, when more and more gas and dust gathers at the centers of the collapsing regions, dense cores are formed within the clumps, which mark the first stage in the formation of a new star (Williams 2005; Draine 2011).

A dense core typically has a density of $1 \times 10^4\,\mathrm{cm}^{-3}$, a diameter of 0.1 pc (Bergin & Tafalla 2007; André et al. 2014), and they are among the coldest objects with an average temperature of $10\,\mathrm{K}$ (Stahler 2015). Moreover, the dust in these cores, and the molecular cloud hosting them, absorbs the visible light from any source within or behind a dense core or cloud, adding excessive amounts of interstellar extinction to stars that lie behind them, letting through only in the infrared and radio regimes (Mathis 1990; Bergin & Tafalla 2007). Dense cores provide ideal conditions for star formation and may be considered as seed points for new stars to form (Evans 1999). Observing these objects however is difficult, since the main constituent again is molecular hydrogen mostly in its ground state (Evans 1999; Lacy et al. 2017). Moreover, the high extinction associated with these structures lets them appear as starless voids in the sky (Bok 1948; Bergin & Tafalla 2007). Only when resorting to certain tracers, such as carbon monoxide molecules (CO) (Mathis 1990; Lacy et al. 2017) or diazenylium (N_2H^+) (Hotzel et al. 2004; Hacar et al. 2020b) we can probe the inner structure of dense cores. We believe that these cores are the transition phase between a dense cloud, or clump, and an object with a central mass concentration and a surrounding envelope (Lada et al. 1993; André et al. 2014), as there have been cores observed with and without young stars in them (Lee & Myers 1999).

1.2.2 Evolution of young stellar objects

In order to evaluate the evolutionary stage of a young stellar object, we can make use of the fact that stars are born in dense cores within molecular clouds. Since dense cores and molecular clouds also contain dust which extincts these young stellar objects, we can observe significant excess emission in the infrared wavelengths from these YSOs. This infrared-excess decreases over time with the evolution of a YSO when the surrounding envelope and circumstellar disk get accreted or dissolved. To measure the infrared-excess, we can use the spectral energy distribution and interpret its shape to make conclusions about the YSO. A commonly used tool utilized here is the infrared spectral index α_{IR} (Lada 1987).

1.2.2.1 IR spectral index

In order to evaluate the shape of the infrared SED, it is common to determine the slope, which is the infrared spectral index α_{IR} of the SED in the range of 2.2 to $10\,\mu\mathrm{m}$ (Lada 1987; André et al. 2000). The IR spectral index is defined in double logarithmic space as the derivative of IR flux by frequency (ν) or wavelength (λ) (see Appendix B for details). Equation 1.1 below shows the definition of the spectral index dependent on the wavelength.

$$\alpha_{\mathrm{IR}} = \frac{d\log(\lambda F_\lambda)}{d\log\lambda} \tag{1.1}$$

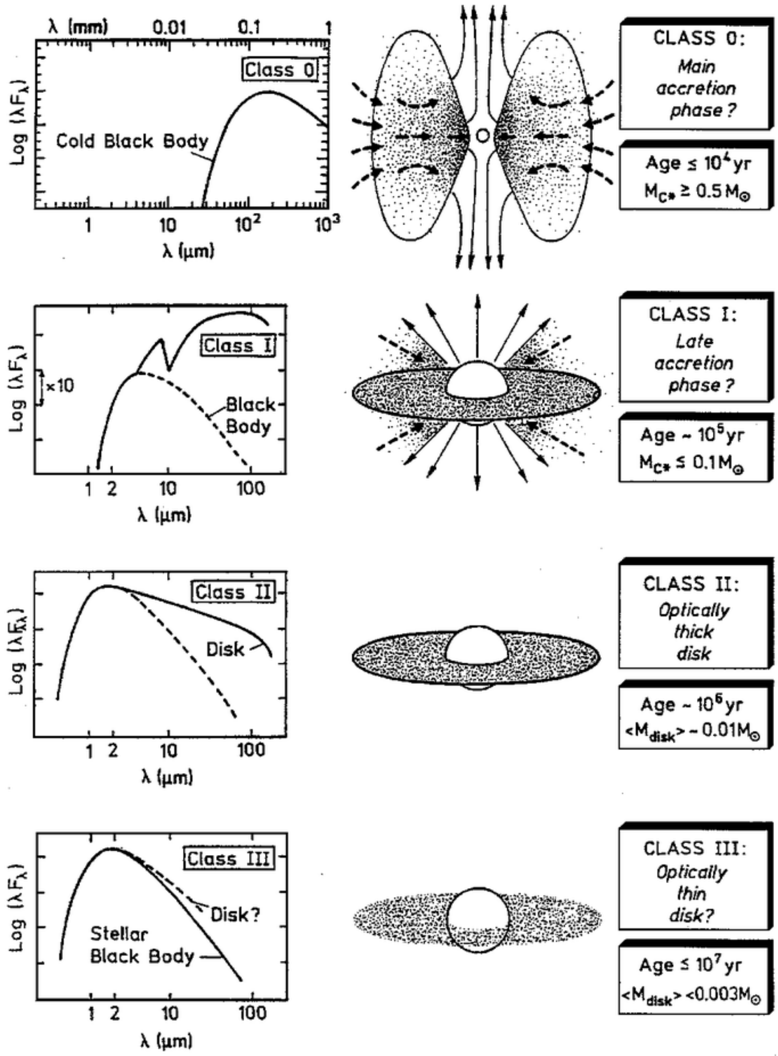

Figure 1.1: Overview of the YSO classification scheme developed by Lada & Wilking (1984), and André et al. (1993). This classification is based on the slope of the infrared spectral energy distribution (IR-SED), called the infrared spectral index $\alpha_{\rm IR}$. Depending on the shape of the SED, we associate individual evolutionary stages to the observed sources. The infrared SEDs are shown in the left column. The inferred evolutionary stage of the objects for each class is schematically depicted in the center column, with additional information in the right column. *Image credit: André (1994)*

1.2.2.2 Evolutionary timeline

From the point in time when the molecular cloud from which a YSO originates started to collapse (e.g., by an external trigger or gravity from its own mass), roughly 10 000 yr have passed and we enter the main accretion phase (Palla 1996; Stahler & Palla 2008). During this time the central prestellar object is deeply embedded in a proto stellar envelope, and the majority of the radiation it emits is being absorbed by the dust and gas of the envelope Lada & Wilking (1984). In return the dust in the envelope is heated up and, therefore, re-emits thermal radiation in the far infrared and radio wavelengths (André et al. 1993; Lada & Wilking 1984).

Thus, these deeply embedded sources are virtually undetectable in wavelengths shorter than 10 µm (Barsony 1994), which is the reason for why this evolutionary stage was discovered after the more advanced stages were characterized and classified by Lada & Wilking (1984). Lada (1987) was the first to introduce a classification scheme for YSOs, where the infrared SED is used, which is commonly known as the *Lada-classification*. Looking at the spectral energy distribution in Figure 1.1 (first row), we see that the peak emission is in the sub-millimeter range; We call these sources Class 0 objects (André et al. 1993). Therefore, in order to observe these objects, we employ telescopes that are capable of detecting signals in the far infrared and radio regime of the electromagnetic spectrum (André et al. 1993), which can be achieved, for example, with the Herschel/PACS (Poglitsch et al. 2010).

In the next 100 000 yr the envelope depletes more and more, subsequently forming a proto stellar disk, which accretes onto the central protostar. In this evolutionary stage, bipolar outflows of the forming star have effectively excavated the polar areas in the envelope of the YSO (Shu et al. 1987; Kenyon et al. 1993; Whitney et al. 2003a). Moreover, at this point of evolution, an accretion disk has formed from the material in the envelope that depletes onto the disk (Terebey et al. 1993). At this point the envelope still contains roughly half the mass of the entire system (Whitney et al. 2003a). Still, a large fraction of the radiation coming from the central body, is absorbed by the dust in the disk and surrounding envelope, thermally exciting dust particles, and re-emitting infrared radiation (Lada & Wilking 1984). Consequently, as is clearly visible in the second row of Figure 1.1, there is significant excess emission in the longer wavelengths, that can not be attributed to the black body radiation of the central object. This surplus of radiation in the mid- and far-infrared wavelengths is also known as infrared-excess Whitney et al. (2003a), the origin of which is the thermal emission of the dust particles in the proto stellar disk and surrounding envelope Lada & Wilking (1984). The observational class we associate with this evolutionary stage are Class I YSOs, originally defined by a IR spectral index in the range of $0 \leq \alpha_{\mathrm{IR}} < 3$ (Lada 1987).

Once the final remnants of the envelope have accreted completely onto the disk, only a thick circumstellar disk remains composed of gas and dust (Adams & Shu 1986; Adams et al. 1987; Evans et al. 2009a). Thus, at this stage the observed SED of such an object is a combination of the central black body of the star plus the infrared-excess from the disk. As a result, the peak of the SED now coincides with the peak of the black body of the central protostar, and has shifted even further towards shorter wavelengths (Adams et al. 1987). However, there is still significant infrared excess coming from the dusty disk, making it the main contributor to infrared excess in this stage, resulting in less infrared emission compared to the previous evolutionary stage. Sources with an infrared SED similar to the one displayed in Figure 1.1 (left column, third row) are also known as Class II YSOs, or classical T-Tauri stars (CTTS) (McKee & Ostriker 2007). Their IR spectral index α_{IR} is in the range of $-2 \leq \alpha_{\mathrm{IR}} < 0$ (Lada 1987).

The final stage is reached once most of the gas in the disk has accreted onto the central star or removed from the system, and most of the dust has either accreted onto the star or has coagulated and have become larger objects such as planetesimals (Pillitteri et al. 2013). The main components of such a disk are large dust grains and larger solid bodies (planetesimals) that are dominated by collisions, which replenish the dust component (Wyatt 2008). Only very little infrared radiation stems from the circumstellar disk resulting in very little or no infrared excess present in the spectral energy distribution of these objects (Adams et al. 1987). In this final stages, the disk component is clearly visible in the radio wavelengths, and may show evidence of ongoing planet formation (Steele et al. 2016). With the infrared SED of these sources being very similar to what we expect from an ordinary main sequence (MS) star, they are hard to distinguish from them when only considering infrared observations. However, since these objects are still very young, typically around $10\,\mathrm{Myr}$ (André 1994), they exhibit excess emission in X-ray measurements (Feigelson & Decampli 1981; Walter et al. 1988; Koyama et al. 1996). Or they can be distinguished in optical color-absolute-magnitude diagrams (equivalent to Hertzsprung-Russel diagrams), where they are still in their pre-main-sequence tracks. Thus, we can separate them from the main sequence population by looking for additional X-ray emission (Feigelson et al. 2002), or by using optical data, such as from the *Gaia* mission (see Section 1.3.2). Pre-main-sequence (PMS) stars with very little infrared excess are designated Class III YSOs with an infrared spectral index in the rage of $-3 \leq \alpha_{\mathrm{IR}} < -2$ (Lada 1987). These evolved PMS stars are also known as weak-line T-Tauri stars (WTTS). However, there is an ambiguity in the occurrence of CTTSs and WTTSs and the observational class they are thought to belong to. Teixeira et al. (2012) found examples for swapped classes in CTTSs and WTTSs. With spectroscopic observations it is possible to be more confident about the object being either a CTTS or a WTTS by analyzing Hα and lithium lines to distinguish between the two different objects (Herbig & Bell 1988; Martín 1997, 1998). Moreover, Class III YSOs can be further distinguished into pre-main-sequence stars with optically thin disks (anemic disks), and those without disks (Lada et al. 2006).

With the evolutionary process established, the individual evolutionary classes can be defined based on the observed infrared (IR) spectral energy distribution (SED). Starting from the deepest embedded sources to evolved pre-main-sequence (PMS) stars, we can associate observational classes with the true evolutionary stages (see e.g. Lada 1987; André et al. 1993; Greene et al. 1994; Whitney et al. 2003b,a, 2004; Robitaille et al. 2006; Evans et al. 2009a; Peterson et al. 2011; Koenig et al. 2012; Koenig & Leisawitz 2014; Dunham et al. 2015; Großschedl et al. 2019).

The original classification scheme had three classes of YSOs, where Class I objects are in their main accretion phase with an accretion disk and an envelope, Class II objects have an optically thick disk, and finally Class III objects have an optically thin disk or no disk (McKee & Ostriker 2007). The discovery of deeply embedded sources by André et al. (1993) called for the need of an additional Class 0 object, which can be associated with the earliest stages of star formation (André & Montmerle 1994; Barsony 1994). Furthermore, Greene et al. (1994) introduced an additional Class of YSO, which is believed to represent an intermediate stage between Class I and II. The infrared SED of these sources does not exhibit a distinctive peak or slope but is rather flat, hence, they are known as flat spectrum sources or flats in short. With the SED being flat, these sources have a spectral index α_{IR} ranging from -0.3 to 0.3 (Greene et al. 1994). Table 1.1 gives an overview of the YSO classes and the ranges of their infrared spectral indices α_{IR} adopted for this theses. As is mentioned above, this classification scheme is based on the shape of the infrared SED (Lada 1987), thus, we can infer an estimate of the true evolutionary stage as is shown in Figure 1.1 (André & Montmerle 1994; Palla 1996).

Table 1.1: YSO class definition, adopted from Großschedl et al. (2019). Class 0 and Class I objects were combined into the same interval while Class 0 sources need additional far-infrared information to detect them or to distinguish them from Class I.

	spectral index range	morphology
Class 0/I	$0.3 \leq \alpha_{\text{IR}}$	deeply embedded protostar or protostar with thick envelope and circumstellar disk
Flat-spectrum source	$-0.3 \leq \alpha_{\text{IR}} < 0.3$	transition stage between protostar with and without envelope
Class II	$-1.6 \leq \alpha_{\text{IR}} < -0.3$	protostar without envelope but with an optically thick disk
Class III optically thin disk	$-2.5 \leq \alpha_{\text{IR}} < -1.6$	Objects with an anemic disk
Class III no disk	$\alpha_{\text{IR}} < -2.5$	Pre-main-sequence and main sequence stars without a disk

1.2.2.3 SED fitting

The method of using the spectral index, however, has a few shortcomings. The IR SED is also sensitive to other effects such as different inclinations of the YSO as seen from the observers point of view (Masunaga & Inutsuka 2000; Whitney et al. 2003b,a, 2004; Robitaille et al. 2006). A Class I YSO may appear as a Class II YSO if the central protostar has had enough time to excavate the polar regions of the envelope due to feedback mechanisms of the accretion process (White et al. 2007). Observing a YSO with a circumstellar disk at different inclination angles of the disk, we receive more or less IR excess just by this projection effect. This can influence the shape of the SED in the wavelength range used for the spectral index computation, which makes the spectral index method not sensitive enough to distinguish between the two different evolutionary stages (Robitaille et al. 2006, 2007).

One alternative method to classify YSOs and compensate for the caveats mentioned above is to use SED fitting. This approach makes use of theoretical models of YSOs (Whitney et al. 2003b,a, 2004; Robitaille et al. 2006, 2007; Robitaille 2017) where radiative transfer simulations are made to produce model SEDs of young stellar objects with different physical properties and different spatial orientations. With a set of theoretical SED models it is then possible to fit the theoretical SEDs to the observational data (Robitaille et al. 2007; Tanti et al. 2012; Robitaille 2017). These simulated SEDs can be tied to the evolutionary stage of the YSO models, thus, the SED that fits the observational data best determines the evolutionary stage. A set of ready to use theoretical model SEDs (e.g. by Robitaille et al. 2006; Robitaille 2017) can be used for classification by SED fitting, as has been demonstrated by Robitaille et al. (2007). This method, however has some limitations, especially when it comes to available photometry. As has been discussed in detail by Robitaille et al. (2006), the most robust results in terms of determining the evolutionary stage of a YSO are achieved when including as many photometric measurements across the electromagnetic spectrum as possible. Moreover, a number of astrophysical parameters are probed during the fitting procedure, which define the evolutionary stage. Robitaille et al. (2007) also note, that their routine is not able to recover all fitting parameters in all cases, which can lead to somewhat ambiguous results in some cases, especially with missing data points.

Therefore, for this study, where the main focus lies in identifying new, previously unknown young stellar objects, using NIR and MIR data, detailed SED fitting is not needed. Moreover, to get a complete sample of YSOs one also needs to include sources, which might miss some photometric measurements across the SED, which can be included in the spectral index classification to get some class estimate. For best results from SED fitting, it should be aimed to gather as much data, covering wavelengths ranging from X-rays to FIR. In my thesis I aim to compile a most complete set of YSOs in a $625\,\mathrm{deg}^2$ science field (see Chapter 2), and the coverage in all wavelengths is only given partially in the chosen science field. Thus, a good fit is not guaranteed for all sources, whereas the spectral index can be applied to most of the selected stars, enabling an estimate of the Evolutionary stage.

1.3 Introduction to the used data

To select YSOs in the CrA star-forming region I use data from different sources. In this section I give a brief overview of the data used for this study on CrA, where I employ infrared as well as optical data.

1.3.1 Infrared data

Young stellar objects are mainly observable in wavelengths onward from the infrared and into the radio regime of the electromagnetic spectrum, because they feature excess emission in these wavelengths (Lada & Wilking 1984; André et al. 1993). The surplus in infrared emission comes from thermally heated dust in the proto-stellar disks and envelopes surrounding pre-main-sequence stars. Hence, resorting to infrared observations (ground based and space bound) is practical when probing the young stellar population of a star-forming region. In order to cover the chosen science field, I make use of the *2MASS* (Skrutskie et al. 2006) and *WISE* (Wright et al. 2010) all-sky surveys in the near-infrared (NIR) and mid-infrared (MIR), respectively. In addition I complement all-sky data with near-infrared data from *VISIONS* and mid-infrared data from *Spitzer* (Werner et al. 2004).

1.3.1.1 2MASS

The Two Micron All Sky Survey (*2MASS*) is a ground based observation campaign, carried out with two $1.3\,\mathrm{m}$ telescopes, located at Whipple Observatory in Arizona, and at Cerro Tololo in the Chilean Andes. It provides photometry for three NIR filters, J, H, and K_s at millijansky sensitivity as well as astrometry with arcsecond resolution (Skrutskie et al. 2006). The filter characteristics and zero magnitude fluxes for the *2MASS* survey (see Table 1.2) are described in detail by Cohen et al. (2003). The *2MASS* survey covers $99.998\,\%$ of the sky, and provides near-infrared photometric and astrometric measurements for $470\,992\,970$ point and $1\,647\,599$ extended sources (Skrutskie et al. 2006). Characteristic parameters for the filters used by *2MASS*

Table 1.2: Overview of the photometric filters used in this study. Listed here are the filter bandwidths, the filter wavelength, and the zero magnitude flux density for all photometric filters used in this study.

Survey	Filter	Bw [µm]	Unc(Bw) [µm]	λ [µm]	Unc(λ) [µm]	$F_{zp}(\nu)$ [Jy]	Unc($F_{zp}(\nu)$) [Jy]
2MASS [a)]	J	0.126	0.001	1.235	0.006	1594.000	27.800
	H	0.251	0.002	1.662	0.009	1024.000	19.950
	K_s	0.262	0.002	2.159	0.011	666.700	12.550
VISIONS [b)]	J	0.180	--	1.250	--	--[e)]	--
	H	0.300	--	1.650	--	--[e)]	--
	K_s	0.300	--	2.150	--	--[e)]	--
WISE [c)]	W1	0.663	0.001	3.353	0.013	306.540	4.600
	W2	1.042	0.001	4.603	0.017	171.787	2.516
	W3	5.507	0.017	11.561	0.045	31.674	0.450
	W4	4.101	0.048	22.089	0.118	8.363	0.293
Spitzer [d)]	I1	0.750	--	3.550	--	280.900	4.100
	I2	1.010	--	4.439	--	179.700	2.600
	I3	1.420	--	5.731	--	115.000	1.700
	I4	2.930	--	7.872	--	64.900	0.900
	M1	5.300	--	23.680	--	7.170	0.110

[a)] Values taken from Cohen et al. (2003). The *2MASS* filter wavelength is given for the monochromatic isophotal wavelength (λ_{iso}) of each filter with the zero magnitude flux density $F_{zp}(\nu_{iso})$ given for this wavelength.

[b)] Values taken from the VIRCAM/VISTA User Manual (`www.eso.org/sci/facilities/paranal/instruments/vircam/doc/VIRCAM_VISTA_User_Manual_20091218.pdf`).

[c)] Values taken from Jarrett et al. (2011). The listed bandwidth BW corresponds to the FWHM of the relative spectral response. The filter wavelength is given as the monochromatic isophotal wavelength (λ_{iso}) and the zero magnitude flux density $F_{zp}(\nu_{iso}$ is given for the isophotal wavelength of each filter.

[d)] IRAC bandwidths and monochromatic isophotal filter wavelengths are taken from Fazio et al. (2004). The bandwidth BW corresponds to the filter FWHM for IRAC and MIPS filters alike. IRAC zero magnitude flux densities ($F_{zp}(\nu)$) are given for filter wavelengths of 3.6 µm, 4.5 µm, 5.8 µm, and 8.0 µm are taken from the Spitzer IRAC Instrument Handbook (`https://irsa.ipac.caltech.edu/data/SPITZER/docs/irac/iracinstrumenthandbook/IRAC_Instrument_Handbook.pdf`). The values for the MIPS M1 filter are taken from the Spitzer MIPS Instrument Handbook (`https://irsa.ipac.caltech.edu/data/SPITZER/docs/mips/mipsinstrumenthandbook/MIPS_Instrument_Handbook.pdf`). The filter wavelength is given as average wavelength λ_{avg} and the zero magnitude flux density for MIPS is given for a filter wavelength of 23.68 µm.

[e)] *VISIONS* uses the same zero magnitude flux density as *2MASS*, as the *VISIONS* photometry has been calibrated with *2MASS* data.

are given in Table 1.2.

1.3.1.2 WISE

The Wide-field Infrared Survey Explorer (*WISE*) is a mid-infrared all-sky survey, carried out by a space observatory of the same name operated by the National Aeronautics and Space Administration (NASA). It provides astrometry and photometry in four mid-infrared filters

W1 to W4 with central wavelengths of 3.4 µm, 4.6 µm, 12 µm, and 22 µm Wright et al. (2010). With the second *WISE* data release, the all-sky images and catalog were released. The *WISE* catalog contains 563 921 584 sources, however, no distinction between extended and point sources were made like for *2MASS* (Cutri et al. 2012). An overview of the filter parameters used by *WISE* is given in Table 1.2.

1.3.1.3 Spitzer

Another infrared satellite operated by NASA is the *Spitzer space telescope*, which is able to obtain photometry from the mid- to far-infrared ranges using two dedicated instruments (Werner et al. 2004). The infrared array camera, IRAC for short, covers the MIR domain with four filters, I1 to I4, located at 3.6 µm, 4.5 µm, 5.8 µm, and 8.0 µm (Fazio et al. 2004). The second imaging instrument aboard the *Spitzer* space craft is MIPS, shorthand for multiband infrared photometer for *Spitzer*, with three far-infrared filters, M1 to M3, located at 24 µm, 70 µm, and 160 µm (Rieke et al. 2004).

In order to improve the selections, I employed data from the *Spitzer* Enhanced Imaging Products (SEIP) (Capak et al. 2012), which compared to *WISE* has higher image resolution and better photometric sensitivity. SEIP provides flux measurements for the four IRAC bands as well as the first MIPS band in tabular form. Further filter characteristics of the used *Spitzer* photometric bands are listed in Table 1.2. To further explore the number of young stellar objects—especially in regions of high dust column density in the vicinity of the Coronet Cluster—I use early data from the ESO public survey named *VISIONS*, which is introduced in detail in Section 1.3.1.4.

1.3.1.4 VISIONS

The *VISIONS* survey[1] (Meingast et al. in prep.) is a multi epoch observation campaign—using the near infrared bands J, H, and K_s— carried out with the ESO *Visible and Infrared Survey Telescope for Astronomy* (VISTA)—a 4 meter class telescope—located at the La Silla Paranal Observatory (Emerson et al. 2004). Furthermore, *VISIONS* is the continuation of its predecessor, the *Vienna Survey in Orion, VISION* (Meingast et al. 2016b,a).

VISIONS aims to provide a most complete catalog of sources in the near infrared, in all star-forming regions closer than 500 pc which are accessible from the southern hemisphere, which includes Corona Australis, Ophiuchus, the Pipe nebula, the Chameleon-Musca complex, Lupus, and the southern Orion complex. An overview of the *VISIONS* observed regions is shown in Figure 1.3. Moreover, *VISIONS* will provide proper motions of infrared sources, complementary to the optical *Gaia* proper motions (Gaia Collaboration et al. 2016). This will be important, in particular for embedded YSOs, which are not detectable by Gaia and which are the ones that are still strongly connected to the molecular cloud (Fűrész et al. 2008; Tobin et al. 2009; Dunham et al. 2015; Heiderman & Evans 2015; Hacar et al. 2016; Großschedl et al. 2019).

VISIONS provides a complement of wide and deep observations, accompanied by control fields in a low extinction region in the immediate vicinity of the science fields. The survey is

[1] VISTA Star Formation Atlas (*VISIONS*): `https://visions.univie.ac.at/`

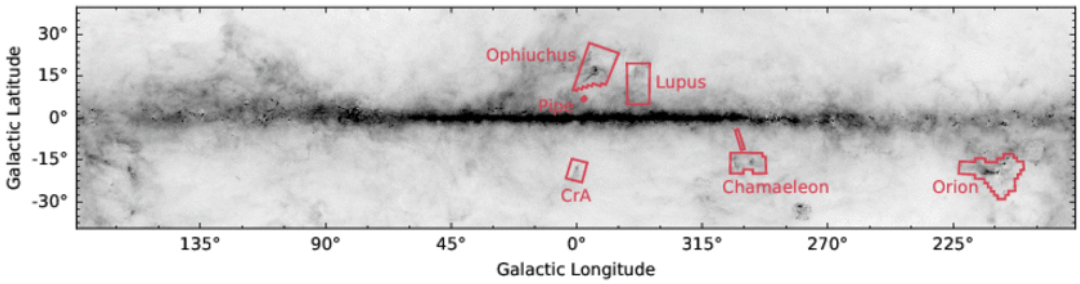

Figure 1.3: *VISIONS* observed regions. The *VISIONS* survey will provide photometry and proper motions for all star-forming regions accessible from the southern hemisphere, which are within a distance of 500 pc of the sun. *Image credit: S. Meingast,* https://visions.univie.ac.at/survey/

designed to include the faint IR sources ($H_{\mathrm{mag}} \approx 20$ mag) in high extinction areas, the brightest stars in the observed fields saturate the detector, rendering any photometric measurement of these unusable. Thus, it is necessary to replace bright and saturated sources in the *VISIONS* catalog with *2MASS* data to compensate for detections, which suffer from unreliable photometry.

Furthermore, *VISIONS* provides high resolutions images for all observed star-forming regions, which can be used to visually inspect targets of interest within the *VISIONS* fields. A demonstration of this can be seen in Figure 1.2 on the following page, which shows a high resolution image of the Corona Australis star forming region, generated from the *VISIONS* deep field observations. To create this false color image, the red, green, and blue layers, corresponding to the K_s, H and J filters, respectively, were combined.

The regions that will be included in the *VISIONS* catalog are Corona Australis, Ophiuchus, the Pipe nebula, the Chameleon-Musca complex, Lupus, and the southern Orion complex, while I focus on the CrA star-forming region (see Section 1.4), which serves as a first validation case for the reduction pipeline, which will be soon described in a dedicated paper by Meingast et al. (in prep.)[2].

1.3.2 Gaia optical data and astrometry

Gaia is a space observatory launched and maintained by the European Space Agency (ESA) which provides high precision multi epoch astrometry and photometry of the entire sky (Gaia Collaboration et al. 2016, 2018, 2021). *Gaia* provides high precision astrometry (parallaxes and proper motions) for billions of stars, which enables us to determine distances, and membership probabilities from kinematics (Galli et al. 2020; Kerr et al. 2021; Esplin & Luhman 2022). Based on these, it is possible to further decrease contamination in the infrared selection of the combined *2MASS-WISE* data used in this thesis (see Section 2.2.2.2), a cross match with *Gaia* EDR3 data (Gaia Collaboration et al. 2021) is made.

This exceptional dataset complements infrared observations towards CrA, which makes it

[2]See also https://www.eso.org/sci/publications/announcements/sciann17483.html, and https://www.eso.org/rm/api/v1/public/releaseDescriptions/190

possible to select sources within a distance of 250 pc by estimating the distance (d) from *Gaia* parallaxes (ϖ) using Equation 1.2.

$$d[\mathrm{pc}] = \frac{1000}{\varpi[\mathrm{mas}]} \tag{1.2}$$

This naturally excludes any background contamination by extragalactic sources such as quasi stellar objects (QSO), active galactic nuclei (AGN), and unresolved star-forming galaxies. By applying such a distance cut, I also exclude the majority of the background contamination coming from AGB stars. Adding *Gaia* data also provides an opportunity to verify and further refine any selection done using the infrared data. I use proper motions and parallaxes for these purposes, see Section 3.1 for further details.

However, cross-matching the infrared data described in Sections 1.3.1.1 to 1.3.1.4 with *Gaia*, excludes sources that are not detected in the visual wavelength range. The incompleteness introduced thereby is handled in two different ways. In the case where I use all-sky data from *2MASS* and *WISE* alone to select YSOs in the large science field (see Figure 2.1), I trust that the majority of YSOs are more evolved and not deeply embedded anymore (Evans et al. 2009a; Großschedl et al. 2019), thus can be detected by *Gaia*, in particular for stellar members in relatively nearby regions, such as CrA, which lies at about 150 pc from earth. In the central molecular cloud region with high dust column density, however, I re-include sources without a *Gaia* counterpart, as I rely on high resolution images from *VISIONS* to visually inspect sources which are not matched by *Gaia*, and decided whether they are possible YSO candidates based on their appearance in the *VISIONS* images and based on color and detailed SED information.

1.4 The Corona Australis star-forming region

In this thesis I focus on the Corona Australis star-forming region (CrA, Reynolds 1916; Taylor & Storey 1984; Forbrich & Preibisch 2007; Neuhäuser & Forbrich 2008; Evans et al. 2009a; Peterson et al. 2011; Dunham et al. 2015; Galli et al. 2020; Esplin & Luhman 2022), which was recently targeted by the *VISIONS* public survey (see Section 1.3.1.4). Since CrA is one of the smallest star-forming regions observed with *VISIONS*, and has low contamination by stars from the Galactic mid-plane, the *VISIONS* team first applied detailed data reduction to the CrA science field. Moreover, by using early *VISIONS* data products, this thesis played a vital role in quality control for the *VISIONS* data reduction pipeline. In the following passages I will give a short introduction to what we know about the CrA star-forming region and where our knowledge can be expanded.

Figure 1.2: False color composite of the CrA *VISIONS* deep field. Shown here is the heart of the Corona Australis star-forming region with the Coronet cluster in the center, and the Globular cluster 6723 to the north east. The image is a false color composite created from *VISIONS* deep field images captured in three near infrared bands, where the blue, green, and red layers correspond to the J, H, and K_s filters in ascending wavelength, respectively. *Image credit: Stefan Meingast, ESO*

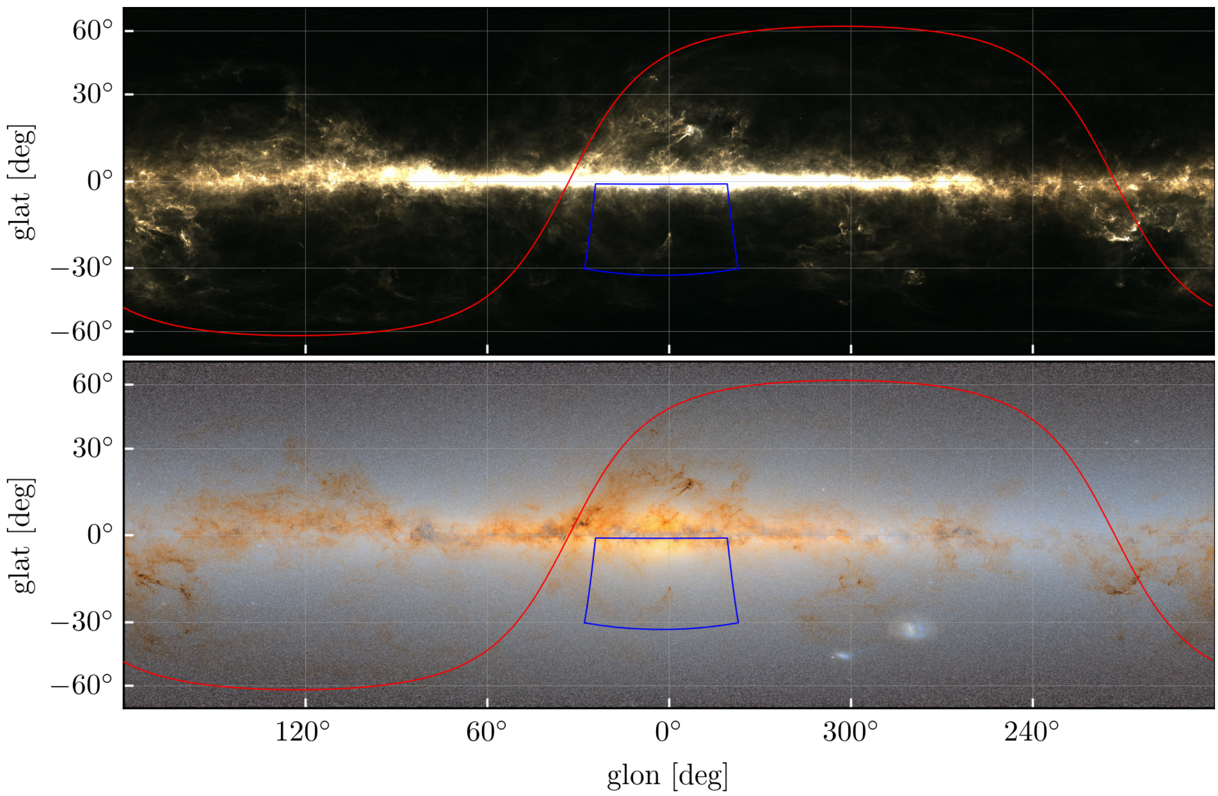

Figure 1.4: A panorama of our Milky Way galaxy as seen by *Planck* (Planck Collaboration et al. 2014) and *Gaia* (Gaia Collaboration et al. 2016). The blue box around the Corona Australis molecular cloud highlights the visible area shown in the zoomed in view of this star-forming region. *Top panel:* Thermal dust emission as detected with Planck. This image is a color composite using the 353 GHz, 545 GHz, and 857 GHz for the red, green and blue component, respectively. *Bottom panel: Gaia* EDR3 color flux map of the Milky Way.

1.4.1 Location and morphology

To put Corona Australis into context of the Milky Way, it is helpful to first look at its position in the sky. The top panel in Figure 1.4 shows thermal dust emission detected with the *Planck* satellite (Planck Collaboration et al. 2014) as a RGB color composite in galactic coordinates l, b. The observed wavelengths 353 GHz, 545 GHz, and 857 GHz correspond to the red, green and blue layers, respectively. The bottom panel shows data from the *Gaia* mission (Gaia Collaboration et al. 2016). This representation does not show an actual image of the Milky Way as seen from the Earth, but rather each pixel shows the average color and brightness of the area this pixel covers on the sky[3]. A cylindrical equal area (CEA) projection was chosen for the depictions of the Galaxy shown in Figure 1.4. In both images we can see the Corona Australis molecular cloud roughly 20 deg below the center of the Milky Way, as is indicated by the blue box, which outlines the field of view for the zoomed in views shown in Figure 1.5. Additionally we find that CrA is located on the southern celestial hemisphere, as is indicated by the red line representing the celestial equator, dividing the sky into a northern (above the red line) and

[3]These and other images are generated with the `hips2fits` python package from the *Gaia* EDR3 color flux map hosted at http://alasky.cds.unistra.fr/ancillary/GaiaEDR3/color-Rp-G-Bp-flux-map/

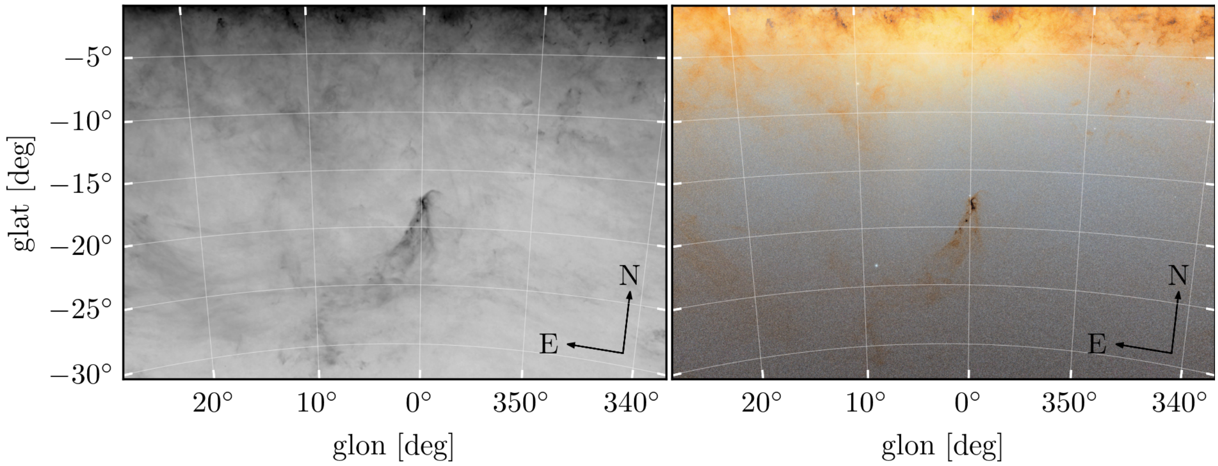

Figure 1.5: A zoomed in view of the CrA molecular cloud. Located at the center in this image is the molecular cloud as seen by *Planck* (Planck Collaboration et al. 2014) and *Gaia* (Gaia Collaboration et al. 2021). *Left panel:* This image shows thermal dust emission at 353 GHz, 545 GHz, and 857 GHz as a color composite. Clearly visible is the tail-like extension of the Molecular cloud, bending to the left in a loop-like manner. *Right panel:* The same bend of the cometary tail is visible in optical wavelengths as dust-extinction reddens background stars.

a southern hemisphere (below the red line). In addition, we see that this star-forming region is quite isolated, compared to other star-forming regions (SFRs) in the solar neighborhood, such as Chameleon-Musca located to the west of CrA, roughly at $(l = 300°, b = -15°)$, or Ophiuchus situated north of CrA, roughly at $(l = 350°, b = 20°)$.

Gaposchkin & Greenstein (1936) were the first to derive a distance of 150 pc based on observations of the variable reflection nebula NGC 6759, whereas other measurements by Marraco & Rydgren (1981) suggest a distance of 129 pc. With the first parallax measurements from the *HIPPARCOS* satellite (Perryman 1981; Perryman et al. 1997), distance measures were rather wide spread (122–170 pc) with large uncertainties of 20–50 % (see e.g. Knude & Hog 1998; Neuhäuser & Forbrich 2008). A recent study by Galli et al. (2020) makes use of the excellent parallax measurements acquired with the *Gaia* satellite, to determine a mean distance of 149.4 ± 0.4 pc between the sun and the Corona Australis young stellar population with high accuracy, interestingly very similar to first estimate by Gaposchkin & Greenstein (1936). This makes Corona Australis one of the closest star-forming regions in the solar neighborhood.

When looking at a zoomed in version of the region around the CrA molecular cloud (see Figure 1.5), we can see clearly that the molecular cloud has a peculiar cometary shape with the head pointing toward the Galactic mid-plane. Moreover, we find the highest dust column density in the northern tip of the cloud, which coincides with the location of the young embedded Coronet cluster (see Taylor & Storey 1984). Tracing down the western edge of the cloud, we find that the tail of the comet shaped cloud bends back up in a loop as if it were to encompass a bubble. This is visible in dust emission (left panel of Figure 1.5), as well as in the visible wavelengths observed by *Gaia* (right panel of Figure 1.5).

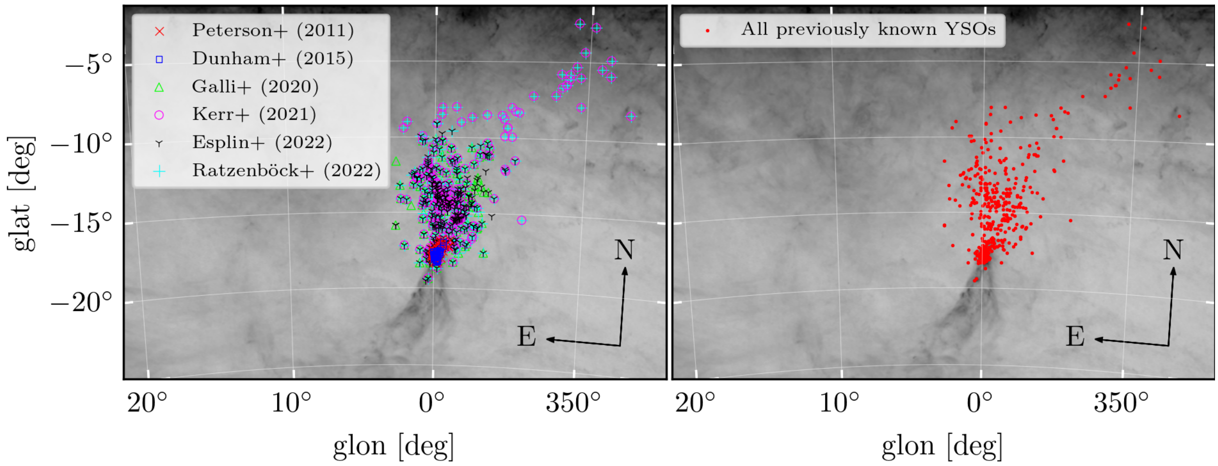

Figure 1.6: Overview of the young stellar population in CrA. Shown here are the so far discovered sources by using infrared observations and *Gaia* data. It is clearly visible, that the true extent of the Corona Australis star-forming region goes far beyond the Coronet cluster located at the high dust column density clump which forms the head of the cometary molecular cloud.

1.4.2 Young stellar population

The CrA star-forming region is considered to predominantly form low and intermediate mass stars (Neuhäuser & Forbrich 2008), with several hundred YSOs identified by previous studies using different techniques. The first member stars associated with the Corona Australis dark cloud were identified by observing reflection nebulae in the immediate vicinity (e.g. by Schmidt 1865; Lassell & Marth 1867; Reynolds 1916), with more variable stars identified (e.g. by Luyten 1927; van Gent 1933), however, not all of them turned out to be true members of CrA. With further research by Knacke et al. (1973), which made use of infrared observations in the range of 2.2 to 22 µm, has discovered an excess in infrared radiation due to thermal dust emission for some of the variable stars identified by Schmidt (1865); Lassell & Marth (1867), and Reynolds (1916), Luyten (1927), and van Gent (1933).

Moreover, Herbig (1960) established that two of the variable stars, and by extension the variable nebula NGC 6729 which they illuminate, as well as some of the surrounding member stars, are still young, which provided first evidence that infrared-excess is associated to young stars. This finding has led to the method of selecting and classifying young stellar objects via their infrared-excess (see e.g. Lada & Wilking 1984; Greene et al. 1994; Forbrich & Preibisch 2007; Evans et al. 2009a; Peterson et al. 2011; Koenig et al. 2012; Koenig & Leisawitz 2014; Dunham et al. 2015; Großschedl et al. 2019). Based on these methods, I select and classify YSOs in CrA, as is described in detail in Sections 2.2 and 2.3.

With data from the *Gaia* satellite, recent studies (e.g. Galli et al. 2020; Kerr et al. 2021; Esplin & Luhman 2022, Ratzenböck et al. submitted[4]) have used high precision astrometric

[4]Full title: Significance Mode Analysis (SigMA) for hierarchical structures – An application to the Sco-Cen OB association; Authors: Sebastian Ratzenböck, Torsten Möller, Josefa E. Großschedl, João Alves, Immanuel Bomze, and Stefan MEingast; Submitted to Astronomy & Astrophysics on March 31st 2022

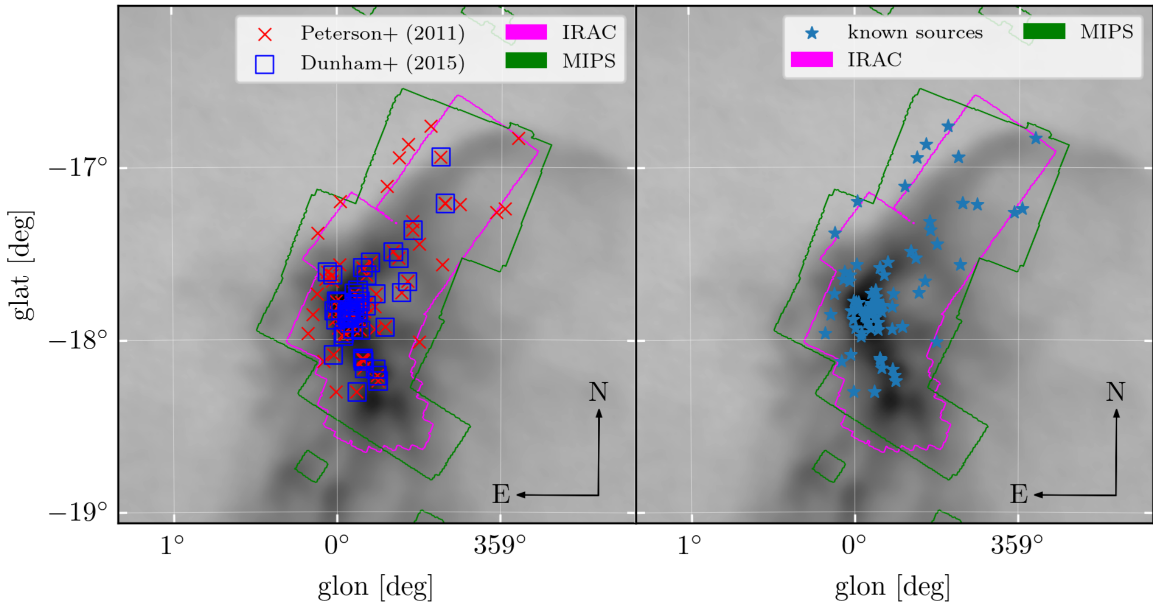

Figure 1.7: overview of the infrared selected sources taken from Peterson et al. (2011) and Dunham et al. (2015). These known sources serve as control sample of known YSOs in Corona Australis, which is used to help guide in the decision on the selection criteria described in Chapter 2. *Left panel:* Shown are the sources from the YSO catalogs compiled by Peterson et al. (2011) (red crosses) and Dunham et al. (2015) (blue boxes). Since both of these studies used *Spitzer* data (see IRAC and MIPS instrument footprints above), the sources are confined to the northern tip of the CrA molecular cloud. *Right panel:* The blue stars show the combined sources from Peterson et al. (2011) and Dunham et al. (2015).

and kinematic parameters to identify sources, which have originated from the Corona Australis Molecular cloud in past star formation events. However, by using optical *Gaia* data, the youngest and embedded sources are missing in such studies, and the slightly more evolved sources dominate *Gaia* selected samples of YSOs. Combining the sources discovered with *Gaia* with infrared observations, brings the number of YSOs and pre-main-sequence stars associated with the Corona Australis star forming region to 491, spanning an area of more than $60\,\mathrm{deg}^2$ as can be seen in Figure 1.6. With the infrared observations being confined to the regions with the highest dust column density at the top of the molecular cloud, the *Gaia* observations (Galli et al. 2020; Kerr et al. 2021; Esplin & Luhman 2022) have uncovered that the young stellar population is much more dispersed and not only confined to the tip of the dark cloud where the Coronet cluster is located (see Figure 1.6). Moreover, recent studies (Kerr et al. 2021, Ratzenböck et al. subm.) suggest that the Corona Australis SFR can be considered as part of the Scorpio-Centaurus (Sco-Cen) Association, with the northern part of CrA pointing towards Sco-Cen, forming a bridge between the CrA molecular cloud and Sco-Cen.

1.4.2.1 Infrared control sample

Since my thesis will use infrared excess to select young stellar members of the CrA star forming region, I employ a subset of all previously identified YSOs, which includes sources that were selected by their infrared excess. This subset consists of sources taken from Peterson et al. (2011) (77 sources) and Dunham et al. (2015) (54 sources). The two catalogs were cross-matched which gave a total 99 sources, with an overlap between the two catalogs of 32 sources. The 99 sources were then cross-matched to the *AllWISE* catalog, resulting in 66 young stellar objects which are used as a reference sample in the color-magnitude and color-color diagrams in Section 2.2 and are referred to as **known sources** from here on.

1.5 Goals

In my Thesis I focus on the Corona Australis star-forming region, one of the closest star forming regions to earth. My goal is to produce a detailed revised YSO catalog for this star-forming region. This includes to revisit early catalogs (e.g. by Forbrich & Preibisch 2007; Evans et al. 2009a; Peterson et al. 2011) and recently published membership lists (e.g. by Galli et al. 2020; Kerr et al. 2021; Esplin & Luhman 2022), but more importantly, I present large scale YSO searches using IR photometry. This allows to go beyond the so far studied regions, confirming the true extent of the CrA stellar population beyond the molecular cloud (see e.g. Galli et al. 2020; Kerr et al. 2021; Esplin & Luhman 2022). Using all-sky infrared data from *WISE* and *2MASS* is challenging when it comes to separating background contamination from viable protostars with infrared excess. Therefore, the benefits and shortcomings of including *Gaia* astrometry, in particular parallaxes, to remove contaminating background sources will be explored.

With Corona Australis being one of the star forming regions observed by the ESO *VISIONS* survey, I have the unique opportunity to use early *VISIONS* data products to verify and potentially improve the quality of future *VISIONS* data releases. In addition, high resolution images from this survey will help in further discriminating between background contamination, and young stellar objects with ambiguous photometric data, since many background galaxies are spatially resolved by *VISIONS* and can be identified based on their extended elliptical shape. Lastly, *VISIONS* promises to improve completeness in the low mass end of this star-forming region. Therefore, this work is the pilot study for using future data products on all other *VISIONS* observed regions.

Finally, a revised catalog listing all sources, which are likely members of the Corona Australis star-forming region will be compiled, listing identifiers to all archival catalogs used in this study, as well as infrared spectral indices and evolutionary class for each source. This will provide another puzzle piece to our knowledge on how stars form in the solar neighborhood.

Chapter 2

Methods

In order to obtain an improved sample of the young stellar population in the Corona Australis star forming region, I rely on a series of color-color (CCD) and color-magnitude (CMD) diagrams by combining the NIR and MIR photometry from various infrared surveys described in Section 1.3. In addition to that, to further refine and confirm sources from this infrared selection, I use *Gaia* EDR3 astrometry and kinematics gathered with the Gaia satellite operated by ESA (see Section 1.3.2), by cross-matching the infrared data. Finally, to assess the current status of the CrA star-forming region, the sources in the selection were classified using the infrared spectral index to get an estimate of their evolutionary stage.

2.1 Science and Control Fields

With recent research (e.g. by Galli et al. 2020; Kerr et al. 2021; Esplin & Luhman 2022, Ratzenböck et al. subm.), it has been uncovered that young stellar members associated with the Corona Australis star-forming region are spread over a much larger portion of the sky compared to what previous data suggested (see e.g. Taylor & Storey 1984; Peterson et al. 2011; Dunham et al. 2015). This new insight was gained using data from the *Gaia* mission's data release 2 (DR2; Gaia Collaboration et al. 2018) and early data release 3 (EDR3; Gaia Collaboration et al. 2021), whereas earlier works (Forbrich & Preibisch 2007; Peterson et al. 2011; Dunham et al. 2015) mostly relied on infrared data. These infrared observations concentrated on the region around the Coronet cluster at the northern most tip of the Corona Australis molecular cloud.

In order to identify new, previously unknown YSO candidates, I decided on expanding the area in which I search for potential members of the CrA star-forming region by their infrared excess. The final science field for which IR all-sky data as well as the *Spitzer* Enhanced Imaging Products[1] had to be acquired for, is shown in Figure 2.1, and spans an area of $625\,\mathrm{deg}^2$ on the sky. The *Spitzer* observed area within this since field covers $8.337\,\mathrm{deg}^2$, which is further split up between IRAC ($2.247\,\mathrm{deg}^2$) and MIPS ($6.896\,\mathrm{deg}^2$). The area covered by both instruments

[1]The *Spitzer* Enhanced Imaging Products are not all-sky data but cover a significant part of the science field in the high dust column density areas at the northern end of the CrA molecular cloud, and also a fraction of the control fields.

spans $0.834 \deg^2$. The *VISIONS* wide field observations of CrA cover an area of $42.340 \deg^2$.

The entire science field ranges from $15°$ to $355°$ in Galactic longitude $(glon)$—crossing the Galactic Prime Meridian—and reaches from $-5°$ to $-30°$ in Galactic latitude $(glat)$. Encompassed in this region of interest, roughly at the center, lies the Corona Australis molecular cloud with the Coronet Cluster located at the head of the cometary shaped cloud. Tracing down the eastern edge of the cloud, clearly visible in dust emission, is what appears to extend into a loop (see Figures 1.5 and 2.1). This region was included in the science field in order to investigate if any recent star formation had taken place in this area. The close proximity to the Galactic plane at the top of the science field was chosen because the results of Galli et al. (2020), Kerr et al. (2021), Esplin & Luhman (2022), and Ratzenböck et al. (subm.) indicate that there are further sources closer to the Galactic plane yet to be further explored. The red boxes in Figure 2.1 highlight the area form which all-sky data was acquired. The bright green boxes show the region covered by the *VISIONS* wide field, as well as the *VISIONS* control field (small box) the *VISIONS* deep field is indicated by the bright green box with dashed lines located at the head of the CrA molecular cloud. Magenta and dark green outlines indicate the *Spitzer* IRAC and MIPS footprints within the analyzed area, respectively.

To estimate the contamination in the science field, two control fields were chosen, which together span across the entire height of the science field along the Galactic latitude. A major requirement for the control fields however is, that the sources within should not suffer from extinction, and most importantly, should not contain any star-forming region. This is particularly challenging close to the Galactic mid plane, since dust lanes are commonly found there. For the northern part of the science field close to the Galactic mid-plane, the Galactic eastern side of the science field seemed to have a lower overall dust column density when compared to the Galactic western side, which features several clumps of high dust column density (see Figure 2.1). At the southern end of the science field, further away from the Galactic plane, the western side exhibits less emission from dust, and therefore less extinction is expected. Thus, the control field has been split up in two parts, one located adjacent to the north-eastern side of the science field, and one located adjacent to the south-western border of the science field, which are referenced to as the north-east control field (NECF) and south-west control field (SWCF), respectively (see Figure 2.1). The NECF spans an area of $82.5 \deg^2$, with its counterpart, the SWCF, being approximately $25\,\%$ larger measuring $105 \deg^2$.

The size of science field introduces a few complications which need to be addressed. For instance, with the northern end of the science field so close beneath the Galactic mid-plane and the southern end located at $-30°$ Galactic latitude, it is expected that the density of field stars decreases significantly when moving away from the mid-plane. This is supported by brightness gradient, which is clearly visible in the right panel of Figure 1.5. This gradient in field star density had to be taken into account for the selection criteria with decreasing Galactic latitude. Hence, it was necessary to slice up the science field into nine individual stripes parallel to the Galactic longitude, where each stripe was analyzed individually. The north-eastern and south western control fields were also sliced up into stripes, so that the height of the stripes in the control fields match the height of the stripes in the science field, as is illustrated in Figure 2.1. In general the height of the stripes was chosen to be $3°$ with two exceptions in order to keep the region around the Coronet cluster in the same stripe.

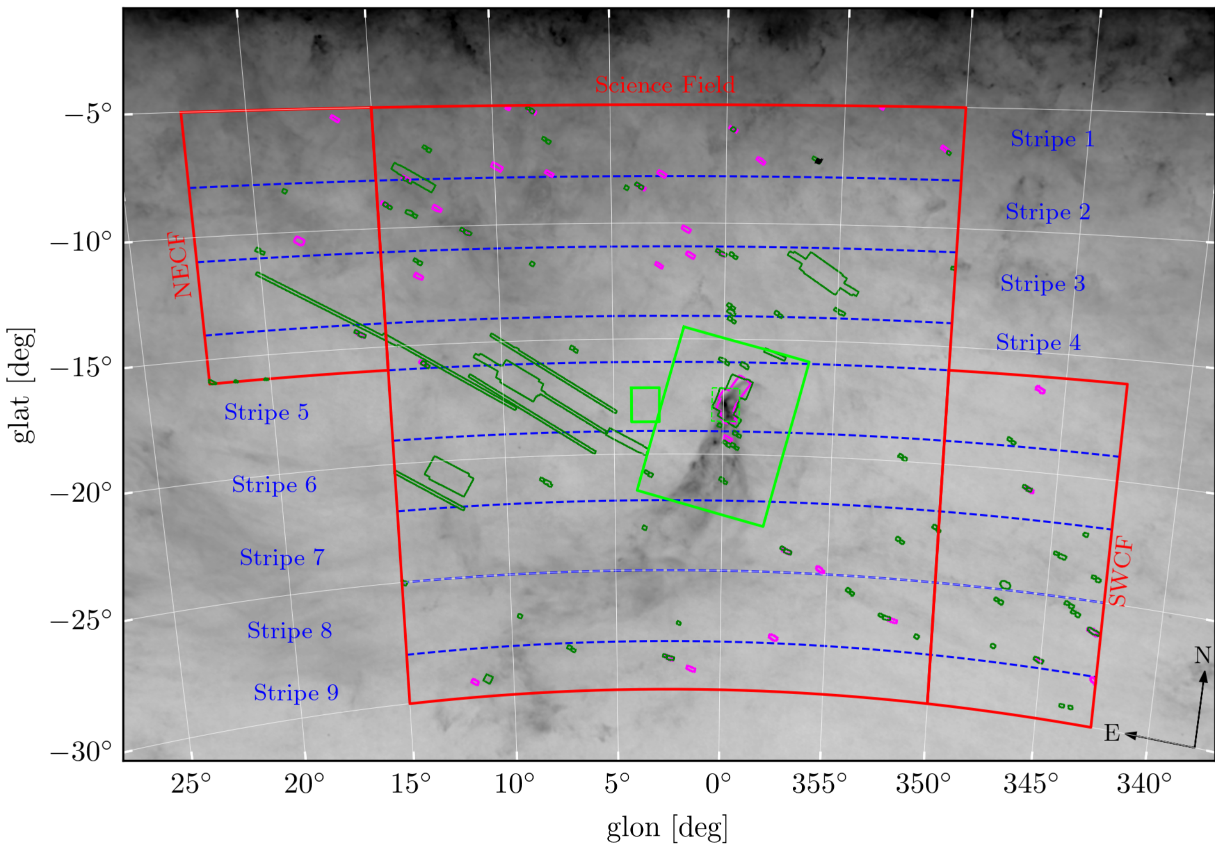

Figure 2.1: Overview of the studied area showing the science and control fields. The dust emission from *Planck* (Planck Collaboration et al. 2014) of CrA is clearly visible at the center of the image. The region which is outlined in red highlights the area from which all-sky data from *2MASS*, *WISE*, and *Gaia* was gathered. The science field stretches over $-5° \geq glat > -30°$ from top to bottom and crosses the Galactic Prime Meridian from $15° \geq glon > 350°$. The control field is split up into a north-east and a south-west part with the NECF spanning $-5° \geq glat > -16°$ in latitude and $22.5° \geq glon > 15°$ in longitude. The SWCF ranges across $-16° \geq glat > -30°$ and $350° \geq glon > 342.5°$. Additionally, the light green box highlights the coverage of the *VISIONS* wide field—and control field—observations used in this study. The *VISIONS* deep field observations concentrating on the head of the CrA molecular cloud is outlined by the light green dashed box. IRAC and MIPS footprints are shown as dark green and magenta outlines, respectively.

Table 2.1: Ranges for $glon$ and $glat$ for each stripe in the science and control field, as well as the area of each stripe is listed in this table. Most stripes in the science and control fields are of the same size except for stripe four and nine, where the height of the stripes is $2°$ rather than $3°$. The width (w) and height (h) of each stripe is given in the column "w×h" The Coronet cluster is located in stripe number five. The NECF contains stripes one to four, whereas the SWCF contains stripes number five to nine.

Stripe	Science field				Control field			
	$glat$	$glat$	w×h	Area	$glon$	$glat$	w×h	Area
1	$15.0° \geq l > 350.0°$	$-5.0° \geq b > -8.0°$	$25.0° \times 3.0°$	$75.0\,\mathrm{deg}^2$	$22.5° \geq l > 15.0°$	$-5.0° \geq b > -8.0°$	$7.5° \times 3.0°$	$22.5\,\mathrm{deg}^2$
2	$15.0° \geq l > 350.0°$	$-8.0° \geq b > -11.0°$	$25.0° \times 3.0°$	$75.0\,\mathrm{deg}^2$	$22.5° \geq l > 15.0°$	$-8.0° \geq b > -11.0°$	$7.5° \times 3.0°$	$22.5\,\mathrm{deg}^2$
3	$15.0° \geq l > 350.0°$	$-11.0° \geq b > -14.0°$	$25.0° \times 3.0°$	$75.0\,\mathrm{deg}^2$	$22.5° \geq l > 15.0°$	$-11.0° \geq b > -14.0°$	$7.5° \times 3.0°$	$22.5\,\mathrm{deg}^2$
4	$15.0° \geq l > 350.0°$	$-14.0° \geq b > -16.0°$	$25.0° \times 2.0°$	$50.0\,\mathrm{deg}^2$	$22.5° \geq l > 15.0°$	$-14.0° \geq b > -16.0°$	$7.5° \times 2.0°$	$15.0\,\mathrm{deg}^2$
5	$15.0° \geq l > 350.0°$	$-16.0° \geq b > -19.0°$	$25.0° \times 3.0°$	$75.0\,\mathrm{deg}^2$	$350.0° \geq l > 342.5°$	$-16.0° \geq b > -19.0°$	$7.5° \times 3.0°$	$22.5\,\mathrm{deg}^2$
6	$15.0° \geq l > 350.0°$	$-19.0° \geq b > -22.0°$	$25.0° \times 3.0°$	$75.0\,\mathrm{deg}^2$	$350.0° \geq l > 342.5°$	$-19.0° \geq b > -22.0°$	$7.5° \times 3.0°$	$22.5\,\mathrm{deg}^2$
7	$15.0° \geq l > 350.0°$	$-22.0° \geq b > -25.0°$	$25.0° \times 3.0°$	$75.0\,\mathrm{deg}^2$	$350.0° \geq l > 342.5°$	$-22.0° \geq b > -25.0°$	$7.5° \times 3.0°$	$22.5\,\mathrm{deg}^2$
8	$15.0° \geq l > 350.0°$	$-25.0° \geq b > -28.0°$	$25.0° \times 3.0°$	$75.0\,\mathrm{deg}^2$	$350.0° \geq l > 342.5°$	$-25.0° \geq b > -28.0°$	$7.5° \times 3.0°$	$22.5\,\mathrm{deg}^2$
9	$15.0° \geq l > 350.0°$	$-28.0° \geq b > -30.0°$	$25.0° \times 2.0°$	$50.0\,\mathrm{deg}^2$	$350.0° \geq l > 342.5°$	$-28.0° \geq b > -30.0°$	$7.5° \times 2.0°$	$15.0\,\mathrm{deg}^2$

Note: The science field stretches across the Galactic Prime Meridian which leads to the longitude ranges to be seemingly mathematically incorrect as the angle jumps from $0°$ to $360°$.

Therefore, stripe four and nine have a lower height of 2° so that stripe five may contain the Coronet cluster and its immediate surrounding latitude wise. The width of the stripes within their respective science and control fields stay the same, measuring 25° and 7.5°, respectively. The coordinate ranges in Galactic longitude and latitude $(glon,\ glat)$ are listed in Table 2.1.

2.2 Source selection

Due to the size of the science field described in the previous Section, stretching over a Galactic latitude range from -5° to -30°, the inhomogeneous density of the stellar background population provides significant challenges, with increasing density toward the Galactic mid-plane. To estimate the influence of the contaminating population on the sample in the science field, it was necessary to divide the science field into nine individual stripes along certain latitude ranges listed in Table 2.1, and shown in Figure 2.1. Each of these stripes has its own control field stripe in the same latitude, located to the west of the science field for the first four stripes closest to the galactic plane, and to the east of the science field for the five stripes the furthest away from the galactic plane as has been described in detail in Section 2.1.

However, regions with a high contaminating fraction, especially close to the Galactic plane and with only few to no YSOs associated with the CrA molecular cloud, were especially difficult to analyze. To compensate for this, I constrained my data set to only include stars that are closer than 250 pc, using a distance estimate from *Gaia* parallaxes (see Equation 1.2). This significantly reduces the number of extragalactic contaminants and background AGB stars. The necessary cross-match with *Gaia* however comes at the caveat that highly reddened or embedded YSOs are excluded as well, due to lacking sensitivity of *Gaia* in the infrared regime. The sources for which this is true are most likely very young class 0 and class I objects which are expected to be found in the regions of high dust column density. Since these are also the regions that are observed with *VISIONS* and *Spitzer*, any sources removed due to a missing *Gaia* counterpart should be included in the selections using *VISIONS* data, where I also rely on high resolution images, see Section 2.2.3.2 for further details.

2.2.1 Infrared Excess in color-color and color-magnitude space

As has been shown by Koenig et al. (2012) and Koenig & Leisawitz (2014), who use *WISE* photometry to select YSOs with infrared-excess, young stellar objects inhabit certain regions in different CCDs and CMDs due to their excess emission in the infrared wavelengths. Similar diagrams have been used by Gutermuth et al. (2009) using *Spitzer* photometry to identify YSOs with one kiloparsec of the sun. The method developed by them has been used in a modified version by Großschedl et al. (2019) to identify and compile a most complete set of young stellar objects in Orion A. Großschedl et al. (2019) used NIR data from *VISION* (Meingast et al. 2016b), which can be seen as pilot project to the later *VISIONS* survey. Therefore, the selection methods in Großschedl et al. (2019) are similar to the methods in this thesis within the *VISIONS* coverage. Based on these studies, as well as the works of Evans et al. (2009a), Peterson et al. (2011) and Dunham et al. (2015), I chose the combinations of filter bands for my YSO selection. The final selection is a combination of several individual sub selections using different combinations of IR bands from several observation campaigns.

2.2.1.1 WISE quality criteria

In order to get a robust sample of *WISE* sources, a number of quality criteria need to be applied to the *WISE* photometric data. In the following I describe the cuts that were applied to remove unreliable photometry, which largely stems from extragalactic objects (e.g. AGNs, Quasars, or unresolved star-forming spiral galaxies), background AGB stars, Herbig-Haro objects (e.g. jets from stellar outflows), or nebulosities of the surrounding ISM.

In general I adopted the scheme described by Koenig & Leisawitz (2014) and Großschedl et al. (2019), and used selection criteria in signal to noise (snr) versus reduced chi-square (χ^2) of the profile fit from *WISE* photometry, to identify and exclude sources with inferior photometry from the *WISE* data. The χ^2 value in the *WISE* catalog estimates how well the model point spread function fits the given source in the image. As is described in Koenig & Leisawitz (2014), the χ^2 takes values close to one for valid point sources. This is also true for fake point sources, as long as the signal to noise ratio is low, for higher snr however, the χ^2 will also increase, hence showing a trail of sources departing upwards from the bottom region of good point sources (see Figure 2.2). According to Koenig & Leisawitz (2014) the fraction of these fake point sources is especially high for the two longer wavelength filters $w3$ and $w4$, as they are very susceptible to nebulous background emission in the images. This results in a large fraction of fake detections in these filters, to which no apparent point source can be attributed to when looking at the *WISE* images.

Moreover, Koenig & Leisawitz (2014) found, that values of the χ^2 greater than two, are a result of either point sources with close neighbors (e.g. binary stars), point sources that are located in regions with extended emission, or the object being an extended source all together, such as a resolved background galaxy or a protostar with outflow cavities. Figure 2.2 shows the distribution of the sources found in the Corona Australis science field, in snr versus χ^2. With the change in stellar population density over the entire science field, the quality criteria for the *WISE* filters $w3$ and $w4$ are slightly different in the last few stripes. The boundaries of the quality cuts are chosen so that the low snr sources with high χ^2 are rejected, whereas sources with high snr and high χ^2 are kept. Moreover, I use the *known sources* (see Section 1.4.2.1) to help guide the decision on where to place the cuts. Due to the higher probability of false detections in the *WISE* $w3$ and $w4$ bands, in combination with the field star density gradient mentioned above, the stripes further away from the Galactic mid-plane have slightly different quality cuts in these two filters, compared to stripes closer to the mid-plane. The exact conditions for each filter in the different stripes are listed in the following. In order to link individual conditions in the equations below I use the logic operators for *and* ($\wedge$) and *or* ($\vee$).

$\boldsymbol{w1}$: Conditions are the same for all stripes.

$$
\begin{aligned}
&[(w1snr > 37.5) \wedge (w1rchi2 < 4\, w1snr - 147.5)] && \vee \\
&[(w1snr > 10) \wedge (w1rchi2 < 2.5)] && \wedge \\
&[w1sigmpro < 0.5] && (2.1)
\end{aligned}
$$

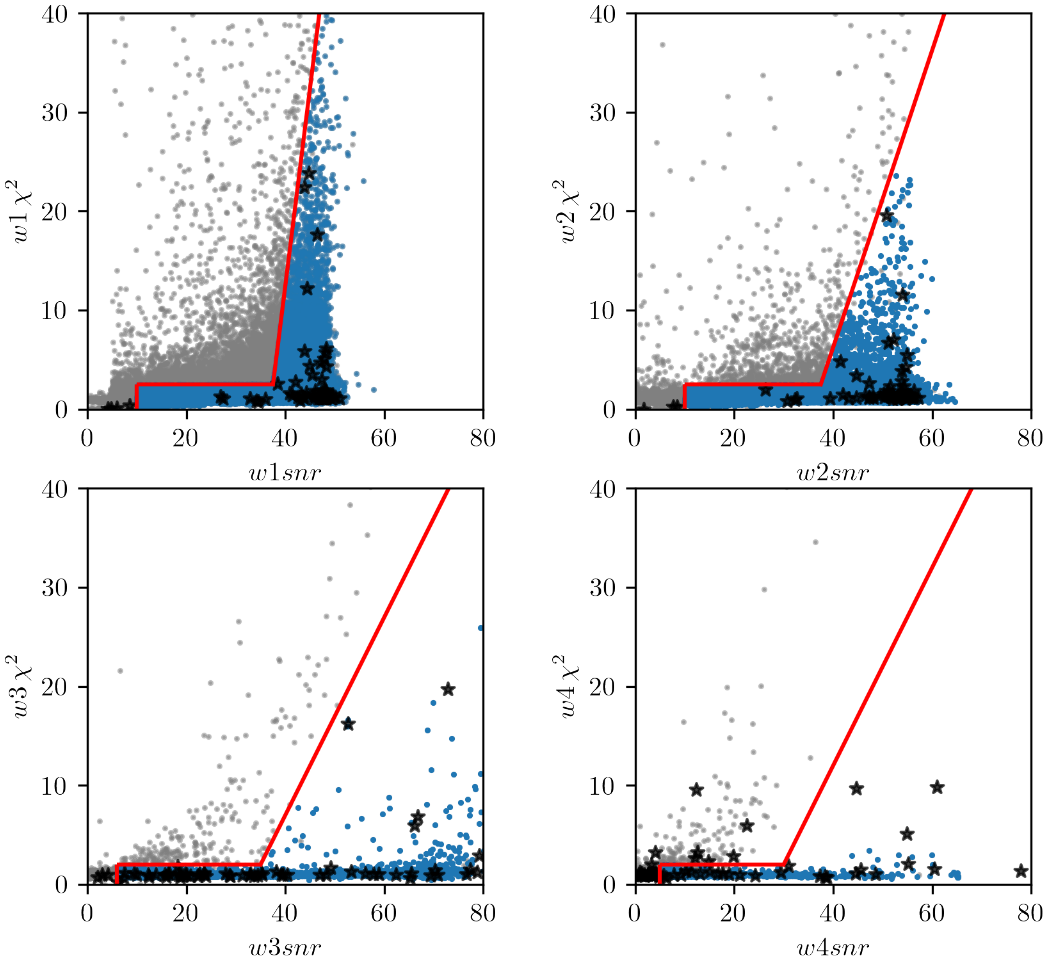

Figure 2.2: *WISE* quality criteria (*snr* versus reduced χ^2), to exclude fake point sources. For true point sources the reduced χ^2 will take values close to one, regardless of the signal to noise ratio. Fake point sources, however, populate the same region for low snr, but χ^2 increases with increasing snr for these sources. Additionally, point sources which are located crowded regions, or exhibit a luminous sky background due to the surrounding medium, or true extended sources such as galaxies, are indicated by a reduced χ^2 values of roughly two (Koenig & Leisawitz 2014). Black stars are the *known sources* introduced in Section 1.4.2.1. The plots shown here were made from the data within stripe 5 of the SF.

$\boldsymbol{w2}$: Conditions are the same for all stripes.

$$\begin{aligned} &[(w1snr > 37.5) \wedge (w1rchi2 < 1.5\, w1snr - 53.75)] && \vee \\ &[(w1snr > 10) \wedge (w1rchi2 < 2.5)] && \wedge \\ &[w1sigmpro < 0.5] && \end{aligned} \tag{2.2}$$

$\boldsymbol{w3}$: Stripes 1–8.

$$\begin{aligned}&[(w1snr > 33) \wedge (w1rchi2 < 1\,w1snr - 33)] &&\vee\\ &[(w1snr > 10) \wedge (w1rchi2 < 2.5)] &&\wedge\\ &[w1sigmpro < 0.5] && \end{aligned} \tag{2.3}$$

Stripe 9.

$$\begin{aligned}&[(w1snr > 30) \wedge (w1rchi2 < 1\,w1snr - 28)] &&\vee\\ &[(w1snr > 6) \wedge (w1rchi2 < 2)] &&\wedge\\ &[w1sigmpro < 0.5] && \end{aligned} \tag{2.4}$$

$\boldsymbol{w4}$: Stripes 1–6.

$$\begin{aligned}&[(w1snr > 30) \wedge (w1rchi2 < 1\,w1snr - 28)] &&\vee\\ &[(w1snr > 5) \wedge (w1rchi2 < 2)] &&\wedge\\ &[w1sigmpro < 0.5] && \end{aligned} \tag{2.5}$$

Stripe 7.

$$\begin{aligned}&[(w1snr > 20) \wedge (w1rchi2 < 1\,w1snr - 18)] &&\vee\\ &[(w1snr > 6) \wedge (w1rchi2 < 2)] &&\wedge\\ &[w1sigmpro < 0.5] && \end{aligned} \tag{2.6}$$

Stripe 8 and 9.

$$\begin{aligned}&[(w1snr > 14) \wedge (w1rchi2 < 1\,w1snr - 12)] &&\vee\\ &[(w1snr > 6) \wedge (w1rchi2 < 2)] &&\wedge\\ &[w1sigmpro < 0.5] && \end{aligned} \tag{2.7}$$

Furthermore, since we expect YSOs to appear as point sources to the instruments of the *WISE* satellite, it is beneficial to filter out extended sources. An exception to point like YSOs are proto-stars with feedback, such as outflow cavities, which also appear as extended sources. However, these sources are the most prominent in images due to their peculiar shapes, and have high probability to have been previously discovered.

One possible approach to filter out extended sources is described by Großschedl et al. (2019), which utilizes aperture measurements of *WISE* sources done with different aperture radii. In principle, the flux of an isolated point source measured with two apertures of different size, should be the same for both apertures. When regarding an extended source however, we expect more flux being measured by the larger aperture of the two, since the smaller aperture may not be able to encompass the entire source. Therefore, when computing the difference between the flux measured by two differently sized apertures, the result is expected to be roughly zero for point like sources, and give values which differ significantly from zero for extended sources. One exception are very bright sources, as they may appear more extended, especially when they are close to being saturated, when compared to faint sources.

For my thesis I adopted the aperture sizes used by Großschedl et al. (2019) on Orion A, which is based on Meisner & Finkbeiner (2014). The plots in Figure 2.3 show the magnitude differences of apertures one and six, as well as the difference between apertures one and eight out of the available aperture sizes, for all four filter bands in *WISE*. The size of the apertures one, six and eight are $5.5''$, $19.25''$, and $49.5''$, respectively. Examining the plots, we see a sequence to the left of the plot, which turns off to the right for very bright sources. This sequence corresponds to sources that were detected as point sources. Additionally there is a wide base of fainter sources, which stretches to the right. For these sources significant additional flux is measured in the largest apertures, which indicates an extended nature of the object. Großschedl et al. (2019) found a distinct second over-density of extended sources, which stems from nebulosities and knots in the Orion A molecular cloud. Compared to Orion A, Corona Australis is a much smaller star-forming region, which exhibits an insufficient number of detections of this origin to form a significant second overdensity similar to the one found in Orion A. Therefore, this second over-density is less pronounced in the plots in Figure 2.3, and only barely visible in the longest wavelength filters $w3$ and $w4$.

In order to solely select point sources, only sources situated to the left and above of the solid line in Figure 2.3 are selected. The slope starting at the bright end of the vertical cut is made to include bright point sources that otherwise would fall into the regime of extended objects, which are in most cases contaminating measurements, such as galaxies and nebulosities. The *WISE* aperture photometry is named as follows: `w?mag_#`, where the question mark is an integer number ranging from 1–4 corresponding to the filter band, and the hash sign can take integer values 1–8, which stand for the aperture size used. The exact condition for all filter bands in all stripes are listed below. The difference between two apertures is indicated by writing the two aperture numbers in subscript, so that $w1mag\_1 - w1mag\_6$ becomes $w1_{16}$ for short.

$\boldsymbol{w1}$:

$$[(w1_{16} < 1.8) \vee (w1 < 12.9 - 3(w1_{16}))] \wedge [(w1_{18} < 2.5) \vee (w1 < 13.5 - 3(w1_{18}))] \tag{2.8}$$

$\boldsymbol{w2}$:

$$[(w1_{16} < 1.8) \vee (w1 < 11.65 - 3(w1_{16}))] \wedge [(w1_{18} < 2.2) \vee (w1 < 12.55 - 3(w1_{18}))] \tag{2.9}$$

$\boldsymbol{w3}$:

$$[(w1_{16} < 2.1) \vee (w1 < 8.2 - 2(w1_{16}))] \wedge [(w1_{18} < 2.1) \vee (w1 < 8.2 - 2(w1_{18}))] \tag{2.10}$$

$\boldsymbol{w4}$:

$$[(w1_{16} < 2.2)] \wedge [(w1_{18} < 2.5)] \tag{2.11}$$

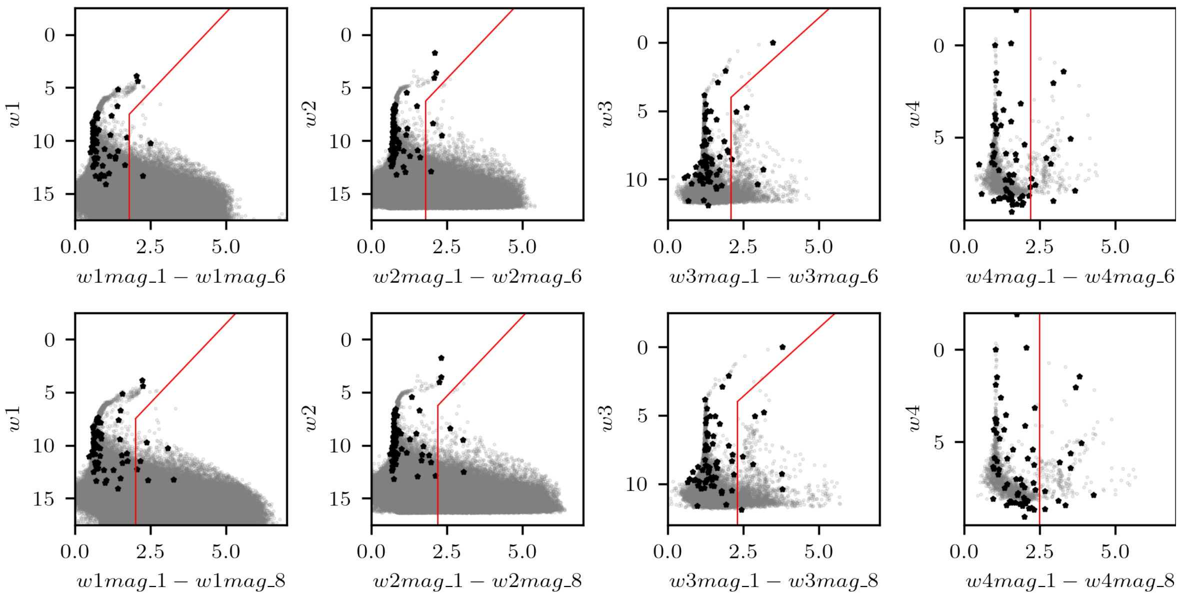

Figure 2.3: *WISE* extended sources filter diagram showing difference in aperture photometry versus PSF photometry. The gray dots show all sources contained in the fifth latitude stripe for which the photometric uncertainty $w?sigmpro < 0.5$ and the signal to noise $w?snr > 5$. The black stars show the distribution of *known sources* from Peterson et al. (2011) and Dunham et al. (2015) introduced in Section 1.4.2.1. The red lines show the criteria to separate point sources and extended sources used in this study. Sources that lie to the right of the line are rejected from the sample. The individual panels plot *WISE* magnitudes from PSF fitting on the y-axis and the difference between the magnitude determined from two different sized apertures on the x-axis. The columns from left to right feature the same plots, but for the four *WISE* bands $w1$ to $w4$. The top row uses the difference between aperture one and six ($w?mag\_1 - w?mag\_6$), whereas the second row shows the difference between aperture one and eight ($w?mag\_1 - w?mag\_8$).

Finally, valid sources are pre-selected by applying an additional cut on quality flags that are provided in the *WISE* catalog, the contamination and confusion flags (`cc_flags`), which indicate any potential problems with the photometric measurements. The main issues are either spurious detections or contamination from bright sources in the vicinity. The artifacts which can negatively influence the flux measurements of a detected source can be diffraction spikes, residual signal from a bright source in the previous exposure, halos, or optical ghosts. Further distinction is made by using either upper case or lower case letters, which differentiate between confusion or contamination. If a detection is flagged as confusion (upper case letter). This means that the detection was made due to one of the contaminating artifacts and not due to an astronomical object, hence, a contamination artifact has been confused for an astronomical object. If a detection is flagged as contamination (lower case letter), an astronomical object was detected, but the photometric measurement is impaired by an artifact such as a diffraction spike of a nearby bright star. The letters used are "D" and "d" for diffraction spikes, "P" and "p" for persistent signal from previous exposures, "H" and "h" for halos, and "O" and "o" for optical ghosts. In order to get a robust working sample, I chose to reject all detections which are not associated with an actual astronomical object, such as a star, which is indicated by Capital letters as mentioned above. This has also been done by Großschedl et al. (2019) in Orion A when using *WISE* data.

2.2.1.2 Spitzer quality criteria

To clean the *Spitzer Enhanced Imaging Products* catalog (see Section 1.3.1.3), I followed the instructions to get a robust sample, given in the *Spitzer Enhanced Imaging Products Explanatory Supplement*[2] (SEIP-ES). It lists a number of conditions regarding signal to noise ratio and detection type for the IRAC and MIPS instruments. These conditions are very general and may exclude a great fraction of sources from the data tables. It is mentioned within the document, that if one wishes to retrieve these sources, the original images should be reduced, and sources extracted personally, rather than using the provided catalogs ready for download. I opted for using the provided data tables and applied the suggested quality cuts given in the SEIP-ES, which are listed below, since doing the data reduction and source extraction myself would have greatly surpassed the scope of this thesis.

1. For the four IRAC flux measurements $i?snr > 3$ and for the MIPS measurement $m1snr > 10$ should be used. These conditions are reflected in the five *fluxtype* columns. If $fluxtype = 1$ the signal to noise ratio is greater than the aforementioned thresholds.

2. Exclude measurements that are influenced by neighboring saturated sources. If this is the case, the $fluxflag$ column is set to 1. Therefore, I select sources with $fluxflag = 0$.

3. Remove MIPS measurements that my have been contaminated by nearby saturated sources by selecting sources which fulfill $m1\_brtfrac < 0.5$ and $m1\_extfrac < 0.5$.

4. Make sure to discard any sources that may have been influenced by soft saturation indicated by the $?softsatflag$, where $?$ acts as a placeholder for the four IRAC bands. I again selected sources with $?softsatflag = 0$.

For all remaining sources that are left after these cuts were applied, it is suggested in the SEIP-ES to use the $3.8''$ aperture for the IRAC filters, indicated by the *_ap1* suffix for IRAC flux density measurements and the PSF fitted flux measurement of the MIPS 1 filter indicated by the *_psf* suffix. For details on the conversion of *Spitzer* fluxes to magnitudes see Appendix B.

2.2.1.3 VISIONS quality criteria

In order to get a robust sample from the *VISIONS* survey, I use the quality flags provided for each filter in the data tables, as provided by Stefan Meingast (private communication). This flag indicates the quality of the measurement and grades them alphabetically ranging from "A" (best) to "C" (worst) and "X" (invalid). Invalid measurements indicated by the "X" have not passed one or more of the following criteria:

[2] All selection criteria for *Spitzer* photometry used in this work were taken from page 9 in the document located at following URL (Date the document was retrieved: December, 2021). https://irsa.ipac.caltech.edu/data/SPITZER/Enhanced/SEIP/docs/seip_explanatory_supplement_v3.pdf

- SExtractor flag < 4 (This means that the detected source can been minimally influenced by nearby sources or bad pixels, or the source has been deblended by the SExtractor algorithm, see Appendix C)
- Did not pass a series of quality filters, meaning that sources are rejected if any of the following conditions are true: ($SNR < 0$, $FLUX < 0.01$, $FWHM < 0.2$)
- The source is very close to the image border
- Did not pass the nebulosity filter (Extended source with low snr)

The source extraction for *VISIONS* is performed with *SExtractor* (develeoped by Bertin & Arnouts 1996), which provides an internal flagging subroutine to indicate any problems encountered during source detection and photometry measurement. For this purpose an 8 bit mask is used where each bit stands for a different complication. Using LSB_0[3] the bits of increasing value also indicate problems of increasing concern. For further details on the *SExtractor* quality control byte see Appendix C. In general all *VISIONS* photometry for which $QFLG == X$ is true, I use *2MASS* photometry if available, which is complementary to the fainter *VISIONS* measurements.

2.2.1.4 Interstellar Extinction

In the following sections I will use a number of color-magnitude and color-color diagrams to select sources by their infrared-excess. Interstellar extinction causes an infrared-excess for sources located behind (or in) regions with high dust column density. This can affect sources both with and without intrinsic infrared-excess. However, the reddening caused by interstellar extinction can often be distinguished in certain CCDs, since sources are shifted on the extinction law relative to the main sequence. Therefore, in order to estimate the direction of interstellar reddening in the following diagrams, I show the reddening vector in K_s magnitudes in each CMD and CCD. To get the direction of reddening to interstellar extinction I use the extinction law by Meingast et al. (2018). Table 2.2 is adopted from Meingast et al. (2018), which gives the extinction law for all filters used in this study.

2.2.2 Selections with all-sky data using 2MASS, WISE, and Gaia

This section focuses on selections that were made by only using all-sky observations from *2MASS*, *WISE*, and *Gaia*, to select sources from the 625 deg^2 science field (see Section 2.1 and Figure 2.1). Therefore, I take data from the *2MASS* survey for near-infrared, and data from *WISE* for the mid-infrared range. Using all-sky NIR and MIR data on a science field of this extent comes with certain complications such as contamination from extragalactic sources, and AGB stars, while the latter get increasingly problematic toward the Galactic center and mid-plane, which is the case for the northern most stripes of the chosen science field. Therefore, the

[3] LSB_0 is a standard where bit enumeration begins on the right with the least significant bit (LSB) and increases to the left until it reaches the most significant bit (MSB). For an 8 bit number, the $n = 0$ bit has the value $2^n = 1$ whereas the $n = 7$ bit has the value $2^n = 128$. Hence the number 11010101 in binary would equate to $2^0 + 2^2 + 2^4 + 2^6 + 2^7 = 1 + 4 + 16 + 64 + 128 = 213$.

Table 2.2: This table lists the interstellar extinction law for all photometric filters used in this thesis. It was derived from the *VISIONS* pilot project *VISION* by Meingast et al. (2018) with *WISE* values for the WISE filters listed in Großschedl et al. (2019).

Filter	$\langle A_{m_\lambda}/A_{K_s} \rangle$
J	2.50
H	1.55
K_s	1.00
W1	0.79
W2	0.55
W3	0.61
W4	0.43
I1	0.64
I2	0.56
I3	0.50
I4	0.51
M1	0.45

2MASS and *WISE* data has been cross-matched with *Gaia*, and a distance cut is applied, to select sources that are no further away from the sun than $250\,\text{pc}$ (see Equation below).

$$d \leq 250\,\text{pc} \tag{2.12}$$

The *Gaia* distance cut is made to pre clean the data from distant background sources, which would otherwise contaminate my selection. This is reasonable, as the majority of YSOs is located in regions with little extinction are, in combination the close distance of CrA ($d \approx 150\,\text{pc}$), likely detected by *Gaia*. Thus, applying this distance cut potentially excludes a negligible number of possible YSO candidates.

The cross-match with *Gaia* adds parallaxes, making it possible to estimate distances to the individual stars, which are estimated form the inverse of the parallax ($^1/_{\varpi['']} \approx d[\text{pc}]$). This is a valid assumption for relatively nearby sources ($d < 1000\,\text{pc}$), such as in CrA and when applying quality criteria to the *Gaia* astrometry. Yet, even with the *Gaia* distance cut to remove contaminating sources at distances greater than $250\,\text{pc}$, I apply the classical methods developed by Koenig et al. (2012); Koenig & Leisawitz (2014) and Großschedl et al. (2019) to identify and remove any sources that can contaminate my YSO selection. Moreover, by adding *Gaia*, I can use absolute magnitudes in favor of observed magnitudes, which are used for the color-absolute-magnitude diagrams (CAMDs) in this section.

In order to distinguish between observed and absolute magnitudes, I will use upper letters to denote absolute magnitudes and lower case letters for observed magnitudes. CAMDs are only used for the selections using the all-sky IR survey described in Sections 2.2.2.1 and 2.2.2.2. The CCDs and CMDs shown in the following sections show the selection criteria for sources in the fifth stripe of the science field (see Figure 2.1) which contains the Coronet cluster. The diagrams will always show the sources of the science field stripe in the left panel, the sources of the control field stripe in the center panel and the IR selected *known sources* in the right panel. Furthermore, gray dots will show all sources in the fifth science or control field stripe, whereas blue dots will show the selected sources, unless specified otherwise in the figure captions. Finally the blue stars shown in the right panels show the known IR selected sources from the literature (see Section 1.4.2.1), in order to estimate which spaces YSOs occupy in the different CCDs and CMDs.

2.2.2.1 WISE selection

The mid-infrared photometry provided by *WISE* plays an integral part in this work when sources with infrared excess emission are selected with a combination of color-absolute-magnitude and color-color diagrams to mitigate the remaining contamination. In a first step I use one selection method described in Koenig & Leisawitz (2014), which combines photometry from the *w1*, *w2*, and *w3* filters, in a color-color and color-magnitude diagram. In general there are two main contaminating components that need to be removed. Extragalactic sources—such as AGN and star-forming galaxies—since they can exhibit the same colors as YSOs. However, the majority of galaxies is fainter when compared to YSOs at the distance of CrA, since they are located far beyond the Milky Way, and field stars that are not associated to the CrA star-forming region.

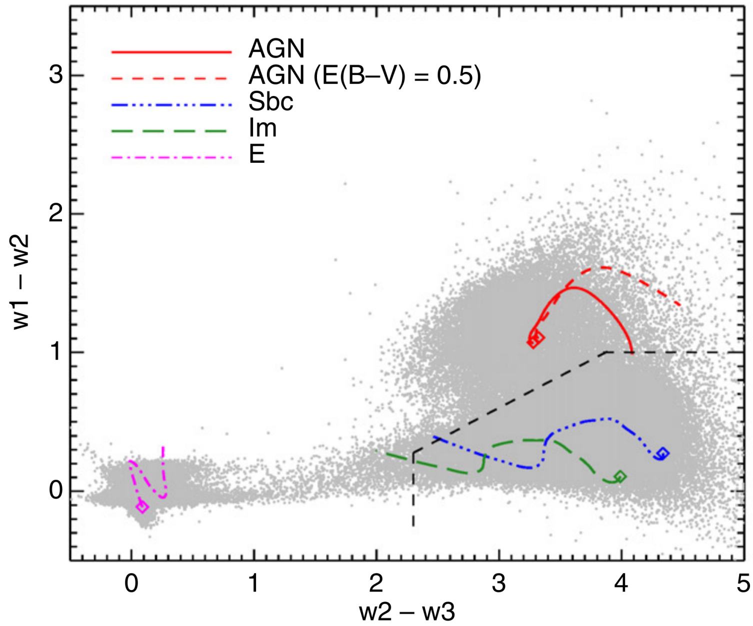

Figure 2.4: *WISE* color-color diagram ($w2 - w3$ versus $w1 - w2$), showing contamination by AGN and galaxies. Shown are the detected sources from a region surrounding the galactic north pole—gray dots—and superimposes the data from the template SEDs for galaxies and active galactic nuclei, to assess where they can be found in this color space. The area below and right to the black dashed line indicates which sources were excluded from the search for young stellar objects by Koenig & Leisawitz (2014). The red, solid and dashed lines represent active galactic nuclei (**AGN**). Star-forming galaxies are represented by the blue triple dot-dashed line, showing spiral galaxies, and the green dashed line for irregular galaxies, of the Hubble classes **Sbc** and **Im**, respectively. Finally, elliptical galaxies (**E**) are highlighted by the magenta dash-dotted line. *Image credit:* Figure 4, in Koenig & Leisawitz (2014)

Extragalactic sources are addressed with the help of a study by Assef et al. (2010), where template spectral energy distributions of extragalactic objects were developed. These templates were in return used by Koenig & Leisawitz (2014) to map the location of AGN and galactic contamination in a *WISE* color-color diagram (see Figure 2.4). The SED-modeles by Assef et al. (2010) take into account elliptical galaxies, spiral galaxies, irregular galaxies, and active galactic nuclei, denoted as **E**, **Sbc**, **Im**, and **AGN**, respectively. In this study I adopt the exclusion cuts for this extragalactic contamination from Koenig & Leisawitz (2014), since the observed regions towards the galactic poles—which were used by Koenig & Leisawitz (2014)—are expected to consist mostly of distant galaxies and only very few stars from our own galaxy. The black dashed lines in Figure 2.3 show the border for sources, which are removed from the data sample if they fall in the area encompassed in the lower right corner. Deriving theoretical colors for **SBc** and **Im** galaxies form the theoretical model SEDs, places these galaxies inside the previously mentioned boxed in area, if they are plotted in a *WISE* CCD. Therefore, it can be argued that this is the domain of star-forming galaxies in the $w2 - w3$ versus $w1 - w2$ color-color space. Due to the distance cut mentioned above, the Koenig & Leisawitz (2014) extragalactic contamination cut does not have to be applied in this selection.

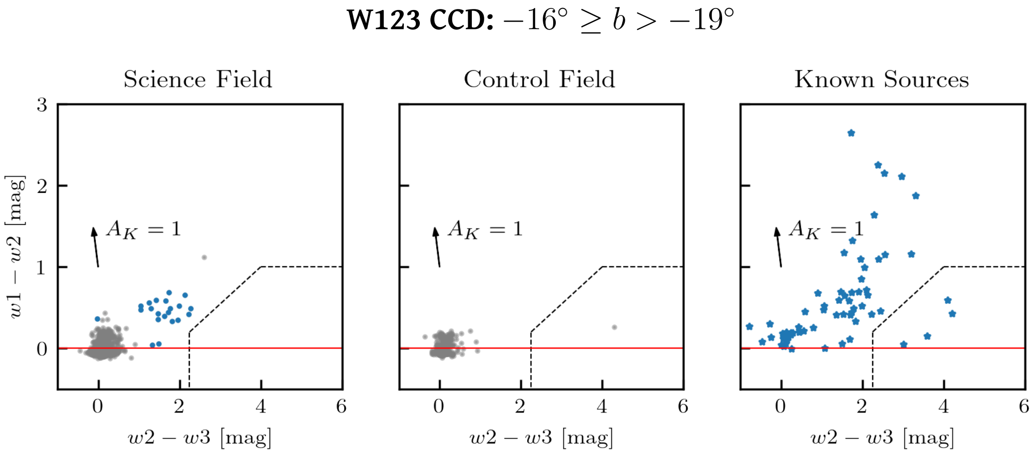

Figure 2.5: *WISE* color-color diagram ($w2 - w3$ versus $w1 - w2$). This color space is used to remove sources with inferior photometry, in combination with the CCD in Figure 2.10 YSO candidates with IR excess are selected. Any detections with $(w1 - w2) < 0$ are most likely due to inferior photometry. In addition to that I show the extragalactic exclusion cut from Koenig & Leisawitz (2014), which is not applied to my data as the distance cut has removed galaxies beforehand. Thus, I only reject sources that fall below the threshold for unreliable photometry described earlier. *Left panel:* Gray dots show sources after the distance cut, whereas blue dots show all sources where the color-magnitude cuts have been applied. *Middle panel:* The same plot for the control field. *Right panel:* It can be seen, that some previously known YSOs fall in the boxed in area to the bottom right, which would be excluded by the Koenig & Leisawitz (2014) extragalactic contamination cut, which in combination with the *Gaia* distance cut supports the decision to ignore extragalactic cut by Koenig & Leisawitz (2014) (black dashed box).

Figure 2.5 shows the color-color diagram ($w2 - w3$ versus $w1 - w2$) with the selection criteria where only those sources are accepted which lie above the red line. Any source that falls below the threshold in $w1 - w2$ color, is regarded to be contamination caused by unreliable photometry. Regardless of the distance cut, it is possible, especially in regions with extended background emission (nebulae) and densely populated areas, that there are sources whose $w3$ photometry has been impaired by these environmental conditions, so that these unreliable sources lie at the bottom of the CCD, showing false infrared-excess. The boxed in area to the bottom right is the extragalactic contamination cut adopted from Koenig & Leisawitz (2014), in which high contamination due to extragalactic sources is expected. Due to the distance cut applied earlier, this area however is already very clean compared to Figure 2.7 where no distance cut was applied to the stars in the CCD. Therefore, I refrain from applying this cut to the data at hand, and trust that any sources left within this domain are potential YSO candidates, which can also fall in this area as can be seen in the right panel of Figure 2.5. To remove any detections that show inferior photometry, I use the following cut on all nine stripes.

$$(w1 - w2) > 0.05 \tag{2.13}$$

To remove more evolved stars and faint sources with inferior photometry color-absolute-

W123 CMD: $-16° \geq b > -19°$

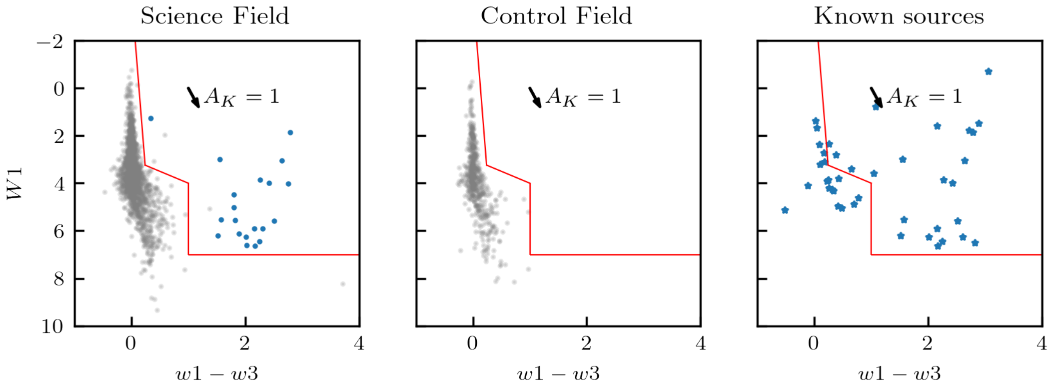

Figure 2.6: *WISE* color-magnitude diagram ($w1 - w3$ versus $W1$). Main sequence stars are removed in this color-magnitude space where sources that fall below the solid red line are removed from the sample. The bottom horizontal part of the cut is not necessarily needed as the *Gaia* distance cut removed all faint extragalactic sources. However, I keep this faint cut in order to remove possible contaminants in this area.

magnitude diagram ($w1 - w3$ versus $W1$) is used, shown in Figure 2.6. The cuts introduced here are based on the ones used by Koenig & Leisawitz (2014) but were adapted to the data for CrA. They were chosen individually for each of the nine galactic latitude stripes, while, some stripes share the same cuts given by equations 2.14-2.15. In the right panel of Figure 2.6, sources that have been previously identified as YSOs using infrared data are shown. These *known sources* are taken from Peterson et al. (2011) and Dunham et al. (2015) as described in Section 1.4.2.1. This is important to get a good estimate where bonafied YSO candidates in CrA are situated in color-magnitude space, so that the selection criteria can be set in a manner to ensure that as many of these forming stars will be left over after the cuts have been applied. The center panel shows the control field, which is used to estimate the typical background for certain Galactic latitudes. The science field is shown in the left panel. The sources that lie above the red solid line are considered to be mostly stars, since the area below this border suffers from a high contaminating fraction of main sequence stars (overdensity to the left). Even with the *Gaia* distance cut I apply a conservative cut on faint sources, which may exclude faint YSOs, but the region below the horizontal red line is sparsely populated with only one YSO candidate to the far right. This sources however turned out to be far off from the CrA young stellar population as seen projected in the sky, and does not share similar proper motions with other CrA members. Since each latitude stripe was evaluated individually, the cuts are adjusted based on the different control fields. The individual cuts are as follows:

Stripes 1–4 and 7:

$$[W1 < (w1 - w3 + 4)] \land [(W1 < 6)] \tag{2.14}$$

Stripe 5:

$$[(W1 < (w1 - w3 + 3))] \vee [((w1 - w3) > 1) \wedge (W1 < 7)] \tag{2.15}$$

Stripes 6, 8, and 9:

$$[W1 < (w1 - w3 + 3.5)] \wedge [W1 < 6] \tag{2.16}$$

With inferior photometry contaminants taken care of, the only remaining source of contamination left are-main-sequence (MS) stars. Asymptotic giant branch (AGB) stars could be another remaining contaminant, but the distance cut done with *Gaia* has already removed the majority of the AGB population, located at larger distances, similar to extragalactic sources which lie at even greater distances.. To remove main sequence stars from the sample an additional cut was applied to the data. The plots shown in Figure 2.6 also feature a steep slope to the upper left, which is drawn with the intention to remove more evolved stars that do not show any infrared-excess in this band combination. The sources that lie to the right of the red line are considered to be objects that are young and still in the formation process. The final selection of sources in the *WISE* selection is presented in Figure 2.6, with sources that fall in the area above and right of the red line being valid YSO candidates. Finally, the slope parameters for the main sequence filter are given in the following equations. These were also chosen individually for each stripe, where more than one stripe can share the same conditions.

Stripes 1–6 and 8.

$$[W1 < (30(w1 - w3) - 4)] \tag{2.17}$$

Stripe 7:

$$[W1 < (30(w1 - w3) - 3.5)] \tag{2.18}$$

Stripe 9:

$$[W1 < (30(w1 - w3) - 8)] \tag{2.19}$$

To demonstrate the effectiveness of the *Gaia* distance cut applied to the dataset before selecting YSO candidates, Figure 2.7 and 2.8 show the same color-color and color-magnitude diagrams as if I had not used *Gaia* data. It can be clearly seen, that the two diagrams are heavily contaminated by background sources. Especially the upper end of the main sequence in the CMD shows the contribution of contamination AGB and extincted main sequence stars, which scatter heavily into the domain of bright YSOs.

2.2.2.2 2MASS—WISE selection

As a first step and in preparation for the *VISIONS-WISE* selection (see Section 2.2.3.2), the data from the two all-sky surveys *2MASS* and *WISE* were combined to make three individual selections from the following filter combinations. The filters used from *2MASS* are H and K_s, and from *WISE* are w1, w2, w3, and w4.

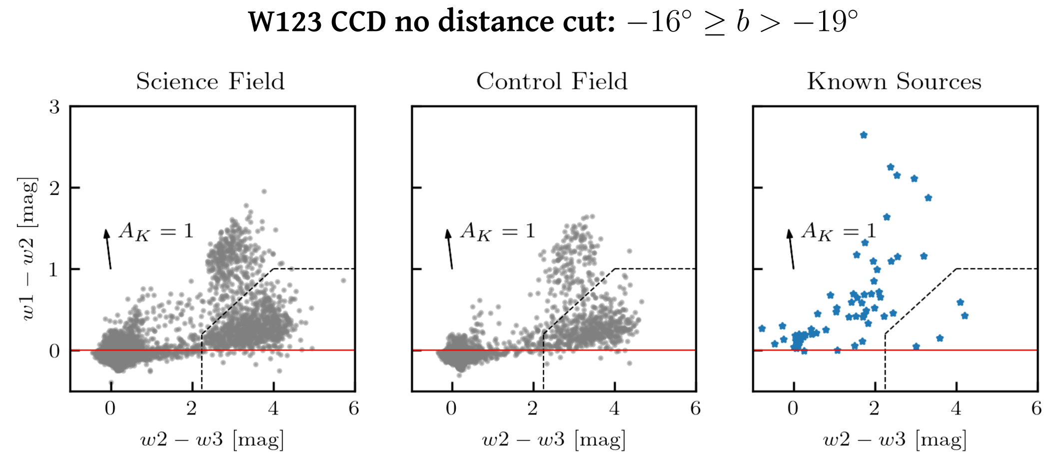

Figure 2.7: *WISE* color-color diagram ($w2 - w3$ versus $w1 - w2$) similar to Figure 2.5, but without making use of *Gaia* data for a distance cut. In direct comparison to the CCD in Figure 2.5, it is clearly visible that with a missing distance cut, the boxed in area to the lower right from the Koenig & Leisawitz (2014) extragalactic cut is densely populated by what are mostly background galaxies. The populated are above the boxed in area to the lower right is populated by AGNs, which occupy a similar color space as protostars. When comparing this Figure to Figure 2.5 we see that the CrA region is dominated by AGNs over YSOs.

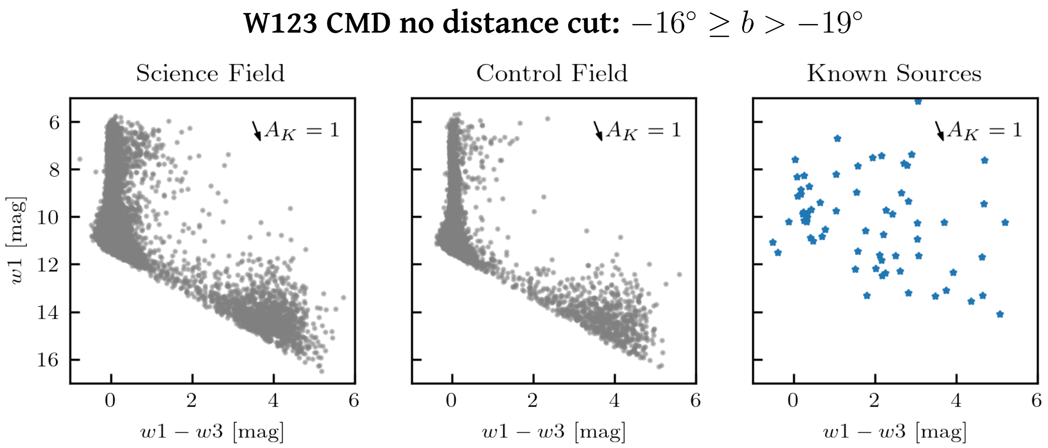

Figure 2.8: *WISE* color-magnitude diagram ($w1 - w3$ versus $w1$) similar to Figure 2.6, but without *Gaia* distance cut and only relying on observed magnitudes. Comparing this CMD to the one where the *Gaia* distance cut has been applied, it clearly suffers form massive contamination. Very prominent in this diagram are bright background stars contaminating the main sequence to the left.

K_sW123 combines K_s, w1, w2, and w3

K_sW124 combines K_s, w1, w2, and w4

HK_sW12 combines H, K_s, w1 and w2

2MASS–WISE K$_s$W123 CMD: $-16° \geq b > -19°$

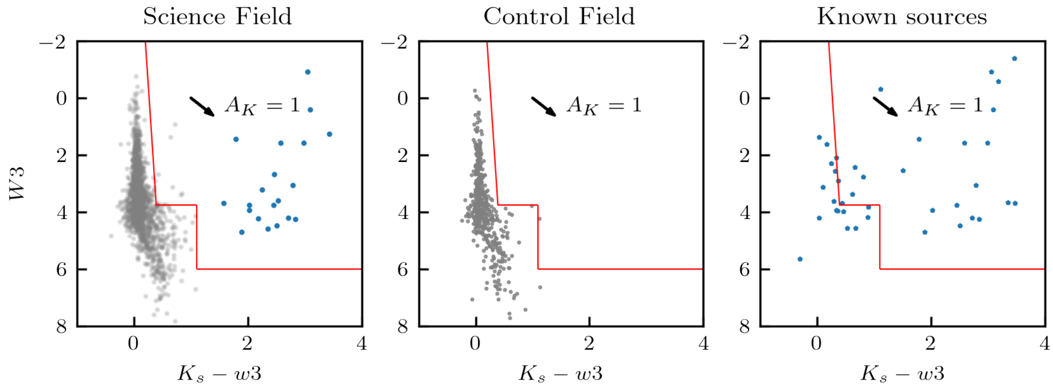

Figure 2.9: *2MASS–WISE* K$_s$W123 color-magnitude diagram ($K_s - w3$ versus $W3_{\rm abs}$). The red lines show the exclusion criteria for main sequence stars and faint sources, where detections that fall in the boxed in are to the top right are accepted. *Left panel:* Gray dots show all sources situated in the fifth stripe of the science field. Blue dots show the stars of the final K$_s$W123 selection.

2.2.2.2.a K$_s$W123 selection

In this selection I use data from *WISE* and *2MASS* in a $W3$ versus $K_s - w3$ color-absolute-magnitude diagram (see Figure 2.9) to remove the evolved population. Complementing the CMD with a color-color diagram (see Figure 2.10) using $w1 - w2$ versus $w2 - w3$, helps to further reduce contamination due to unreliable photometry. The cuts to exclude faint sources for the nine stripes of the science field are given below.

Stripes 1 and 2:

$$[W3 < 5] \wedge [W3 < (4(K_s - w3) + 3)] \tag{2.20}$$

Stripes 3 and 4:

$$[W3 < 5] \wedge [W3 < (4(K_s - w3) + {}^4\!/_3)] \tag{2.21}$$

Stripe 5:

$$[W3 < 3.75] \vee [((K_s - w3) > 1.1) \wedge (W3 < 6)] \tag{2.22}$$

Stripes 6, 7 and 8:

$$[W3 < 3] \vee [((K_s - w3) > 1) \wedge (W3 < 5)] \tag{2.23}$$

Stripe 9:

$$[W3 < 3.5] \vee [((K_s - w3) > 1) \wedge (W3 < 5)] \tag{2.24}$$

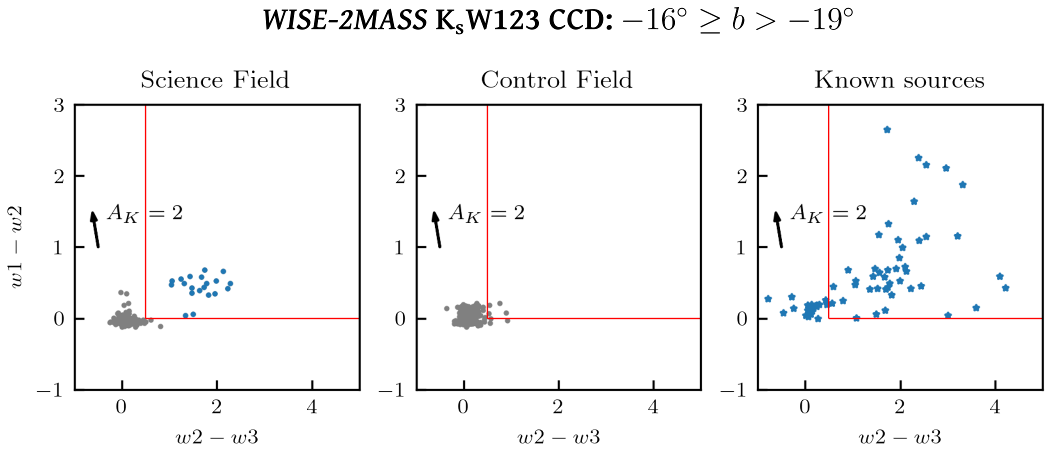

Figure 2.10: *2MASS–WISE* K$_s$W123 color-color diagram ($w2-w3$ versus $w1-w2$). The boxed in area indicated by the red lines, shows the domain of selected sources. Detections below the lower bound are expected to be contamination caused by unreliable photometry, and sources that lie to the left of the vertical cut are main sequence stars or Class III without IR-excess. *Left panel:* Gray dots show the stars within the fifth stripe of the science field. Blue dots correspond to the finally selected sources of the K$_s$W123 selection. *Middle panel:* Gray dots are the sources in the control field for the fifth stripe. *Right panel:* The infrared selected previously *known sources* are shown here and were used to make an informed decision of the cuts based on the color-color distribution of known YSOs.

To reject evolved stars from the selection in color-magnitude space, a slope roughly parallel to the main sequence is chosen. I use the same conditions for all nine stripes with the following parameters.

$$W3 < (30(K_s - w3) - 8)$$

Finally, removing contamination caused by inferior photometry is done in color-color space. More importantly, a more robust constraint for main sequence stars is implemented in the CCD and can be seen in Figure 2.10. The MS cut in color-color space is more reliable since sources without intrinsic IR-excess are located around (0, 0), and sources with intrinsic IR-excess are shifted to the right. As interstellar extinction shifts sources along the reddening vector, sources with and without intrinsic IR-excess are kept separate in color-color space (see Figure 2.10), whereas in color-magnitude space interstellar extinction shifts sources with little to no intrinsic IR-excess into the domain of sources with intrinsic IR-excess. The chosen condition for a YSO candidate in $w1 - w2$ versus $w2 - w3$ space are the same for all nine stripes and is given in the following.

$$[(w1 - w2) > 0] \wedge [(w2 - w3) > 0.5] \tag{2.25}$$

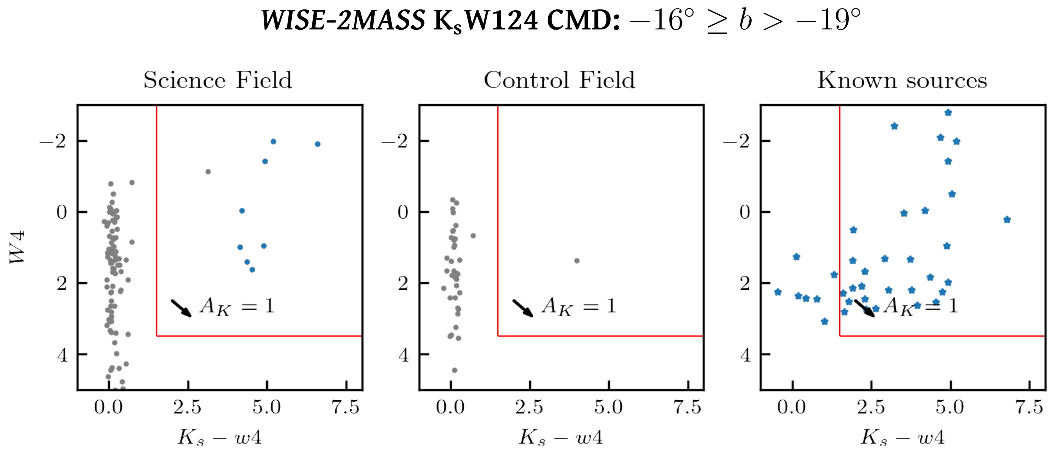

Figure 2.11: *WISE-2MASS* K_sW124 color-magnitude diagram ($K_s - w4$ versus $W4_{abs}$). Similar to the K_sW123 selection (see Figure 2.9). The vertical red line to the left represents the main sequence cut, whereas the horizontal red line towards the bottom shows the cut to exclude faint sources. Gray dots in the science field represent all sources in the fifth stripe, whereas the blue dots show the selected sources.

2.2.2.2.b K_sW124 selection

In the previous K_sW123 selection, some sources may not yet show enough infrared excess to be selected. Therefore, replacing the $w3$-band with the $w4$-band spreads out sources with IR-excess even more, separating them more clearly from evolved sources. This promises to reveal candidate YSOs which were overlooked in the previous selection. However, only a small fraction of all detections in $w4$ have robust photometric measurements as in this wavelength there is a large contaminating fraction from fake point sources due to extended background emission (see Section 2.2.1.1). In general the color-magnitude and color-color diagrams used in this K_sW124 selection are constructed similar as in Section 2.2.2.2.a. Again, I use a CMD ($W4_{abs}$ versus $K_s - w4$) to remove the main sequence population from the sample. Figure 2.11 illustrates the distribution of sources in this color-magnitude space, taken from stripe 5 of the science field, and shows the cuts to select potential YSOs. The conditions a source has to fulfill in order to be considered as a YSO candidate in this space are the same in all stripes of the science field and are given below.

$$[W4 < 3.5] \wedge [(K_s - w4) > 1.5] \tag{2.26}$$

Repeating the general idea from the previous selection, the color-color diagram here is used to reject detections with inferior photometry and give additional constraint on the main sequence population. Figure 2.12 shows the detections with photometry that has passed the quality cuts (see Section 2.2.1.1), within the latitude range of the fifth stripe, and highlights the selection criteria for sources with infrared excess. The boundaries drawn in Figure 2.12 are the same for the entire science field and are defined by the following expression.

$$[(w1 - w2) > 0] \wedge [(w2 - w4) > 0.25] \tag{2.27}$$

WISE-2MASS K_sW124 CCD: $-16° \geq b > -19°$

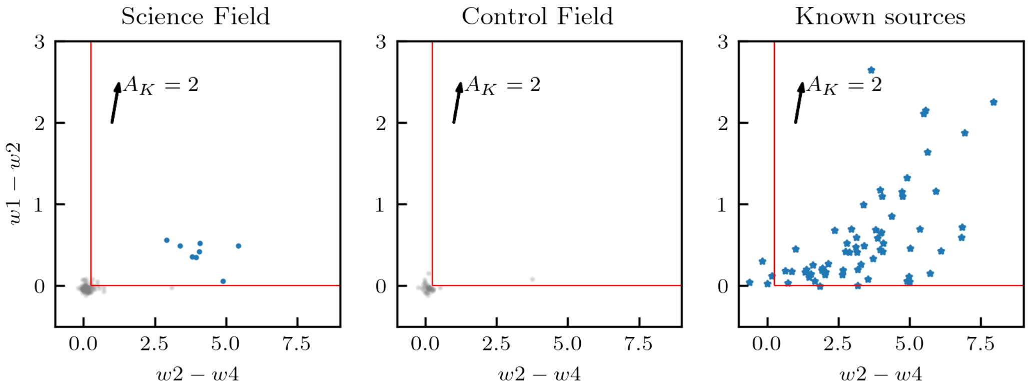

Figure 2.12: *WISE-2MASS* K_sW124 color-color diagram ($w2 - w4$ versus $w1 - w2$) to remove inferior photometry and main sequence stars. This diagram is similar to the CCD from the K_sW123 selection (see Figure 2.10), with the red lines highlighting the selection criteria. Sources above and left of the red line are selected as YSO candidates.

2.2.2.2.c HK$_s$W12 selection

In this selection I aim to reclaim any sources that may have been excluded by the previous selections. Due to a high contaminating fraction of fake point sources in the $w3$ and $w4$ band, it is likely that YSOs have been removed by the quality control criteria. As has been pointed out by Koenig & Leisawitz (2014) and Großschedl et al. (2019), the usage of near infrared photometry is helpful to regain wrongfully excluded sources. Therefore, this final combination of infrared filters aims to recover sources, that have been rejected by the selections that use the two longer wavelength filters of *WISE*. The cuts to remove faint sources and main sequence stars from the CMD are listed in the following, where stars need to fulfill the conditions given, so that they are considered as YSO candidates.

Stripes 1–4:

$$[W1 < (8(w1 - w2) + 4)] \wedge [(w1 - w2) > 0.1] \tag{2.28}$$

Stripes 5–9:

$$[W1 < (8(w1 - w2) + 3.5)] \wedge [(w1 - w2) > 0.1] \tag{2.29}$$

The CCD in Figure 2.14 is used to separate sources without IR-excess from YSOs with IR-excess. By drawing a selection boundary that runs parallel to the extinction vector it is intended to reject any main sequence stars that suffer from interstellar extinction, for example if they are located behind the Corona Australis molecular cloud. The boundaries in this space are defined by the following conditions, which must be true for sources to be YSO candidates.

$$[(K_s - w2) > 0.75] \wedge [(H - K_s) < (1.22(K_s - w2) - 0.665)] \tag{2.30}$$

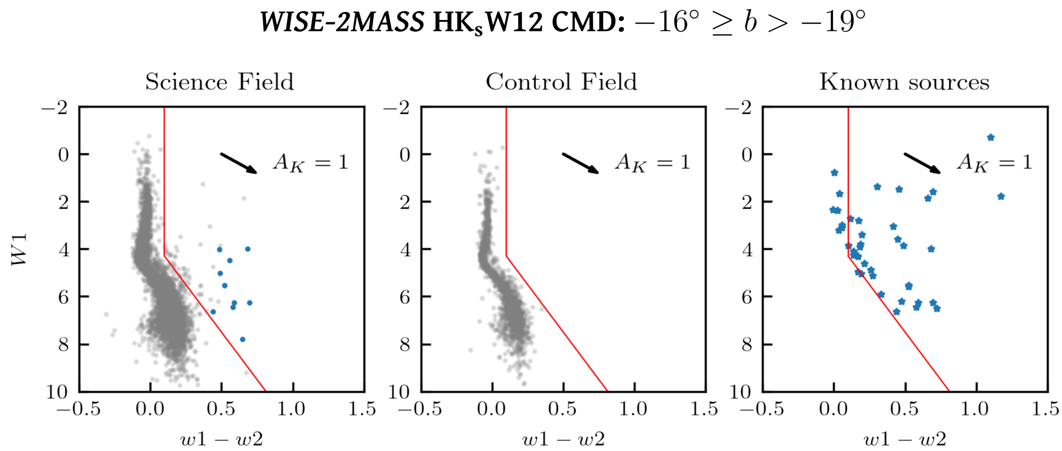

Figure 2.13: *WISE-2MASS* HK$_s$W12 color-magnitude diagram ($w1 - w2$ versus $W1_{\mathrm{abs}}$). To remove MS and AGB stars, sources that lie left of the red line, which highlights the selection criteria, are discarded. *Left panel:* Gray dots show the entire sample of latitude stripe 5 with quality cuts applied, and the blue dots show the final selection of YSO candidates in this selection (see also Figure 2.14). *Middle panel:* The gray dots show all sources after quality cuts were applied for the control filed belonging to stripe 5. *Right panel:* The blue stars are the IR selected known YSOs in CrA.

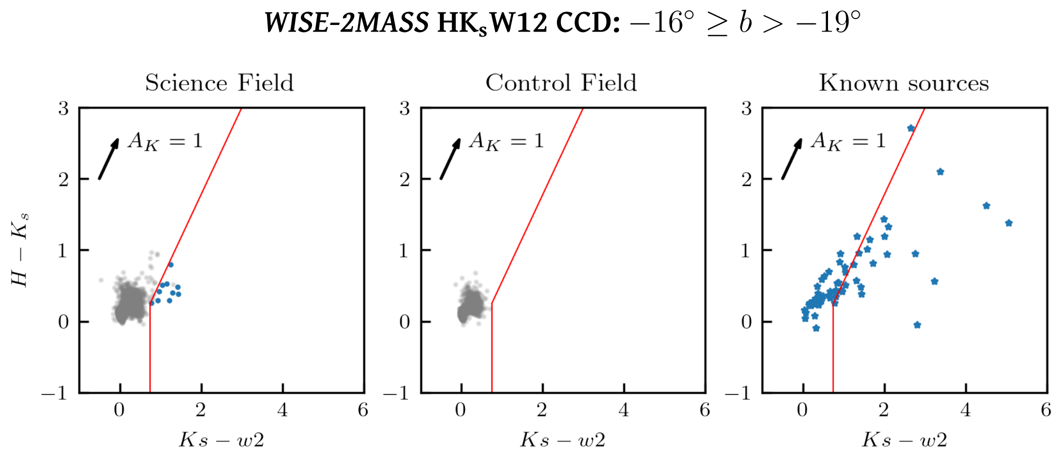

Figure 2.14: *2MASS-WISE* HK$_s$W12 color-color diagram ($K_s - w2$ versus $H - K_s$). The red line shows the selection boundary in these diagrams. Any source that is situated right of the line, is considered to be a YSO candidate. *Left panel:* Gray dots show all sources in the fifth science field stripe. Blue dots indicate the sources that are ultimately chosen for the HK$_s$W12 selection. *Middle panel:* Gray dots show the sources of the corresponding control field. *Right panel:* The blue stars are the known YSOs from the literature. They are used to help with the choice of the final selection criteria.

2.2.3 YSO selection with partial sky coverage

In contrast to the previous selections mentioned in Section 2.2.2, where I used data from all-sky surveys (*Gaia*, *2MASS*, *WISE*), I now focus on the data that do not cover the entire sky. By including data from *VISIONS* and *Spitzer* we can take advantage of superior resolution and sensitivity in the near- and mid-infrared, respectively, albeit only being available in certain parts of the entire science field (see Figure 2.1). The following selections will not use a *Gaia* distance cut to pre clean the sample from background contamination. This is done to select the youngest, deeply embedded YSOs from the IR data, which are undetectable by *Gaia*. Any selected contaminating sources will be removed in the end when the selection is refined using *Gaia* data and *VISIONS* high resolution images (see Section 3.1).

2.2.3.1 2MASS—Spitzer selection

In the following I describe the selections in which *Spitzer* has been used to replace *WISE* data in the mid-infrared regime. Here I still use *2MASS* instead of *VISIONS* as *Spitzer* partially covers areas outside the *VISIONS* observed fields (see Figure 2.1). Similar to the previous selections I use a series of color-magnitude and color-color diagrams to select YSO candidates from the sample. With *Spitzer* providing photometry in similar wavelengths as *WISE* (see Table 1.2), the improvement over *WISE* lies in *Spitzer's* superior resolution and sensitivity. This promises to reveal YSOs, which are missed when using *WISE* data instead. I use data from the *Spitzer* IRAC and MIPS instruments, all four filters ($i1$, $i2$, $i3$, and $i4$) from IRAC, and one filter ($m1$) from MIPS. I use three different combinations of filters for my selection listed below:

HK$_s$I24: Combines H, K$_s$, $i1$, and $i4$

HK$_s$M1: Combines H, K$_s$, and $m1$

HK$_s$I24: Combines H, K$_s$, $i1$, and $i2$

As has been mentioned before, some of the *Spitzer* filters are located at similar wavelengths as the *WISE* filters. I use these similarities between the three filter systems used by IRAC, MIPS and *WISE* to substitute $w1$ with $i1$, $w2$ with $i2$, $w3$ with $i4$ and $w4$ with $m1$. This is especially helpful in the longest wavelengths of the MIPS 1 band at 24 µm, and the $w4$ band at 22 µm. The selections will be similar to the *2MASS-WISE* selections described in Section 2.2.2.2, however, with the difference that a *Gaia* distance cut will not be applied. This makes it possible to select deeply embedded YSOs, which are not detected by *Gaia*. On the other hand, not applying a distance cut leaves a large number of contaminants in the sample, and a number of specialized cuts need to be applied to remove them.

The *2MASS-Spitzer* selection, just as the *2MASS-WISE* selection, uses the entire l and b range of the science field (albeit only partially in terms of area), and therefore had to be divided up into the nine stripes along the full latitude range. However, there are far less data points in this sample, since *Spitzer* data is not all-sky, and thus incomplete over the entire science field described in section 2.1. In addition to, and because of that, the *Spitzer* control field stripes in the NECF and SWCF are combined and only separated into a eastern and a western control field (see Figure 2.1). I then used the eastern control field for the science field stripes (1 to 4), and the western control field for the lower five stripes (5 to 9).

In the following *2MASS–Spitzer* CMDs it seems as if the control field contains more faint sources when comparing it to the science field. Moreover, the *known sources* appear to be brighter than the than the sources in the science field, which seems to be oddly cropped at

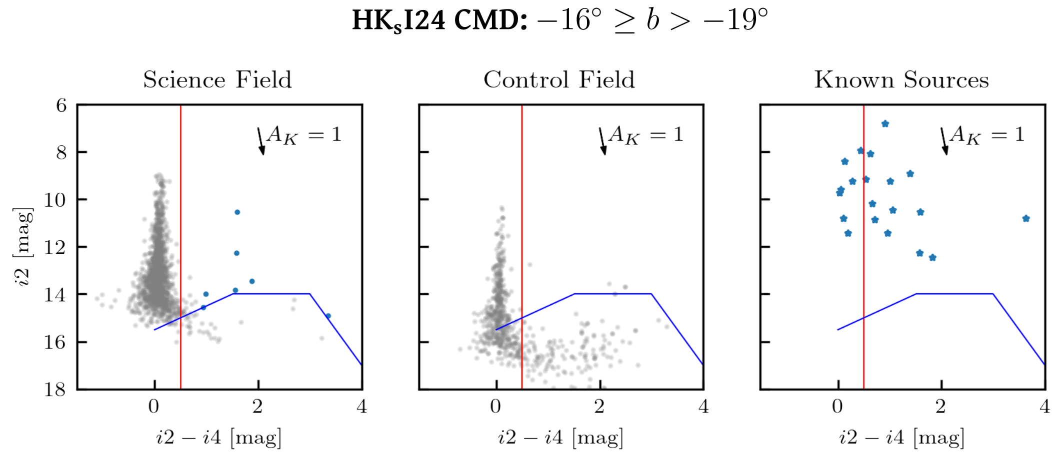

Figure 2.15: *2MASS-Spitzer* HK_sI24 color-magnitude diagram ($i2 - i4$ versus $i2$). The red line indicates the main sequence cut, and the blue line towards the bottom is drawn to exclude extragalactic contaminants. *Left panel:* The gray dots show all sources that are in the fifth latitude stripe and the blue dots represent the stars that were finally chosen in the HK_sI24 selection. *Middle panel:* The gray dots show all sources in the left control field. *Right panel:* The infrared selected *known sources* from the literature are shown here to help in the decision of the final selection criteria.

the bright end. This cropping of the bright and faint sources is caused by the applied quality criteria (see Section 2.2.1.2). Even though the same quality criteria are applied to the control field, more faint sources remain. One explanation for this could be that the data available from the SEIP which falls into the NECF and SWCF come from observation campaigns that focused on faint, possible extragalactic sources.

2.2.3.1.a HK_sI24 selection

this selection is similar to the $k_s w123$ selection described in section 2.2.2.2.a, and uses a combination of a color-magnitude, and color-color diagram to select young stellar objects. following the general structure of the previous figures, I present the color-magnitude diagram of this selection in Figure 2.15, showing the main sequence cut (red line), as well as an extragalactic exclusion cut (blue line). Since the distance cut with *Gaia* is missing here, contaminating background sources are still in the sample and need to be removed. The selection conditions in color-magnitude space for the nine stripes of the science field are listed below.

Stripes 1–4:

$$[(i2 - i4) > 0.75] \wedge [(i2 < 14) \vee (i2 < (15.5 - (i2 - i4))) \vee (i2 < (5 + 3(i2 - i4)))] \tag{2.31}$$

Stripes 5–9:

$$[(i2 - i4) > 0.5] \wedge [(i2 < 14) \vee (i2 < (15.5 - (i2 - i4))) \vee (i2 < (5 + 3(i2 - i4)))] \tag{2.32}$$

HK$_s$I24 CCD: $-16° \geq b > -19°$

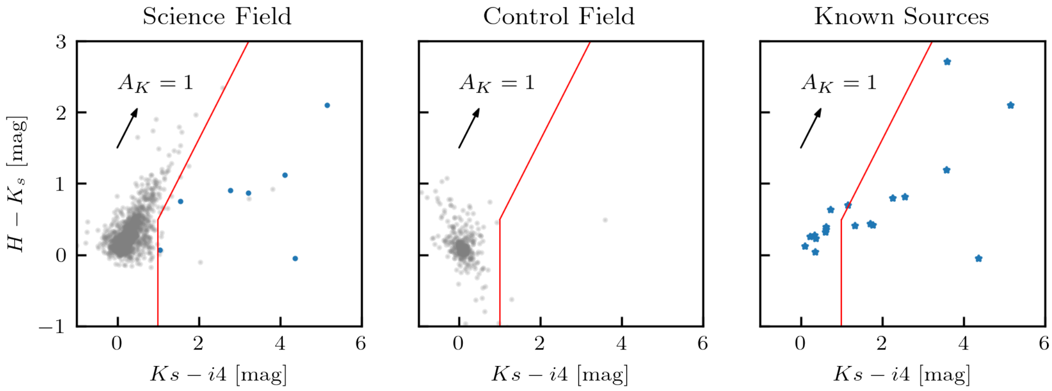

Figure 2.16: *2MASS-Spitzer* HK$_s$I24 color-color diagram ($K_s - i4$ versus $H - K_s$). The red line shows the selection criterion for YSO candidates. Sources that lie to the left of this boundary are likely main sequence stars, which may also suffer from reddening, hence they are rejected.*Left panel:* The gray dots show all sources that are in the fifth latitude stripe and the blue dots represent the stars that were finally chosen in the HK$_s$I24 selection. *Middle panel:* The gray dots show all sources in the left control field. *Right panel:* The infrared selected *known sources* from the literature are shown here to help in the decision of the final selection criteria.

A complementary color-color diagram is used to further refine the selection. To distinguish between main sequence stars that suffer from reddening, and the young stellar population in CrA, I chose a dividing line parallel to the reddening vector which can be seen in Figure 2.16. An additional criterion to reduce contamination by main sequence stars is given by the vertical line in the lower region of the CCD. The boundaries for the YSO selection in the CCD are the same for all nine science field stripes and can be seen below:

$$[(K_s - i4) > 1] \wedge [(H - K_s) < (1.122(K_s - i4) - 0.63)] \tag{2.33}$$

2.2.3.1.b HK$_s$M1 selection

By incorporating MIPS 1 band of *Spitzer* I aim to make up for the shortcomings of *WISE* $w4$ and include any sources that were previously rejected. For this selection I also use a color-magnitude diagram to first exclude faint sources of extragalactic nature and make a preliminary constraint on evolved sources—see Figure 2.17. The selection conditions in this color-magnitude space are given by the following equations for the different latitude ranges:

Stripes 1–4:

$$[(m1 < 6.5) \vee (m1 < (13.5 - (Ks - m1)))] \wedge [m1 > (12 - 2(K_s - m1))] \tag{2.34}$$

Stripes 5–9:

$$[(m1 < 6.5) \vee (m1 < (13.5 - (Ks - m1)))] \wedge [m1 > 1] \tag{2.35}$$

HK$_s$M1 CMD: $-16° \geq b > -19°$

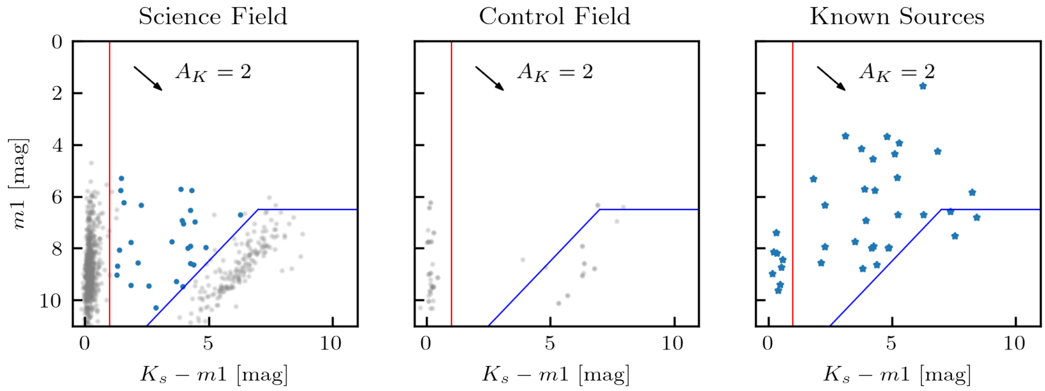

Figure 2.17: *2MASS-Spitzer* HK$_s$M1 color-magnitude diagram ($K_s - m1$ versus $m1$) to remove extragalactic contamination and main sequence stars. The red line shows the cut for main sequence stars, whereas the blue boundaries show the exclusion criteria for extragalactic contaminants. *Left panel:* Gray dots represent all sources in the fifth stripe of the science field. Blue dots show the sources that were finally selected for the HK$_s$M1 selection. *Middle panel:* The gray dots show the stars detected in the left control field. *Right panel:* Previously known YSOs from the literature that were selected with infrared data are plotted here in order to guide the decision on the selection criteria.

Similar to the previous section (see Section 2.2.3.1.a), the color-color diagram is used to add another condition for evolved sources based on the reddening law. Since the *Spitzer* data sample has no constraint on the distance, the CCD also shows of extragalactic nature, such as distant star-forming galaxies and active galactic nuclei. These sources are , which is indicated by the red lines featured in the lower left of Figure 2.18. The boundaries in the color-color diagram are, just like in the color-color diagram, in the upper part of the science field, different from the lower part. The equations for the selection criteria are shown below:

Stripes 1–4:

$$[(K_2 - m1) < 6] \wedge [(H - K_s) < (K_s - m1) - 1] \tag{2.36}$$

Stripes 4–9:

$$[(H - K_s) < (K_s - m1) - 1] \wedge [((K_s - m1) < 5) \vee ((H - Ks) > 1.25)] \tag{2.37}$$

$\mathbf{HK_sM1}$ CCD: $-16° \geq b > -19°$

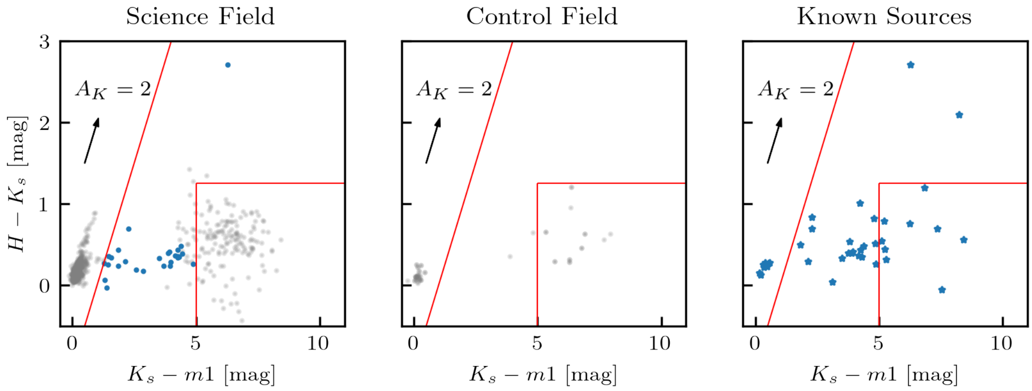

Figure 2.18: *2MASS-Spitzer* HK_sM1 color-color diagram ($K_s - m1$ versus $H - K_s$) to refine the YSO selection. The red line shows the cut for main sequence stars, whereas the blue boundaries show the exclusion criteria for extragalactic contaminants. *Left panel:* Gray dots represent all sources in the fifth stripe of the science field. Blue dots show the sources that were finally selected for the HK_sM1 selection. *Middle panel:* The gray dots show the stars detected in the left control field. *Right panel:* Previously known YSOs from the literature that were selected with infrared data are plotted here in order to guide the decision on the selection criteria.

2.2.3.1.c HK_sI12 selection

The following two sub-selections in color-magnitude and color-color space are very similar to the HK_sW12 selection using *WISE* photometry (see Section 2.2.2.2.c). Due to the similarity of the first two IRAC bands ($i1$, $i2$) compared to the first two *WISE* bands ($w1$, $w2$), this selection will support its *WISE* counterpart with the superior resolution and sensitivity over *WISE*. The CMD in Figure 2.19 shows the cuts for faint sources and main sequence stars as a red line. Faint sources are excluded by the shallower slope in the lower section of the plots, whereas main sequence stars are targeted by the steep slope in the upper part of the diagram. The exact selection conditions in color-magnitude space are the same for all nine stripes of the science field and are given below:

$$[i1 < (4(i1 - i2) + 13)] \wedge [i1 < 40(i1 - i2)] \tag{2.38}$$

In the CCD in Figure 2.20, the division line between reddened main sequence stars and the YSOs runs in parallel to the reddening vector. For stars that are located closer to the main clustering visible in the lower left of Figure 2.19 a vertical line is chosen to distinguish YSOs from the more evolved stars. Selection criteria, just as for the CMD, are the same for all stripes in the science field and are listed in the following condition:

$$[(K_s - i2) > 1] \wedge [(H - K_s) < (1.25(K_s - i2) - 0.55)] \tag{2.39}$$

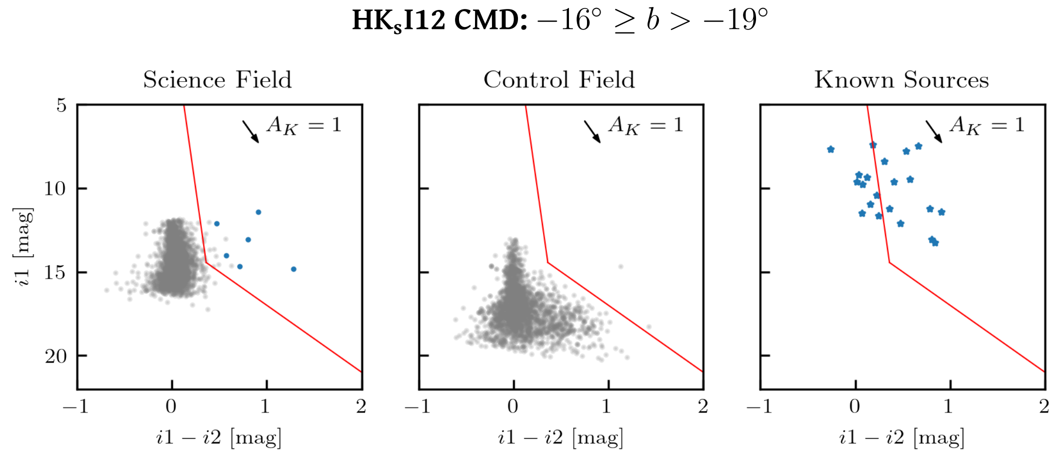

Figure 2.19: *2MASS-Spitzer* HK$_s$I12 color-color diagram ($i1 - i2$ versus $i1$). The lower right part of the red line depicts the rejection cut fro faint sources, which may include extragalactic objects, whereas the upper left part aims to exclude more evolved stars. *Left panel:* The gray dots represent all stars found in stripe number five of the science field. Blue dots show the sources that are left after all selection criteria for the HK$_s$I12 selection have been applied. *Middle panel:* All sources found in the control field to the right of the science field are shown as gray dots. *Right panel:* Literature YSOs that were selected using infrared excess are shown here to help with the decision on faint and main sequence cuts.

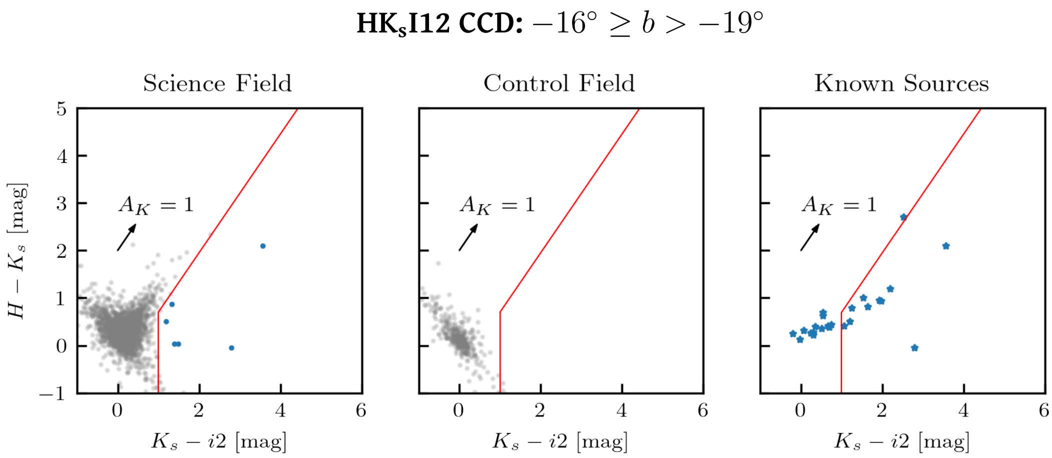

Figure 2.20: *2MASS-Spitzer* HK$_s$I12 color-color diagram ($K_s - i2$ versus $H - K_s$). Similar to Figure 2.16. The main division between reddened sources and stars with infrared excess is the red line that runs in parallel to the extinction vector. For the lower left part, the vertical cut excludes the main sequence and other evolved stellar objects.

2.2.3.2 VISIONS—WISE selection

VISIONS provides near-infrared photometry and images in the immediate surrounding of the Corona Australis molecular cloud (green boxes in Figure 2.1), that is superior in both resolution and sensitivity, compared to the *2MASS* all-sky survey. In this section I repeat the selection made in Section 2.2.2.2 and take advantage of the benefits of *VISIONS* over *2MASS*. Thus, I use *VISIONS* data, which has been complemented with *2MASS* photometry (see Section 2.2.1.3), and use the same filter combinations to select sources with infrared excess within the *VISIONS* observed region of Corona Australis, which is highlighted by the bright green borders in Figure 2.1.

2.2.3.2.a W123 selection

The first step in the selection within the *VISIONS* observed field, is to repeat the *WISE* W123 selection described in Section 2.2.2.1. This allows me to add any selected sources which have no counterpart in the *Gaia* catalog, to be re-included in the end. This is justified with the availability of high resolution images from *VISIONS*, which allows me to inspect these re-included sources by eye and reject objects that do not resemble YSOs morphologically, such as distant background galaxies.

Similar to Figure 2.6 I use a color-magnitude diagram to remove main sequence stars, but additionally I apply a cut to remove faint background galaxies, as well as bright AGB stars with and without interstellar extinction. The extragalactic contaminants are generally located in the lower right of the CMD in Figure 2.21, whereas AGB stars are found in the upper left corner, where they fan out from the top part of the main sequence (over density to the left). The blue line in the lower part of the diagrams indicates the extragalactic cut applied, and the red line to the left shows the boundary to remove main sequence and AGB stars. The conditions for the extragalactic (GAL), MS and AGB cuts applied in color-magnitude space are listed in the following:

GAL cut:

$$[w1 < (w1 - w3) + 9.25] \wedge [w1 < 12] \vee [w1 < 2(w1 - w3) + 2.5] \tag{2.40}$$

MS cut:

$$w1 < 30(w1 - w3) - 4 \tag{2.41}$$

AGB cut:

$$w1 > -2(w1 - w3) + 11 \tag{2.42}$$

In the next step (see Figure 2.22) I apply the galaxy cut used by Koenig & Leisawitz (2014) to remove extragalactic contaminants such as star forming galaxies. In addition to this, I remove unreliable photometry from the sample with a cut in color-color space. This is a similar condition used in Section 2.2.2.1, Figure 2.5, and cuts off all sources with negative $w1 - w2$ color (compare Equation 2.13). The entire combined condition imposed on sources in color-color space can be seen below:

Inferior photometry cut:

$$(w1 - w3) > 0 \tag{2.43}$$

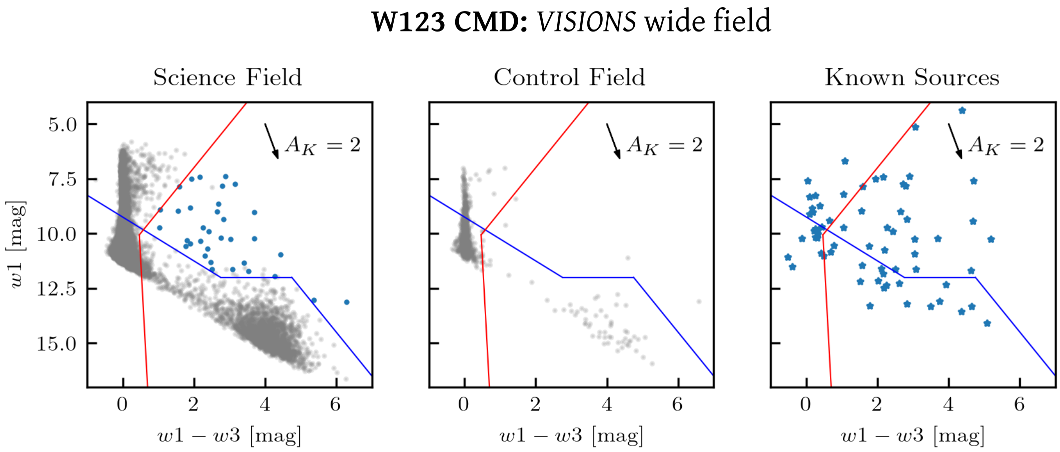

Figure 2.21: *VISIONS-WISE* W123 color-magnitude diagram ($w2 - w3$ versus $w1$) to remove field stars and AGN. The red line represents the rejection cut for main sequence and AGB stars. The blue line shows the exclusion cut for AGN and extragalactic contaminants. Sources which fall below or left of these boundaries are rejected. *Left panel:* Representative for all sources with viable *WISE* data in the *VISIONS* wide field are gray dots, whereas the blue dots show the selected stars. *Middle panel:* Gray dots show the stars of the *VISIONS* control field. *Right panel:* Literature YSOs also selected using infrared data are shown here to guide choosing of the selection cuts.

GAL cut:

$$[(w2 - w3) < 2.25] \vee [(w1 - w2) > 1] \vee [(w1 - w2) > 0.457(w2 - w3) - 0.829] \quad (2.44)$$

2.2.3.2.b K_sW123 selection

In this selection I combine *VISIONS* data with *WISE* data, to select YSOs similarly as is described in Section 2.2.2.2. The color-magnitude diagram will again be used to identify and remove extragalactic contaminants, as well as the main sequence and AGB stars from the sample. With the solid, red lines in Figure 2.23 encasing the area from which YSO candidates are selected, I reject all sources that lie outside this boxed-in region. The shape of the box is a result of combining the different cuts. The vertical line to the left addresses main sequence stars, the slope in the upper part of the diagram takes care of the AGB stars, and the lower slope that leads into the horizontal line to the right, both aim to reject the extragalactic component of the contaminating sources. The dashed, red line is part of a more complex condition that is intertwined with the selection criteria in color-color space. The reason for the added complexity is to select fainter sources which do not suffer from unreliable photometry indicated by negative or slightly positive ($w1 - w2$) color excess (see Figure 2.24). The conditions a source needs to fulfill in color-magnitude space, in order to be considered a YSO candidate are given in the following:

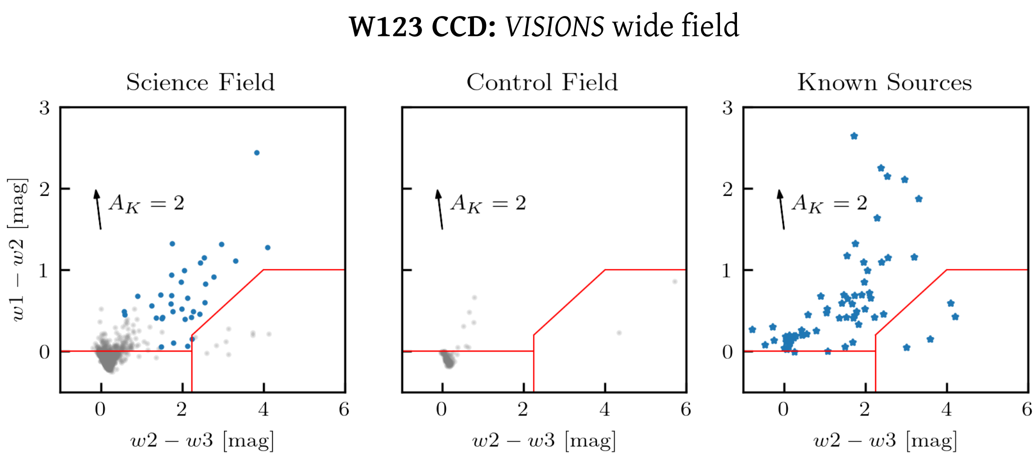

Figure 2.22: *VISIONS-WISE* W123 color-color diagram ($w2 - w3$ versus $w1 - w2$) to remove galaxies and sources with inferior photometry. The red boxed in area to the lower right is the area where extragalactic contaminants are dominating. To remove sources with unreliable photometry, the red line in the lower left was drawn. Only stars that are above the red boundary are allowed. *Left panel:* Gray dots are all sources in the *VISIONS* science field that are left after the faint sources and galaxies have been removed in color-magnitude space (see blue line in Figure 2.21). Blue dots show the finally selected stars. *Middle panel:* Stars from the *VISIONS* control field have also been cleaned by the CMD cuts. *Right panel:* Previously known young stellar objects in CrA from the literature which was also selected using infrared data.

GAL cut:

$$[w3 < 6] \vee [w3 < -(K_s - w3) + 12.5] \tag{2.45}$$

MS cut:

$$(K_s - w3) > 1 \tag{2.46}$$

AGB cut:

$$w3 > -1.5(K_s - w3) + 11 \tag{2.47}$$

This leads up to Figure 2.24, showing the CCD of this selection. Similarly to the conditions in *WISE* W123 color-color space, sources with unreliable photometry measurements are removed by the lower boundary cut represented by the horizontal, solid red line. However, if a star is bright enough in $w3$, it may still be selected from the region that is boxed in by the dashed red line in the lower part of the CCD. This brightness threshold is indicated by the horizontal, dashed red line in Figure 2.23. The following two equations show the conditions in the two cases for when a source lies above or below the brightness threshold indicated in the CMD:

Condition for sources brighter than 8 mag in $w3$:

$$[(w1 - w2) > 0] \wedge [(w2 - w3) > 1] \wedge [w3 < 8] \tag{2.48}$$

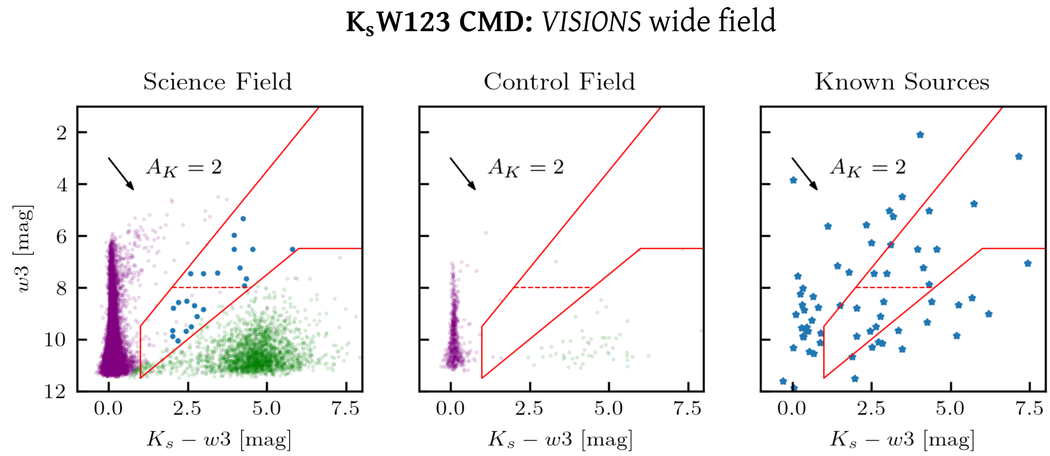

Figure 2.23: *VISIONS-WISE* K$_s$W123 color-magnitude diagram ($K_s - w3$ versus $w3$) to remove field stars and AGN. The boxed in area surrounded by the red solid lines is the region from which YSO candidates are selected. An additional condition for sources that fall into the area in color-color space, which is outlined by the dashed red lines in Figure 2.24, is indicated by the dashed, horizontal line. If a source falls in the dashed box of the CCD, it has to be above the dashed line here in the CMD to be accepted. Since the *VISIONS* data has been enhanced with *2MASS* data for bright sources, it is color coded to show from which survey the K$_s$ photometry is taken. Purple dots are from *2MASS* and green dots are taken from *VISIONS*.

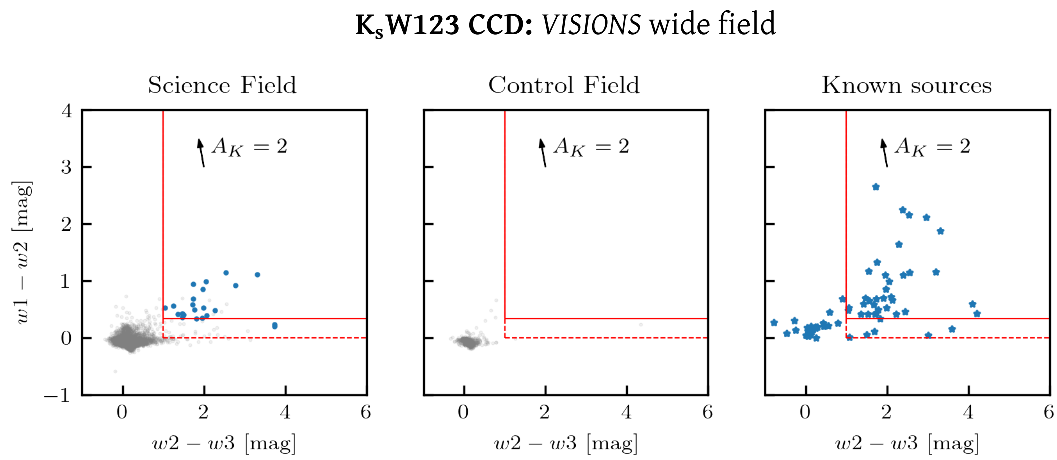

Figure 2.24: *VISIONS-WISE* K$_s$W123 color-color diagram ($w2 - w3$ versus $w1 - w2$) to remove sources with inferior photometry. The main sequence is rejected by the vertical line to the left, with sources lying left of this border being excluded. The cut to remove unreliable photometry consists of two boundaries. All sources that are above the horizontal solid line are selected, however, if a star falls in the area between the solid and dashed lines, it simultaneously needs to be brighter than the 8 mag limit shown by the dashed line in Figure 2.23

Condition for sources fainter than 8 mag in $w3$:

$$[(w1 - w2) > 1/3] \wedge [(w2 - w3) > 1] \tag{2.49}$$

K_sW124 CMD: *VISIONS* wide field

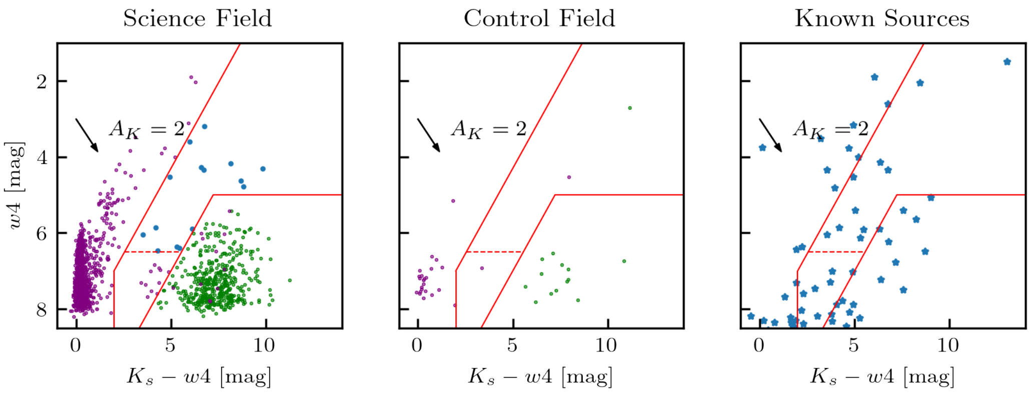

Figure 2.25: *VISIONS-WISE* K_sW124 color magnitude diagram ($K_s - w4$ versus $w4$) to remove field stars and extragalactic sources. Similar to Figure 2.23: Red lines show the selection criteria for YSOs with an additional magnitude threshold in $w4$ for sources in the color-color diagram (see Figure 2.26).

2.2.3.2.c K_sW124 selection

This sub-selection, similar to the selection in *2MASS* and *WISE* (see Section 2.2.2.2.b), aims to add sources that were not selected when using $w3$. Albeit the completeness of $w4$ strongly suffers from a large contamination by extended background emission, using the 22 µm filter band from *WISE* spreads out sources with infrared-excess even more, separating clearly from the MS and AGB stars. The color-magnitude diagram presented in Figure 2.25 shows the boundaries for YSO selection. Only sources that fall within the region that is surrounded by the solid lines are selected as YSO candidates. The source rejection criteria in this color-magnitude space used for the different contamination components are listed in the following:

GAL cut:

$$[w4 < 5] \vee [w4 < -0.9(K_s - w4) + 11.5] \tag{2.50}$$

MS cut:

$$(K_s - w4) > 2.75 \tag{2.51}$$

AGB cut:

$$w4 > -0.9(K_s - w4) + 8.8 \tag{2.52}$$

Similar to the previous selection (see Section 2.2.3.2.b) with $w4$ instead of $w3$, I use the CCD in Figure 2.26 to clean the selection from sources with inferior photometry. The conditions in this color-color space also rely on an additional brightness constraint in $w4$ for sources which fall below a certain $w1 - w2$ color threshold, which is done to give a more robust and complete

K_sW124 CCD: *VISIONS* wide field

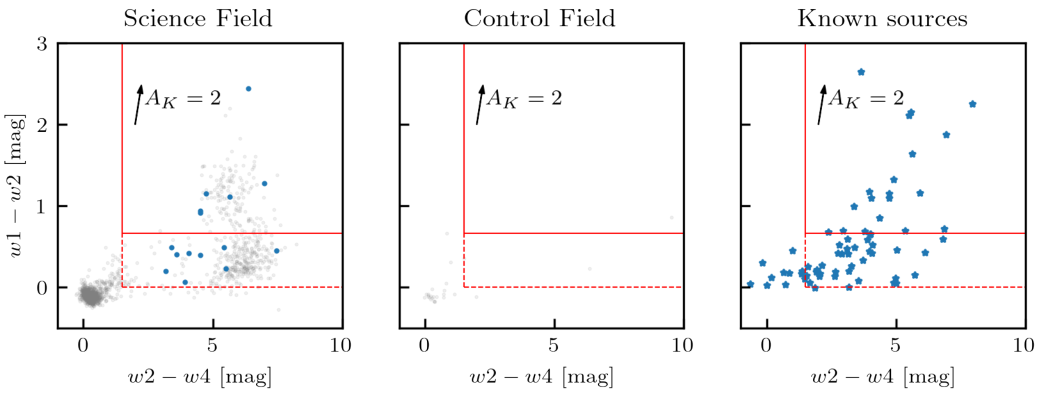

Figure 2.26: *VISIONS-WISE* K_sW124 color-color diagram ($w2 - w4$ versus $w1 - w2$) to remove sources with inferior photometry. Similar to Figure 2.24: Red lines show the selection criteria in this color-color space including the region for which an additional brightness threshold in $w4$ (see Figure 2.25) is required.

selection. The cuts used for the YSO selection shown in this CCD are listed below. Similar to before, they are shown separately for sources above and below the brightness threshold:

Condition for sources brighter than 6.5 mag in $w4$:

$$[(w1 - w2) > 0.66] \wedge [(w2 - w4) > 1.5] \tag{2.53}$$

Condition for sources fainter than 5.6 mag in $w4$:

$$[(w1 - w2) > 0] \wedge [(w2 - w4) > 1.5] \wedge [W4 > 6.5] \tag{2.54}$$

2.2.3.2.d HK$_s$W12 selection

For the same reasons mentioned in Section 2.2.2.2.c, I combine the first two *WISE* bands with *VISIONS* NIR bands in order to select sources that were not included in the other two NIR and MIR filter combinations of the *VISIONS-WISE* selection. Moreover, since the *Gaia* distance cut is not applied, extragalactic sources—such as AGN and distant, unresolved galaxies—and AGB stars need to be considered as well when selecting YSO candidates from this sample. The color-magnitude diagrams shown in Figure 2.27 feature a separate AGB cut (blue solid line) in the lower section of the plots. The vertical red line to the left cuts off main sequence stars, and leads into a slope oriented to the right in order to also remove AGB stars that fan out to the right from the bright end of the main sequence. The exact conditions used to clean the sample from these three major contaminating constituents are given below:

GAL cut:

$$[w1 < -4(w1 - w2) + 14.4] \vee [w1 < 12.8] \vee [w1 < 2(w1 - w2) + 10.3] \tag{2.55}$$

HK_sW12 CMD: *VISIONS* wide field

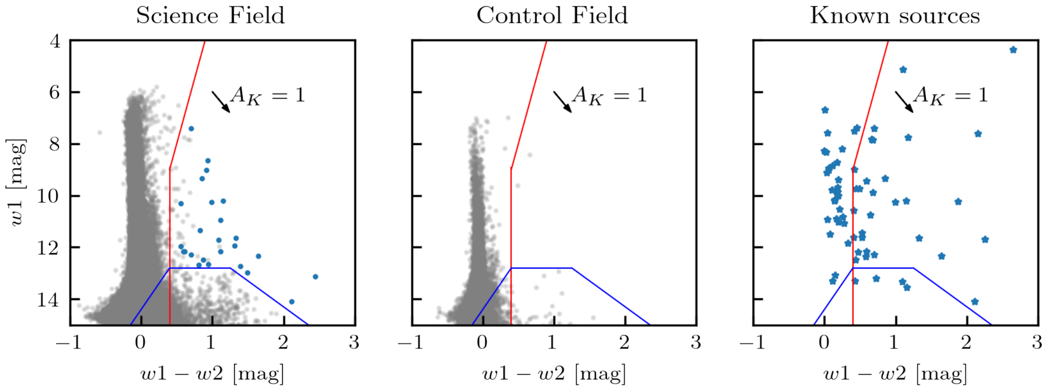

Figure 2.27: *VISIONS-WISE* HK_sW12 color-magnitude diagram ($w1-w2$ versus $w1$) to remove AGN, MS and AGB stars. This figure is similar to Figure 2.13: The AGN cut is shown by the blue line to the bottom, whereas the red solid line to the left represents the MS and AGB cut applied.

MS cut:

$$(w1 - w2) > 0.4 \tag{2.56}$$

AGB cut:

$$w1 > -10(w1 - w2) + 13 \tag{2.57}$$

To further refine the YSO selection, a color-color diagram similar to the one shown in Figure 2.14 is used to add additional constraints on main sequence stars and remove sources with unreliable photometry. In the CCDs shown in Figure 2.28, the additional conditions of this selection are highlighted by the red solid lines. The horizontal cut aims to remove sources with inferior photometry, whereas main sequence stars and diskless Class III YSOs are separated from the YSOs with disks by the vertical line leading up into the slope tilting to the right from the bottom. The slope aims to remove main sequence stars that suffer from interstellar reddening caused by the molecular cloud and dust associated with the Corona Australis star-forming region. The slope runs in parallel to the extinction vector shown in Figure 2.28, using the extinction law from Meingast et al. (2018). The exact conditions to remove diskless stars and inferior photometry in this color-color space are listed below:

Inferior photometry cut:

$$(H - K_s) > 0 \tag{2.58}$$

MS cut:

$$[(K - w2) > 1.2] \wedge [(H - K_s) < 1.22(K_s - w2) - 0.964] \tag{2.59}$$

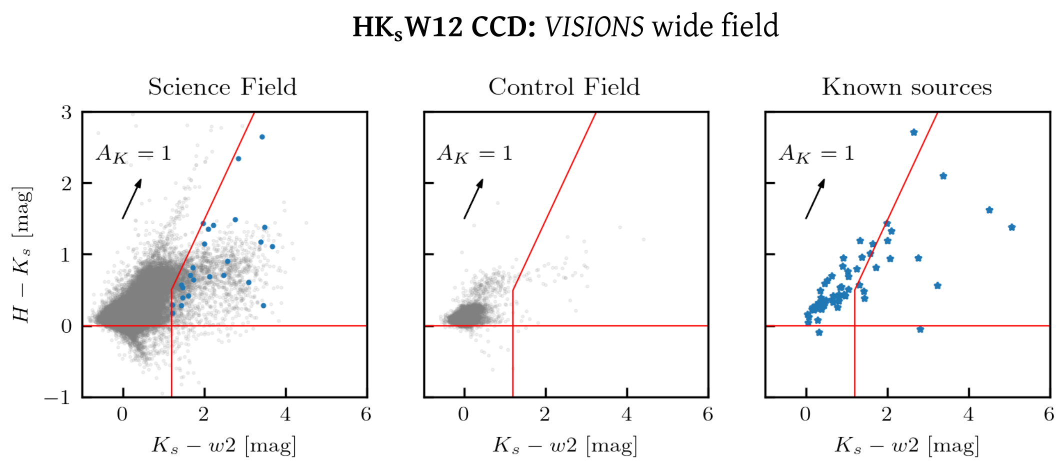

Figure 2.28: *VISIONS-WISE* HK_sW12 color-color diagram ($K_s - w2$ versus $H - K_s$) to select YSOs and reject inferior photometry. Similar to Figure 2.13: The red horizontal line in this figure shows the cut to exclude sources with inferior photometry. The red line running from bottom to top represents the border to remove diskless stars with and without reddening.

2.2.3.3 VISIONS—Spitzer selection

With the same intention as in Section 2.2.3.1, I replace *WISE* data with *Spitzer* observations to take of advantage of *Spitzer's* superior resolution and sensitivity over *WISE*. Especially in combination with *VISIONS*, the filter combinations used in this selection has the potential to reveal previously unknown YSO candidates. Similar to the selection described in Section 2.2.3.1, I use the same three sub selections listed there, with the individual cuts to remove contamination being updated. However, due to the applied *Spitzer* quality cut described in Section 2.2.1.2, only sources with the most robust photometric measurements remain in the sample, which may in some cases be too restrictive (see Section 2.2.3.3.b for details). Similar to to previous selections in the *VISIONS* observed field (see Section 2.2.3.2), a *Gaia* distance cut is not applied. Any contaminating sources are removed later as described in Section 3.1. Moreover, uncertain candidates can be visually inspected using the high resolution images provided by *VISIONS*. Thereby background sources, such as resolved galaxies which passed the extended sources filters of *VISIONS* can be rejected..

2.2.3.3.a HK_sI24 selection

This selection is similar to the K_sW123 selection described in the Sections 2.2.2.2.a and 2.2.3.2.b due to the similarity of the used *Spitzer* filters compared to the *WISE* filters from the mentioned selections. With this filter combination of *VISIONS* NIR and *Spitzer* MIR passbands, I select YSOs from a combination of a color-magnitude with a color-color diagram. In color-magnitude space (see CMDs in Figure 2.33) I apply an extragalactic cut—shown as blue solid line towards the bottom of the diagrams—and a main sequence cut represented by the vertical red line to the left. This intends to remove contamination from distant background sources such as AGN, and evolved field stars, respectively. With no AGB stars visible in either the control field nor the science field, which for instant were well represented by a fanning out distribution from

HK$_s$I24 CMD: *VISIONS* wide field

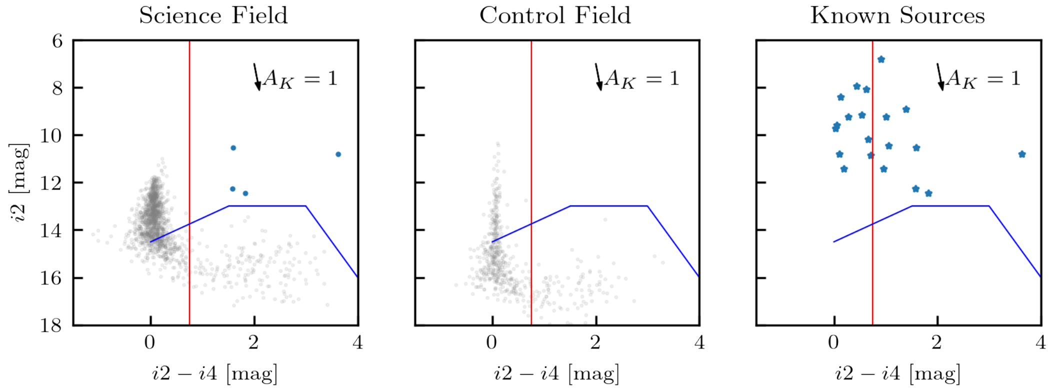

Figure 2.29: *VISIONS-Spitzer* HK$_s$I24 color-magnitude diagram ($i2 - i4$ versus $i2$) to remove filed stars and AGN. Similar to Figure 2.15: The blue line to the bottom aims to remove AGN, whereas the vertical red line to the left is chosen to reject evolved field stars.

the top of the main sequence (for reference see Figures 2.21 or 2.23). The conditions a source has to meet in order to remain in the selection, are shown below:

GAL cut:

$$[i2 < 13] \vee [i2 < 14.5 - (i2 - i4)] \vee [i2 < 3(i2 - i4) + 4] \tag{2.60}$$

MS cut:

$$(i2 - i4) > 0.75 \tag{2.61}$$

A color-color diagram (see Figure 2.30) is used to set a further constraint on main sequence stars by choosing a cut that runs parallel to the extinction vector, and cuts off the overdensity associated with main sequence stars located roughly at $(0, 0)$ in the CCD of the control filed (see center panel of Figure 2.30). To reject main sequence stars that suffer from interstellar reddening, the slope in the upper part of the line runs parallel to the extinction vector. The exact line definitions can be seen in the following equation:

$$[(H - K_s) < 1.225(K_s - i4) - 1.24] \wedge [(K_s - i4 > 1.2)] \tag{2.62}$$

2.2.3.3.b HK$_s$M1 selection

Similar to the selection in Section 2.2.3.1.b including $m1$ photometry in order to compensate for the shortcomings of the *WISE* $w4$ filter. The adopted *Spitzer* quality criteria (see Section 2.2.1.2) are especially restrictive in the area around the Coronet cluster, resulting in a large number of excluded MIPS 1 measurements, due to extended background emission from

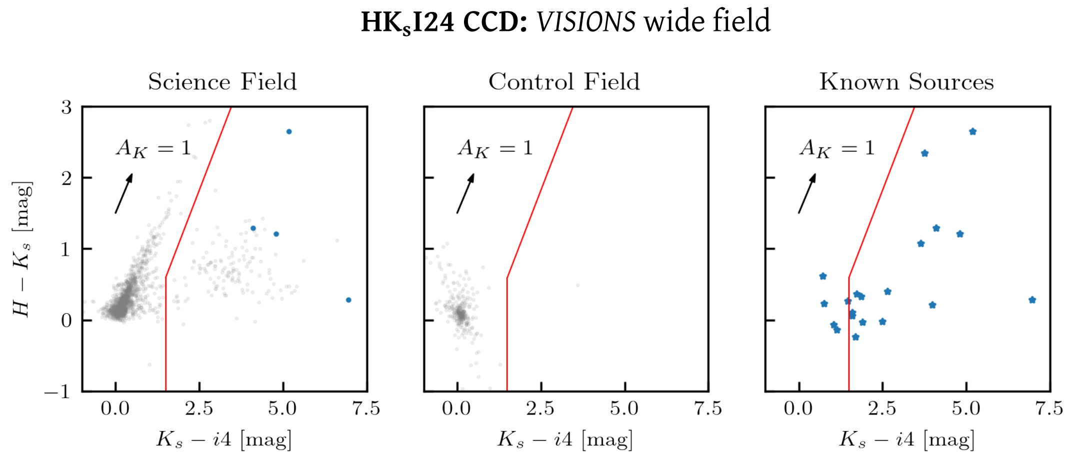

Figure 2.30: *VISIONS-Spitzer* HK$_s$I24 color-color diagram ($K_s - i4$ versus $H - K_S$) to select YSOs. Similar to Figure 2.16: The red line represents the selection criterion for YSO candidates.

the surrounding medium. The remaining sources with $m1$ photometry populate the area were star forming are expected (see Figure 2.32 and 2.32). Shown in Figure 2.31, are the cuts to remove AGN and unresolved galaxies (blue line encasing the bottom right corner) and the cut to remove main sequence and AGB stars (red line). However, due to the absence of a main sequence due to the missing $m1$ photometry, the MS and AGB cut is loosely based on the MS cut in of the K$_s$W124 selection (see Equation 2.51 in Section 2.2.3.2.c). The exact criteria to remove AGN and evolved field stars is listed in the following:

GAL cut:

$$[m1 < 6] \vee [m1 < 13 - (K_s - m1)] \tag{2.63}$$

MS cut:

$$m1 > 12 - 2(K_s - m1) \tag{2.64}$$

In the complementing color-color diagram, I define cuts in a similar manner as is described in Section 2.2.3.1.b, by running a line parallel to the extinction vector, to separate main sequence stars with and without reddening, from YSO candidates. Again, as has been mentioned above, due to the *Spitzer* quality criteria for the $m1$ filter, the main sequence population is virtually non existent in this selection and mostly extragalactic sources remain. The red line in the CCD is given by the following conditions to select YSOs:

$$[(K_s - m1) > 1] \wedge [(H - K_s) < (K_s - m1) - 1] \tag{2.65}$$

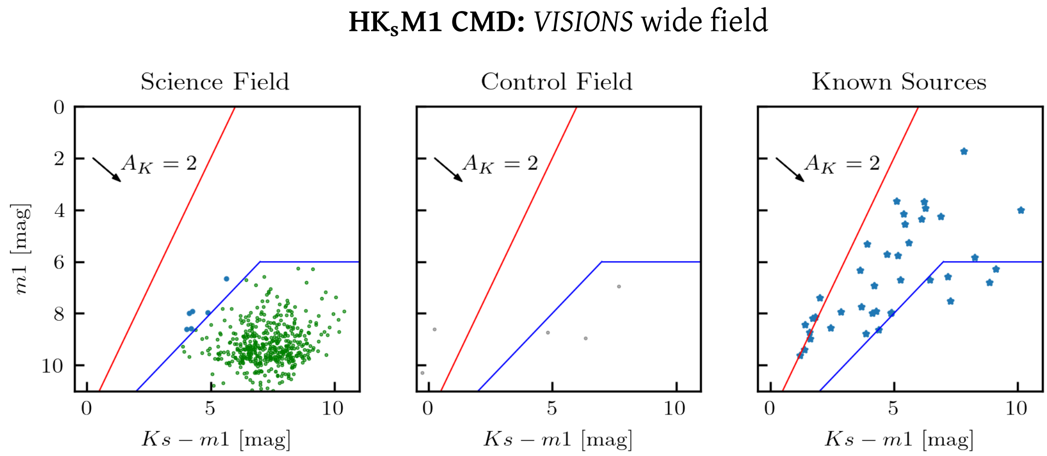

Figure 2.31: *VISIONS-Spitzer* HK$_s$M1 color-color diagram ($K_s - m1$ versus $m1$). Similar to Figure 2.17: Due to the applied *Spitzer* quality criteria (see Section 2.2.1.2) the $m1$ photometry has been removed for most sources outside the blue box to the lower right. The blue line represents the galaxy cut, and the red slope to the left indicates the MS and AGB cut. The main sequence and AGB criteria however, are loosely based on the cut shown in Figure 2.17 due to the absence of a significant main sequence in the science and control fields (left and center panel).

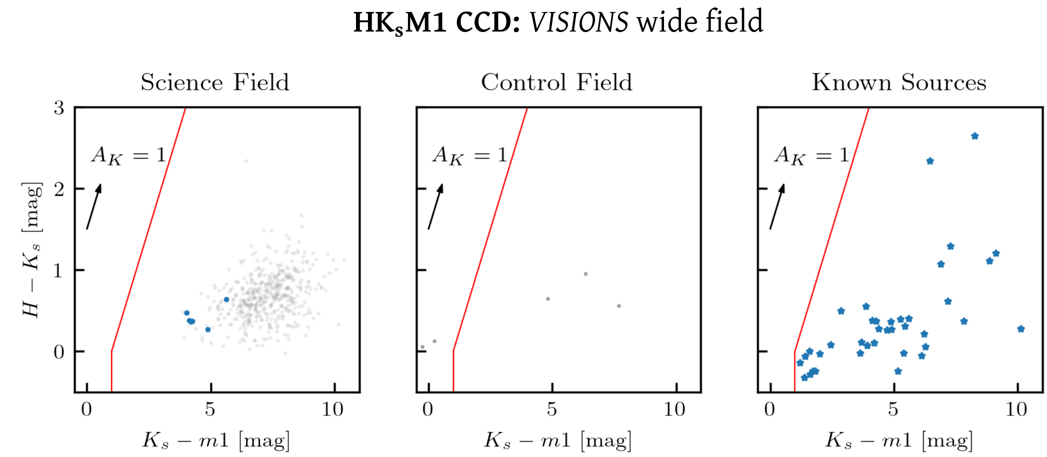

Figure 2.32: *VISIONS-Spitzer* HK$_s$M1 color-color diagram ($K_s - m1$ versus $H - K_s$) to select YSOs from the sample.

2.2.3.3.c HK$_s$I12 selection

This final sub-selection, similar to the HK$_s$W12 mentioned in Sections 2.2.2.2.c and 2.2.3.2.d, aims to select sources which were previously overlooked in the selections using photometry in longer wavelengths. As is the case with *WISE* photometry in the longest wavelengths ($w3$ and $w4$), the *Spitzer* $m1$ photometry may be impaired in areas where there is extended background emission from young stars heating and illuminating the surrounding interstellar medium. Same as in the previous selections, I rely on a combination of a color magnitude with a color-color diagram, to select YSOs from the sample. Figure 2.33 shows the color-magnitude diagram, and the exclusion criteria used in this space. Compared to the selections

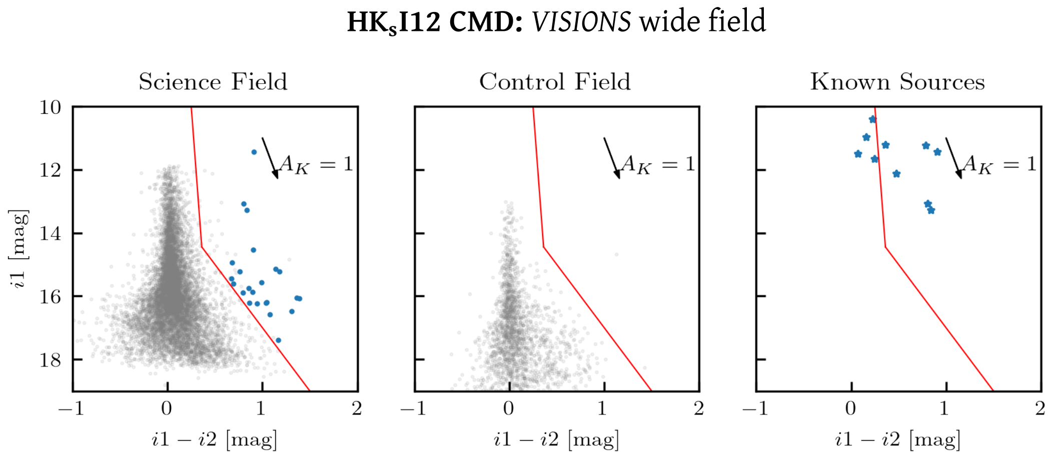

Figure 2.33: *VISIONS-Spitzer* HK$_s$I12 color-magnitude diagram ($i1 - i2$ versus $i1$) to remove AGN and main sequence stars. Similar to Figure 2.19: The red line running from bottom to top, indicates the combined MS and AGN cut, where the lower part addresses AGN and the upper part MS stars.

made with longer wavelength photometry, the extragalactic contamination component is less pronounced in the redder parts of this CMD. Therefore, a modified main sequence cut, which gets shallower for faint sources (lower part of the red line) is applied to account for AGN. Same as with the HK$_s$I24 selection in Section 2.2.3.3.a, no significant AGB population can be observed fanning out of the bright end of the CMD (compare Figure 2.21). The rejection criteria in the color-magnitude space of this selection is given below:

GAL cut:

$$i1 < 4(i1 - i2) + 13 \tag{2.66}$$

MS cut:

$$i1 < 40(i1 - i2) \tag{2.67}$$

Similar to the previous selection, the cut in color-color space (see Figure 2.32), runs in parallel to the extinction vector to separate reddened evolved stars from the young stellar population. In addition, a vertical cut is included to reject main sequence stars which show only little evidence of extinction in the overdensity to the lower left. The exact conditions for YSOs to be selected, are given in the following.

$$[(H - K_s) < 1.25(K_s - i2) - 0.575] \wedge [(K - i2) > 1.5] \tag{2.68}$$

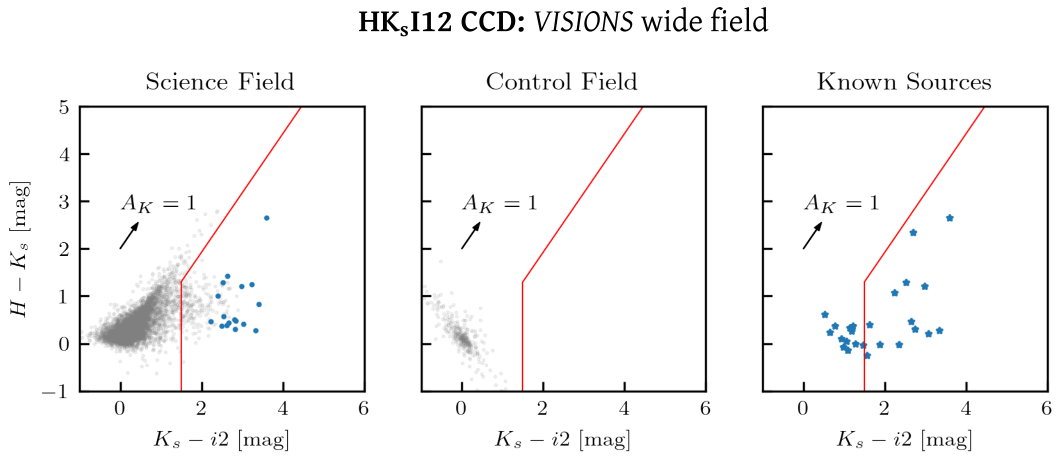

Figure 2.34: *VISIONS-Spitzer* HK$_s$I12 color-color diagram ($K_s - i2$ versus $H - K_s$) to select YSOs from the sample. Similar to Figure 2.19: The red line indicates the selection criteria for young stellar members.

2.3 Source classification

To assess the evolutionary state of a star-forming region, it is essential to determine the evolutionary stage of the YSOs associated with the region. YSOs can consist of multiple components, the star in the center, an circumstellar disk, and an envelope, which all evolve over time. In order to determine the evolutionary stage of a YSO, we rely on the photometry that we get from the entire system, including the envelope, disk, and the central star. We can now, from a physics standpoint, try to associate certain artifacts in the measured flux over a certain wavelength range, with the real physical components of the object at hand. Therefore, we use classes that allow us to estimate the true evolutionary stage of a YSO. One method to distinguish between YSO classes, is to use the positions of the individual sources in color-color space (e.g. Koenig & Leisawitz 2014; Großschedl et al. 2021). A second, more accurate approach is to determine the infrared spectral index of the YSO (e.g. Lada & Wilking 1984; Lada 1987; Greene et al. 1994; Großschedl et al. 2019).

2.3.1 Color-color diagram

When looking at the color space, young stellar objects inhabit certain regions depending on what class of YSO they belong to. The idea is simple, in reality however, we are left with a more complex problem. The measured flux, and thus the magnitudes which are used in the color-color diagrams are not solely dependent on the evolutionary stage of the PMS star. There are other physical properties that affect the detected signal, including the inclination of the proto-stellar disk (Robitaille et al. 2006), or stellar outbursts due to accretion (e.g. Kenyon et al. 1990; Teixeira et al. 2018). These can lead to a shift in color-color space and as a result we may find a source of one class, in an area that is typical to another class. Moreover, the hard borders first introduced by Koenig et al. (2012) using *WISE* colors, should be understood as guidelines rather than a fixed criterion, especially for sources that are in close proximity

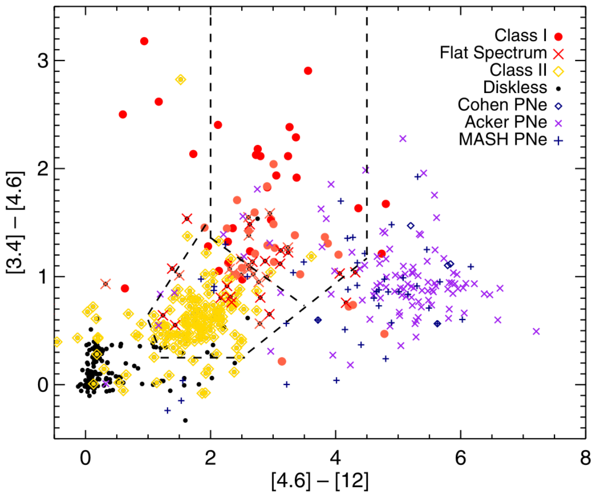

Figure 2.35: Simple classification scheme using a *WISE* color-color diagram. A color-color diagram using *WISE* data can be used to make a color-based classification of YSOs. The boundaries visible in this diagram were defined by Koenig & Leisawitz (2014) and show the general areas that are populated by different YSO classes in Taurus (Rebull et al. 2010) and planetary nebulae (PNe) from Acker et al. (1992), Parker et al. (2006), and Cohen et al. (2011). We can see that class I objects concentrate in the upper, central part of the diagram, whereas class II objects cluster in the middle. Both regions are highlighted by the dashed black lines. *Image source:* Left panel of Figure 10, in Koenig & Leisawitz (2014)

to these lines.

With all this in mind we can still use these diagrams and the regions within them, to roughly estimate the class of a PMS star, which also provides a sanity check for other classification methods. In addition to that, we can probe the disk fraction of the young stellar population, as there is a clear divide between more evolved PMS stars without disks, such as class III and PMS stars with disks, and the younger protostars, see for instance Koenig et al. (2012); Koenig & Leisawitz (2014); Evans et al. (2009a); Dunham et al. (2015); Großschedl et al. (2021). As can be seen in Figure 2.35, this is easily achieved by defining a slope through the general area of the divide. This method may however be insensitive to certain class III sources, that may be scattered further towards redder colors.

2.3.2 Infrared spectral index

In my thesis I rely on the slope method to classify YSOs judging by the shape of their IR SED (see e.g. Lada & Wilking 1984). In order to estimate the slope of the infrared SED $\alpha_{\rm IR}$ (see Equation 1.1) in the range from 2 to 24 µm I use linear regression to fit a line to the infrared SED in log-space. The flux densities for each star in every filter was determined, with exception for the *Spitzer* data, which already provides flux measurements in Jy. The conversion from magnitudes to Jansky is described the following equation with the zero magnitude flux densities $F_{\rm zp}(\nu)$ listed in Table 1.2.

$$F_\nu = F_{\rm zp}(\nu) * 10^{-0.4\,m} \tag{2.69}$$

Furthermore, in order to get the slope of the IR SED, the infrared flux for each filter wavelength λF_λ is computed with Equation 2.70. For details on the identity between F_ν and F_λ see Appendix B.

$$\lambda F_\lambda = \lambda F_\nu * 2.99792458 \times 10^{-9} \frac{\text{Hz erg}}{\text{s cm}^2\ \mu\text{m}} \tag{2.70}$$

In order to determine the spectral index of a source accurately, it is necessary to probe the SED as completely as possible. However, due to the different coverage of the various infrared surveys used in this study, photometry in all filters is not available for all selected stars. Moreover, measurement errors and spurious detections (especially affecting *WISE* W3 and W4 filters), can cause a fake IR-excess in some SED shape (see Section 1.3.1.3). This is especially problematic, as the infrared flux measured in the longest MIR filters can be an indicator for so called Transition Disk objects (TDs) (Calvet et al. 2005) which show excess emission beyond wavelengths of 20 µm (Espaillat et al. 2012). Thus, to get an informed estimate of the spectral index α_{IR}, I determine the spectral index from several combinations of filters. For instance, a commonly used variant is the IRAC spectral index α_{IRAC} for sources detected in all four IRAC bands (Lada et al. 2006). On the other hand, sources for which no *Spitzer* observations are available I use *WISE* photometry to compute the spectral index α_{WISE}. Further variants include K_s from *2MASS* or *VISIONS*, and MIPS M1 photometry from *Spitzer* to get the SED slope over a greater wavelength range from 2.2 to 24 µm, as a measure for the spectral index α_{KIWM} over all available photometric measurements.

Except for α_{KIWM}, which uses all reliable flux measurements ranging from the K_s to M1 filter bands, spectral indices are only computed if the source was detected in all the photometric bands needed for the specific spectral index. For instance, α_{IRAC} is only calculated if all four IRAC channels have detected the given source. However, not all flux measurements are reliable, creating ambiguity in YSO Class assignment, especially when considering in the longer wavelength filters W3 and W4. Therefore, in the case where a source has been detected in all necessary filters for the individual spectral indices, I only consider reliable photometric measurements for the determination of the spectral index. Thus, I use the conditions given in Table 2.3 to determine if a photometric measurement is reliable or unreliable for the spectral index computation.

To estimate the errors of the log fluxes used in the SED plots, I computed the upper and lower boundaries from the available magnitude or flux density uncertainties, and converted these values to fluxes. The error bars shown in the SED plots represent the distance between the upper and lower boundary. Furthermore, reliable measurements according to the conditions given in Table 2.3 are depicted as solid circles, whereas unreliable data points are shown as open circles, in some cases also with missing error bars, as some unreliable measurements have undefined errors with no entry, indicating a highly unreliable source. For instance, this is the case for *WISE* photometry where $snr < 2$, which means that the magnitude was computed using the 95 % confidence upper flux limit, and the magnitude uncertainty is set to `null`[4].

[4]See *Explanatory Supplement to the AllWISE Data Release Products* Section II.1.d.i located at the following url: https://wise2.ipac.caltech.edu/docs/release/allwise/expsup/index.html

Table 2.3: Photometric quality conditions for spectral index computation. This table lists the conditions for photometric measurements to be considered reliable for the spectral index computation.

Filter	Condition
K_s	K_s_err not NaN
W1	$(w1snr > 10) \wedge (w1sigmpro < 0.5)$
I1	$i1\_snr > 6$
I2	$i2\_snr > 6$
W2	$(w2snr > 10) \wedge (w2sigmpro < 0.5)$
I3	$i3\_snr > 6$
I4	$i4\_snr > 6$
W3	$(w3snr > 6) \wedge (w3sigmpro < 0.5)$
W4	$(w4snr > 5) \wedge (w4sigmpro < 0.5)$
M1	$m1\_snr > 10$

Note: Since the spectral index only uses photometry from filters with wavelengths longer than 2 µm, conditions for J and H band photometry are not needed. However, I use the same condition as for K_s to indicate unreliable photometry in these two bands in the SED plots, where the bands are shown for compöetenes.

Figures 2.36 and 2.37 show five representative SEDs which correspond to the different YSO classes, including the so called Transition Disk objects, which are believed to be an intermediate step between Class II and III. Using the classification scheme described in Section 1.2.2.2 (see Table 1.1) I do not assign an individual class to these Transition Disks, which show infrared excess in the longest *WISE* filters and the *MIPS* 1 band (see e.g. Cieza et al. 2010, 2012; Romero et al. 2012). As mentioned above, in the classification I use for my thesis, I do not assign transition disks a class of themselves, but depending on the slope of the line fit of the SED they may be assigned either Class II or Class III.

As can be seen in Figure 2.36 and 2.37 I computed a number of different spectral indices (see Table 2.4), based on the available photometric measurements. Consequently, more spectral indices were determined for SEDs with a full complement of fluxes, compared to SEDs with missing or unreliable fluxes. For instance, SEDs of sources which lie outside the *Spitzer* observed areas can not have spectral indices which use measurements from *Spitzer* photometry, such as α_{IRAC}. Moreover, if a source has fluxes in three of the WISE filters and one measurement is missing, α_{WISE} is not calculated, since one of the necessary measurements for α_{WISE} is missing. On the other hand, if the W4 flux measurement is missing then, α_{W3} is computed. However, should W4 be a unreliable measurement, then α_{WISE} will be determined, but the computation will only use the fluxes of W1, W2, and W3. There is only one spectral index (α_{KIWM}), which uses fluxes from all Filters ranging from K_s to M1, that will always be computed, as long

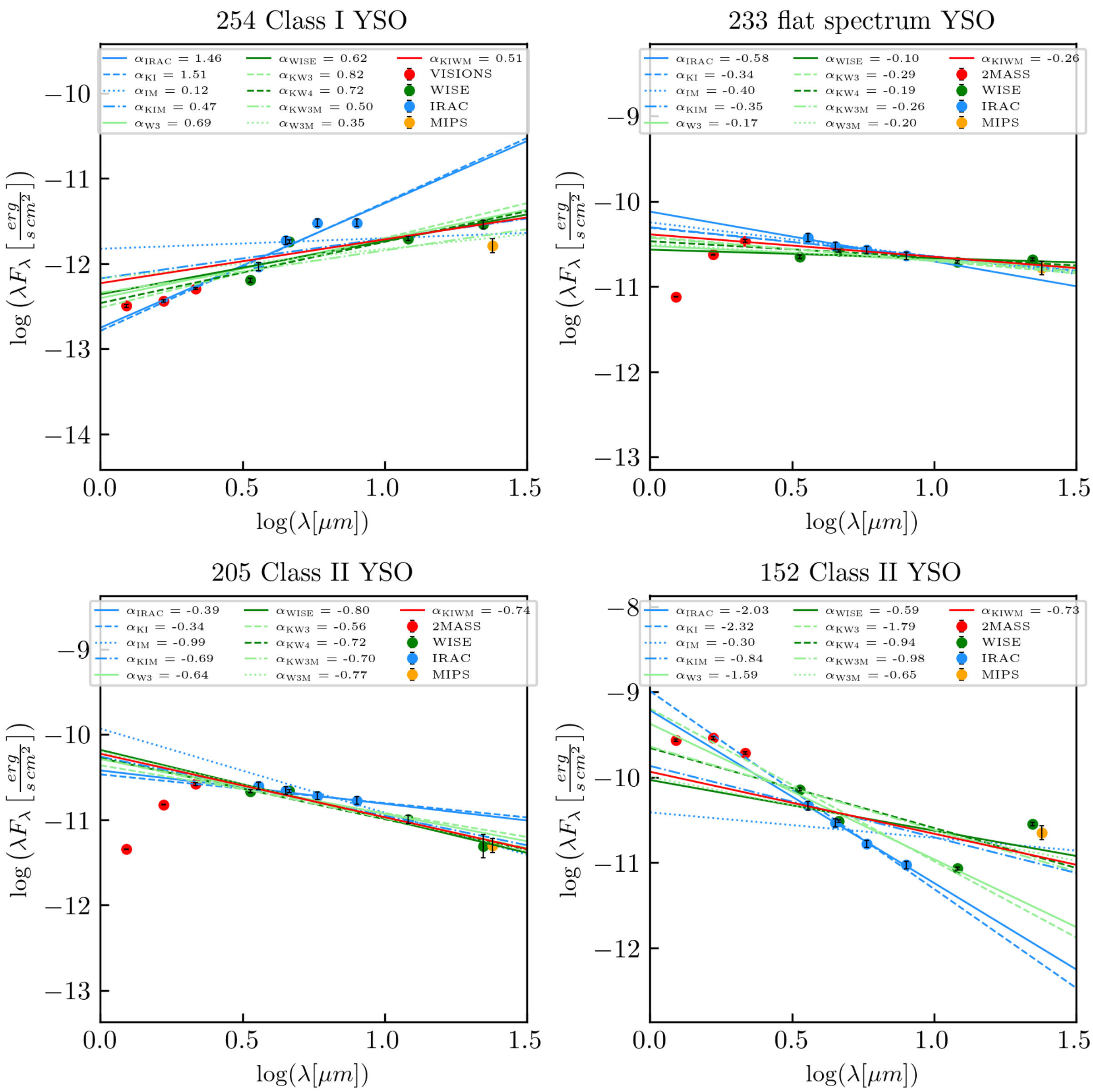

Figure 2.36: Representative SEDs for Class 0/I, Flat spectrum, Class II, and Transition Disk objects. The solid circles in each of the four SEDs shown here indicate reliable photometry, whereas open circles show sources with large or missing measurement errors. The error bars shown in the plots are an estimate of the error from computing upper and lower bounds in magnitude (or Flux density for *IRAC* and *MIPS*) and propagating them to the log Flux space used for the SEDs. The SEDs shown here correspond to Class 0/I YSO (top left), Flat spectrum source (top right), Class II (bottom left), and Transition Disk object (bottom right).

as there are at least two reliable fluxes out of the 10 filters used for this spectral index. This is also the spectral index used to assign YSO classes according to Table 1.1. A full list of spectral indices computed, and which filter combination they use is given in Table 2.4.

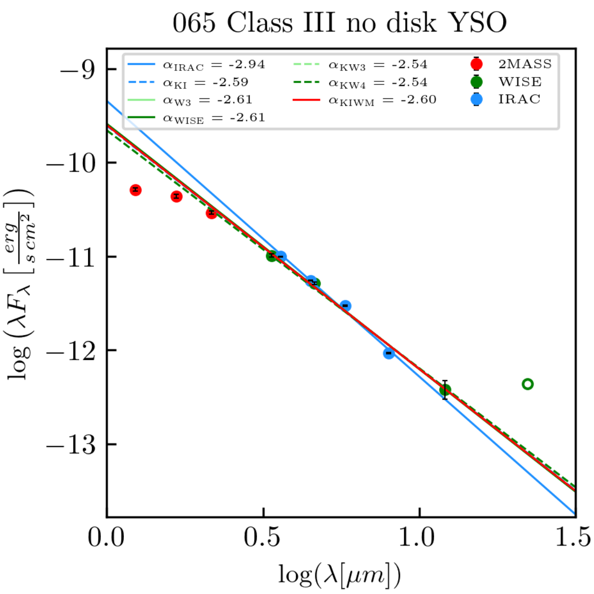

Figure 2.37: Representative SED for a Class III YSO. Continuation of Figure 2.36, showing a typical SED of a Class III YSO with no disk.

Table 2.4: Spectral indices used in this study. Listed below are the spectral indices which were computed in this study and which filter combinations were used for each index.

Spectral index	Filtercombination
α_{IRAC}	I1, I2, I3, I4
α_{KI}	K_s, I1, I2, I3, I4
α_{IM}	I1, I2, I3, I4, M1
α_{KIM}	K_s, I1, I2, I3, I4, M1
α_{W3}	W1, W2, W3
α_{WISE}	W1, W2, W3, W4
α_{KW3}	K_s, W1, W2, W3
α_{KW4}	K_s, W1, W2, W3, W4
α_{KW3M}	K_s, W1, W2, W3, M1
α_{W3M}	W1, W2, W3, M1
α_{KIWM}	K_s, I1, I2, I3, I4, W1, W2, W3, W4, M1

Chapter 3

Results

In the search for new, previously undiscovered young stellar objects associated with the Corona Australis star-forming region, I applied methods developed by Koenig et al. (2012); Koenig & Leisawitz (2014), and Großschedl et al. (2019), and modified these methods so that they would better fit the data towards CrA. Thereby, I selected potential YSOs from near to mid infrared surveys. By complementing the selection with data from *Gaia* EDR3, I further confined the selection. Finally I combined my selection with YSO catalogs from the literature (see e.g. Peterson et al. 2011; Dunham et al. 2015; Galli et al. 2020; Kerr et al. 2021; Esplin & Luhman 2022, and Ratzenböck et al. subm.[1]) to create a comprehensive catalog containing all known YSOs associated with the CrA star-forming region. Using this catalog I determined spectral indices for most sources (a few stars did not have enough data points to complete a linear fit of the IR-SED) to estimate the disk-fraction of this star-forming region. Furthermore, I briefly investigate the disk-fraction of the CrA young stellar population, which can be divided in three sub-clusters, according to the separation presented in Ratzenböck et al. (subm.). In the following sections I present the results of my study, where Section 3.1 focuses on my selection and the final YSO catalog. In Section 3.2 presents the results from the YSO classification, and Section 3.3 presents the disk-fraction and the three sub-clusters of Corona Australis.

3.1 Selected YSO sample

By selecting sources by their infrared-excess I gain a sample of 169 sources within the specified science field (see Figure 2.1). Out of these 169 sources, 30 have no counterpart in the *Gaia* EDR3 catalog. Of the remaining 139 stars slightly more than half (76) have non negative parallaxes and lie at an estimated distance ($d = {}^{1000}/_{\varpi}$) closer than 300 pc. To further refine the selection I rejected all sources without a *Gaia* counterpart, sources with negative *Gaia* parallax, and those which lie at a distance greater than 300 pc. Moreover, I remove sources which do not share similar proper motions with the YSO selections by other authors (e.g. by Galli et al. 2020; Kerr et al. 2021; Esplin & Luhman 2022).

In order to determine if a source deviates in proper motion space, I plotted literature YSOs for which *Gaia* proper motions are available in a $pmra$ versus $pmdec$ diagram and defined an

[1] Preliminary CrA catalog received through private communication.

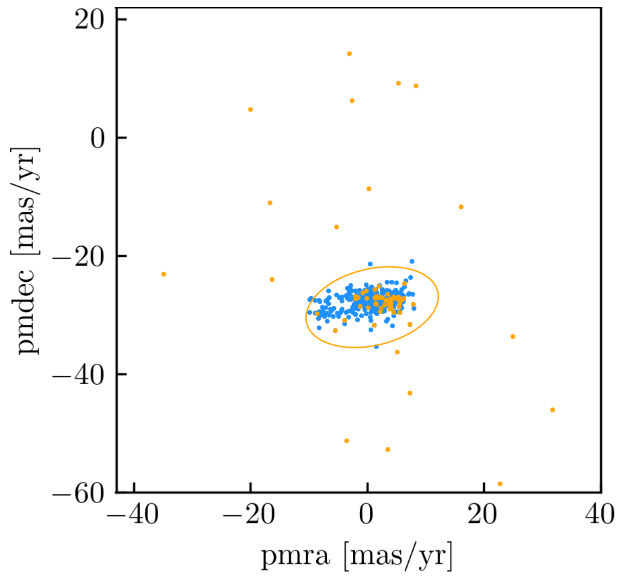

Figure 3.1: Literature and candidate YSOs from this study in proper motion space. This Figure shows the literature YSOs from Galli et al. (2020); Kerr et al. (2021) and Esplin & Luhman (2022) in proper motions space (*pmra* vs. *pmdec*). The orange ellipse highlights the area withing YSO candidates are selected in proper motion space. If a star lies outside of the ellipse it is rejected from my sample. The blue dots represent the literature YSOs and the orange dots show the stars from my selection for which *Gaia* measurements are available.

ellipse around them (see Figure 3.1). I reject stars that fall outside of the orange ellipse as I consider them to not have similar proper motions, hence, they are not associated with the CrA star-forming region. The conditions that need to be met for a star to lie inside the ellipse in proper motion space, are given by the following Equation:

$$(8.73 \times 10^{-2} * (pmra - 0.9) + 5.37 \times 10^{-3} * (pmdec + 28.7))^2 + (-2.71 \times 10^{-2} * (pmra - 0.9) + 0.152 * (pmdec + 28.7))^2 < 1 \quad (3.1)$$

After refining the sample using proper motions, I re-included sources, which have not been detected by *Gaia* if they have been observed with *VISIONS*, as for these sources high resolution images are available. This makes it possible to inspect these sources by eye in order to decide if they should be considered in the final sample. This left me with a total of 84 YSO candidates which were selected by their infrared excess. Finally, visual inspection of the *VISIONS* observed sources revealed that out of the 84 sources, seven are resolved galaxies, and one is a Herbig-Haro object. This brings the final number down to 76 YSO candidates of which I remove three more sources, because they are too far away from the general population of Corona Australis, as becomes apparent in cartesian 3D space (see Figure 3.2), and which have not been previously mentioned in the literature. Therefore, the final selection of infrared selected sources comes to 73. Figure 3.3 shows the number of selected sources versus the number of ultimately accepted in my final sample, as they appear in the sky.

The 73 sources of my final selection were then merged with the sources from the literature. This resulted in a total of 557 sources associated with the Corona Australis star-forming region,

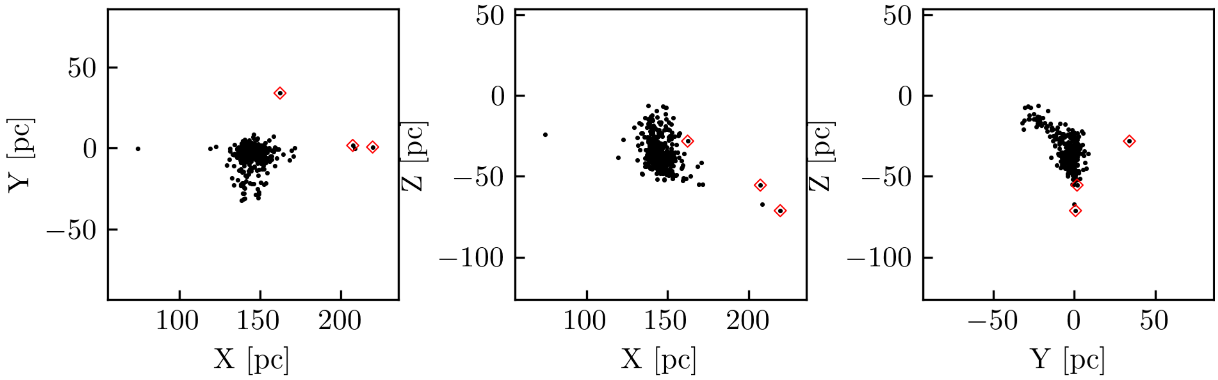

Figure 3.2: Corona Australis young stellar members in Cartesian Heliocentric Galactic coordinates. The black dots represent all sources in the final sample. Red diamonds highlight the three sources that were removed from the sample as they are too far away from the majority of CrA members in cartesian 3D space, as can be seen when viewing the sources in Cartesian Heliocentric Galactic coordinates. The two sources located roughly at 70 pc and 200 pc in X were not removed since they are previously known sources. X increases towards the galactic center, Y increases towards the direction of Galactic rotation, and Z increases towards the Galactic north pole.

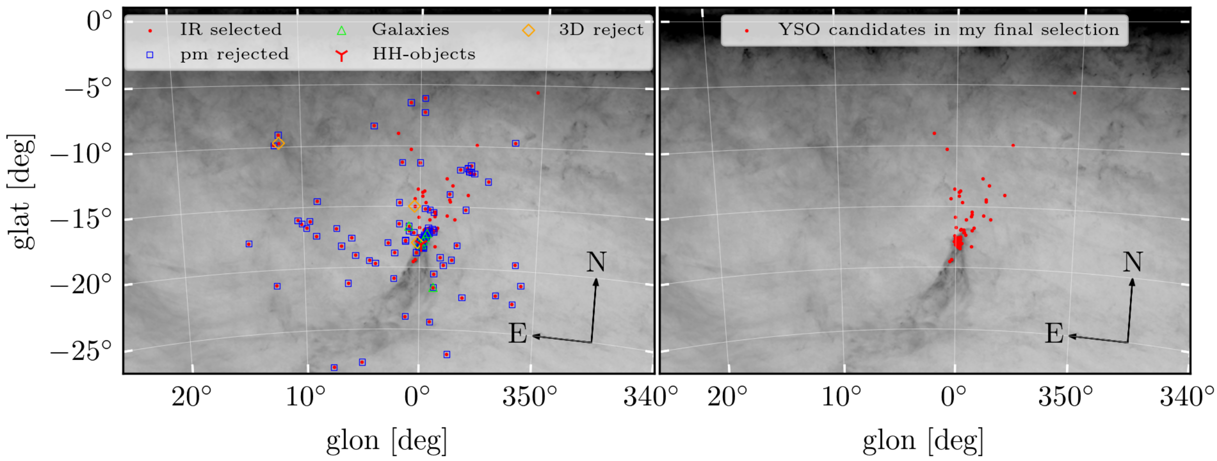

Figure 3.3: IR-selected sources versus accepted sources. The YSO candidates which were selected by their infrared-excess versus the sources that were finally accepted in the sample are plotted over the Planck dustmap (similar to Figure 1.6). *Left panel:* All sources which were selected by their infrared-excess are shown here. In addition, all sources which were later removed from the sample to further refine my selection. I reject 115 sources with mismatching proper motions (blue boxes), 7 resolve galaxies (green triangles), one HH-object (red tristar), and 3 sources which lie far off in 3D space (orange diamonds). *Right panel:* All 73 YSO candidates which were accepted in my final selection, including 56 known sources and 17 new YSO candidates.

of which there are 17 new, previously unreported candidate young stellar objects. Out of the *Spitzer* selected infrared known sources from Peterson et al. (2011) and Dunham et al. (2015), I recover 20 sources. Moreover, the 17 new candidates lie in the same *Spitzer* observed region

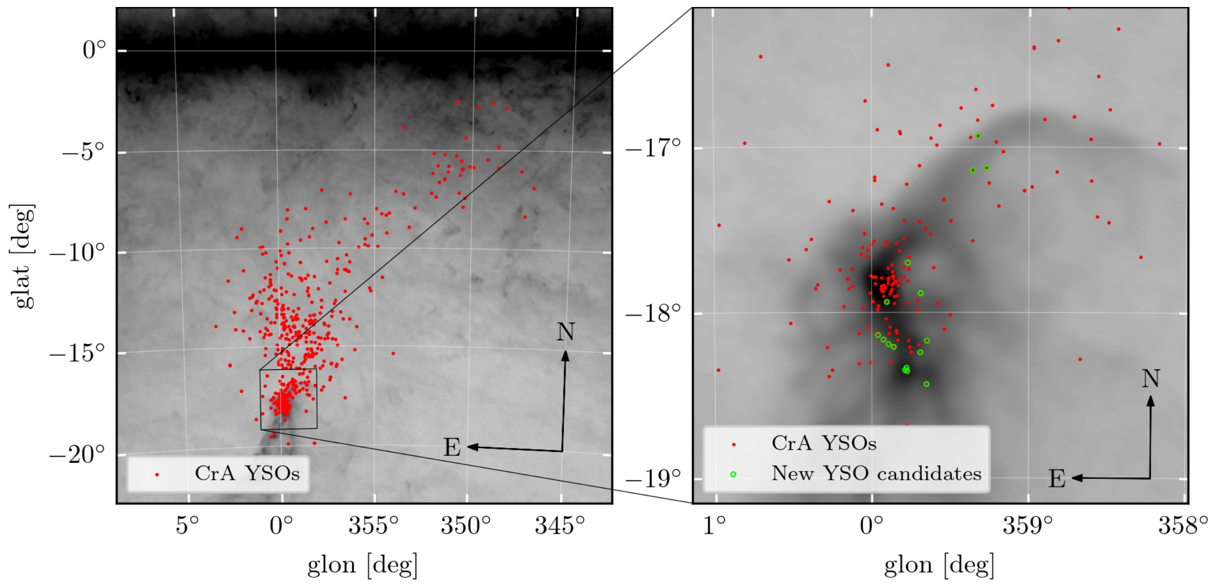

Figure 3.4: All YSOs from the literature and from my selection shown in Galactic projection on top of a Planck map. *Left panel:* Overview of the CrA star-forming region including the location of all YSOs. *Right panel:* Zooming in on the region around the Coronet cluster to highlight the new YSO candidates (green dots).

as the infrared known sources. The remaining 36 sources from my selection lie outside the *Spitzer* fields, and are all recovered sources from the *Gaia* selected samples (see Galli et al. 2020; Kerr et al. 2021; Esplin & Luhman 2020, Ratzenböck et al. subm.). In summary I recover 56 sources from the literature YSO catalogs, confirming these sources from previous selections. Furthermore, none of the reviewed literature sources have been rejected or reclassified. The few selected galaxies and Herbig-Haro objects which were identified by visual inspection of the *VISIONS* images, have already been flagged as such by Peterson et al. (2011) or Dunham et al. (2015) by visually inspecting *Spitzer* images. The 557 sources in my YSO catalog are used in the following to plots and charts to investigate different aspects of Corona Australis.

The 17 new sources were all detected within the *Spitzer* and *VISIONS* observed regions. However, with the chosen science field for this study, I expanded the area in which I searched for sources exhibiting infrared-excess far beyond the *Spitzer* observed regions, which were at the focus of other studies using infrared observations (see e.g. Peterson et al. 2011; Dunham et al. 2015). In this extended area I identified a number of candidate YSOs, which have been discovered using *Gaia* astrometry (see e.g. Galli et al. 2020; Kerr et al. 2021; Esplin & Luhman 2022), but not by their infrared-excess. In Figure 3.4 I present all sources associated with the Corona Australis SFR.

The entire catalog of sources is given in tabular form in Appendix A. Table 3.2 gives an overview of the columns in the catalog. The first column named "ID" assigns each source in the catalog a unique identifier which is used in this study only. Columns two and three list the source identifiers of the optical *Gaia* survey's early data release 3 and data release 2, respectively. Columns four to seven hold the source identifiers of the infrared surveys *2MASS*, *WISE*, *VISIONS*, and *Spitzer*. Since I used early *VISIONS* data, I provide early *VISIONS* IDs which

Table 3.1: This table lists all 17 new YSO candidates, featuring the unique source ID to match them to the main source catalog produced in this thesis. Additionally I list the Classes they were assigned and whether they are uncertain candidates.

ID	Class	uncertain
243	I	yes
248	I	yes
251	flat	yes
255	I	yes
271	I	yes
278	I	yes
283	I	yes
295	flat	yes
296	flat	yes
300	I	yes
303	I	yes
317	I	yes
320	flat	yes
334	flat	yes
341	II	
350	I	yes
352	I	yes

were generated from each source's ra and dec coordinates. In the case of the *Spitzer* IDs I refer to the source identifiers used by the *Spitzer enhanced imaging products* point source catalog (see Section 1.3.1.3). Columns eight, nine and ten show the source IDs used by Peterson et al. (2011), Dunham et al. (2015), and Kerr et al. (2021), respectively. The "references" column indicates by witch of the mentioned previous studies a source in my catalog has been previously identified. The following column "type" holds information on the nature of the source. *YSO* stands for young stellar object or candidate young stellar object, *G* indicates a galaxy, *HH* stands for Herbig-Haro object, and *R* marks sources which were removed due to their position in 3D space. The "new" column indicates if the source has been newly discovered in this thesis. The final three columns provide the right ascension and declination $(ra,\ dec)$ coordinates of the source as well as from which survey or catalog the coordinates were taken. The complete catalog contains 571 sources, containing 557 YSOs and YSO candidates, 9 galaxies, 2 Herbig-Haro objects, and 3 rejected sources which are too far from the majority of sources associated with CrA.

Table 3.2: YSO catalog for Corona Australis as compiled in this study. The first five rows are shown as example, while the whole table is added in the Appendix. The first column named "ID" gives a unique source identifier which is used for this catalog only. The column "references" gives the respective literature reference if a source was identified in a previous study.

ID	ra	dec	coord source[g)]	Gaia EDR3 source id	Gaia DR2 source id	2MASS	WISE	early VISIONS ID	SEIP	ID pet[a)]	ID dun[b)]	ID Kerr[d)]	references	type	new
1	278.839	−37.572	Gaia	6733045308825699328	6733045308825699328	18352140-3734184	J183521.41-373418.6						c) e)	YSO	False
2	285.007	−36.618	Gaia	6731268601100885888	6731268601100885888	19000157-3637054	J190001.57-363705.8	285.006571-36.618300	SSTSL2 J190001.57-363706.1	52		16944	a) c) d) e) f)	YSO	False
3	285.419	−36.742	Gaia	6731220085150343552		19014055-3644320	J190140.56-364432.3	285.419020-36.742340		72			a) e)	YSO	False
4	285.817	−37.236	Gaia	6719167857158732416		19031609-3714080	J190316.10-371408.2	285.817044-37.235702	SSTSL2 J190316.11-371408.2	45			a) e)	YSO	False
5	280.054	−36.816	Gaia	6733456560533083008	6733456560533083008	18401286-3648553	J184012.86-364855.7					15668	c) d) e) f)	YSO	False
⋮															

a) Peterson et al. (2011)
b) Dunham et al. (2015)
c) Galli et al. (2020)
d) Kerr et al. (2021)
e) Esplin & Luhman (2022)
f) Ratzenböck et al. (subm.)
g) If not specified otherwise, "Gaia" refers to *Gaia* EDR3.

3.2 YSO classification

In order to assess the evolutionary stage of the Corona Australis star-forming region, I assigned the YSO classes for the sources in my final catalog. I estimated the infrared spectral index α_{IR}, as described in Section 2.3, for 506 objects. The remaining 51 sources which were not classified, did not have enough reliable photometric measurements (e.g. only J, H, and K_s measurements) for a least square linear regression to derive a spectral index in the range from 2 to 24 µm. Out of the various computed spectral indices, which all use a different combination of photometric filters (see Table 2.4), I chose to use α_{KIWM} to assign the different YSO classes (see Table 1.1) to the sources in my catalog.

In order to assess the star formation history (SFH) it is necessary to know the number of sources with, and without infrared-excess. Therefore, I differentiate two distinct cases in regard to which sources have IR-excess and which do not.

1. Optically thick disks only
2. Optically thick and thin disks

In the first case I only consider sources with optically thick disks, and in the second case I also add optically thin disks to the sources with infrared-excess. With only thick disks I find 133 (23.9 %) sources with IR-excess, whereas when also including thin disks this number increases to 307 (55.1 %). The percentages given correspond to the fractions of sources with IR-excess versus all YSOs in the catalog, including the ones for which no spectral index was computed. The sources with infrared-excess can be divided into the following Classes; Class 0/I, flat spectrum sources (flat), Class II, and Class III with thin disks, depending on which one of the two

Table 3.3: Number of YSOs per Class. Listed here are the total numbers and fractions of sources in each class, for CrA as a whole and all three sub-groups (CrA-Main, CrA-North, and Scorpio-Sting) discussed in Section 3.3.

group		Class 0/I	flat	Class II	Class III		Nr. of YSOs
					thin disk	no disk	
CrA-all	total nr.	29	22	82	174	199	557
	fraction	5.2 %	4.0 %	14.7 %	31.2 %	35.7 %	
CrA-Main	total nr.	29	22	57	44	58	220
	fraction	13.2 %	10.0 %	25.9 %	20.0 %	26.4 %	
CrA-North	total nr.	0	0	25	118	125	301
	fraction	0.0 %	0.0 %	8.3 %	39.2 %	41.5 %	
Sco-Sting	total nr.	0	0	0	12	16	36
	fraction	0.0 %	0.0 %	0.0 %	33.3 %	44.4 %	

previously mentioned cases is considered. The total number (and fractions) of sources of each class is listed in Table 3.3.

The reason for the distinction of the two cases mentioned above is due to the nature of the Class III sources. When determining the number of sources with infrared-excess, it is necessary to understand what component of the YSO contributes the excess infrared emission. In the case of thick disk sources this excess emission stems from the dust in the envelope and the circumstellar accretion disk where the dust from the envelope settles. However, Class III YSOs with optically thin disk, have only little dust left compared to earlier Classes, and therefore contribute only little additional IR radiation, leading to less IR-excess. These thin disk objects are in fact very similar to Class III sources without disks, where the thin disk is interpreted as an debris-disk consisting mostly of planetesimals, and diskless objects do not show signs of such a circumstellar disk at all. In this thesis where I use the IR spectral index fro classification, the only distinction between the two is a different slope (α_{IR}) of the spectral energy distribution (see Table 1.1).

3.3 Corona Australis sub-clusters

Recent studies using *Gaia* data (see e.g. Galli et al. 2020; Kerr et al. 2021; Esplin & Luhman 2022, Ratzenböck et al. subm.) found young stellar members associated with the CrA star-forming region which extend far beyond the embedded Coronet cluster. These findings are supported by the results of my thesis, where I find sources with infrared-excess which have been previously identified with *Gaia*. Moreover, Galli et al. (2020) suggest that CrA young stellar population can be divided into two sub groups, one on-cloud and one off-cloud population. Furthermore, Kerr et al. (2021) found an additional population to the north-west located loosely around 350° Galactic longitude and -5° Galactic latitude, which seems to build a bridge between CrA and the Scorpio-Centaurus (Sco-Cen or Sco-OB2) association. These findings are supported by results from Ratzenböck et al. (subm.) who divide CrA in three distinct sub-clusters, which includes the north-west region mentioned previously. Table 3.4 lists the total number of sources in each sub-group.

Table 3.4: Number of cluster members in each sub-cluster.

CrA-all	CrA-Main	CrA-North	Scorpio-Sting
557	220	301	36

Using the results from Ratzenböck et al. (subm.) I assign all YSOs that are not in the Ratzenböck et al. (subm.) to one of the three sub-clusters by eye, based on their location projected on the sky. Ratzenböck et al. (subm.) named these three clusters CrA-Main, at the location of the Coronet cluster, CrA-North, stretching out to the north of the Coronet, and Scorpio-Sting to the north-west, which is the farthest away from the CrA-Main (see Figure 3.5).

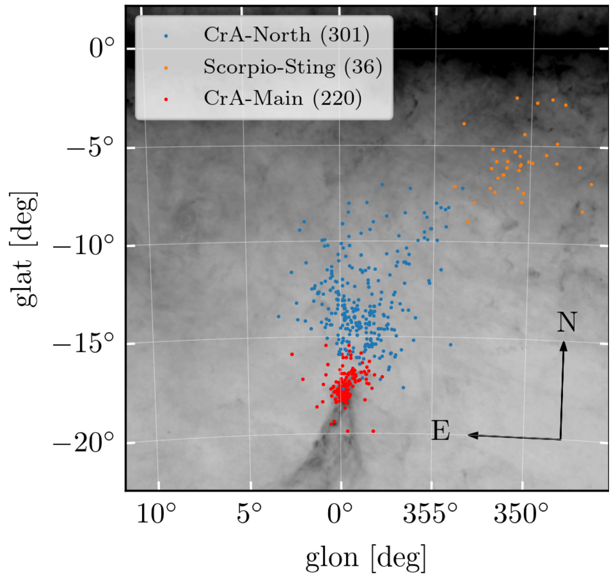

Figure 3.5: Sub-clusters of the CrA young stellar population. Located at the head of the molecular cloud lies CrA-Main (red dots), including the Coronet cluster. To the north west lies Scorpio-Sting (orange dots), and spanning the space to the north of CrA-Main, bridging the divide between CrA-Main and Scorpio-Sting lies CrA-North (blue dots). The number of sources in each sub-cluster is given in the legend in parenthesis and are listed separately in Table 3.4.

Table 3.5: Disk-fractions for the Corona Australis star-forming region. The disk-fraction for all YSOs in CrA is given, as well separately for the three sub-groups of the region. The table lists the total number n as well as the fraction relative to the total number of sources in each group given in parenthesis. Two cases are considered (as in Figure 3.6): (1) only the fraction of sources with thick disks is given, and (2) the fraction of all disks is given (incl. Class III with thin disks).

	CrA-all	CrA-Main	CrA-North	Scorpio-Sting
	n (%)	n (%)	n (%)	n (%)
without thin disks	174(23.9 %)	108(49.1 %)	25(8.3 %)	0(0.0 %)
with thin disk	307(55.3 %)	152(69.1 %)	143(47.8 %)	12(33.3 %)

As described in the previous section, two cases are considered regarding sources with infrared excess. These two cases are also applied when determining the disk-fraction of the sources in CrA. Figure 3.6 shows the disk-fraction for the CrA star-forming region in total and the three sub-groups introduced by Ratzenböck et al. (subm.) in a bar chart. Table 3.5 lists the total number of disks and the disk-fraction in percent per each sub-cluster.

For the entire young stellar population of the Corona Australis SFR, I estimate the disk-fraction, as the number of disks relative to the total number of YSOs. For the two cases I get a disk-fraction of 23.9 % and 55.3 % for thick disks only (case 1) and including thin disks (case

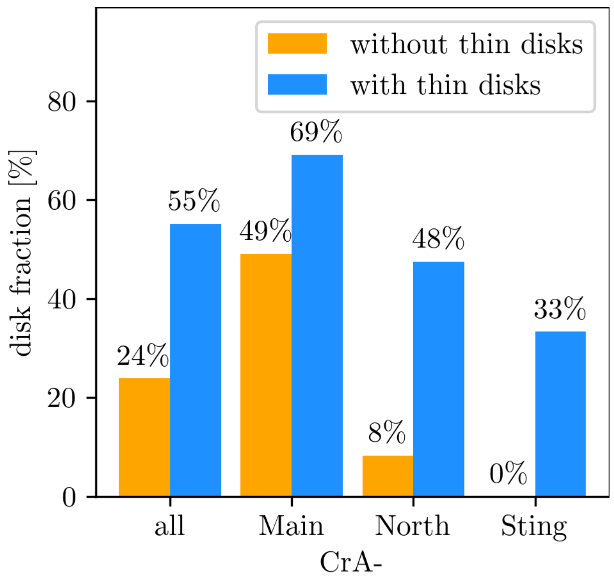

Figure 3.6: Disk-fraction of the CrA young stellar population and of the individual sub-clusters. Two cases were considered: (1) Only YSOs with thick disks are considered (orange bars), and (2) also sources classifies as Class III with thin disks where added to the disk sample (blue bars). See also Table 3.5 and the text for more explanations.

2), respectively. Moreover, the disk-fractions for the three sub-clusters were also determined and compared between the individual sub-clusters. The bar chart in Figure 3.6 visualizes the disk-fractions of the sub-clusters and the young stellar population of CrA in total. In Table 3.5 I list the disk-fractions for the CrA star-forming region in total, and for its three sub-clusters in tabular from.

In Figure 3.6 a decline of the disk-fraction is clearly visible, in the sub-clusters further away from the head of the molecular. CrA-Main shows the highest number of disks relative to the total number of sources in the sub-group, which correlates directly to the age of the sources in the sub-cluster. With increasing distance from the head of the cloud where the dust column density is the highest, the disk-fractions also decrease, with Scorpio-Sting being the sub-cluster with the lowest number of disks, indicating that this group is older than CrA-Main and CrA-North. This suggests the presence of an age gradient in the CrA young stellar population. Similar findings have been reported e.g. by Kerr et al. (2021) and Ratzenböck et al. (subm.) who used different methods. The here presented decline of the disk-fraction for the CrA stellar groups delivers an independent confirmation of the observed age gradient.

In order to estimate the contamination the selected YSOs can be plotted in a *Gaia* color-absolute-magnitude-diagram (CAMD) with model isochrones. These isochrones are lines in the CAMD which indicate where sources of differing mass but with the same age are located in the CAMD. In Figure 3.7 the CAMD shows all YSOs which are detected by *Gaia* and plots $G - RP$ versus G. I show the 10 and 20 Myr *PARSEC* isochrones (Bressan et al. 2012) to roughly estimate an age limit of the young stellar population in CrA. It is expected that sources in the whole CrA sample are younger than about 15 Myr, based on age estimates by Ratzenböck et al. (in prep.).

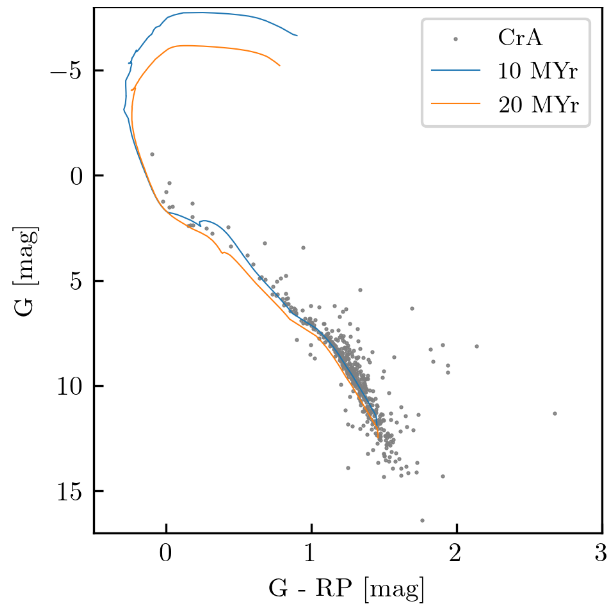

Figure 3.7: *Gaia* color-absolute-magnitude-diagram ($G - RP$ versus G).

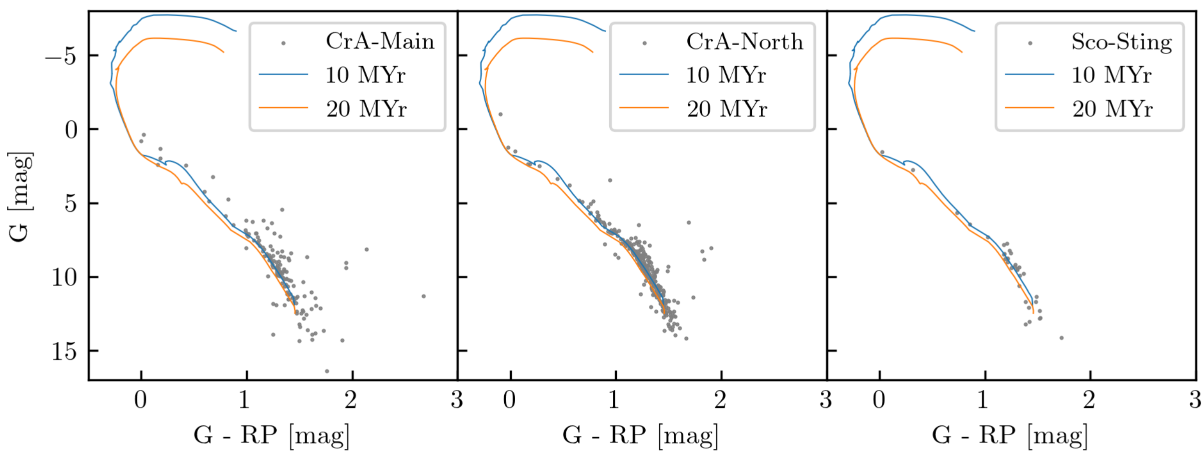

Figure 3.8: *Gaia* color-absolute-magnitude-diagram ($G - RP$ versus G).

As is mentioned in the previous paragraph, there seems to be an age gradient over the three sub-clusters that compose the young stellar population of CrA. Figure 3.8 shows three CAMDs, similar to the CAMD in Figure 3.7, one for each sub-cluster in CrA. It can be clearly seen that the majority of the young stellar population in CrA is located on the right side of the 20 Myr isochrone (orange line). Thus the stellar members of CrA are at the most 20 Myr old. Moreover, the age gradient can be also seen in the three different CAMDs in Figure 3.8. The youngest group in the left panel, CrA-Main, shows a significant number of sources scattered far to the right, whereas CrA-North (middle panel) has most of its sources close to both isochrones, with few sources occupying the region to the right. Scorpio-sting, the oldest of the three sub-groups, has all its sources scattered closely around the isochrones, which indicates that this is the most evolved stellar group of the three.

Any sources that fall on the right side of the isochrones, can either be YSOs with large astrometric or photometric uncertainties, or contamination in the sample, while a scatter due to uncertainties generally tends to increase for faint sources at the low mass end of the CAMD. Looking at Figure 3.7 we find four sources to the left of the isochrones, which are roughly at 8 mag in the *Gaia* G band. These four sources were selected in 5D phase space by Ratzenböck et al. (subm.) and have parallax errors of less than 0.03 mas. Hence, these four sources could be contamination from older unrelated sources, and should be studied in more detail. When looking at the faint end of the CAMD in Figure 3.7, we see a few more sources on the left side of the isochrones, of which 13 sources fainter than 10 mag in the G band were briefly followed up. Out of theses 13 sources, 11 have been selected in 5D phase space by Ratzenböck et al. (subm.). Two sources not selected by Ratzenböck et al. (subm.) show large parallax uncertainties ($\sigma_{\varpi} > 1$ mas). However, one of these two sources has been previously identified by Peterson et al. (2011) using *Spitzer* data. Three more sources, two of which were not selected by Ratzenböck et al. (subm.), are in the selection by Esplin & Luhman (2022), and two (both in Ratzenböck et al. subm.) are in the selection by Galli et al. (2020). These faint YSO candidates, are generally subjected to larger errors, hence, more scatter is expected. Therefore, faint sources (with $G \lesssim 10$ mag) that fall on the left side of the isochrones could still be viable.

Finally, all computed spectral indices, the assigned Class corresponding to α_{KIWM}, as well as to which sub-cluster each source has been assigned to is given in Table A.2. A short version providing an overview of the columns in Table A.2 is given in Table 3.6. The table's first column named "ID" is the same unique identifier as in the YSO catalog (see Table 3.2 and A.1), so that the spectral indices and classes can be matched with the correct sources.

Table 3.6: CrA spectral indices, assigned class and cluster membership. This is a short version of Table A.2, listing the estimated spectral indices for 11 different band combinations. Only the first 5 rows are given in this example. The full table is given in Appendix A.2. The different YSO classes given in the "Class" column were assigned according to the classification scheme given in Table 1.1 using the α_{KIWM} spectral index, as is described in Section 3.2.

ID	cluster	α_{IRAC}	α_{KI}	α_{IM}	α_{KIM}	α_{W3}	α_{WISE}	α_{KW3}	α_{KW4}	α_{KW3M}	α_{W3M}	α_{KIWM}	Class
1	CrA-North					−1.164	−0.494	−1.416				−0.800	II
2	CrA-Main					−0.820	−0.691	−1.069		−0.893	−0.721	−0.847	II
3	CrA-Main					−2.672	−2.672	−2.613		−2.692	−2.743	−2.710	III no disk
4	CrA-Main	−0.698	−0.388	−0.39	−0.339	−0.934	−0.575	−0.534	−0.388	−0.454	−0.631	−0.404	II
5	CrA-North					−2.488	−2.488	−2.443				−2.443	III thin disk
⋮													

Chapter 4

Discussion and Conclusion

In this chapter I briefly discuss the results presented in the previous chapter. Section 4.1 will focus on the quality of the infrared selection made in this thesis. Section 4.2 briefly reviews the star formation history (SFH) based on the insight gained by this study. An assessment of the ESO *VISIONS* public survey is given in Section 4.3 and finally I summarize the conclusions from my thesis in Section 4.4.

4.1 Quality of the infrared selected members of CrA

I selected young stellar objects by their infrared-excess based on methods developed by Koenig & Leisawitz (2014) and Großschedl et al. (2019). When only considering previous studies such as Peterson et al. (2011) or Dunham et al. (2015) who rely mainly on *Spitzer* observations, my use of the all-sky infrared surveys *2MASS* and *WISE* was successful in finding new YSO candidates with infrared-excess beyond the *Spitzer* observed regions. Recent studies using optical data from the *Gaia* space observatory have managed to identify hundreds of new members of the Corona Australis star-forming region (see e.g. Galli et al. 2020; Kerr et al. 2021; Esplin & Luhman 2022), selected based on 5D phase space properties which allows to identify comoving stellar groups. Using all-sky infrared surveys to select new sources beyond the Spitzer observed regions allowed me to independently identify and confirm stellar members with infrared-excess in the somewhat more evolved stellar groups (CrA-North and Scorpio-Sting) beyond the Coronet cluster.

Towards the head of the Corona Australis Molecular cloud where the dust column-density is high, resulting in highly extincted sources, *Gaia* suffers from incompleteness due to optical extinction. This is the region where many YSOs are located, especially the very young embedded protostars. Therefore, the use of high resolution infrared observations from *Spitzer* and *VISIONS* becomes essential when searching for new members of the Corona Australis young stellar population. Consequently, all 17 new candidate YSOs fall within the *Spitzer* and *VISIONS* observed regions. However, upon visual inspection using high resolution color composite images from *VISIONS*, all but one (the source with ID 341) appear very faint and are thus uncertain candidates as they could be very luminous background sources. This is further supported when comparing the SEDs of the new sources with SEDs of known resolved galaxies within the

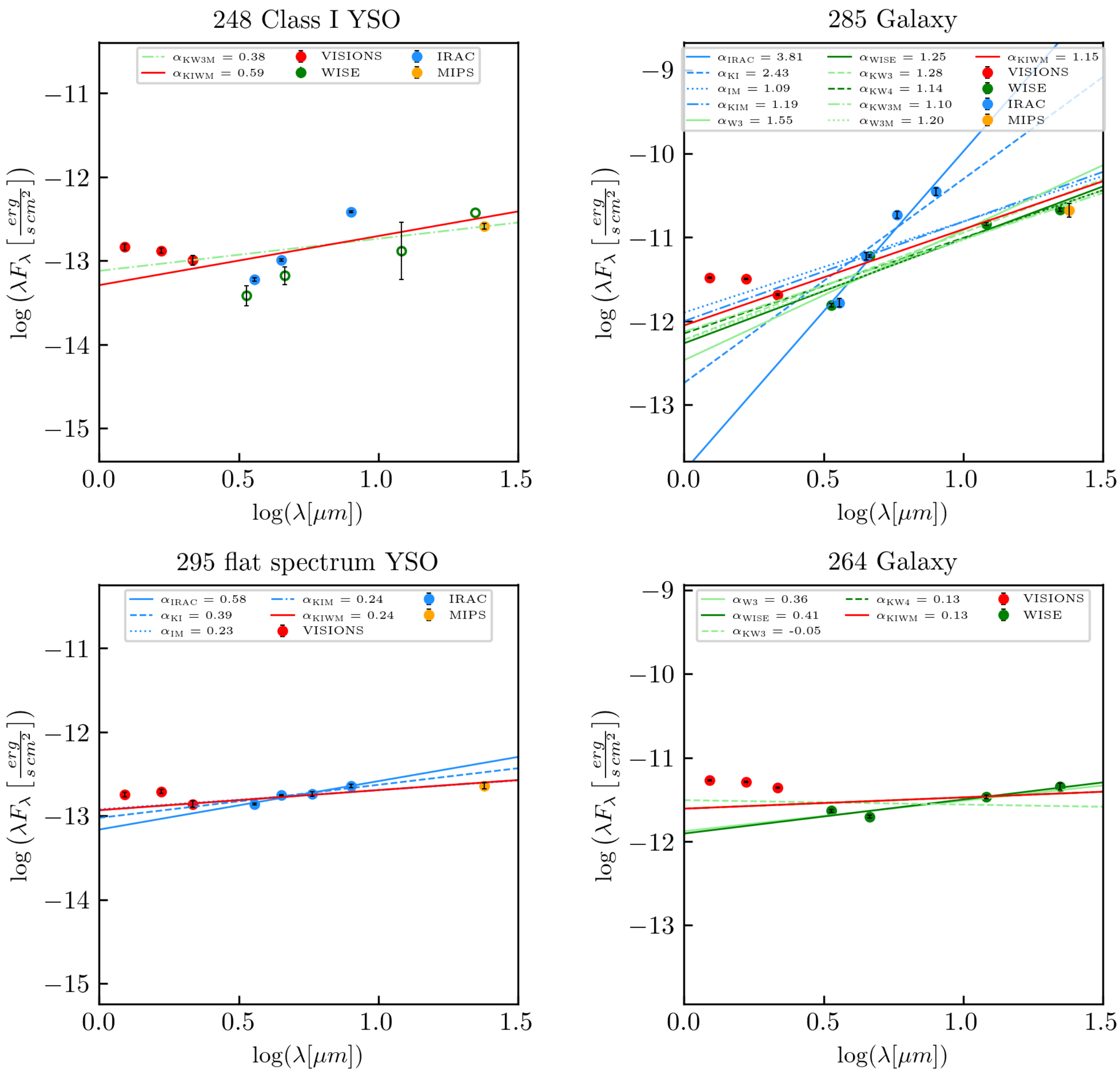

Figure 4.1: SEDs of two new YSO candidates as well as those of two resolved galaxies within the *VISIONS* observed area. The two panels to the left show SEDs of candidate YSOs where the SEDs of the galaxies are shown in the right panel. When comparing the SEDs side by side like this, the similarity in shape can be clearly seen.

VISIONS observed area. Star-forming galaxies, such as late type spirals or irregulars, including interacting galaxies, which have many star-forming regions with YSOs in them can in general mimic the SEDs of single nearby YSOs within our own Galaxy. Figure 4.1 places the SEDs of two new YSO candidates (IDs 248 and 092) and two resolved galaxies, one is an interacting galaxy (ID 285) and the other is a face on spiral galaxy (ID 211) side by side to showcase similarities between the SEDs, which suggests that the new uncertain candidates could very well be distant star-forming galaxies.

The source with the ID 341 is the only one out of the 17 new candidates, which is not considered as uncertain candidate based on visual inspection of the *VISIONS* images. The reason for the large number of uncertain candidates can be attributed to the quality of the *Spitzer* data used in this study. By applying the recommended quality cuts (see Section 2.2.1.2) to the *Spitzer* Enhanced Imaging Products (SEIP) I have removed a large number of sources at the location of the Coronet cluster, as this region features extended background emission from reflection nebulae and the molecular cloud, which is irradiated by the embedded young stars. This can be seen exceptionally well in Figure 2.31 and 2.32, where the entire main sequence is missing from the CMD and CCD, and faint sources only remain in the area where we expect high contamination due to faint background AGN and star-forming galaxies (see Figure 2.4). Moreover, the selection cuts in the *VISIONS-Spitzer* color-color diagram (Figure 2.32) run along the very border of this region in the CCD, which likely contributes to a high contamination fraction.

Due to the restrictions imposed by using the *Spitzer* Enhanced Imaging Products (see Section 2.2.1.2) the IR-selection within the *Spitzer* observed regions could be significantly improved by reprocessing the *Spitzer* raw images. By fine tuning the calibration pipeline to the particularities of the CrA region, the resulting custom *Spitzer* source catalog would be an improvement over the SEIP as they were processed to best fit all Spitzer observations in the SEIP archive. By relying on the SEIP, I only one fifth of the IR selected sources from Peterson et al. (2011) and Dunham et al. (2015) (20 out of 99 sources). However, by using all-sky IR archival catalogs (*2MASS* and *WISE*) I was able to select sources far beyond the *Spitzer* observed regions, selecting even one source with infrared-excess in the Scorpio-Sting sub-group. Therefore, I argue that the infrared-selection done in this thesis has confirmed the extended nature of the CrA star-forming region, which was first suggested by Galli et al. (2020); Kerr et al. (2021); Esplin & Luhman (2022), and Ratzenböck et al. (subm.), by finding 31 additional sources in the CrA-Main group, 21 sources in CrA-North and one source in Scorpio-Sting, which have not been previously selected by their IR-excess. This indicates an overall good performance of the methods applied and speaks for the quality of the selection.

4.2 Reviewing the star-formation history of CrA

To study the star formation history (SFH) of the Corona Australis star-forming region in greater detail, a complete catalog of sources associated to this region is needed. Since previous studies using infrared data mainly focused on the *Spitzer* observed regions (see e.g. Forbrich et al. 2007; Peterson et al. 2011; Dunham et al. 2015), which was the basis of the *known sources* (see Section 1.4.2.1), these observations only covered a small subregion of what is investigated in this study. Therefore, I expanded the region of interest with the goal to identify new, previously unknown YSO candidates in the surrounding area around the CrA molecular cloud (see Figure 2.1). The region north of the Coronet cluster as well as to the east were of special interest to me. The northern reaches are the area where additional sources associated to the CrA star-forming region were found using *Gaia* data (Galli et al. 2020; Kerr et al. 2021; Esplin & Luhman 2022, Ratzenböck et al. subm.), whereas the area to the east exhibits a loop-like pattern clearly visible in dust emission (e.g. Planck, see Figure 1.5). In order to explore the possibility of this loop being connected to a bubble driven by massive stellar feedback, which may have led to a star-forming event located east of the Coronet, the search area was expanded to encompass this region.

Therefore, it is investigated if the peculiar upwards bend of the south-west tail of the cloud is maybe the remnant of a supernova driven bubble. These expanding supernova bubbles can be the cause for triggered star formation (see e.g. Cohen et al. 2003; Churchwell et al. 2006). No YSO candidates were found in this region, which suggests that the amount of interstellar medium amassed at the outer shell of the expanding bubble is not large enough for gravitational collapse to start. A different explanation for missing YSOs in the bubble shaped tail could be due to projection effects, which means that the bubble shape is merely coincidentally and not connected to stellar feedback mechanisms at all. Hence the tail would consist only of thin interstellar medium which is not capable of star formation at all. This interpretation of the loop-like structure is supported by 3D dustmaps of the solar neighborhood (e.g. Leike et al. 2020) where we see a long tail extending away from the observer, and the loop is only seen projected on the sky.

The only part of the Corona Australis molecular cloud with active star formation is the head of the cloud. This northern most tip of the molecular cloud is the location of the embedded Coronet cluster, one of the three sub-clusters of the CrA young stellar population, as introduced in Section 3.3. These three sub-clusters, CrA-Main, CrA-North, and Scorpio-Sting, spanning over $21°$, stretching from the head of the molecular cloud to the north-west in this order (see Figure 3.5). The disk-fraction of the three sub-clusters points toward an age gradient over the three clusters, with the largest disk-fraction in CrA-Main (including the Coronet cluster), and with declining disk-fractions in the two other sub-clusters CrA-North and Scorpio-Sting. This is supported by isochronal age estimates by Kerr et al. (2021) or Ratzenböck et al. (subm.). Additionally, the age gradient is supported, for example, by Hernández et al. (2007) or Ribas et al. (2015), who computed disk-fractions for several star forming regions and showed that age correlates to the disk-fraction, where a higher fraction corresponds to a younger age.

Having selected sources by their infrared-excess from all three sub-groups, I confirm the extended nature of the CrA YSO population. The sub-groups of CrA, CrA-Main, CrA-North, and Scorpio-Sting, span more than $20°$ on the sky, with the north-west sub-cluster Scorpio-Sting appearing in the sting of the constellation Scorpio, as projected in the sky. Therefore, it can be suspected that CrA is connected to the Sco-Cen association, as has been suggested by Mamajek & Feigelson (2001), later confirmed using *Gaia* data by Kerr et al. (2021) and Ratzenböck et al. (subm.). This provides further evidence to Corona Australis being considered as part of the Sco-Cen association. Moreover, the age gradient found in the CrA young stellar association further suggests that the Corona Australis star-forming region originates from Sco-Cen. (Mamajek & Feigelson 2001) suggested that star formation in CrA was triggered by either cloud turbulence or an expanding super bubble.

4.3 Quality of the VISIONS survey

In this thesis I used early data from *VISIONS*–VISTA Star Formation Atlas, a near-infrared survey of all star formation regions accessible from the southern hemisphere, which are within a distance of 500 pc. The photometric source catalog produced by the *VISIONS* team contained 6 202 478 sources, which were detected in at least one photometric band. Moreover, *VISIONS* provides high resolution false color images for all *VISIONS* observed regions, which were used to visually inspect the infrared selected sources within the *VISIONS* coverage.

In order to achieve the photometric sensitivity of the survey, there exists an upper brightness limit in each filter of roughly 12 mag. Any sources brighter than this limit are saturated in the *VISIONS* photometry catalogs and thereby can not be used to derive reliable photometry. In order to compensate this caveat, I replaced the photometry of *VISIONS* saturated sources, with photometry from the *2MASS* catalog (see Section 2.2.1.3 for details). In the final *VISIONS* catalog produced by the *VISIONS*-team this will have been already done to provide a homogeneous photometric catalog. In the case of Corona Australis, which lies at a distance of $d \approx 150$ pc, a significant fraction of sources associated with CrA is saturated and the photometry had to be substituted. Consequently, the *VISIONS* photometry of most of the sources on, and approaching the main sequence has been replaced by *2MASS* photometry (see Figures 2.23 and 2.25). Vice versa, faint sources of CrA benefit of the sensitivity of the *VISIONS* survey, however, the faint stellar members of CrA are easily confused with background extragalactic sources. This is where future *VISIONS* data releases, which will include proper motions, will make it possible to select sources based on kinematics in addition to photometry and positions alone, filling in the low mass end of the CrA young stellar population.

In addition to photometry, I further included *VISIONS* false color images in my study, to visually inspect uncertain sources in my infrared selection. These images were provided to me by the *VISIONS* team in the form of a HiPS (Hierarchical Progressive Survey) as RGB color images, where the red, green and blue channel correspond to the K_s, H and J filters, respectively. The highest resolution at level 10 of the HiPS corresponds to a pixel scale of 402.6 mas per pixel. With such a high resolution, many background galaxies are resolved sources and can be excluded from the sample, whereas in other infrared surveys such as *2MASS* and *WISE* these sources appear as point sources. Using the high resolution images from *VISIONS* to visually inspect the IR selected sources from this study, I identified nine sources, which appear to be resolved background galaxies and were removed from the sample. Out of these nine galaxies, three have been previously identified as such by Peterson et al. (2011), within the *Spitzer* observed field, as *Spitzer* provides similarly high resolution images.

4.4 Conclusion

By selecting potential young stellar members of the Corona Australis SFR by their infrared-excess I identified candidate YSOs beyond the *Spitzer* regions. Recent studies (e.g. Galli et al. 2020; Kerr et al. 2021; Esplin & Luhman 2022) using *Gaia* data have independently found stellar members beyond the Coronet cluster, including all sources in my selection located outside the regions of high extinction. This leaves 17 new YSO candidates in CrA, of which 16 are considered uncertain candidates. I conclude that the young stellar population of the Corona Australis star-forming region is already very well characterized in terms of completeness. Any undiscovered members with IR-excess are most likely located in the immediate vicinity of the Coronet cluster, as this is the region of the molecular cloud with the highest dust column density. Using *VISIONS* and *Spitzer* in combination has revealed 17 new YSO candidates in this region, of which 16 are uncertain candidates. By improving the *Spitzer* data, for instance by reprocessing the images in the *Spitzer* Heritage Archive, additional YSO candidates of higher confidence could be found there. Most importantly I was able to independently confirm the extended nature of the Corona Australis star-forming region by selecting YSO candidates by their IR-excess. By adding this part of information to the greater picture of CrA, has contributed to our knowledge of the SFH in CrA.

Regarding possible star formation events in the past, located in the tail of the Corona Australis molecular cloud, the absence of any of any newly detected YSO candidates, indicates that the tail is not actively forming stars. The bubble shape of this tail can be explained either by massive stellar feedback such as supernovae, or as the result of projection effects. In the case of an expanding supernova bubble, the plowed up interstellar matter is not massive or dense enough to produce new stars. If the peculiar shape is attributed to projection effects, the tail probably consists of thin gas which is equally unable to form stars.

By determining the disk-fraction in the three sub-clusters of the CrA young stellar population, I find an age gradient from south to north. The Coronet exhibits the highest disk-fraction, which decreases with increasing distance from the Coronet. The sub-cluster with the lowest disk-fraction (Scorpio-Sting) is located the farthest from the Coronet to the north-west. As higher relative numbers of disks in a cluster are an indication for an overall younger evolutionary stage of a cluster, the youngest stellar sub-group is located at the Coronet region, with increasing age towards the North. This supports the results of Galli et al. (2020), Kerr et al. (2021), Esplin & Luhman (2022), and Ratzenböck et al. (subm.) who found similar age gradients for Corona Australis.

With this thesis acting as a pilot study using early *VISIONS* data products as a part of the quality control in the data reduction pipeline for the upcoming *VISIONS* data release, I assessed the quality of the NIR photometry as well as the image products produced by the *VISIONS* team. Making use of this data has shown that *VISIONS* so far provides excellent photometry and images, and no major flaws were apparent in the dataset. As has been described in Section 2.2.1.3, there exists a brightness threshold, beyond which sources are saturated in the *VISIONS* catalog. To compensate for this, I replaced the photometry of saturated *VISIONS* sources with *2MASS* photometry. Due to the close distance of Corona Australis, most of the YSO candidates selected in the *VISIONS* selections (see Section 2.2.3.2 and 2.2.3.3), are mostly saturated, and have been replaced by *2MASS* photometry (see especially Figure 2.23 and 2.25).

By using all-sky infrared surveys in my thesis, I was able to select YSO candidates with infrared-excess outside the *Spitzer* observed fields. This confirmed the extended nature of the CrA young stellar population, and supports findings by Kerr et al. (2021) and Ratzenböck et al. (subm.), which indicate that Corona Australis is part of the Sco-Cen association. From the disk-fraction, which was computed individually for each of the three sub-groups of CrA, an age gradient was observed, with the youngest cluster located at the head of the Corona Australis molecular cloud, and the oldest group, Scorpio-Sting, which is the farthest away from the molecular cloud, acting as a bridge between CrA and Sco-Cen. This further leads to the conclusion that star formation in CrA originated from Sco-Cen, as suggested e.g. by Mamajek & Feigelson (2001). By combining young stellar members from recent studies using *Gaia* (Galli et al. 2020; Kerr et al. 2021; Esplin & Luhman 2020, Ratzenböck et al. subm.), with IR selected sources from the literature (Peterson et al. 2011; Dunham et al. 2015) and from this study, I compiled a most complete catalog of young stellar members of CrA, with 17 previously unknown candidate YSOs. With these insights gained from my thesis, I have added a new puzzle piece to this already well characterized star-forming region.

Chapter 5

Outlook

In this chapter I want to give a brief outlook on possible future research topics based on this thesis, and future data releases of the *VISIONS* survey. The main focus of this thesis lies on the detection of new YSOs in the Corona Australis star-forming region using infrared photometry, in an area beyond the previously infrared-analyzed regions. I selected sources which have already been discovered by optical data from *Gaia* (see e.g. Galli et al. 2020; Kerr et al. 2021; Esplin & Luhman 2022). Due to the thorough previous searches for young stellar members in CrA, in combination with the here presented analysis, the current catalog of CrA members is one of the most complete sample of YSOs for any known star-forming region. *VISIONS* is a multi epoch survey, which will include proper motions in a future data release making it possible to select sources based on astrometry in addition to the photometric methods described in Section 2.2. Moreover, the *VISIONS* source catalog for Corona Australis alone contains more than six million sources detected in at least one near-infrared filter, and promises completeness down to Brown dwarf masses, which are most likely overlooked in this thesis. Using proper motions may very well include these low mass members in a future study revisiting the results of my thesis.

Gaining a more complete set of YSOs in the *VISIONS* observed regions is not the only use of infrared proper motions. Großschedl et al. (2021) have demonstrated that it is possible to derive the 3D motion of molecular clouds by probing the proper motions of the young stellar population associated with the cloud, and combining them with radio radial velocity measurements of the gas, which was done for the southern Orion complex. However, Großschedl et al. (2021) made use of *Gaia* DR2 data, which neglected the youngest, deeply embedded protostars, which have the tightest connection to the cloud they formed in. Consequently, it can be expected that *VISIONS* IR proper motions will improve such 3D space motion analysis in the future.

Future *VISIONS* data releases will provide photometry and astrometry for all *VISIONS* observed star-forming regions beyond Corona Australis, including Ophiuchus, the Pipe nebula, the Chameleon-Musca complex, Lupus, and the southern Orion complex. This gives rise to the opportunity to review these star-forming regions in a similar manner as has been done for Corona Australis in this thesis, making use of the excellent *VISIONS* dataset. Using *VISIONS* data to compile a most complete selection of YSOs in the nearby SFRs down to objects at the hydrogen burning limit, such as brown dwarfs, will add another aspect to the low mass end of the initial mass function in the solar neighborhood (see e.g. Luhman 2004; Lodieu et al. 2012; Alves de Oliveira 2013).

The high resolution images produced by *VISIONS*—down to 100 to 250 AU for the closest star-forming regions—can be further used to explore the importance of YSO morphology for young stellar object classification. This can be done for instance by applying machine learning methods to the images from *VISIONS* among other surveys, in order to find prototypes of morphological classes, which can be interpreted and compared to the standard classification used in this thesis. Therefore, *VISIONS* images can provide a wealth of data from several star-forming regions, which may be used in such an analysis to complement other high resolution images in different wavelengths.

In Section 2.3 I described how YSO classification was done by computing the infrared spectral index $\alpha_{\rm IR}$, using different combinations of infrared bands, and assigning them to classes, based on the classification scheme developed by Lada & Wilking (1984). Depending on the shape of the spectral energy distribution, and the combination of filter bands, the spectral index can vary significantly and thus lead to ambiguity in YSO classification. Therefore, future improvement in classification could be achieved by including SED fitting using models from the literature (see e.g. Whitney et al. 2003b,a, 2004; Robitaille et al. 2006, 2007; Robitaille 2017). This would also include adding additional photometric measurements, especially in the optical and far-infrared regime, as this thesis only includes near- and mid-infrared measurements to create the SEDs. Moreover, X-ray measurements can be used to further distinguish Class III YSOs from main sequence stars, as disk-less pre-main-sequence stars exhibit X-ray excess (Feigelson & Decampli 1981; Koyama et al. 1996; Feigelson et al. 2002).

With a better characterization of the young stellar population of Corona Australis, an extended analysis of the star-formation history of CrA can be made. Especially revisiting the YSO classification, using a better estimate of the YSO class and based upon this recompute the disk-fraction of the three sub-clusters more accurately may give further constraints on the ages of the these sub-clusters. Hernández et al. (2007) and Ribas et al. (2015) have demonstrated how relative ages can be derived from the disk-fraction in different star-forming regions. Moreover, other methods such as isochrone fitting (see e.g., Johnston et al. 2019) or by using dynamical traceback analysis (see e.g., Miret-Roig et al. 2020) to estimate the ages of the CrA sub-groups with higher accuracy could be explored. A different approach to deriving ages is used by Esplin & Luhman (2020, 2022) to derive relative ages from dereddened absolute K magnitudes. With *VISIONS* providing photometry in the K_s this method could be used to further constrain the age estimates for the young stellar population of the *VISIONS* observed star-forming regions.

With this thesis, I added another puzzle piece to our knowledge of the Corona Australis star-forming region. The YSO catalog that was created in the setting of this work is a wonderful basis for future studies in this region focusing on star formation. With future *VISIONS* data releases, a revision of all other *VISIONS* observed regions is planned, which will help getting a more complete image of star formation in the solar neighborhood.

Bibliography

Acker, A., Cuisinier, F., Stenholm, B., & Terzan, A. 1992, Astronomy & Astrophysics, Vol. 264, pp. 217

Adams, F. C., Lada, C. J., & Shu, F. H. 1987, The Astrophysical Journal, Vol. 312, pp. 788

Adams, F. C. & Shu, F. H. 1986, The Astrophysical Journal, Vol. 308, pp. 836

Alves de Oliveira, C. 2013, Memorie Della Societa Astronomica Italiana, 84, 905

André, P. 1994, in The Cold Universe, ed. T. Montmerle, C. J. Lada, I. F. Mirabel, & J. Tran Thanh Van, pp. 179

André, P. 2015, in Encyclopedia of Astrobiology, ed. M. Gargaud, W. M. Irvine, R. Amils, I. Cleaves, Henderson James (Jim), D. L. Pinti, J. C. Quintanilla, D. Rouan, T. Spohn, S. Tirard, & M. Viso (Springer, Berlin, Heidelberg), pp. 2308–2313

André, P., Di Francesco, J., Ward-Thompson, D., et al. 2014, in Protostars and Planets VI, ed. H. Beuther, R. S. Klessen, C. P. Dullemond, & T. Henning (University of Arizona Press), pp. 27

André, P. & Montmerle, T. 1994, The Astrophysical Journal, Vol. 420, pp. 837

André, P., Ward-Thompson, D., & Barsony, M. 1993, The Astrophysical Journal, Vol. 406, pp. 122

André, P., Ward-Thompson, D., & Barsony, M. 2000, in Protostars and Planets IV, ed. V. Mannings, A. P. Boss, & S. S. Russell (University of Arizona Press), pp. 59

Assef, R. J., Kochanek, C. S., Brodwin, M., et al. 2010, The Astrophysical Journal, Vol. 713, pp. 970

Astropy Collaboration, Price-Whelan, A. M., Sipőcz, B. M., et al. 2018, The Astronomical Journal, 156, 123

Astropy Collaboration, Robitaille, T. P., Tollerud, E. J., et al. 2013, Astronomy & Astrophysics, 558, A33

Barsony, M. 1994, in Astronomical Society of the Pacific Conference Series, Vol. 65, Clouds, Cores, and Low Mass Stars, ed. D. P. Clemens & R. Barvainis, pp. 197

Beckwith, S., Staude, J., Quetz, A., & Natta, A. 1996, Lecture Notes in Physics, Vol. 465, Disks and Outflows Around Young Stars: Proceedings of a Conference Honouring Hans Elsässer Held at Heidelberg, Germany, 6–9 September 1994 (Berlin, Heidelberg: Springer, Berlin, Heidelberg)

Bergin, E. A., Goldsmith, P. F., Snell, R. L., & Ungerechts, H. 1994, The Astrophysical Journal, Vol. 431, pp. 674

Bergin, E. A. & Tafalla, M. 2007, Annual Reviews of Astronomy & Astrophysics, Vol. 45, pp. 339

Bertin, E. & Arnouts, S. 1996, Astronomy & Astrophysics Supplement Series, Vol. 117, pp. 393

Beuther, H., Klessen, R. S., Dullemond, C. P., & Henning, T., eds. 2014, Protostars and Planets VI (University of Arizona Press)

Blitz, L. 1987, in NATO Advanced Study Institute (ASI) Series C, Vol. 210, Physical Processes in Interstellar Clouds, ed. G. E. Morfill & M. Scholer, pp. 35–58

Blitz, L. 1993, in Protostars and Planets III, ed. E. H. Levy & J. I. Lunine (University of Arizona Press), pp. 125

Bok, B. J. 1948, Dimensions and Masses of Dark Nebulae, Vol. 7 (Harvard Observatory), pp. 53

Bressan, A., Marigo, P., Girardi, L., et al. 2012, Monthly Notice of the Royal Astronomical Society, 427, 127

Burkert, A. 2017, Memorie Della Societa Astronomica Italiana, Vol. 88, pp. 533

Calvet, N., D'Alessio, P., Watson, D. M., et al. 2005, The Astrophysical Journal Letters, 630, L185

Capak, P. L., Teplitz, H., Hanish, D., et al. 2012, in American Astronomical Society Meeting Abstracts, Vol. 219, American Astronomical Society Meeting Abstracts #219, pp. 410.01

Chira, R.-A. 2018, arXiv e-prints, pp. arXiv:1806.02286

Chira, R. A., Kainulainen, J., Ibáñez-Mejía, J. C., Henning, T., & Mac Low, M. M. 2018, Astronomy & Astrophysics, Vol. 610, pp. A62

Churchwell, E., Povich, M. S., Allen, D., et al. 2006, The Astrophysical Journal, 649, 759

Cieza, L. A., Schreiber, M. R., Romero, G. A., et al. 2010, The Astrophysical Journal, 712, 925

Cieza, L. A., Schreiber, M. R., Romero, G. A., et al. 2012, The Astrophysical Journal, 750, 157

Clark, P. C., Glover, S. C. O., Ragan, S. E., & Duarte-Cabral, A. 2019, Monthly Notice of the Royal Astronomical Society, Vol. 486, pp. 4622

Cohen, M., Green, A. J., Parker, Q. A., Mader, S., & Cannon, R. D. 2002, Monthly Notice of the Royal Astronomical Society, 336, 736

Cohen, M., Parker, Q. A., Green, A. J., et al. 2011, Monthly Notice of the Royal Astronomical Society, Vol. 413, pp. 514

Cohen, M., Wheaton, W. A., & Megeath, S. T. 2003, The Astronomical Journal, Vol. 126, pp. 1090

Cutri, R. M., Wright, E. L., Conrow, T., et al. 2012, Explanatory Supplement to the WISE All-Sky Data Release Products, Explanatory Supplement to the WISE All-Sky Data Release Products

Draine, B. T. 2011, Physics of the Interstellar and Intergalactic Medium, Princeton series in astrophysics (Princeton: Princeton University Press)

Dunham, M. M., Allen, L. E., Evans, Neal J., I., et al. 2015, The Astrophysical Journal Supplement Series, Vol. 220, pp. 11

Elmegreen, B. G. & Scalo, J. 2004, Annual Reviews of Astronomy & Astrophysics, Vol. 42, pp. 211

Emerson, J. P., Sutherland, W. J., McPherson, A. M., et al. 2004, The Messenger, 117, 27

Espaillat, C., Ingleby, L., Hernández, J., et al. 2012, The Astrophysical Journal, 747, 103

Esplin, T. L. & Luhman, K. L. 2020, The Astronomical Journal, 159, 282

Esplin, T. L. & Luhman, K. L. 2022, The Astronomical Journal, Vol. 163, pp. 64

Evans, Neal J., I. 1999, Annual Reviews of Astronomy & Astrophysics, Vol. 37, pp. 311

Evans, Neal J., I., Dunham, M. M., Jørgensen, J. K., et al. 2009a, The Astrophysical Journal Supplement Series, Vol. 181, pp. 321

Evans, N., Calvet, N., Cieza, L., et al. 2009b, arXiv e-prints, pp. arXiv:0901.1691

Fazio, G. G., Hora, J. L., Allen, L. E., et al. 2004, The Astrophysical Journal Supplement Series, 154, 10

Feigelson, E. D., Broos, P., Gaffney, James A., I., et al. 2002, The Astrophysical Journal, Vol. 574, pp. 258

Feigelson, E. D. & Decampli, W. M. 1981, The Astrophysical Journal Letters, Vol. 243, pp. L89

Fűrész, G., Hartmann, L. W., Megeath, S. T., Szentgyorgyi, A. H., & Hamden, E. T. 2008, The Astrophysical Journal, 676, 1109

Forbrich, J. & Preibisch, T. 2007, Astronomy & Astrophysics, Vol. 475, pp. 959

Forbrich, J., Preibisch, T., Menten, K. M., et al. 2007, Astronomy & Astrophysics, 464, 1003

Gaia Collaboration, Brown, A. G. A., Vallenari, A., et al. 2018, Astronomy & Astrophysics, Vol. 616, pp. A1

Gaia Collaboration, Brown, A. G. A., Vallenari, A., et al. 2021, Astronomy & Astrophysics, Vol. 649, pp. A1

Gaia Collaboration, Prusti, T., de Bruijne, J. H. J., et al. 2016, Astronomy & Astrophysics, Vol. 595, pp. A1

Galli, P. A. B., Bouy, H., Olivares, J., et al. 2020, Astronomy & Astrophysics, Vol. 634, pp. A98

Gaposchkin, S. & Greenstein, J. L. 1936, Harvard College Observatory Bulletin, Vol. 904, pp. 8

Gargaud, M., Amils, R., Quintanilla, J. C., et al. 2011, Encyclopedia of Astrobiology (Springer, Berlin, Heidelberg)

Genzel, R. & Stutzki, J. 1989, Annual Reviews of Astronomy & Astrophysics, Vol. 27, pp. 41

Ginsburg, A., Sipőcz, B. M., Brasseur, C. E., et al. 2019, The Astronomical Journal, 157, 98

Green, G. M. 2018, The Journal of Open Source Software, Vol. 3, pp. 695

Greene, T. P., Wilking, B. A., André, P., Young, E. T., & Lada, C. J. 1994, The Astrophysical Journal, Vol. 434, pp. 614

Großschedl, J. E., Alves, J., Meingast, S., & Herbst-Kiss, G. 2021, Astronomy & Astrophysics, Vol. 647, pp. A91

Großschedl, J. E., Alves, J., Teixeira, P. S., et al. 2019, Astronomy & Astrophysics, Vol. 622, pp. A149

Gutermuth, R. A., Megeath, S. T., Myers, P. C., et al. 2009, The Astrophysical Journal Supplement Series, 184, 18

Hacar, A., Alves, J., Forbrich, J., et al. 2016, Astronomy & Astrophysics, 589, A80

Hacar, A., Bosman, A., & van Dishoeck, E. F. 2020a, VizieR Online Data Catalog, pp. J/A+A/635/A4

Hacar, A., Hogerheijde, M. R., Harsono, D., et al. 2020b, Astronomy & Astrophysics, Vol. 644, pp. A133

Hacar, A., Tafalla, M., Forbrich, J., et al. 2018, Astronomy & Astrophysics, 610, A77

Hacar, A., Tafalla, M., Kauffmann, J., & Kovács, A. 2013, Astronomy & Astrophysics, Vol. 554, pp. A55

Heiderman, A. & Evans, Neal J., I. 2015, The Astrophysical Journal, 806, 231

Herbig, G. H. 1960, The Astrophysical Journal Supplement Series, Vol. 4, pp. 337

Herbig, G. H. & Bell, K. R. 1988, Third Catalog of Emission-Line Stars of the Orion Population : 3 : 1988 (University of California Press)

Hernández, J., Hartmann, L., Megeath, T., et al. 2007, The Astrophysical Journal, 662, 1067

Heyer, M. & Dame, T. M. 2015, Annual Reviews of Astronomy & Astrophysics, Vol. 53, pp. 583

Hopkins, P. F. 2014, Nature, Vol. 516, pp. 44

Hopkins, P. F., Cox, T. J., Hernquist, L., et al. 2013, Monthly Notice of the Royal Astronomical Society, Vol. 430, pp. 1901

Hotzel, S., Harju, J., & Walmsley, C. M. 2004, Astronomy & Astrophysics, Vol. 415, pp. 1065

Jarrett, T. H., Cohen, M., Masci, F., et al. 2011, The Astrophysical Journal, 735, 112

Johnston, C., Aerts, C., Pedersen, M. G., & Bastian, N. 2019, Astronomy & Astrophysics, 632, A74

Kennicutt, R. C. & Evans, N. J. 2012, Annual Reviews of Astronomy & Astrophysics, Vol. 50, pp. 531

Kenyon, S. J., Hartmann, L. W., Strom, K. M., & Strom, S. E. 1990, The Astronomical Journal, 99, 869

Kenyon, S. J., Whitney, B. A., Gomez, M., & Hartmann, L. 1993, The Astrophysical Journal, Vol. 414, pp. 773

Kerr, R. M. P., Rizzuto, A. C., Kraus, A. L., & Offner, S. S. R. 2021, The Astrophysical Journal, 917, 23

Knacke, R. F., Strom, K. M., Strom, S. E., Young, E., & Kunkel, W. 1973, The Astrophysical Journal, Vol. 179, pp. 847

Knude, J. & Hog, E. 1998, Astronomy & Astrophysics, Vol. 338, pp. 897

Koenig, X. P. & Leisawitz, D. T. 2014, The Astrophysical Journal, Vol. 791, pp. 131

Koenig, X. P., Leisawitz, D. T., Benford, D. J., et al. 2012, The Astrophysical Journal, Vol. 744, pp. 130

Koyama, K., Hamaguchi, K., Ueno, S., Kobayashi, N., & Feigelson, E. D. 1996, Publications of the Astronomical Society of Japan, Vol. 48, pp. L87

Krumholz, M. R. & Federrath, C. 2019, Frontiers in Astronomy and Space Sciences, Vol. 6, pp. 7

Lacy, J. H., Sneden, C., Kim, H., & Jaffe, D. T. 2017, The Astrophysical Journal, Vol. 838, pp. 66

Lada, C. J. 1987, in Star Forming Regions, ed. M. Peimbert & J. Jugaku, Vol. 115, pp. 1

Lada, C. J. 2005, Progress of Theoretical Physics Supplement, Vol. 158, pp. 1

Lada, C. J. & Adams, F. C. 1992, The Astrophysical Journal, Vol. 393, pp. 278

Lada, C. J. & Lada, E. A. 2003, Annual Reviews of Astronomy & Astrophysics, Vol. 41, pp. 57

Lada, C. J., Muench, A. A., Luhman, K. L., et al. 2006, The Astronomical Journal, 131, 1574

Lada, C. J. & Wilking, B. A. 1984, The Astrophysical Journal, Vol. 287, pp. 610

Lada, E. A., Strom, K. M., & Myers, P. C. 1993, in Protostars and Planets III, ed. E. H. Levy & J. I. Lunine (University of Arizona Press), pp. 245

Larson, R. B. 2003, Reports on Progress in Physics, Vol. 66, pp. 1651

Lassell, W. & Marth, A. 1867, Monthly memories of the Royal Astronomical Society, 36, 45

Lee, C. W. & Myers, P. C. 1999, The Astrophysical Journal Supplement Series, Vol. 123, pp. 233

Leike, R. H., Glatzle, M., & Enßlin, T. A. 2020, Astronomy & Astrophysics, 639, A138

Levi, E. H. & Lunine, J. I., eds. 1993, Protostars and planets III (University of Arizona Press)

Lodieu, N., Burningham, B., Day-Jones, A., et al. 2012, Astronomy & Astrophysics, 548, A53

Luhman, K. L. 2004, The Astrophysical Journal, 617, 1216

Luyten, W. J. 1927, Harvard College Observatory Bulletin, Vol. 844, pp. 2

Mac Low, M.-M. & Klessen, R. S. 2004, Reviews of Modern Physics, Vol. 76, pp. 125

Mamajek, E. E. & Feigelson, E. D. 2001, in Astronomical Society of the Pacific Conference Series, Vol. 244, Young Stars Near Earth: Progress and Prospects, ed. R. Jayawardhana & T. Greene, 104–115

Mannings, V., Boss, A. P., & Russell, S. S., eds. 2000, Protostars and Planets IV (University of Arizona Press)

Marraco, H. G. & Rydgren, A. E. 1981, The Astronomical Journal, Vol. 86, pp. 62

Martín, E. L. 1997, Astronomy & Astrophysics, Vol. 321, pp. 492

Martín, E. L. 1998, The Astronomical Journal, Vol. 115, pp. 351

Masunaga, H. & Inutsuka, S.-i. 2000, The Astrophysical Journal, 531, 350

Mathis, J. S. 1990, Annual Reviews of Astronomy & Astrophysics, Vol. 28, pp. 37

McKee, C. F. & Ostriker, E. C. 2007, Annual Reviews of Astronomy & Astrophysics, Vol. 45, pp. 565

Megeath, S. T., Gutermuth, R., Muzerolle, J., et al. 2012, The Astronomical Journal, Vol. 144, pp. 192

Meingast, S., Alves, J., & Lombardi, M. 2018, Astronomy & Astrophysics, Vol. 614, pp. A65

Meingast, S., Alves, J., Mardones, D., et al. 2016a, VizieR Online Data Catalog, pp. J/A+A/587/A153

Meingast, S., Alves, J., Mardones, D., et al. 2016b, Astronomy & Astrophysics, Vol. 587, pp. A153

Meisner, A. M. & Finkbeiner, D. P. 2014, The Astrophysical Journal, 781, 5

Mestel, L. & Spitzer, L., J. 1956, Monthly Notice of the Royal Astronomical Society, Vol. 116, pp. 503

Miret-Roig, N., Galli, P. A. B., Brandner, W., et al. 2020, Astronomy & Astrophysics, 642, A179

Neuhäuser, R. & Forbrich, J. 2008, The Corona Australis Star Forming Region, ed. B. Reipurth, Vol. 5 (Astronomical Society of the Pacific), pp. 735

Palla, F. 1996, The Quest for Evolutionary Diagrams of Young Stellar Objects (Review), ed. S. Beckwith, J. Staude, A. Quetz, & A. Natta, Vol. 465 (Springer, Berlin, Heidelberg), pp. 143

Parker, Q. A., Acker, A., Frew, D. J., et al. 2006, Monthly Notice of the Royal Astronomical Society, Vol. 373, pp. 79

Pearson, W. J., Wang, L., Alpaslan, M., et al. 2019, Astronomy & Astrophysics, Vol. 631, pp. A51

Pendleton, Y. J. 1997, Origins of Life and Evolution of the Biosphere, Vol. 27, pp. 53

Perryman, M. A. C. 1981, Bulletin d'Information du Centre de Donnees Stellaires, 21, 40

Perryman, M. A. C., Lindegren, L., Kovalevsky, J., et al. 1997, Astronomy & Astrophysics, 323, L49

Peterson, D. E., Caratti o Garatti, A., Bourke, T. L., et al. 2011, The Astrophysical Journal Supplement Series, Vol. 194, pp. 43

Pillitteri, I., Wolk, S. J., Megeath, S. T., et al. 2013, The Astrophysical Journal, Vol. 768, pp. 99

Planck Collaboration, Abergel, A., Ade, P. A. R., et al. 2014, Astronomy & Astrophysics, Vol. 571, pp. A11

Poglitsch, A., Waelkens, C., Geis, N., et al. 2010, Astronomy & Astrophysics, 518, L2

Rebull, L. M., Padgett, D. L., McCabe, C. E., et al. 2010, The Astrophysical Journal Supplement Series, Vol. 186, pp. 259

Reipurth, B. 2008, Handbook of Star Forming Regions, Volume II: The Southern Sky, Vol. 5 (Astronomical Society of the Pacific)

Reipurth, B., Jewitt, D., & Keil, K., eds. 2007, Protostars and Planets V (University of Arizona Press)

Rey-Raposo, R., Dobbs, C., Agertz, O., & Alig, C. 2017, Monthly Notice of the Royal Astronomical Society, Vol. 464, pp. 3536

Reynolds, J. H. 1916, Monthly Notice of the Royal Astronomical Society, Vol. 76, pp. 645

Ribas, Á., Bouy, H., & Merín, B. 2015, Astronomy & Astrophysics, 576, A52

Rieke, G. H., Young, E. T., Engelbracht, C. W., et al. 2004, The Astrophysical Journal Supplement Series, 154, 25

Robitaille, T. P. 2017, Astronomy & Astrophysics, 600, A11

Robitaille, T. P., Whitney, B. A., Indebetouw, R., & Wood, K. 2007, The Astrophysical Journal Supplement Series, Vol. 169, pp. 328

Robitaille, T. P., Whitney, B. A., Indebetouw, R., Wood, K., & Denzmore, P. 2006, The Astrophysical Journal Supplement Series, Vol. 167, pp. 256

Romero, G. A., Schreiber, M. R., Cieza, L. A., et al. 2012, The Astrophysical Journal, 749, 79

Scalo, J. & Elmegreen, B. G. 2004, Annual Reviews of Astronomy & Astrophysics, Vol. 42, pp. 275

Schmidt, J. F. J. 1865, Astronomische Nachrichten, 65, 261

Schneider, S. & Elmegreen, B. G. 1979, The Astrophysical Journal Supplement Series, Vol. 41, pp. 87

Shu, F. H., Adams, F. C., & Lizano, S. 1987, Annual Reviews of Astronomy & Astrophysics, Vol. 25, pp. 23

Skrutskie, M. F., Cutri, R. M., Stiening, R., et al. 2006, The Astronomical Journal, Vol. 131, pp. 1163

Spitzer, L., J., Cochran, W. D., & Hirshfeld, A. 1974, The Astrophysical Journal Supplement Series, Vol. 28, pp. 373

Stahler, S. W. 2015, in Encyclopedia of Astrobiology, ed. M. Gargaud, W. M. Irvine, R. Amils, I. Cleaves, Henderson James (Jim), D. L. Pinti, J. C. Quintanilla, D. Rouan, T. Spohn, S. Tirard, & M. Viso (Springer), pp. 625–626

Stahler, S. W. & Palla, F. 2008, The Formation of Stars, 1st edn. (Hoboken: Wiley-VCH)

Steele, A., Hughes, A. M., Carpenter, J., et al. 2016, The Astrophysical Journal, Vol. 816, pp. 27

Stutzki, J., Bensch, F., Heithausen, A., Ossenkopf, V., & Zielinsky, M. 1998, Astronomy & Astrophysics, Vol. 336, pp. 697

Tanti, K. K., Roy, J., & Duorah, K. 2012, Advances in Astronomy and Space Physics, 2, 139

Taylor, K. N. R. & Storey, J. W. V. 1984, Monthly Notice of the Royal Astronomical Society, Vol. 209, pp. 5P

Teixeira, G. D. C., Kumar, M. S. N., Smith, L., et al. 2018, Astronomy & Astrophysics, 619, A41

Teixeira, P. S., Lada, C. J., Marengo, M., & Lada, E. A. 2012, Astronomy & Astrophysics, Vol. 540, pp. A83

Terebey, S., Chandler, C. J., & André, P. 1993, The Astrophysical Journal, Vol. 414, pp. 759

Tobin, J. J., Hartmann, L., Furesz, G., Mateo, M., & Megeath, S. T. 2009, The Astrophysical Journal, 697, 1103 van der Marel, N., Verhaar, B. W., van Terwisga, S., et al. 2016, Astronomy & Astrophysics, 592, A126

van Dishoeck, E. F. 2004, Annual Reviews of Astronomy & Astrophysics, Vol. 42, pp. 119

van Gent, H. 1933, Bulletin of the Astronomical Institutes of the Netherlands, Vol. 7, pp. 21

Walter, F. M., Brown, A., Mathieu, R. D., Myers, P. C., & Vrba, F. J. 1988, The Astronomical Journal, Vol. 96, pp. 297

Werner, M. W., Roellig, T. L., Low, F. J., et al. 2004, The Astrophysical Journal Supplement Series, Vol. 154, pp. 1

White, R. J., Greene, T. P., Doppmann, G. W., Covey, K. R., & Hillenbrand, L. A. 2007, in Protostars and Planets V, ed. B. Reipurth, D. Jewitt, & K. Keil (University of Arizona Press), pp. 117

Whitney, B. A., Indebetouw, R., Bjorkman, J. E., & Wood, K. 2004, The Astrophysical Journal, 617, 1177

Whitney, B. A., Wood, K., Bjorkman, J. E., & Cohen, M. 2003a, The Astrophysical Journal, Vol. 598, pp. 1079

Whitney, B. A., Wood, K., Bjorkman, J. E., & Wolff, M. J. 2003b, The Astrophysical Journal, Vol. 591, pp. 1049

Williams, D. A. 2005, in Journal of Physics Conference Series, Vol. 6, Journal of Physics Conference Series, pp. 1–17

Williams, J. P., Blitz, L., & McKee, C. F. 2000, in Protostars and Planets IV, ed. V. Mannings, A. P. Boss, & S. S. Russell (University of Arizona Press), pp. 97

Wilson, R. W., Jefferts, K. B., & Penzias, A. A. 1970, The Astrophysical Journal Letters, Vol. 161, pp. L43

Wright, E. L., Eisenhardt, P. R. M., Mainzer, A. K., et al. 2010, The Astronomical Journal, Vol. 140, pp. 1868

Wyatt, M. C. 2008, Annual Reviews of Astronomy & Astrophysics, Vol. 46, pp. 339

Zucker, C., Goodman, A. A., Alves, J., et al. 2022, Nature, Vol. 601, pp. 334

Appendix A

Catalogs

Presented here are the long versions of the Corona Australis YSO catalogs compiled in this thesis. Section A.1 contains the YSO source catalog containing unique source identifiers from this study, Peterson et al. (2011), Dunham et al. (2015), and Kerr et al. (2021). Moreover, the table lists the identifiers of archival survey data from *Gaia* EDR3, *Gaia* DR2, *2MASS*, *WISE*, *VISIONS*, and *Spiter* SEIP. Section A.2 contains a table with additional information listing spectral indicies, YSO Classes, and cluster memberships.

A.1 YSO catalog IDs

In the following the I present the YSO catalog, as compiled in this thesis, for the Corona Australis star forming region. Listed in this table are the source identifiers for *Gaia* EDR3, *Gaia* DR2, *2MASS*, *WISE*, *VISIONS*, *Spitzer* (SEIP - Spitzer enhanced imaging products), as well as the unique source identifiers from the literature catalogs by Peterson et al. (2011), Dunham et al. (2015), and Kerr et al. (2021). Se also the example table in Section 3.1 in the main part of this thesis.

Table A.1: Young stellar objects associated with the Corona Australis star-forming region. A supplemental description of the columns is given in Chapter 3, alongside with the description of the references column which provides literature references for the sources in this table.

ID	ra	dec	coord origin	Gaia EDR3 source id	Gaia DR2 source id	2MASS	WISE	early VISIONS ID	SEIP	ID pet	ID dun	ID Kerr	references	type	new
1	278.839	-37.572	Gaia	6733045308825699328	6733045308825699328	18352140-3734184	J183521.41-373418.6						c) e)	YSO	False
2	285.007	-36.618	Gaia	6731268601100885888	6731268601100885888	19000157-3637054	J190001.57-363705.8	285.006571-36.618300	SSTSL2 J190001.57-363706.1	52		16944	a) c) d) e) f)	YSO	False
3	285.419	-36.742	Gaia	6731220085150343552		19014055-3644320	J190140.56-364432.3	285.419020-36.742340		72			a) e)	YSO	False
4	285.817	-37.236	Gaia	6719167857158732416		19031609-3714080	J190316.10-371408.2	285.817044-37.235702	SSTSL2 J190316.11-371408.2	45			a) e)	YSO	False
5	280.054	-36.816	Gaia	6733456560533083008	6733456560533083008	18401286-3648553	J184012.86-364855.7					15668	c) d) e) f)	YSO	False
6	277.787	-35.463	Gaia	6734257829648099456	6734257829648099456	18310898-3527474	J183108.98-352747.6						f)	YSO	False
7	278.862	-36.442	Gaia	6733352519233844352	6733352519233844352	18352693-3626312	J183526.95-362631.4						c) e) f)	YSO	False
8	280.699	-36.068	Gaia	6733599016010166912	6733599016010166912	18424781-3604038	J184247.81-360404.1						c) e) f)	YSO	False
9	283.223	-36.744	Gaia	6731041414516060800	6731041414516060800	18525362-3644382	J185253.62-364438.4	283.223441-36.744075					e) f)	YSO	False
10	278.802	-32.598	Gaia	6736644010405213312	6736644010405213312	18351241-3235539	J183512.42-323554.2						f)	YSO	False
11	284.384	-33.809	Gaia	6732777027985714176	6732777023674059136	18573216-3348333	J185732.17-334833.5						e)	YSO	False
12	269.02	-39.383	Gaia	4036401674850523008	4036401674850523008	17560476-3922583	J175604.75-392258.6					12987	d) f)	YSO	False
13	270.089	-37.741	Gaia	4037022383526596096	4037022383526596096	18002133-3744285	J180021.33-374428.8						f)	YSO	False
14	282.519	-37.844	Gaia	6729449420453843584	6729449420453843584	18500458-3750361	J185004.58-375036.5	282.519083-37.843523				14732	c) d) e) f)	YSO	False
15	284.508	-36.896	Gaia	6730871505608505600	6730871505608505600	18580182-3653451	J185801.82-365345.5	284.507584-36.896038	SSTSL2 J185801.83-365346.1	61			a) c) e)	YSO	False
16	267.287	-39.572	Gaia	5958152252771926784	5958152252771926784	17490896-3934176	J174908.94-393417.9					396	d) f)	YSO	False
17	282.19	-35.656	Gaia	6732093922015431168	6732093922015431168	18484554-3539194	J184845.54-353919.5						c) e) f)	YSO	False
18	282.443	-34.233	Gaia DR2		6735323118961200000	18494631-3413566		282.442956-34.232553					c)	YSO	False
19	285.139	-36.734	Gaia	6731263202321082112	6731263202321082112	19003326-3644027	J190033.26-364403.0	285.138626-36.734230				16504	c) d) e) f)	YSO	False
20	280.18	-33.847	Gaia	6736294400055660800	6736294400055660800	18404325-3350472	J184043.18-335048.3					19430	c) d) e) f)	YSO	False
21	284.712	-36.666	Gaia	6730906891834942592	6730906891834942592	18585087-3639555	J185850.87-363955.8	284.711990-36.665569				21331	c) d) e) f)	YSO	False
22	276.083	-36.241	Gaia	6728301775168256128	6728301775168256128	18241986-3614279	J182419.88-361427.4						c) e) f)	YSO	False
23	282.028	-37.552	Gaia	6730221900396669952	6730221900396669952	18480666-3733074	J184806.66-373307.8	282.027786-37.552220				18502	c) d) f)	YSO	False
24	286.042	-36.768	Gaia	6719216128293613312	6719216128293613312	19041001-3646043	J190410.02-364604.6	286.041759-36.767997				5587	c) d) e) f)	YSO	False
25	280.445	-36.493	Gaia DR2		6733490645394178176	18414669-3629339							c)	YSO	False
26	285.777	-37.278	Gaia	6719167341762656640	6719167341762656640	19030636-3716409	J190306.37-371641.1	285.776567-37.278160	SSTSL2 J190306.37-371641.0			5234	c) d) e) f)	YSO	False
27	284.375	-36.577	Gaia	6731092507445791488	6731092507445791488	18572999-3634366	J185730.00-363437.0	284.374993-36.576993				15243	c) d) e) f)	YSO	False
28	284.735	-36.675	Gaia	6730903872482036992	6730903872482036992	18585650-3640297	J185856.51-364029.9	284.735471-36.675039		63		20679	a) c) d) e) f)	YSO	False
29	285.357	-37.082	Gaia	6730821645323509248	6730821645323509248	19012562-3704535	J190125.63-370453.8	285.356829-37.081673	SSTSL2 J190125.64-370453.5	67		20098	a) c) d) e) f)	YSO	False
30	281.977	-38.572	Gaia	6729328753356336896	6729328753356336896	18475452-3834178	J184754.52-383418.0	281.977213-38.571738				27774	c) d) e) f)	YSO	False
31	271.6	-35.763	Gaia	4038832591978376832	4038832591978376832	18062390-3545467							f)	YSO	False
32	285.413	-36.892	Gaia	6731200598883145600	6731200598883145600	19013912-3653292		285.413172-36.891651		54			a) e) f)	YSO	False
33	283.072	-37.003	Gaia	6731011315385156224	6731011315385156224	18521730-3700119	J185217.30-370012.2	283.072091-37.003459	SSTSL2 J185217.29-370012.1			13929	c) d) e) f)	YSO	False
34	280.104	-36.989	Gaia	6730449842905592448	6730449842905592448	18402487-3659181	J184024.87-365918.4					15415	c) d) e) f)	YSO	False
35	286.072	-36.984	Gaia	6719200395831344128		19041725-3659030	J190417.25-365903.3	286.071912-36.984298	SSTSL2 J190417.23-365903.0				e)	YSO	False

Continued on next page

TableA.1 – continued from previous page

ID	ra	dec	coord origin	Gaia EDR3 source id	Gaia DR2 source id	2MASS	WISE	early VISIONS ID	SEIP	ID pet	ID dun	ID Kerr	references	type	new
36	285.708	-36.773	Gaia	6731205138664331392	6731205138664331392	19024980-3646236	J190249.81-364623.9	285.707549-36.773356	SSTSL2 J190249.81-364623.6	76			a) e) f)	YSO	False
37	279.716	-32.105	Gaia DR2		6736763921557552000	18385190-3206170							c)	YSO	False
38	282.055	-37.214	Gaia	6730264815713680512	6730264815710861824	18481314-3712485	J184813.13-371248.9	282.054763-37.213603					e) f)	YSO	False
39	280.86	-35.617	Gaia	6733647841199256320	6733647841199256320	18432648-3537008	J184326.48-353701.0					29410	c) d) e) f)	YSO	False
40	285.508	-37.129	Gaia	6719183147242324480	6719183147242324480	19020197-3707435	J190201.98-370743.7	285.508263-37.128895	SSTSL2 J190201.98-370743.4	74			a) c) e) f)	YSO	False
41	280.26	-33.843	Gaia	6735544189525498368	6735544189525498368	18410243-3350354	J184102.44-335035.8					15532	c) d) e) f)	YSO	False
42	280.751	-34.269	Gaia	6735469315334725632	6735469315334725632	18430029-3416068	J184300.29-341607.1						c) e) f)	YSO	False
43	281.506	-35.705	Gaia	6732127663290781056	6732127663290781056	18460149-3542158	J184601.50-354216.0					19645	c) d) e) f)	YSO	False
44	280.039	-36.51	Gaia	6733498097146957184	6733498097146957184	18400935-3630346	J184009.39-363035.0					16809	c) d) e) f)	YSO	False
45	282.536	-37.259	Gaia	6730252167025513984	6730252167025513984	18500856-3715337	J185008.55-371534.0	282.535699-37.259497				24634	c) d) e) f)	YSO	False
46	278.491	-36.865	Gaia	6733311253181834368		18335788-3651542	J183357.88-365154.4						e)	YSO	False
47	285.54	-36.776	Gaia	6731207509487315072	6731207509487315072	19020968-3646345	J190209.67-364634.7	285.540346-36.776360	SSTSL2 J190209.67-364634.5				c) e) f)	YSO	False
48	284.386	-38.091	Gaia	6730670226260687232	6730670226260687232	18573253-3805286	J185732.53-380528.9	284.385590-38.091418				18618	c) d) e) f)	YSO	False
49	285.707	-36.773	Gaia	6731205138658643584	6731205138658643584	19024980-3646236	J190249.81-364623.9						f)	YSO	False
50	280.956	-35.105	Gaia	6735207738950579456	6735207738950579456	18434948-3506165	J184349.48-350617.0						c) e) f)	YSO	False
51	282.515	-36.397	Gaia	6731838491728165248	6731838491728165248	18500368-3623485	J185003.69-362348.8	282.515357-36.396952					f)	YSO	False
52	282.941	-36.081	Gaia	6731872336071183360	6731872336071183360	18514581-3604499	J185145.82-360450.1	282.940945-36.080636					f)	YSO	False
53	279.901	-36.747	Gaia	6733459579882241408		18393631-3644499	J183936.32-364450.0						e)	YSO	False
54	281.365	-36.226	Gaia	6730597585472277248	6730597585472277248	18452761-3613332	J184527.61-361333.6						c) e) f)	YSO	False
55	285.007	-36.466	Gaia	6731283135270321792	6731283135270321792	19000169-3627576	J190001.69-362757.8	285.007079-36.466122				16945	c) d) e) f)	YSO	False
56	281.399	-37.648	Gaia	6730182279316291072	6730182279316291072	18453576-3738508						26593	c) d) e) f)	YSO	False
57	285.501	-37.04	Gaia	6731194379766533632	6731194379766533632	19020012-3702220	J190200.12-370222.4	285.500539-37.039598		73		15910	a) c) d) e) f)	YSO	False
58	285.594	-36.928	Gaia	6731202488668747904	6731202488668747904	19022244-3655385	J190222.45-365538.5	285.593552-36.927504					c) e) f)	YSO	False
59	282.076	-37.425	Gaia	6730224408657648000	6730224408657648000	18481819-3725304	J184818.19-372531.0	282.075848-37.425251				18505	c) d) e) f)	YSO	False
60	285.186	-37.036	Gaia	6730834431450092160	6730834431450092160	19004455-3702108	J190044.55-370211.1	285.185671-37.036457				20093	c) d) e) f)	YSO	False
61	272.708	-38.359	Gaia	4037497132033831040	4037497132033831040	18105003-3821335	J181050.02-382133.7						f)	YSO	False
62	276.037	-37.301	Gaia	6728030230146525568	6728030230146525568	18240886-3718047	J182408.85-371804.9						c) e)	YSO	False
63	285.268	-37.062	Gaia	6730822302462393088	6730822302462393088	19010430-3703415	J190104.31-370341.9	285.267920-37.061679	SSTSL2 J190104.29-370341.7				e) f)	YSO	False
64	280.039	-36.708	Gaia	6733460614982251136	6733460614982251136	18400947-3642294	J184009.45-364229.5					15669	c) d) e) f)	YSO	False
65	285.132	-36.871	Gaia	6730840238245942400	6730840238245942400	19003158-3652136	J190031.58-365213.8	285.131617-36.870561	SSTSL2 J190031.57-365213.7			20092	c) d) e) f)	YSO	False
66	271.652	-37.32	Gaia	4037835231856994816	4037835231856994816	18063642-3719126	J180636.41-371912.9					2475	d) f)	YSO	False
67	281.131	-35.69	Gaia	6733632619834916864	6733632619834916864	18443146-3541229	J184431.47-354123.2		SSTSL2 J184431.47-354122.7				c) e) f)	YSO	False
68	266.694	-40.119	Gaia	5958041167736059136	5958041167736059136	17464654-4007077	J174646.53-400708.0					17513	d) f)	YSO	False
69	278.868	-35.454	Gaia	6733826786720969088	6733826786720969088	18352823-3527135	J183528.23-352714.0					18745	c) d) e) f)	YSO	False
70	279.935	-35.179	Gaia	6733895403117662592	6733895403117662592	18394434-3510438	J183944.34-351044.1					13662	c) d) e) f)	YSO	False
71	275.631	-33.458	Gaia	4044760647651736064	4044760647651736064	18223129-3327275							f)	YSO	False
72	283.842	-37.802	Gaia	6730717024223786112	6730717024223786112	18552205-3748048		283.841819-37.801547				19167	c) d) e) f)	YSO	False
73	275.624	-34.57	Gaia	4044364406781706112	4044364406781706112	18222970-3434131	J182229.70-343413.6						e) f)	YSO	False
74	279.533	-34.443	Gaia	6734749517499911040	6734749517499911040	18380786-3426361	J183807.85-342636.2					2251	c) d) e) f)	YSO	False

Continued on next page

TableA.1 – continued from previous page

ID	ra	dec	coord origin	Gaia EDR3 source id	Gaia DR2 source id	2MASS	WISE	early VISIONS ID	SEIP	ID pet	ID dun	ID Kerr	references	type	new
75	280.887	-36.442	Gaia	6730568006046885120	6730568006046885120	18433285-3626303	J184332.85-362630.7					17271	c) d) e) f)	YSO	False
76	279.116	-39.049	Gaia	6729805803970686592	6729805803970686592	18362779-3902561	J183627.78-390256.4					6344	d) e) f)	YSO	False
77	284.673	-36.862	Gaia	6730895797943280640	6730895797943280640	18584157-3651430	J185841.58-365143.2	284.673261-36.862068				20676	c) d) e) f)	YSO	False
78	280.421	-35.449	Gaia	6733708825419987712	6733708825419987712	18414092-3526559	J184140.90-352656.2					15595	c) d) e) f)	YSO	False
79	280.59	-37.15	Gaia	6730406858871544704	6730406858871544704	18422158-3708599	J184221.57-370900.1					24854	c) d) e) f)	YSO	False
80	285.73	-37.08	Gaia	6719181493677099520	6719181493677099520	19025518-3704459	J190255.18-370446.2	285.729957-37.079558	SSTSL2 J190255.18-370445.9				e) f)	YSO	False
81	275.177	-37.028	Gaia	6728162648254144128	6728162648254144128	18204248-3701412	J182042.48-370141.5					2617	c) d) e) f)	YSO	False
82	280.755	-36.876	Gaia	6730463548135072256	6730463548135072256	18430115-3652324	J184301.15-365232.6						c) e) f)	YSO	False
83	267.204	-44.093	Gaia	5954839222405630720	5954839222405630720	17484891-4405331	J174848.91-440533.3					9634	d) f)	YSO	False
84	284.171	-37.686	Gaia	6730739254974258944	6730739254974258944	18564094-3741094	J185640.94-374109.8	284.170587-37.686115				19165	d) e) f)	YSO	False
85	280.784	-36.978	Gaia	6730415448806354944	6730415448806354944	18430804-3658388	J184308.01-365838.6					24842	c) d) e) f)	YSO	False
86	278.764	-34.08	Gaia	6734809818842676096	6734809818842676096	18350324-3404464	J183503.25-340446.6						c) e) f)	YSO	False
87	282.843	-36.529	Gaia	6731808766248601088	6731808766248601088	18512223-3631432	J185122.23-363143.4	282.842648-36.528799				15295	c) d) e) f)	YSO	False
88	285.409	-36.438	Gaia	6731274785854399104	6731274785854399104	19013807-3626155	J190138.08-362615.6	285.408684-36.437773				16938	c) d) e) f)	YSO	False
89	281.847	-36.216	Gaia	6732043134026964224	6732043134026964224	18472320-3612564	J184723.26-361255.4					18751	c) d) e) f)	YSO	False
90	287.681	-36.986	Gaia	6719057081363106048		19104337-3659092	J191043.37-365909.6	287.680750-36.986057					e)	YSO	False
91	286.185	-36.845	Gaia	6719203178970162176	6719203178970162176	19044441-3650410	J190444.41-365041.2	286.185082-36.844833					c) e) f)	YSO	False
92	282.105	-23.089	Gaia	4078265786235642624		18482532-2305211	J184825.32-230521.4							R	False
93	280.806	-33.809	Gaia	6735533331847699968	6735533331847699968	18431342-3348327	J184313.42-334833.0					15531	c) d) e) f)	YSO	False
94	280.836	-35.838	Gaia	6733626503801586176	6733626503801586176	18432065-3550154	J184320.64-355015.7					12918	c) d) e) f)	YSO	False
95	273.889	-35.331	Gaia	4038485592980978176	4038485592980978176	18153347-3519524	J181533.47-351952.6					6740	d) f)	YSO	False
96	285.162	-36.971	Gaia	6730835664096904320		19003894-3658146	J190038.94-365814.8	285.162294-36.970835	SSTSL2 J190038.94-365815.1	7	J190038.9-365814		a) b)	YSO	False
97	268.193	-40.991	Gaia	5957086860368729984	5957086860368729984	17524625-4059283	J175246.25-405928.6						f)	YSO	False
98	278.315	-37.506	Gaia	6733008780119631360	6733008780119631360	18331569-3730197	J183315.70-373019.8						c) e)	YSO	False
99	277.094	-32.868	Gaia	4044934748406262912	4044934748406262912	18282252-3252047	J182822.52-325205.1						e) f)	YSO	False
100	279.749	-34.369	Gaia	6734004907607126912	6734004907607126912	18385977-3422094	J183859.82-342209.6					17156	c) d) e) f)	YSO	False
101	280.166	-33.853	Gaia	6736271134195442304	6736271134195442304	18403995-3351107						12861	c) d) e) f)	YSO	False
102	265.197	-43.691	Gaia	5955756386871312512	5955756386871312512	17404719-4341267							f)	YSO	False
103	281.078	-35.64	Gaia	6733635914059722752	6733635914059722752	18441878-3538244							f)	YSO	False
104	274.291	-33.292	Gaia	4045468080338936576	4045468080338936576	18170980-3317303						4059	d) f)	YSO	False
105	272.775	-37.253	Gaia	4037617116232319232	4037617116232319232	18110605-3715100	J181106.05-371510.2					17788	d) f)	YSO	False
106	266.212	-40.382	Gaia	5958055362697753344	5958055362697753344	17445088-4022551	J174450.86-402255.3						f)	YSO	False
107	285.189	-37.197	Gaia	6730819244445651584	6730819244445651584	19004530-3711480	J190045.31-371148.3	285.188835-37.196814	SSTSL2 J190045.29-371148.8	8	J190045.3-371148	20095	a) b) d) e) f)	YSO	False
108	286.033	-37.047	Gaia	6719175966057662208	6719175966057662208	19040795-3702476	J190407.95-370247.9	286.033150-37.046684	SSTSL2 J190407.93-370247.4	77			a) c) e) f)	YSO	False
109	284.024	-37.122	Gaia	6731052203472422144	6731052203472422144	18560573-3707191	J185605.74-370719.4	284.023929-37.122118				14569	c) d) e) f)	YSO	False
110	285.414	-37.036	Gaia	6731197167204782720		19013933-3702074	J190139.34-370207.7	285.413929-37.035528		71			a) e)	YSO	False
111	283.376	-36.371	Gaia	6731896521018591616	6731896521018591616	18533035-3622145	J185330.35-362214.8	283.376468-36.370832	SSTSL2 J185330.33-362214.4				c) e) f)	YSO	False
112	280.714	-36.125	Gaia	6733595648755786240	6733595648755786240	18425140-3607294	J184251.40-360729.8					19319	c) d) e) f)	YSO	False
113	285.659	-36.576	Gaia	6731245511357055360	6731245511357055360	19023813-3634321	J190238.14-363432.5	285.658926-36.575711				16505	c) d) e) f)	YSO	False

Continued on next page

TableA.1 – continued from previous page

ID	ra	dec	coord origin	Gaia EDR3 source id	Gaia DR2 source id	2MASS	WISE	early VISIONS ID	SEIP	ID pet	ID dun	ID Kerr	references	type	new
114	284.939	-36.93	Gaia	6730885146424037120	6730885146424037120	18594535-3655475	J185945.36-365547.8	284.939001-36.930017				20677	c) d) e) f)	YSO	False
115	283.281	-36.088	Gaia	6731916488333198720	6731916488333198720	18530736-3605163	J185307.36-360516.5	283.280694-36.087963	SSTSL2 J185307.36-360516.2			17012	c) d) e) f)	YSO	False
116	276.967	-34.028	Gaia	4044800745434225408	4044800745434225408	18275211-3401415	J182752.10-340142.0					17342	c) d) e) f)	YSO	False
117	284.543	-38.345	Gaia	6718654316514345344	6718654316514345344	18581041-3820398	J185810.41-382040.1	284.543408-38.344529					c) f)	YSO	False
118	287.167	-39.16	Gaia	6717610635161939968	6717610635161939968	19084013-3909350	J190840.13-390935.2						f)	YSO	False
119	282.267	-33.414	Gaia	6735794259693554304	6735794259693554304	18490419-3324507	J184904.18-332450.9					2432	c) d) e) f)	YSO	False
120	280.37	-37.822	Gaia	6729978186777308416	6729978186777308416	18412872-3749198	J184128.72-374920.2						c) e)	YSO	False
121	276.085	-37.254	Gaia	6728036277460482176	6728036277460482176	18242041-3715138	J182420.42-371514.0						c) e) f)	YSO	False
122	285.799	-37.151	Gaia	6719180123585335808		19031185-3709020	J190311.84-370902.3	285.799390-37.150704	SSTSL2 J190311.85-370902.0	35	J190311.8-370902		a) b) e)	YSO	False
123	264.149	-41.092	Gaia	5960594852214489856	5960594852214489856	17363575-4105322	J173635.74-410532.6					7011	d) f)	YSO	False
124	283.016	-38.792	Gaia	6729159016246149760	6729159016246149760	18520378-3847322	J185203.78-384732.5	283.015804-38.792428				14778	d) f)	YSO	False
125	281.82	-34.593	Gaia	6735294978334708480	6735294978334708480	18471676-3435348	J184716.78-343535.1						f)	YSO	False
126	279.551	-36.786	Gaia	6733467727447986048	6733467727447986048	18381212-3647108	J183812.12-364711.0					15663	c) d) e) f)	YSO	False
127	285.48	-37.395	Gaia	6718800753416250112	6718800753416250112	19015523-3723407	J190155.24-372341.0	285.480199-37.394803	SSTSL2 J190155.21-372340.8	55			a) e) f)	YSO	False
128	281.11	-35.657	Gaia	6733632894712864128	6733632894712864128	18442635-3539251	J184426.35-353925.4					12917	c) d) e) f)	YSO	False
129	282.817	-38.768	Gaia	6729170831698336896	6729170831698336896	18511610-3846032	J185116.12-384603.6	282.817145-38.767696				14770	c) d) e) f)	YSO	False
130	280.111	-34.931	Gaia	6733923268848039168	6733923268848039168	18402648-3455526							e) f)	YSO	False
131	275.628	-33.458	Gaia	4044760643280597504	4044760643280597504	18223063-3327291	J182230.65-332729.3					15530	d) e) f)	YSO	False
132	273.152	-36.129	Gaia	4037969170495945088	4037969170495945088	18123638-3607430	J181236.38-360743.2					10768	d) f)	YSO	False
133	279.658	-36.615	Gaia	6733517686509604992	6733517686509604992	18383789-3636519	J183837.87-363652.1					18074	c) d) e) f)	YSO	False
134	269.969	-38.142	Gaia	4036945490831946368	4036945490831946368	17595255-3808323	J175952.56-380832.4					17224	d) f)	YSO	False
135	279.969	-35.258	Gaia	6733883102331075456	6733883102331075456	18395248-3515277	J183952.48-351527.9					13665	c) d) e) f)	YSO	False
136	280.889	-36.442	Gaia	6730568006046883968	6730568006046883968	18433345-3626320	J184333.44-362632.3					17270	c) d) e) f)	YSO	False
137	283.891	-36.493	Gaia	6731132708340104576	6731132708340104576	18553379-3629349	J185533.80-362935.2	283.890844-36.493168				15240	c) d) e) f)	YSO	False
138	279.169	-37.655	Gaia	6733029400266587392	6733029400266587392	18364056-3739183	J183640.56-373918.5						c) e)	YSO	False
139	280.177	-33.848	Gaia	6736294395734484480	6736294395734484480	18404239-3350522	J184042.39-335052.5					19429	c) d) e) f)	YSO	False
140	282.51	-32.43	Gaia	6736139678127040512	6736139678127040512	18500238-3225464	J185002.38-322546.6						f)	YSO	False
141	266.189	-39.849	Gaia	5958109681059207680	5958109681059207680	17444531-3950544	J174445.31-395054.6						f)	YSO	False
142	284.881	-36.768	Gaia	6730890162945943552	6730890162945943552	18593149-3646042	J185931.49-364604.5	284.881258-36.767965				20681	c) d) e) f)	YSO	False
143	280.094	-34.871	Gaia	6733926704822176640	6733926704822176640	18402257-3452150	J184022.57-345215.2					14899	c) d) e) f)	YSO	False
144	277.241	-33.266	Gaia	4044910383038094464	4044910383038094464	18285778-3315584	J182857.77-331558.7						e) f)	YSO	False
145	284.317	-36.947	Gaia	6730873288013953536	6730873288013953536	18571605-3656502	J185716.05-365650.3	284.316912-36.947387				20678	c) d) e) f)	YSO	False
146	285.967	-36.507	Gaia	6731237917854733824	6731237917854733824	19035205-3630238	J190352.06-363024.0	285.966933-36.506738				16507	c) d) e) f)	YSO	False
147	282.687	-37.157	Gaia	6731004958834262400	6731004958834262400	18504489-3709240	J185044.89-370924.2	282.687080-37.156796				13932	c) d) e) f)	YSO	False
148	285.323	-36.446	Gaia	6731275129451843840	6731275129451843840	19011758-3626436	J190117.58-362643.9	285.323282-36.445575				16939	c) d) e) f)	YSO	False
149	281.319	-33.013	Gaia	6735689977887062144	6735689977887062144	18451665-3300446	J184516.65-330044.9						c) e) f)	YSO	False
150	280.452	-35.429	Gaia	6733697211827236480	6733697211827236480	18414855-3525437	J184148.56-352543.9		SSTSL2 J184148.54-352543.6				c) e) f)	YSO	False
151	274.368	-37.403	Gaia	6727797099338437632	6727797099338437632	18172837-3724092	J181728.35-372409.3						f)	YSO	False
152	285.242	-36.751	Gaia	6731216408658348032	6731216408658348032	19005804-3645048	J190058.05-364505.1	285.241874-36.751473	SSTSL2 J190058.04-364505.0	9	J190058.0-364505	16498	a) b) c) d) e) f)	YSO	False

Continued on next page

TableA.1 – continued from previous page

ID	ra	dec	coord origin	Gaia EDR3 source id	Gaia DR2 source id	2MASS	WISE	early VISIONS ID	SEIP	ID pet	ID dun	ID Kerr	references	type	new
153	285.385	-36.968	Gaia	6731198640378040192		19013232-3658030	J190132.33-365803.3	285.384732-36.967632		15	J190132.3-365803		a) b) e)	YSO	False
154	281.126	-37.645	Gaia	6730190598677375488	6730190598677375488	18443018-3738433	J184430.18-373843.5					26591	c) d) e) f)	YSO	False
155	284.828	-35.862	Gaia	6731503999671574656	6731503999671574656	18591874-3551423	J185918.74-355142.5	284.828107-35.861863					f)	YSO	False
156	285.47	-35.895	Gaia	6731326600340226176	6731326600340226176	19015271-3553415	J190152.71-355341.7	285.469636-35.894981				17547	c) d) e) f)	YSO	False
157	284.166	-37.123	Gaia	6730864599300176512		18563974-3707205	J185639.74-370720.8	284.165608-37.122508	SSTSL2 J185639.78-370721.2	1	J185639.7-370720		a) b) e)	YSO	False
158	285.318	-36.941	Gaia	6731210326984584192	6731210326984584192	19011629-3656282	J190116.29-365628.6	285.317883-36.941306	SSTSL2 J190116.29-365628.3	12		16499	a) c) d) e) f)	YSO	False
159	280.167	-33.449	Gaia	6736321849190089216	6736321849190089216	18404006-3326558	J184040.06-332656.1						e) f)	YSO	False
160	282.993	-37.149	Gaia	6731007948130724224	6731007948130724224	18515837-3708556	J185158.38-370855.9	282.993346-37.148948				13930	d) f)	YSO	False
161	284.183	-35.759	Gaia	6731563613818179200	6731563613818179200	18564400-3545321	J185644.04-354532.3	284.183393-35.759086					c) e)	YSO	False
162	284.393	-37.543	Gaia	6730746985915310336	6730746985915310336	18573418-3732332	J185734.14-373233.1	284.392569-37.542685	SSTSL2 J185734.18-373233.9	59		19614	a) c) d) e) f)	YSO	False
163	285.424	-36.998	Gaia	6731197648241121664	6731197648241121664	19014164-3659528	J190141.64-365953.2	285.423544-36.998140		41	J190141.6-365952	15918	a) b) c) d) e) f)	YSO	False
164	280.034	-33.565	Gaia	6736313710229031424	6736313710229031424	18400806-3333537	J184008.06-333353.9					20143	c) d) e) f)	YSO	False
165	285.412	-36.891	Gaia	6731200603178623616	6731200603178623616	19013892-3653264	J190138.97-365327.2	285.412256-36.890853					c) e) f)	YSO	False
166	285.681	-37.04	Gaia	6719184792212420608		19024346-3702248	J190243.46-370225.2	285.681126-37.040385	SSTSL2 J190243.47-370224.9				e)	YSO	False
167	286.486	-36.196	Gaia	6719333608539318144	6719333608539318144	19055673-3611464	J190556.74-361146.6	286.486476-36.196369					c) e) f)	YSO	False
168	279.097	-34.416	Gaia	6734742473752797184	6734742473752797184	18362324-3424555	J183623.25-342455.7					2248	c) d) e) f)	YSO	False
169	285.46	-36.673	Gaia	6731220703626866944	6731220703626866944	19015039-3640226	J190150.38-364023.0	285.459985-36.673088				16506	c) d) e) f)	YSO	False
170	285.329	-36.975	Gaia	6731198399854452736	6731198399854452736	19011893-3658282	J190118.94-365828.5	285.328942-36.974631	SSTSL2 J190118.94-365828.3	13	J190118.9-365828		a) b) c) e) f)	YSO	False
171	284.176	-37.339	Gaia	6730764715540783872	6730764715540783872	18564227-3720185	J185642.25-372018.7	284.176179-37.338602	SSTSL2 J185642.26-372018.5			19624	d) e) f)	YSO	False
172	285.613	-36.97	Gaia	6731195582357354752		19022708-3658132	J190227.09-365813.5	285.612888-36.970476	SSTSL2 J190227.09-365813.7	30			a) e)	YSO	False
173	286.383	-37.385	Gaia	6719129924007616640	6719129924007616640	19053189-3723054	J190531.89-372305.6	286.382915-37.384951				5231	c) d) e) f)	YSO	False
174	282.348	-36.334	Gaia	6731852957178180352	6731852957178180352	18492354-3620007	J184923.54-362000.9	282.348121-36.333651				16060	c) d) e) f)	YSO	False
175	283.585	-38.619	Gaia	6729141458420442112	6729141458420442112	18542038-3837080	J185420.38-383708.3	283.584962-38.619022				14777	c) d) e) f)	YSO	False
176	285.788	-36.956	Spitzer (c2d or gb)			19030916-3657220		285.788161-36.956173	SSTSL2 J190309.15-365722.0	34	J190309.1-365722		a) b)	YSO	False
177	281.545	-34.944	Gaia	6735189150342584448	6735189150342584448	18461069-3456394	J184610.71-345639.6						c) e) f)	YSO	False
178	283.307	-36.516	Gaia	6731051069602876800	6731051069602876800	18531366-3630559	J185313.66-363056.2	283.306940-36.515682				14570	c) d) e) f)	YSO	False
179	285.856	-36.918	Gaia	6719193145926882432	6719193145926882432	19032547-3655051	J190325.48-365505.4	285.856192-36.918230	SSTSL2 J190325.48-365505.3	57			a) c) e) f)	YSO	False
180	284.325	-36.71	Gaia	6731065019657201664	6731065015350814464	18571798-3642360	J185717.99-364236.3	284.324969-36.710144					e)	YSO	False
181	282.21	-37.2	Gaia	6730262822834357248	6730262822834357248	18485045-3711580	J184850.46-371158.3	282.210270-37.199594				24640	c) d) e) f)	YSO	False
182	285.57	-36.764	Gaia	6731207475127574656	6731207475127574656	19021667-3645493	J190216.68-364549.6	285.569523-36.763843	SSTSL2 J190216.60-364549.2	56		16497	a) c) d) e) f)	YSO	False
183	280.628	-35.092	Gaia	6733721233595545216	6733721233595545216	18423080-3505290	J184230.80-350529.3						c) e) f)	YSO	False
184	283.817	-37.042	Gaia	6730975031500584192	6730975031500584192	18551598-3702304	J185515.99-370230.7	283.816644-37.041915				13510	c) d) e) f)	YSO	False
185	281.97	-37.272	Gaia	6730241244929688960	6730241244929688960	18475288-3716182	J184752.89-371618.5	281.970393-37.271866				18503	c) d) e) f)	YSO	False
186	281.671	-37.354	Gaia	6730281274014730368	6730281274014730368	18464111-3721156	J184641.12-372116.4					24631	c) d) e) f)	YSO	False
187	284.127	-37.276	Gaia	6730768873062730624	6730768873062730624	18563044-3716330	J185630.45-371633.2B	284.127191-37.275809					e) f)	YSO	False
188	285.164	-36.804	Gaia	6731215790182995968	6731215790182995968	19003930-3648121	J190039.30-364812.5	285.163775-36.803522		65		16508	a) c) d) e) f)	YSO	False
189	285.495	-36.964	Gaia	6731196273845607168		19015878-3657498	J190158.76-365750.2						e)	YSO	False
190	285.371	-37.03	Gaia	6731197304643738368	6731197304643738368	19012901-3701484	J190129.03-370148.7	285.370981-37.030258	SSTSL2 J190128.99-370148.4	14	J190129.0-370148	15916	a) b) c) d) e) f)	YSO	False
191	285.528	-36.362	Gaia	6731251799189397248	6731251799189397248	19020680-3621418	J190206.79-362142.1	285.528325-36.361731					c) e) f)	YSO	False

Continued on next page

TableA.1 – continued from previous page

ID	ra	dec	coord origin	Gaia EDR3 source id	Gaia DR2 source id	2MASS	WISE	early VISIONS ID	SEIP	ID pet	ID dun	ID Kerr	references	type	new
192	285.29	-36.798	Gaia	6731212354209151360	6731212354209151360	19010971-3647528	J190109.71-364753.1	285.290460-36.798134	SSTSL2 J190109.71-364753.0	66		16501	a) c) d) e) f)	YSO	False
193	279.916	-36.881	Gaia	6733451784529154944	6733451784529154944	18393982-3652515	J183939.81-365251.8						c) e)	YSO	False
194	285.466	-37.18	Gaia	6718807664024747520	6718807664024747520	19015180-3710478	J190151.83-371047.5S	285.465924-37.180102				3669	c) d) e) f)	YSO	False
195	281.395	-37.839	Gaia	6730127303744818816	6730127303744818816	18453485-3750195	J184534.85-375019.7						e) f)	YSO	False
196	285.264	-37.061	Gaia	6730822302462396160	6730822302462396160	19010325-3703392	J190103.24-370339.4	285.263555-37.061030	SSTSL2 J190103.24-370339.3	11	J190103.2-370339		a) b) c) e) f)	YSO	False
197	282.358	-37.278	Gaia	6730249800505083392	6730249800505083392	18492595-3716390	J184925.95-371639.3	282.358197-37.277634					f)	YSO	False
198	285.728	-36.772	Gaia	6731205306163438080		19025464-3646191	J190254.65-364619.4	285.727737-36.772101	SSTSL2 J190254.65-364619.1				e)	R	False
199	280.553	-35.611	Gaia	6733691134471875456	6733691134471875456	18421282-3536378	J184212.82-353638.1					14164	c) d) e) f)	YSO	False
200	284.337	-36.717	Gaia	6731064950935554304	6731064950935554304	18572084-3643005	J185720.84-364300.8	284.336867-36.716956					c) e)	YSO	False
201	266.288	-36.46	Gaia	4040900777756487552	4040900777756487552	17450918-3627369							f)	YSO	False
202	285.592	-36.928	Gaia	6731196617449019392	6731196617449019392	19022213-3655409	J190222.13-365541.0	285.592238-36.928181	SSTSL2 J190222.18-365540.6	75		15911	a) c) d) e) f)	YSO	False
203	285.456	-37.008	Gaia	6731194723363917952	6731194723363917952	19014936-3700285	J190149.36-370029.4	285.455724-37.008079	SSTSL2 J190149.36-370028.6			15909	c) d) e) f)	YSO	False
204	275.163	-34.9	Gaia	4044324656915501184	4044324656915501184	18203913-3454006	J182039.14-345400.9						f)	YSO	False
205	285.463	-36.903	2MASS			19015112-3654122	J190151.13-365412.7	285.463069-36.903567		21	J190151.1-365412		a) b) e)	YSO	False
206	283.033	-36.692	Gaia	6731791655097086848	6731791655097086848	18520787-3641319	J185207.88-364132.1	283.032831-36.692294					c) e) f)	YSO	False
207	267.798	-39.613	Gaia	5957978190716237952	5957978190716237952	17511159-3936450	J175111.59-393645.3					18388	d) f)	YSO	False
208	284.203	-36.444	Gaia	6731109618595716352	6731109618595716352	18564863-3626397	J185648.63-362640.0	284.202647-36.444495				15230	c) d) e) f)	YSO	False
209	282.339	-36.239	Gaia	6731855912115752320	6731855912115752320	18492137-3614183	J184921.37-361418.5	282.339072-36.238549					c) e)	YSO	False
210	283.677	-38.196	Gaia	6730701321822246784	6730701321822246784	18544255-3811455	J185442.56-381145.8	283.677355-38.196121				19152	c) d) e) f)	YSO	False
211	285.097	-37.207	Spitzer (c2d or gb)			19002346-3712242		285.097759-37.206748		39	J190023.4-371224		a) b)	G	False
212	281.932	-38.58	Gaia	6729329165673220480	6729329165673220480	18474369-3834489	J184743.70-383449.2	281.932103-38.580399				27776	c) d) e) f)	YSO	False
213	283.059	-35.295	Gaia	6732025374345005184	6732025374345005184	18521426-3517414	J185214.27-351741.7	283.059485-35.294972				18749	c) d) e) f)	YSO	False
214	285.395	-37.016	Gaia	6731197235924261504	6731197235924261504	19013485-3700565	J190134.86-370056.8	285.395282-37.015860	SSTSL2 J190134.87-370056.6	70		15917	a) c) d) e) f)	YSO	False
215	280.044	-35.173	Gaia	6733883888287392768	6733883888287392768	18401049-3510222	J184010.49-351022.6					13663	c) d) e) f)	YSO	False
216	285.543	-36.896	Spitzer (c2d or gb)			19021046-3653446		285.543570-36.895739		27	J190210.4-365344		a) b)	YSO	False
217	282.04	-37.238	Gaia	6730264678271906816	6730264678271906816	18480955-3714170	J184809.56-371417.3	282.039836-37.238189				24637	c) d) e) f)	YSO	False
218	285.357	-36.989	Gaia	6731198228055759360		19012576-3659191	J190125.77-365919.4	285.357400-36.988769	SSTSL2 J190125.76-365919.1	40			a) e)	YSO	False
219	285.778	-37.088	Gaia	6719187128674626304	6719187128674626304	19030682-3705165	J190306.82-370516.9	285.778449-37.088055	SSTSL2 J190306.81-370516.6				c) e) f)	YSO	False
220	282.818	-38.769	Gaia	6729170835996189824	6729170835996189824	18511628-3846066	J185116.31-384607.1	282.817903-38.768618				14772	d) f)	YSO	False
221	285.121	-36.934	Gaia	6730838756473386240	6730838756473386240	19002906-3656036	J190029.06-365603.8	285.121129-36.934463	SSTSL2 J190029.05-365603.6	6			a) e) f)	YSO	False
222	283.353	-37.275	Gaia	6730944623132382336	6730944623132382336	18532467-3716278	J185324.68-371627.9	283.352865-37.274507					c) e) f)	YSO	False
223	285.638	-36.973	Gaia	6731201389153163520		19023308-3658212	J190233.09-365821.6	285.637874-36.972721	SSTSL2 J190233.07-365821.6	31			a) e)	YSO	False
224	282.429	-35.772	Gaia	6732082411514529024	6732082411514529024	18494303-3546202	J184943.03-354620.5	282.429315-35.772423				19644	c) d) e) f)	YSO	False
225	283.05	-36.538	Gaia	6731797947236370304	6731797947236370304	18521211-3632175		283.050497-36.538359				15296	c) d) e) f)	YSO	False
226	281.078	-36.051	Gaia	6730615697364684032	6730615697364684032	18441868-3603036	J184418.68-360303.8					18078	c) d) e) f)	YSO	False
227	284.882	-36.841	Gaia	6730889303952443136	6730889303952443136	18593179-3650261	J185931.79-365026.4	284.882476-36.840732	SSTSL2 J185931.76-365026.3			20683	c) d) e) f)	YSO	False
228	281.689	-36.606	Gaia	6730527938284896384	6730527938284896384	18464537-3636218	J184645.38-363622.0						c) e) f)	YSO	False
229	285.391	-36.962	2MASS			19013385-3657448	J190133.86-365745.1	285.391126-36.962586		16			a) e)	YSO	False
230	276.264	-36.926	Gaia	6728067471780966016	6728067471780966016	18250347-3655349	J182503.48-365535.2					6317	c) d) e) f)	YSO	False

Continued on next page

TableA.1 – continued from previous page

ID	ra	dec	coord origin	Gaia EDR3 source id	Gaia DR2 source id	2MASS	WISE	early VISIONS ID	SEIP	ID pet	ID dun	ID Kerr	references	type	new
231	274.02	-37.634	Gaia	6727798641186958848	6727798641186958848	18160486-3738004	J181604.86-373800.8						f)	YSO	False
232	282.981	-37.705	Gaia	6729429977144779264	6729429977144779264	18515544-3742177	J185155.44-374218.0	282.981018-37.705060				14733	c) d) e) f)	YSO	False
233	285.851	-37.252	Gaia	6719167062590662656		19032429-3715076	J190324.29-371507.9	285.851244-37.252238	SSTSL2 J190324.30-371507.6	36			a) e)	YSO	False
234	277.861	-35.504	Gaia	6734256695776640128	6734256695776640128	18312671-3530137	J183126.71-353014.0					1143	c) d) e) f)	YSO	False
235	279.948	-35.987	Gaia	6733565240388574336	6733565240388574336	18394759-3559129	J183947.59-355913.3					19321	c) d) e) f)	YSO	False
236	283.275	-36.173	2MASS			18530598-3610228	J185305.98-361023.0	283.274896-36.173127	SSTSL2 J185305.95-361023.0				e)	YSO	False
237	285.37	-36.992	Gaia	6731198266716413184	6731198266716413184	19012872-3659317	J190128.73-365932.0	285.369737-36.992288		69		15920	a) c) d) e) f)	YSO	False
238	281.034	-34.923	Gaia	6735217875085023872	6735217875085023872	18440805-3455220	J184408.06-345522.3						c) e) f)	YSO	False
239	282.975	-37.38	Gaia	6730986473294930432	6730986473294930432	18515410-3722490	J185154.10-372249.3	282.975449-37.380410				13926	c) d) e) f)	YSO	False
240	278.105	-37.488	Gaia	6733198347086699776	6733198347086699776	18322512-3729153							c) e)	YSO	False
241	277.393	-35.704	Gaia	6734227146400420608	6734227146400420608	18293425-3542150	J182934.25-354215.3					18766	c) d) e) f)	YSO	False
242	282.877	-36.367	Gaia	6731815466398973824	6731815466398973824	18513039-3621598	J185130.39-362200.2	282.876661-36.366753				15297	c) d) e) f)	YSO	False
243	285.855	-37.11	VISIONS				J190325.14-370635.0	285.854811-37.109732	SSTSL2 J190325.15-370634.8					YSO	True
244	266.419	-38.974	Gaia	5961245561303843200	5961245561303843200	17454069-3858266	J174540.71-385826.8						f)	YSO	False
245	285.664	-36.887	Gaia	6731202286805849344	6731202286805849344	19023940-3653111	J190239.41-365311.5	285.664222-36.886570	SSTSL2 J190239.41-365311.3			15913	c) d) e) f)	YSO	False
246	262.622	-39.08	Gaia	5961745529846435712	5961745529846435712	17302932-3904477	J173029.32-390448.1					9861	d) f)	YSO	False
247	285.768	-37.164	VISIONS				J190304.35-370948.7	285.768130-37.163685	SSTSL2 J190304.35-370948.9					G	False
248	284.337	-37.28	VISIONS				J185720.96-371649.1	284.337364-37.280385	SSTSL2 J185720.98-371649.7					YSO	True
249	276.08	-37.402	Gaia	6728028404761019520	6728028404761019520	18241914-3724081	J182419.11-372408.3					29670	c) d) e) f)	YSO	False
250	285.435	-37.295	Gaia	6718806628937346432		19014447-3717414	J190144.47-371741.7	285.435331-37.295019					e)	YSO	False
251	284.136	-37.161	VISIONS					284.135903-37.160799	SSTSL2 J185632.60-370938.8					YSO	True
252	285.55	-37.053	Gaia	6731194865102308224	6731194865102308224	19021201-3703093	J190211.95-370309.2	285.550110-37.052744	SSTSL2 J190212.01-370309.3	28	J190212.0-370309	15921	a) b) c) d) e) f)	YSO	False
253	285.532	-37.199	Gaia	6719181905993948544	6719181905993948544	19020768-3711557	J190207.70-371156.1	285.532075-37.198960	SSTSL2 J190207.67-371155.7				c) e) f)	YSO	False
254	285.065	-36.966	VISIONS			19001553-3657578	J190015.56-365757.7	285.064831-36.966096	SSTSL2 J190015.55-365758.0	5	J190015.5-365757		a) b)	YSO	False
255	285.406	-37.181	VISIONS				J190137.48-371053.5	285.405824-37.181255	SSTSL2 J190137.39-371052.3					YSO	True
256	283.985	-37.002	Spitzer (Peterson)			18555629-3700066		283.984588-37.001852	SSTSL2 J185556.31-370007.2	46			a)	YSO	False
257	278.63	-33.766	Gaia	6735008830453899392	6735008830453899392	18343120-3345559	J183431.20-334556.2						f)	YSO	False
258	282.564	-36.681	Gaia	6731786398058670720	6731786398058670720	18501530-3640502	J185015.31-364050.6	282.563806-36.680760					c) e) f)	YSO	False
259	285.474	-37.01	Gaia	6731194689005003264	6731194689005003264	19015374-3700339	J190153.76-370034.1	285.474004-37.009579		23			a) c) e) f)	YSO	False
260	272.263	-34.382	Gaia	4039500446614073600	4039500446614073600	18090308-3422555	J180903.07-342255.8						f)	YSO	False
261	284.168	-36.922	Gaia	6731055944382779392	6731055944382779392	18564024-3655203	J185640.23-365520.6	284.167694-36.922469	SSTSL2 J185640.29-365521.0	47		14571	a) c) d) e) f)	YSO	False
262	282.042	-38.845	Gaia	6729252612175923968	6729252612175923968	18481012-3850421	J184810.13-385042.5	282.042255-38.845180					c) e) f)	YSO	False
263	280.521	-37.924	Gaia DR2	6729972895366111232	6729972895366111232	18420506-3755259	J184205.09-375526.0						c)	YSO	False
264	284.493	-35.611	VISIONS			18575841-3536404	J185758.40-353640.3	284.493427-35.611230						G	False
265	283.577	-37.843	Gaia	6730724858243386240	6730724858243386240	18541838-3750326	J185418.39-375033.0	283.576627-37.842550					c) e) f)	YSO	False
266	264.767	-39.436	Gaia	5960986213991287680	5960986213991287680	17390408-3926100	J173904.08-392610.2					6487	d) f)	YSO	False
267	284.962	-37.109	Gaia	6730829994739866624	6730829994739866624	18595094-3706313	J185950.95-370631.7	284.962296-37.108870	SSTSL2 J185950.96-370631.7	4	J185950.9-370631		a) b) c) e) f)	YSO	False
268	285.413	-37.005	Gaia	6731197613875423616	6731197613875423616	19013913-3700173	J190139.14-370017.7	285.413099-37.004966					e) f)	YSO	False
269	285.402	-36.928	Gaia	6731198880896209280	6731198880896209280	19013642-3655386	J190136.44-365539.1	285.401789-36.927558					e) f)	YSO	False

Continued on next page

TableA.1 – continued from previous page

ID	ra	dec	coord origin	Gaia EDR3 source id	Gaia DR2 source id	2MASS	WISE	early VISIONS ID	SEIP	ID pet	ID dun	ID Kerr	references	type	new
270	282.557	-36.007	Gaia	6731882845847140480	6731882845847140480	18501356-3600248	J185013.56-360025.1	282.556534-36.007042				16056	c) d) e) f)	YSO	False
271	285.728	-37.319	VISIONS					285.727635-37.319452	SSTSL2 J190254.64-371909.7					YSO	True
272	285.737	-37.122	Spitzer (c2d or gb)					285.736786-37.122130	SSTSL2 J190256.83-370719.3	32	J190256.8-370719		a) b)	YSO	False
273	286.948	-35.996	Gaia	6719350685330266624	6719350681030620672	19074742-3559454	J190747.43-355945.5	286.947642-35.996052					f)	YSO	False
274	284.933	-37.067	Spitzer (c2d or gb)			18594391-3704000		284.932988-37.066718	SSTSL2 J185943.89-370400.2		J185943.9-370400		b)	YSO	False
275	287.758	-37.913	Gaia	6718198564641656320	6718198564641656320	19110191-3754452	J191101.91-375445.5	287.757959-37.912688					f)	YSO	False
276	285.337	-37.051	Gaia	6730822023280685440	6730822023280685440	19012083-3703027	J190120.84-370303.0	285.336867-37.050888	SSTSL2 J190120.84-370302.8			20081	c) d) e) f)	YSO	False
277	282.634	-35.201	Gaia	6732206067902438144	6732206067902438144	18503214-3512035		282.633910-35.201109					c) f)	YSO	False
278	285.409	-37.184	VISIONS				J190138.08-371100.4	285.408709-37.183561	SSTSL2 J190138.08-371100.7					YSO	True
279	280.426	-35.433	Gaia	6733708864096481408	6733708864096481408	18414231-3525598	J184142.31-352600.2					15590	c) d) e) f)	YSO	False
280	285.808	-37.012	Gaia	6719188056390848128		19031388-3700419	J190313.88-370042.1	285.807860-37.011766	SSTSL2 J190313.87-370041.9				e)	YSO	False
281	285.348	-37.168	VISIONS			19012353-3710060	J190123.53-371006.1	285.348071-37.168393	SSTSL2 J190123.52-371006.0					G	False
282	285.504	-36.736	Gaia	6731219535395752704	6731219535395752704	19020087-3644090	J190200.87-364409.3	285.503649-36.735969					c) e) f)	YSO	False
283	285.975	-37.261	VISIONS				J190354.09-371537.9	285.975396-37.260602	SSTSL2 J190354.09-371537.9					YSO	True
284	284.923	-37.199	VISIONS			18594151-3711564	J185941.51-371156.3	284.922983-37.199044	SSTSL2 J185941.50-371156.8					G	False
285	284.469	-37.244	Spitzer (c2d or gb)			18575262-3714402	J185752.61-371440.0	284.469231-37.244459	SSTSL2 J185752.59-371439.9	2	J185752.6-371440		a) b)	G	False
286	285.528	-36.978	Gaia	6731196097754245120		19020682-3658411	J190206.81-365841.4	285.528451-36.978225		26	J190206.8-365841		a) b) e)	YSO	False
287	285.493	-37.007	2MASS			19015833-3700267	J190158.33-370027.1	285.493108-37.007577					e)	YSO	False
288	284.468	-37.246	Spitzer (Peterson)			18575220-3714460		284.467491-37.246051	SSTSL2 J185752.18-371445.6	50			a)	G	False
289	285.598	-37.393	Gaia	6718801651070440832	6718801651070440832	19022358-3723356	J190223.59-372335.9	285.598298-37.393344				3662	c) d) e) f)	YSO	False
290	274.032	-37.826	Gaia	6727761193408968192	6727761193408968192	18160759-3749314	J181607.58-374931.6					21298	d) f)	YSO	False
291	285.269	-37.025	Gaia	6730822985358131968	6730822985358131968	19010460-3701292	J190104.61-370129.5	285.269223-37.024925	SSTSL2 J190104.61-370129.4				c) e) f)	YSO	False
292	281.684	-37.152	Gaia	6730292642798112896	6730292642798112896	18464410-3709058	J184644.09-370906.2					10567	c) d) e) f)	YSO	False
293	283.36	-37.277	Gaia	6730944618831282048	6730944618831282048	18532644-3716364	J185326.37-371636.4	283.360231-37.276931				13508	c) d) e) f)	YSO	False
294	282.406	-36.021	Gaia	6731884873071695616	6731884873071695616	18493739-3601138	J184937.38-360114.2	282.405826-36.020645				16055	c) d) e) f)	YSO	False
295	284.393	-37.209	VISIONS					284.392797-37.208599	SSTSL2 J185734.23-371230.9					YSO	True
296	286.038	-37.409	VISIONS				J190409.22-372433.2	286.038437-37.409191	SSTSL2 J190409.24-372432.9					YSO	True
297	285.745	-37.126	2MASS			19025870-3707346	J190258.69-370736.0	285.744592-37.126212					e)	YSO	False
298	285.39	-37.009	Gaia	6731197442076732928	6731197442076732928	19013357-3700304	J190133.59-370030.9	285.389929-37.008578	SSTSL2 J190133.57-370030.5				c) e) f)	YSO	False
299	283.239	-37.395	Gaia	6730942252310427520	6730942252310427520	18525735-3723410		283.239001-37.394845					f)	YSO	False
300	285.226	-37.042	VISIONS				J190054.21-370232.5	285.225695-37.042435	SSTSL2 J190054.15-370232.5					YSO	True
301	285.754	-37.131	Spitzer (c2d or gb)			19030103-3707533	J190301.03-370753.6	285.754338-37.131626	SSTSL2 J190301.04-370753.5	33	J190301.0-370753		a) b)	YSO	False
302	285.298	-36.76	Gaia	6731216889694682240	6731216889694682240	19011149-3645337	J190111.50-364534.1	285.297928-36.759512	SSTSL2 J190111.47-364533.9	53		16500	a) c) d) e) f)	YSO	False
303	285.828	-37.307	VISIONS				J190318.73-371824.3	285.828084-37.306604	SSTSL2 J190318.73-371823.8					YSO	True
304	283.217	-36.24	Gaia	6731902087299776000	6731902087299776000	18525206-3614233	J185252.08-361423.6	283.216952-36.239933					c) e) f)	YSO	False
305	285.767	-37.108	VISIONS				J190304.13-370628.9	285.767327-37.108439	SSTSL2 J190304.12-370630.7					HH	False
306	282.103	-37.367	Gaia	6730236705141318528	6730236705141318528	18482466-3722010	J184824.67-372201.4	282.102816-37.367093				18493	c) d) e) f)	YSO	False
307	271.73	-37.897	Gaia	4036266404946684288	4036266404946684288	18065523-3753495	J180655.22-375349.9						f)	YSO	False
308	286.242	-36.841	Gaia	6719208225556239104	6719208225556239104	19045816-3650279	J190458.15-365028.1	286.242345-36.841181					e) f)	YSO	False

Continued on next page

TableA.1 – continued from previous page

ID	ra	dec	coord origin	Gaia EDR3 source id	Gaia DR2 source id	2MASS	WISE	early VISIONS ID	SEIP	ID pet	ID dun	ID Kerr	references	type	new
309	287.167	-39.16	Gaia	6717610639454377344	6717610639454377344	19084013-3909350		287.167276-39.159903					f)	YSO	False
310	284.573	-37.431	Gaia	6730796292140202112	6730796292140202112	18581761-3725527	J185817.62-372552.9	284.573427-37.431433	SSTSL2 J185817.60-372552.9			20094	c) d) e) f)	YSO	False
311	284.138	-37.9	Gaia	6730688540000272768	6730688540000272768	18563312-3753595	J185633.12-375359.8	284.138023-37.900018				18619	c) d) e) f)	YSO	False
312	281.704	-35.16	Gaia	6735171077119945600	6735171077119945600	18464894-3509362	J184648.94-350936.4					13686	c) d) e) f)	YSO	False
313	271.729	-37.894	Gaia	4036266404946692992	4036266404946692992	18065501-3753387						4103	d) f)	YSO	False
314	281.911	-38.853	Gaia	6729254016622857472	6729254016622857472	18473853-3851092	J184738.54-385109.5	281.910625-38.852703				26239	c) d) e) f)	YSO	False
315	282.409	-35.408	Gaia	6732196795081776384		18493819-3524286	J184938.18-352428.8	282.409130-35.408065						R	False
316	276.475	-38.84	Gaia	6727023524166168704	6727023524166168704	18255404-3850230	J182554.05-385023.4					13789	d) e) f)	YSO	False
317	285.819	-37.03	VISIONS				J190316.57-370149.0	285.819016-37.030214	SSTSL2 J190316.55-370148.6					YSO	True
318	284.376	-38.012	Gaia	6730672730219764736	6730672730219764736	18573011-3800444	J185730.11-380044.7	284.375503-38.012485					e) f)	YSO	False
319	285.466	-37.179	Gaia	6718807664024747776	6718807664024747776		J190151.83-371047.5N	285.466154-37.179196	SSTSL2 J190151.87-371044.4	22			a) e) f)	YSO	False
320	285.997	-37.272	VISIONS				J190359.29-371618.2	285.997052-37.271707	SSTSL2 J190359.33-371617.8					YSO	True
321	284.283	-36.901	Gaia	6731061304500058496	6731061304500058496	18570785-3654041	J185707.88-365404.4	284.282781-36.901236	SSTSL2 J185707.88-365404.9	48			a) c) e) f)	YSO	False
322	283.12	-36.046	Gaia	6731919202752668160	6731919202752668160	18522888-3602469	J185228.88-360247.1	283.120359-36.046488				17006	c) d) e) f)	YSO	False
323	277.245	-36.863	Gaia	6734017174039282688	6734017174039282688	18285877-3651475	J182858.78-365147.8					18143	c) d) e) f)	YSO	False
324	282.711	-35.786	Gaia	6731894841699927552	6731894841699927552	18505070-3547081	J185050.69-354708.6	282.711264-35.785727				16057	c) d) e) f)	YSO	False
325	284.893	-37.362	Spitzer (Peterson)			18593428-3721410		284.892984-37.361379	SSTSL2 J185934.22-372142.0	51			a)	YSO	False
326	283.88	-37.171	Gaia DR2		6730960218154606464	18553130-3710156		283.880449-37.171116					c)	YSO	False
327	281.607	-36.154	Gaia	6730557595045553664	6730557595045553664	18462578-3609128	J184625.78-360913.1					17266	c) d) e) f)	YSO	False
328	282.33	-38.218	Gaia	6729434199093960576	6729434199093960576	18491926-3813040	J184919.26-381304.3	282.330264-38.217907					e) f)	YSO	False
329	284.904	-37.017	Gaia	6730878682489282816	6730878682489282816	18593684-3700589	J185936.85-370059.3	284.903556-37.016518					c) e) f)	YSO	False
330	279.695	-34.687	Gaia	6733990579595949056	6733990579595949056	18384687-3441143	J183846.87-344114.5					17169	c) d) e) f)	YSO	False
331	284.344	-37.578	Spitzer (Peterson)			18572247-3734427		284.343661-37.578550	SSTSL2 J185722.48-373442.0	49			a)	YSO	False
332	280.742	-35.545	Gaia	6733646363730649856	6733646363730649856	18425797-3532427	J184257.98-353243.1		SSTSL2 J184257.96-353242.4			12925	c) d) e) f)	YSO	False
333	285.401	-36.967	Spitzer (c2d or gb)			19013627-3658030		285.401182-36.967571		17	J190136.2-365803		a) b)	YSO	False
334	285.837	-37.071	VISIONS					285.836917-37.071421	SSTSL2 J190320.83-370417.1					YSO	True
335	282.849	-36.302	Gaia	6731816604565998464	6731816604565998464	18512364-3618070	J185123.65-361807.5	282.848528-36.302115					f)	YSO	False
336	278.664	-37.972	Gaia	6732936766415012352	6732936766415012352	18343930-3758180	J183439.31-375818.4						c) e)	YSO	False
337	267.266	-38.957	Gaia	5958255714311844224	5958255714311844224	17490381-3857235	J174903.80-385723.8					10576	d) f)	YSO	False
338	283.73	-37.658	Gaia	6730733826136155904	6730733826136155904	18545508-3739270	J185455.09-373927.3	283.729551-37.657628				19166	c) d) e) f)	YSO	False
339	282.152	-33.805	Gaia	6735395171334235008	6735395171334235008	18483653-3348166	J184836.53-334816.9					18461	c) d) e) f)	YSO	False
340	281.941	-37.517	Gaia	6730233887645446272	6730233887645446272	18474580-3730598	J184745.81-373100.3	281.940878-37.516736				18498	c) d) e) f)	YSO	False
341	285.561	-37.009	VISIONS			19021464-3700328	J190214.65-370033.1	285.561061-37.009256	SSTSL2 J190214.65-370033.1					YSO	True
342	280.372	-35.915	Gaia	6733611175046196224	6733611175046196224	18412924-3554545	J184129.24-355455.0					12923	c) d) e) f)	YSO	False
343	285.16	-36.88	Gaia	6730839512392306944	6730839512392306944	19003840-3652471	J190038.40-365247.4	285.160024-36.879894					e) f)	YSO	False
344	281.998	-37.436	Gaia	6730234785298700800	6730234785298700800	18475945-3726085	J184759.44-372608.7	281.997730-37.435831				18500	c) d) e) f)	YSO	False
345	281.999	-38.183	Gaia	6729355206055074944	6729355206055074944	18475974-3810589	J184759.74-381059.1	281.998948-38.183165					c) e) f)	YSO	False
346	285.489	-37.053	2MASS			19015741-3703117	J190157.42-370312.1	285.489265-37.053416	SSTSL2 J190157.42-370311.9				e)	YSO	False
347	285.249	-36.787	Gaia	6731215545363943296	6731215545363943296	19005974-3647109	J190059.74-364711.3	285.248953-36.786533	SSTSL2 J190059.74-364711.0	10	J190059.7-364711		a) b) c) e) f)	YSO	False

Continued on next page

TableA.1 – continued from previous page

ID	ra	dec	coord origin	Gaia EDR3 source id	Gaia DR2 source id	2MASS	WISE	early VISIONS ID	SEIP	ID pet	ID dun	ID Kerr	references	type	new
348	289.516	-39.236	VISIONS			19180379-3914104	J191803.77-391410.5	289.515723-39.236225						G	False
349	278.331	-33.906	Gaia	6735012678745195392	6735012678745195392	18331941-3354205	J183319.41-335420.8						e) f)	YSO	False
350	285.861	-37.144	VISIONS				J190326.65-370839.5	285.861016-37.144379	SSTSL2 J190326.64-370839.6					YSO	True
351	282.256	-35.987	Gaia	6732073374903202432	6732073374903202432	18490142-3559143	J184901.37-355914.8	282.255917-35.987444					f)	YSO	False
352	285.996	-37.258	VISIONS				J190358.93-371527.3	285.995561-37.257603	SSTSL2 J190358.95-371527.3					YSO	True
353	285.719	-36.911	VISIONS				J190252.60-365439.8	285.719098-36.911161	SSTSL2 J190252.57-365439.8					G	False
354	271.782	-37.656	Gaia	4036279422901945088	4036279422901945088	18070775-3739224	J180707.77-373922.8					4977	d) f)	YSO	False
355	285.98	-37.16	Spitzer (Peterson)				J190355.24-370935.9	285.980178-37.159984	SSTSL2 J190355.25-370935.9	37			a)	YSO	False
356	285.46	-36.944	Spitzer (c2d or gb)					285.460032-36.944045			J190150.4-365638		b)	YSO	False
357	280.649	-36.081	Gaia	6733598775492008320	6733598775492008320	18423571-3604519	J184235.70-360452.3					19316	c) d) e) f)	YSO	False
358	285.46	-36.944	Spitzer (Peterson)					285.460392-36.944057		42			a)	YSO	False
359	285.42	-36.876	Gaia	6731200706257840384		19014081-3652337	J190140.82-365236.4				J190140.8-365233		b) e)	YSO	False
360	280.11	-34.931	Gaia	6733923264549194368	6733923264549194368	18402648-3455526	J184026.49-345552.7						c) e) f)	YSO	False
361	276.87	-35.049	Gaia	6734509613481584896	6734509613481584896	18272891-3502564	J182728.91-350256.5					12374	c) d) e) f)	YSO	False
362	285.778	-37.214	Gaia	6719168132036642432	6719168132036642432	19030674-3712494	J190306.78-371249.2	285.778126-37.213888			J190306.8-371249		b) e) f)	YSO	False
363	284.392	-37.543	Gaia	6730746985915311360	6730746985915311360			284.391594-37.542518				19613	c) d) e) f)	YSO	False
364	279.801	-34.871	Gaia	6733973361050980352	6733973361050980352	18391234-3452141	J183912.36-345214.4						c) f)	YSO	False
365	278.764	-34.077	Gaia	6734809818842679552	6734809818842679552	18350328-3404369	J183503.29-340437.0					4949	c) d) e) f)	YSO	False
366	275.63	-33.458	Gaia	4044760647636888576	4044760647636888576	18223129-3327275	J182231.31-332727.3						e) f)	YSO	False
367	285.485	-36.958	IRAC								J190156.4-365728		b) e)	YSO	False
368	285.744	-37.127	Spitzer (Peterson)						SSTSL2 J190258.68-370736.2	44			a)	YSO	False
369	279.75	-34.369	Gaia	6734004907607126784			J183859.82-342209.6						e)	YSO	False
370	279.55	-36.786	Gaia	6733467727430619136	6733467727430619136								e) f)	YSO	False
371	276.871	-35.049	Gaia	6734509617794516480	6734509617794516480								c) e) f)	YSO	False
372	281.672	-37.355	Gaia	6730281274026219776	6730281274026219776							24636	c) d) e) f)	YSO	False
373	284.933	-37.067	Spitzer (Peterson)							3			a)	YSO	False
374	284.681	-37.108	Spitzer (Peterson)							62			a)	YSO	False
375	283.829	-37.499	Spitzer (Peterson)							58			a)	YSO	False
376	274.638	-34.847	Gaia	4038524595658266240	4038524595658266240	18183306-3450488	J181833.06-345049.1					8336	d) f)	YSO	False
377	285.98	-37.16	Spitzer (c2d or gb)								J190355.2-370935		b)	YSO	False
378	285.851	-37.252	Spitzer (c2d or gb)								J190324.2-371507		b)	YSO	False
379	285.817	-37.236	Spitzer (c2d or gb)								J190316.0-371408		b)	YSO	False
380	285.744	-37.126	Spitzer (c2d or gb)								J190258.6-370735		b)	YSO	False
381	285.638	-36.972	Spitzer (c2d or gb)								J190233.0-365821		b)	YSO	False
382	285.612	-36.97	Spitzer (c2d or gb)								J190227.0-365813		b)	YSO	False
383	285.561	-37.009	Spitzer (c2d or gb)							29	J190214.6-370032		a) b)	YSO	False
384	285.495	-36.964	Spitzer (c2d or gb)								J190158.7-365749		b)	YSO	False
385	281.588	-37.329	Gaia	6730284469481982208	6730284469481982208	18462112-3719428	J184621.12-371943.2						c) e) f)	YSO	False
386	285.494	-36.952	Spitzer (c2d or gb)								J190158.5-365708		b)	YSO	False

Continued on next page

TableA.1 – continued from previous page

ID	ra	dec	coord origin	Gaia EDR3 source id	Gaia DR2 source id	2MASS	WISE	early VISIONS ID	SEIP	ID pet	ID dun	ID Kerr	references	type	new
387	285.482	-36.948	Spitzer (c2d or gb)							24	J190155.6-365651		a) b)	YSO	False
388	285.48	-36.956	Spitzer (c2d or gb)								J190155.3-365721		b)	YSO	False
389	285.474	-37.009	Spitzer (c2d or gb)								J190153.7-370033		b)	YSO	False
390	285.466	-37.179	Spitzer (c2d or gb)								J190151.8-371044		b)	YSO	False
391	285.461	-36.969	Spitzer (c2d or gb)								J190150.6-365809		b)	YSO	False
392	278.136	-35.958	Gaia	6734184024926986752	6734184024926986752	18323261-3557298	J183232.61-355730.0						c) e) f)	YSO	False
393	285.452	-36.954	Spitzer (c2d or gb)								J190148.4-365714		b)	YSO	False
394	268.783	-41.141	Gaia	5957048892851994624	5957048892851994624	17550801-4108275	J175508.01-410827.7					3233	d) f)	YSO	False
395	285.391	-36.962	Spitzer (c2d or gb)								J190133.8-365744		b)	YSO	False
396	285.317	-36.941	Spitzer (c2d or gb)								J190116.2-365628		b)	YSO	False
397	285.121	-36.934	Spitzer (c2d or gb)								J190029.0-365603		b)	YSO	False
398	261.881	-39.62	Gaia	5960413948239559040	5960413948239559040		J172731.32-393711.7						f)	YSO	False
399	285.286	-36.956	Gaia	6731210258265107584	6731210258265107584								e) f)	YSO	False
400	280.761	-37.463	Gaia	6730364218421821312	6730364218421821312								e) f)	YSO	False
401	277.467	-33.928	Gaia	6734979418518297856	6734979418518297856	18295207-3355401	J182952.08-335540.5					12581	c) d) e) f)	YSO	False
402	283.842	-37.801	Gaia	6730717024217228928			J185522.11-374804.5	283.842302-37.801173					e)	YSO	False
403	285.469	-36.95	IRAC					285.469362-36.950104					e)	YSO	False
404	282.052	-34.895	Gaia	6732272214708936448	6732272214708936448	18481251-3453408	J184812.53-345341.2					2730	c) d) e) f)	YSO	False
405	284.127	-37.276	Gaia	6730768873069264128	6730768873069264128		J185630.45-371633.2A	284.126613-37.276115					c) e) f)	YSO	False
406	284.812	-37.192	Gaia	6730828693373852032	6730828693373852032	18591487-3711317		284.811791-37.192450	SSTSL2 J185914.86-371132.1	64		20091	a) c) d) e) f)	YSO	False
407	281.173	-37.205	Gaia	6730394553778846720	6730394553778846720	18444146-3712192	J184441.46-371219.4						c) e) f)	YSO	False
408	279.849	-37.497	Gaia	6730058103224748672	6730058103224748672	18392375-3729504	J183923.74-372950.8						c) e)	YSO	False
409	285.474	-36.952	Gaia	6731199293213061632		19015367-3657081	J190153.78-365709.1				J190153.6-365708		b) e)	YSO	False
410	281.303	-36.963	Gaia	6730492650830636928	6730492650830636928	18451266-3657471	J184512.67-365747.4						e) f)	YSO	False
411	284.812	-37.192	Gaia	6730828693373851904	6730828693373851904		J185914.89-371131.9	284.812369-37.191999				20099	c) d) e) f)	YSO	False
412	285.494	-36.952	IRAC				J190158.52-365708.8	285.494058-36.952519		43			a) e)	YSO	False
413	285.488	-36.868	Spitzer (c2d or gb)					285.488653-36.868007		25	J190157.2-365205		a) b)	HH	False
414	285.286	-36.956	Gaia	6731210253964165632	6731210253964165632	19010860-3657200	J190108.61-365720.6	285.285908-36.955730	SSTSL2 J190108.60-365720.1		J190108.6-365720		b) e) f)	YSO	False
415	283.373	-37.703	Gaia	6730917753816052352	6730917753816052352		J185329.63-374211.6	283.373190-37.703473					f)	YSO	False
416	285.461	-36.969	2MASS			19015067-3658096	J190150.72-365809.6	285.461195-36.969459					e)	YSO	False
417	285.452	-36.954	2MASS			19014846-3657148		285.452144-36.954081	SSTSL2 J190148.46-365715.0	20			a) e)	YSO	False
418	284.185	-35.759	Gaia	6731563613818178304	6731563613818178304			284.184633-35.759062				19704	c) d) e) f)	YSO	False
419	268.176	-39.445	Gaia	4036442258090761600	4036442258090761600	17524221-3926422	J175242.21-392642.6					7258	d) f)	YSO	False
420	285.48	-36.956	IRAC			19015545-3657231	J190155.35-365722.4						e)	YSO	False
421	279.758	-34.862	Gaia	6733973605884925312	6733973605884925312	18390199-3451444	J183901.99-345144.7					16028	c) d) e) f)	YSO	False
422	281.273	-36.553	Gaia	6730522135794742912	6730522135794742912	18450544-3633103	J184505.43-363310.7					16318	c) d) e) f)	YSO	False
423	266.606	-40.114	Gaia	5958041786218206720	5958041786218206720	17462540-4006514							f)	YSO	False
424	278.314	-36.01	Gaia	6733430992578156544	6733430992578156544	18331545-3600366	J183315.46-360036.9					14254	c) d) e) f)	YSO	False
425	279.812	-37.705	Gaia	6730036907572443008	6730036907572443008	18391482-3742175	J183914.82-374217.8						c) e)	YSO	False

Continued on next page

TableA.1 – continued from previous page

ID	ra	dec	coord origin	Gaia EDR3 source id	Gaia DR2 source id	2MASS	WISE	early VISIONS ID	SEIP	ID pet	ID dun	ID Kerr	references	type	new
426	281.495	-34.797	Gaia	6735199698782414336	6735199698782414336	18455879-3447490	J184558.79-344749.3					13685	c) d) e) f)	YSO	False
427	274.699	-36.375	Gaia	4038090215470220160	4038090215470220160	18184772-3622280							f)	YSO	False
428	279.785	-37.44	Gaia	6730059378841092480	6730059378841092480	18390833-3726239	J183908.32-372624.2					4307	c) d) e) f)	YSO	False
429	265.19	-40.952	Gaia	5957652872713410304	5957652872713410304	17404558-4057082	J174045.57-405708.6					13214	d) f)	YSO	False
430	281.13	-37.393	Gaia	6730203376193388032	6730203376193388032	18443116-3723347	J184431.17-372335.0					26592	d) e) f)	YSO	False
431	279.046	-34.105	Gaia	6734821084509554432	6734821084509554432	18361102-3406173	J183611.03-340617.6					4955	c) d) e) f)	YSO	False
432	280.318	-35.276	Gaia	6733714499093829888	6733714499093829888	18411639-3516324	J184116.39-351632.7					15594	c) d) e) f)	YSO	False
433	279.637	-34.757	Gaia	6733966562137689472	6733966562137689472	18383277-3445258	J183832.78-344526.0					16027	c) d) e) f)	YSO	False
434	261.683	-40.323	Gaia	5960181268413575552	5960181268413575552	17264400-4019220	J172643.98-401922.6						f)	YSO	False
435	278.529	-36.133	Gaia	6733422402643171840	6733422402643171840	18340692-3607599	J183406.92-360800.3						c) e)	YSO	False
436	271.513	-38.0	Gaia	4036264686959919488	4036264686959919488	18060307-3800007							f)	YSO	False
437	275.48	-37.301	Gaia	6728140520578676480	6728140520578676480	18215513-3718049	J182155.13-371805.2					19315	c) d) e) f)	YSO	False
438	277.018	-32.976	Gaia	4044932480678173312	4044932480678173312	18280442-3258331	J182804.42-325833.2					1710	d) f)	YSO	False
439	279.274	-37.039	Gaia	6733083168946807680	6733083168946807680	18370580-3702184	J183705.79-370218.5						c) e)	YSO	False
440	278.899	-34.156	Gaia	6734798170891123456	6734798170891123456	18353582-3409219						3994	c) d) e) f)	YSO	False
441	280.251	-36.035	Gaia	6733608671096579968	6733608671096579968	18410032-3602062	J184100.34-360207.2					12926	c) d) e) f)	YSO	False
442	280.72	-37.598	Gaia	6730358720877034752	6730358720877034752	18425287-3735534	J184252.80-373554.5						c) e)	YSO	False
443	273.289	-37.715	Gaia	4037541872762763904	4037541872762763904	18130933-3742529						13650	d) f)	YSO	False
444	279.349	-33.93	Gaia	6734826414587434496	6734826414587434496	18372377-3355474	J183723.79-335547.8					4950	c) d) e) f)	YSO	False
445	280.787	-36.76	Gaia	6730466640511571968	6730466640511571968	18430890-3645358	J184308.90-364535.9						f)	YSO	False
446	281.822	-37.567	Gaia	6730228424440331904	6730228424440331904	18471728-3734010	J184717.28-373401.3					18495	c) d) e) f)	YSO	False
447	269.106	-39.686	Gaia	4035638446353675264	4035638446353675264	17562532-3941098							f)	YSO	False
448	275.629	-36.695	Gaia	6728265147685134464	6728265147685134464	18223090-3641413	J182230.90-364141.6						e) f)	YSO	False
449	279.565	-33.793	Gaia	6736330198582343552	6736330198582343552	18381569-3347356	J183815.68-334736.0						e) f)	YSO	False
450	280.95	-35.731	Gaia	6733633856789001728	6733633852472949376	18434791-3543524	J184347.90-354352.6					12915	c) d) e) f)	YSO	False
451	280.55	-39.397	Gaia	6729644893010390784		18421190-3923496	J184211.91-392349.9						e)	YSO	False
452	280.629	-36.923	Gaia	6730457986164326272	6730457986164326272	18423088-3655236	J184230.86-365524.0					15414	c) d) e) f)	YSO	False
453	280.464	-38.127	Gaia	6729781335527729024	6729781335527729024	18415143-3807380	J184151.43-380738.3						e) f)	YSO	False
454	280.867	-35.461	Gaia	6733653643694443648	6733653643694443648	18432811-3527385	J184328.11-352738.9						c) e) f)	YSO	False
455	281.161	-36.616	Gaia	6730520211649421440	6730520211649421440	18443868-3636558	J184438.66-363656.2					16330	c) d) e) f)	YSO	False
456	276.153	-34.065	Gaia	4044461133792715008		18243665-3403531	J182436.65-340353.4						e)	YSO	False
457	278.993	-38.241	Gaia	6729915205380292352	6729915205380292352	18355821-3814270	J183558.21-381427.3						c) e)	YSO	False
458	276.549	-31.62	Gaia	4046078511045267072	4046078511045267072	18261182-3137112	J182611.81-313711.5					15871	d) f)	YSO	False
459	281.775	-35.08	Gaia	6735177635516522368	6735177635516522368	18470611-3504481	J184706.10-350448.5					13683	c) d) e) f)	YSO	False
460	277.646	-35.624	Gaia	6734231510086998528	6734231510086998528	18303498-3537246	J183034.98-353724.8					18765	c) d) e) f)	YSO	False
461	277.891	-36.46	Gaia	6733393647861596032	6733393647861596032	18313375-3627351	J183133.74-362735.5					14256	c) d) e) f)	YSO	False
462	270.389	-39.021	Gaia	4036140235985529216	4036140235985529216	18013325-3901156	J180133.24-390115.9						f)	YSO	False
463	268.086	-40.603	Gaia	5957852567138380032	5957852567138380032	17522071-4036119							f)	YSO	False
464	281.453	-36.469	Gaia	6730543507552577024	6730543507552577024	18454868-3628066	J184548.68-362806.8					17267	c) d) e) f)	YSO	False

Continued on next page

TableA.1 – continued from previous page

ID	ra	dec	coord origin	Gaia EDR3 source id	Gaia DR2 source id	2MASS	WISE	early VISIONS ID	SEIP	ID pet	ID dun	ID Kerr	references	type	new
465	278.55	-36.146	Gaia	6733419413347826176	6733419413347826176	18341201-3608459	J183412.00-360846.3						e) f)	YSO	False
466	280.232	-35.371	Gaia	6733690309826250880		18405565-3522154	J184055.63-352215.5						e)	YSO	False
467	281.126	-37.654	Gaia	6730190426878681344	6730190426878681344	18443023-3739128	J184430.24-373913.1					26573	c) d) e) f)	YSO	False
468	279.772	-37.44	Gaia	6730059374535019520	6730059374535019520	18390529-3726217	J183905.28-372622.0		SSTSL2 J183905.30-372621.6				c) e)	YSO	False
469	279.788	-41.283	Gaia	6722635575100579072	6722635575100579072	18390907-4116599	J183909.07-411700.2					9973	d) f)	YSO	False
470	280.715	-38.492	Gaia	6729752954388414976	6729752954388414976	18425148-3829312							c) f)	YSO	False
471	281.14	-36.459	Gaia	6730570651746598016	6730570651746598016	18443370-3627302	J184433.70-362730.6					17272	c) d) e) f)	YSO	False
472	266.133	-40.569	Gaia	5958051613102657920	5958051613102657920	17443191-4034089							f)	YSO	False
473	280.409	-35.043	Gaia	6733911449115951488	6733911449115951488	18413826-3502327	J184138.26-350233.0					14903	d) e) f)	YSO	False
474	276.057	-37.516	Gaia	6727979343370860288	6727979343370860288	18241356-3730581	J182413.57-373058.5					3419	c) d) e) f)	YSO	False
475	279.165	-34.857	Gaia DR2		6734711957980514432	18363954-3451257							c)	YSO	False
476	266.715	-38.453	Gaia	5961285757876107648	5961285757876107648	17465175-3827115							f)	YSO	False
477	281.582	-35.997	Gaia	6732107769002061312	6732107769002061312	18461959-3559490	J184619.59-355949.3					19648	c) d) e) f)	YSO	False
478	281.606	-35.928	Gaia	6732109143391621760	6732109143391621760	18462548-3555387	J184625.48-355538.8					19643	c) d) e) f)	YSO	False
479	279.816	-35.764	Gaia	6733584275683948032	6733584275683948032	18391587-3545493	J183915.87-354549.6					19317	c) d) f)	YSO	False
480	281.16	-36.366	Gaia	6730572335374109440	6730572335374109440	18443848-3621556	J184438.48-362156.1					17268	c) d) e) f)	YSO	False
481	283.738	-39.855	Gaia	6717001471361208192	6717001471361208192	18545721-3951182	J185457.22-395118.6						c) e) f)	YSO	False
482	285.46	-36.944	2MASS			19015037-3656390	J190150.56-365638.5						e)	YSO	False
483	273.286	-37.718	Gaia	4037541872762215424	4037541872762215424	18130870-3743041						13649	d) f)	YSO	False
484	278.846	-38.535	Gaia	6729884522133011072	6729884522133011072	18352315-3832071	J183523.14-383207.4						c) e)	YSO	False
485	277.752	-35.36	Gaia	6734262120287926784	6734262120287926784	18310058-3521345	J183100.58-352134.7					1142	c) d) e) f)	YSO	False
486	273.74	-34.097	Gaia	4039372967587862016	4039372967587862016	18145757-3405480						14528	d) f)	YSO	False
487	280.639	-37.784	Gaia	6730350577618959488	6730350577618959488	18423337-3747019	J184233.37-374702.2						c) e)	YSO	False
488	267.024	-40.191	Gaia	5958031547009032704	5958031547009032704	17480569-4011279							f)	YSO	False
489	279.743	-35.148	Gaia	6733898632932962432	6733898632932962432	18385839-3508514	J183858.38-350851.7						f)	YSO	False
490	284.384	-33.793	Gaia	6732777027982641024	6732777027982641024	18573207-3347353	J185732.08-334735.6						c) e)	YSO	False
491	280.991	-36.282	Gaia	6730588072134320512	6730588072134320512	18435780-3616552	J184357.80-361655.4					17263	c) d) f)	YSO	False
492	280.155	-34.129	Gaia	6735512990881822336	6735512990881822336	18403726-3407431	J184037.26-340743.6					15533	c) d) e) f)	YSO	False
493	281.753	-37.658	Gaia	6730226264083604608	6730226264083604608	18470066-3739299	J184700.66-373930.4					18504	c) d) e) f)	YSO	False
494	277.367	-34.364	Gaia	6734929047140217216	6734929047140217216	18292799-3421507	J182927.99-342151.1						c) e) f)	YSO	False
495	263.08	-38.075	Gaia	5962092597547610624	5962092597547610624	17321930-3804292	J173219.31-380429.8					12642	d) f)	YSO	False
496	278.608	-34.029	Gaia	6735001374390357248	6735001374390357248	18342583-3401428	J183425.82-340143.0					869	c) d) e) f)	YSO	False
497	279.55	-35.92	Gaia	6733763599160670848	6733763599160670848	18381201-3555127	J183812.01-355513.0					17044	c) d) e) f)	YSO	False
498	279.818	-35.467	Gaia	6733873477286353280	6733873477286353280	18391629-3527594	J183916.29-352759.7						c) e) f)	YSO	False
499	267.866	-38.927	Gaia	4036660957736702208	4036660957736702208	17512787-3855350	J175127.85-385535.5						f)	YSO	False
500	271.709	-39.23	Gaia	4035855217571358208	4035855217571358208	18065014-3913485	J180650.13-391348.8						f)	YSO	False
501	280.429	-38.289	Gaia	6729771169352813696	6729771169352813696	18414299-3817188	J184142.99-381719.1					10256	c) d) e) f)	YSO	False
502	278.907	-36.989	Gaia	6733121999764431232	6733121999764431232	18353757-3659216	J183537.57-365921.9					11803	c) d) e) f)	YSO	False
503	281.042	-36.893	Gaia	6730507803475258624	6730507803475258624	18441016-3653350	J184410.12-365335.2						c) e) f)	YSO	False

Continued on next page

TableA.1 – continued from previous page

ID	ra	dec	coord origin	Gaia EDR3 source id	Gaia DR2 source id	2MASS	WISE	early VISIONS ID	SEIP	ID pet	ID dun	ID Kerr	references	type	new
504	280.264	-33.846	Gaia	6735543983367061760	6735543983367061760	18410325-3350459	J184103.25-335046.2					15529	c) d) e) f)	YSO	False
505	281.081	-35.642	Gaia	6733635914056263296	6733635914056263296	18441936-3538311	J184419.35-353831.0		SSTSL2 J184419.39-353830.8			29409	c) d) e) f)	YSO	False
506	277.322	-37.764	Gaia	6727177417120993024		18291733-3745494	J182917.32-374549.7						e)	YSO	False
507	285.45	-36.956	2MASS			19014805-3657219	J190148.04-365722.2			19	J190148.0-365722		a) b) e)	YSO	False
508	281.814	-34.883	Gaia	6735184443058287360	6735184443058287360	18471530-3452574	J184715.31-345257.8					13684	c) d) e) f)	YSO	False
509	276.652	-34.309	Gaia	4044416328691645824	4044416328691645824	18263652-3418322	J182636.53-341832.6					22232	c) d) e) f)	YSO	False
510	267.821	-39.598	Gaia	5957978293795450496	5957978293795450496	17511697-3935532	J175116.97-393553.5					18387	d) f)	YSO	False
511	280.722	-36.869	Gaia	6730464170917216000	6730464170917216000	18425317-3652079	J184253.17-365208.1					15417	c) d) e) f)	YSO	False
512	277.847	-34.75	Gaia	6734855001900424704	6734855001900424704	18312324-3445002	J183123.23-344500.5						c) e) f)	YSO	False
513	278.905	-35.039	Gaia	6734615686316679936	6734615686316679936	18353718-3502193	J183537.18-350219.7					10430	c) d) e) f)	YSO	False
514	280.171	-36.79	Gaia	6733456182575931520	6733456182575931520	18404099-3647220	J184041.00-364722.5					15665	c) d) e) f)	YSO	False
515	272.602	-37.016	Gaia	4037822866732172416	4037822866732172416	18102445-3700556	J181024.45-370055.9					2476	d) f)	YSO	False
516	276.508	-36.966	Gaia	6728069984365602944	6728069984365602944	18260191-3657567	J182601.92-365756.9					6318	c) d) f)	YSO	False
517	266.924	-39.433	Gaia	5958206786034397824	5958206786034397824	17474186-3925595	J174741.88-392559.4					5499	d) f)	YSO	False
518	265.299	-41.665	Gaia	5957478325219310464	5957478325219310464	17411184-4139533	J174111.84-413953.7					1254	d) f)	YSO	False
519	280.172	-35.973	Gaia	6733656736060577024	6733656736060577024	18404136-3558209	J184041.35-355821.2						f)	YSO	False
520	280.892	-34.667	Gaia	6735238246097073152	6735238246097073152	18433398-3440010	J184333.98-344001.3					14956	c) d) e) f)	YSO	False
521	277.803	-34.128	Gaia	6734958115480349312	6734958115480349312	18311282-3407410	J183112.83-340741.3					11491	c) d) e) f)	YSO	False
522	281.447	-39.004	Gaia	6728921242556174848	6728921242556174848	18454721-3900154	J184547.21-390015.7						c) e) f)	YSO	False
523	277.122	-31.598	Gaia	4045352184905807104	4045352184905807104	18282916-3135528						11460	d) f)	YSO	False
524	277.86	-34.911	Gaia	6734664472824575616	6734664472824575616	18312648-3454402	J183126.48-345440.6						f)	YSO	False
525	281.396	-37.843	Gaia	6730127204958679552	6730127204958679552	18453509-3750348							e) f)	YSO	False
526	280.168	-36.103	Gaia	6733514559772646144	6733514559772646144	18404036-3606088	J184040.36-360609.1					16807	c) d) f)	YSO	False
527	273.713	-37.488	Gaia	4037633437113480064	4037633437113480064	18145115-3729162	J181451.15-372916.5						f)	YSO	False
528	279.829	-36.948	Gaia	6733451264825017728	6733451264825017728	18391888-3656520							c) e)	YSO	False
529	280.781	-36.975	Gaia	6730415448806356480	6730415448806356480	18430753-3658293	J184307.52-365829.6						f)	YSO	False
530	280.234	-37.838	Gaia	6729988185461217792	6729988185461217792	18405612-3750171	J184056.14-375017.9					17758	c) d) e) f)	YSO	False
531	279.101	-34.513	Gaia	6734738625461995008	6734738625461995008	18362422-3430471	J183624.22-343047.4					2253	c) d) e) f)	YSO	False
532	277.297	-36.031	Gaia	6734125579019324160	6734125579019324160	18291128-3601529	J182911.28-360153.4						f)	YSO	False
533	281.691	-36.605	Gaia	6730527942591027968		18464585-3636164	J184645.85-363616.5						e)	YSO	False
534	281.804	-37.47	Gaia	6730232238372827392	6730232238372827392	18471306-3728105	J184713.06-372810.8					18501	c) d) e) f)	YSO	False
535	275.447	-39.166	Gaia	6726671920967135360	6726671920967135360	18214722-3909565	J182147.22-390956.8					22413	d) e) f)	YSO	False
536	274.792	-33.466	Gaia	4045406542035455616	4045406542035455616	18190996-3327562						725	d) f)	YSO	False
537	281.113	-36.617	Gaia	6730520898844223104	6730520898844223104	18442702-3636595	J184427.02-363659.8					16320	c) d) e) f)	YSO	False
538	280.993	-35.986	Gaia	6730618549223057664	6730618549223057664	18435838-3559096	J184358.38-355909.9					18076	d) e) f)	YSO	False
539	279.525	-36.828	Gaia	6733467555649287040	6733467555649287040	18380592-3649396	J183805.91-364940.1						f)	YSO	False
540	285.612	-34.825	Gaia	6731676172019810944	6731676172019810944	19022686-3449301	J190226.86-344930.4	285.611946-34.825176				13329	c) d) e) f)	YSO	False
541	266.098	-39.524	Gaia	5961120384410461568	5961120384410461568	17442348-3931274	J174423.48-393127.9					3103	d) f)	YSO	False
542	282.526	-38.125	Gaia	6729394994630895616	6729394994630895616	18500621-3807301	J185006.21-380730.4	282.525898-38.125178				20762	c) d) e) f)	YSO	False

Continued on next page

TableA.1 – continued from previous page

ID	ra	dec	coord origin	Gaia EDR3 source id	Gaia DR2 source id	2MASS	WISE	early VISIONS ID	SEIP	ID pet	ID dun	ID Kerr	references	type	new
543	277.366	-33.13	Gaia	4045006594634833152	4045006594634833152	18292780-3307469	J182927.79-330747.0					4137	c) d) e) f)	YSO	False
544	280.497	-36.711	Gaia	6730481316426843392	6730481316426843392	18415927-3642383	J184159.27-364238.7						c) e)	YSO	False
545	283.814	-38.579	Gaia	6729133555682667264	6729133590033609088	18551532-3834448	J185515.31-383445.0	283.813825-38.579240					c) e) f)	YSO	False
546	276.629	-34.3	Gaia	4044416569172725888	4044416569172725888	18263093-3417595	J182630.95-341759.6						c) e) f)	YSO	False
547	281.091	-35.696	Gaia	6733632688554418688		18442192-3541435	J184421.92-354143.8		SSTSL2 J184421.93-354143.2				e)	YSO	False
548	285.624	-36.581	Gaia	6731245648796025472	6731245648796025472	19022975-3634503	J190229.75-363450.6	285.623963-36.580769				16502	c) d) e) f)	YSO	False
549	285.423	-36.975	2MASS			19014156-3658312	J190141.58-365831.6	285.423244-36.975464	SSTSL2 J190141.57-365831.3		J190141.5-365831		b) e)	YSO	False
550	281.698	-35.638	Gaia	6732122440610486912	6732122440610486912	18464760-3538175	J184647.60-353817.9					19642	c) d) e) f)	YSO	False
551	278.81	-34.719	Gaia	6734638707323221376	6734638707323221376	18351442-3443062	J183514.42-344306.5					11409	c) d) e) f)	YSO	False
552	285.197	-36.797	Gaia	6731215858902470528	6731215858902470528	19004728-3647467	J190047.28-364747.0	285.197038-36.796442					e) f)	YSO	False
553	281.299	-35.917	Gaia	6730623389635497600	6730623389635497600	18451184-3555011	J184511.85-355501.4						c) e)	YSO	False
554	279.886	-33.54	Gaia	6736317421080943232	6736317421080943232	18393260-3332251	J183932.60-333225.5						c) e) f)	YSO	False
555	282.802	-36.722	Gaia	6731772070046218752	6731772070046218752	18511244-3643201	J185112.45-364320.3	282.801886-36.722367					c) e) f)	YSO	False
556	280.22	-35.778	Gaia	6733662955168139392	6733662955168139392	18405271-3546410	J184052.70-354641.3					14158	c) d) e) f)	YSO	False
557	280.761	-37.462	Gaia	6730364218435247488	6730364218435247488	18430268-3727430	J184302.69-372743.6					4149	c) d) e) f)	YSO	False
558	264.653	-42.734	Gaia	5955946636792294144	5955946636792294144	17383674-4244020	J173836.74-424402.2						f)	YSO	False
559	281.829	-37.549	Gaia	6730228531826367616	6730228531826367616	18471904-3732552	J184719.03-373255.5					18494	c) d) e) f)	YSO	False
560	280.958	-36.471	Gaia	6730572812103102848	6730572812103102848	18434988-3628167	J184349.88-362816.9					17269	c) d) e) f)	YSO	False
561	285.418	-36.862	Gaia	6731200770681837696		19014041-3651422	J190140.43-365142.8	285.418447-36.861888		18	J190140.4-365142		a) b) e)	YSO	False
562	281.003	-35.637	Gaia	6733635368614113536	6733635368614113536	18440069-3538135	J184400.70-353813.8					12920	c) d) e) f)	YSO	False
563	287.441	-37.074	Gaia	6719035052475592576	6719035052475592576	19094592-3704261	J190945.92-370426.4	287.441334-37.074050				4874	c) d) e) f)	YSO	False
564	276.581	-38.928	Gaia	6727010364386181248	6727010364386181248	18261951-3855395	J182619.51-385539.9					13788	d) e) f)	YSO	False
565	276.782	-33.854	Gaia	4044819093492085120	4044819093492085120	18270760-3351133	J182707.63-335113.7						c) e) f)	YSO	False
566	285.445	-38.224	Gaia	6718694586124956160	6718694586124956160	19014689-3813268	J190146.90-381327.1	285.445448-38.224263				2712	c) d) e) f)	YSO	False
567	282.076	-37.184	Gaia	6730265223722584320	6730265223722584320	18481828-3711033	J184818.28-371103.6	282.076210-37.184393					c) e) f)	YSO	False
568	285.363	-36.986	Gaia	6731198266716413312	6731198266716413312	19012717-3659085	J190127.17-365908.9	285.363255-36.985838	SSTSL2 J190127.17-365908.6	68		15919	a) c) d) e) f)	YSO	False
569	273.792	-38.264	Gaia	6727651757647477632	6727651757647477632	18151017-3815503	J181510.17-381550.7					21393	d) f)	YSO	False
570	280.235	-37.839	Gaia	6729988185461217024	6729988185461217024	18405631-3750205						17756	c) d) e) f)	YSO	False
571	284.438	-37.327	Spitzer (Peterson)			18574512-3719378		284.438079-37.327294	SSTSL2 J185745.11-371937.9	60			a)	YSO	False

A.2 YSO spectral indices and Classes

The following table lists spectral indices for all sources listed in Table A.1. The first column named “ID” is the same unique identifier as in Table A.1, so that the spectral indices can be matched to each source in the catalog.

Table A.2: This table lists spectral indices, YSO Classes and memberships for all sources in the main YSO catalog.

ID	cluster	α_{IRAC}	α_{KI}	α_{IM}	α_{KIM}	α_{W3}	α_{WISE}	α_{KW3}	α_{KW4}	α_{KW3M}	α_{W3M}	α_{KIWM}	Class
1	CrA-North					-1.164	-0.494	-1.416				-0.8	II
2	CrA-Main					-0.82	-0.691	-1.069		-0.893	-0.721	-0.847	II
3	CrA-Main					-2.672	-2.672	-2.613		-2.692	-2.743	-2.71	III no disk
4	CrA-Main	-0.698	-0.388	-0.39	-0.339	-0.934	-0.575	-0.534	-0.388	-0.454	-0.631	-0.404	II
5	CrA-North					-2.488	-2.488	-2.443				-2.443	III thin disk
6	CrA-North					-2.506	-2.506	-2.476				-2.476	III thin disk
7	CrA-North					-2.034	-2.034	-2.102				-2.102	III thin disk
8	CrA-North					-2.605	-2.605	-2.556				-2.556	III no disk
9	CrA-Main					-2.171	-2.171	-2.249				-2.249	III thin disk
10	CrA-North					-2.567	-2.567	-2.541				-2.541	III no disk
11	CrA-Main					-2.554	-2.554	-2.521				-2.521	III no disk
12	Scorpio-Sting					-2.712	-2.712	-2.676				-2.676	III no disk
13	Scorpio-Sting					-2.824	-2.824	-2.785				-2.785	III no disk
14	CrA-North					-2.662	-2.662	-2.622				-2.622	III no disk
15	CrA-Main					-2.714	-2.714	-2.717		-2.798	-2.819	-2.798	III no disk
16	Scorpio-Sting					-2.826	-2.826	-2.752				-2.752	III no disk
17	CrA-North					-2.113	-2.113	-2.277				-2.277	III thin disk
18	CrA-North												–
19	CrA-Main					-2.524	-2.524	-2.489				-2.489	III thin disk
20	CrA-North					-2.45	-2.45	-2.282				-2.282	III thin disk
21	CrA-Main					-2.224	-2.224	-2.346				-2.346	III thin disk
22	CrA-North					-2.732	-2.732	-2.58				-2.58	III no disk
23	CrA-North					-2.582	-2.582	-2.541				-2.541	III no disk
24	CrA-Main					-2.267	-2.267	-2.282				-2.282	III thin disk
25	CrA-North												–
26	CrA-Main	-2.632	-2.411	-2.632	-2.411	-2.44	-2.44	-2.394	-2.411	-2.394	-2.44	-2.428	III thin disk
27	CrA-Main					-2.632	-2.632	-2.601				-2.601	III no disk
28	CrA-Main					-2.565	-2.565	-2.583		-2.652	-2.662	-2.652	III no disk
29	CrA-Main	-2.425	-2.296	-2.834	-2.683	-2.075	-2.075	-2.198	-2.296	-2.698	-2.788	-2.674	III no disk
30	CrA-North					-2.139	-2.139	-2.213				-2.213	III thin disk
31	CrA-North												–
32	CrA-Main	-0.495	-2.558	0.17	-0.828				-2.558			-0.828	II
33	CrA-North					-1.336	-0.229	-1.622		-0.638	-0.227	-0.443	II
34	CrA-North					-2.515	-2.515	-2.508				-2.508	III no disk
35	CrA-Main					-1.39	-1.005	-1.557		-1.253	-1.087	-1.156	II
36	CrA-Main					-2.646	-2.646	-2.555		-2.693	-2.776	-2.715	III no disk
37	CrA-North												–
38	CrA-North					-2.529	-2.529	-2.476				-2.476	III thin disk
39	CrA-North					-2.145	-2.145	-2.182				-2.182	III thin disk
40	CrA-Main	-2.704	-2.73	-2.825	-2.807	-2.581	-2.083	-2.596	-2.73	-2.771	-2.811	-2.463	III thin disk
41	CrA-North					-2.575	-2.575	-2.525				-2.525	III no disk
42	CrA-North					-2.677	-2.677	-2.671				-2.671	III no disk
43	CrA-North					-2.711	-2.711	-2.633				-2.633	III no disk
44	CrA-North					-2.411	-2.411	-2.202				-2.202	III thin disk
45	CrA-North					-1.558	-1.558	-1.769				-1.769	III thin disk
46	CrA-North					-1.24	-1.24	-1.388				-1.388	II
47	CrA-Main					-2.531	-2.531	-2.491				-2.489	III thin disk
48	CrA-Main					-2.45	-2.45	-2.427				-2.427	III thin disk
49	CrA-Main					-2.646	-2.646	-2.555				-2.555	III no disk
50	CrA-North					-2.037	-2.037	-1.998				-1.998	III thin disk

Continued on next page

TableA.2 – continued from previous page

ID	cluster	α_{IRAC}	α_{KI}	α_{IM}	α_{KIM}	α_{W3}	α_{WISE}	α_{KW3}	α_{KW4}	α_{KW3M}	α_{W3M}	α_{KIWM}	Class
51	CrA-Main					-2.64	-2.64	-2.62				-2.62	III no disk
52	CrA-North					-2.876	-2.876	-2.734				-2.734	III no disk
53	CrA-North					-2.218	-2.218	-2.171				-2.171	III thin disk
54	CrA-North					-2.587	-2.587	-2.569				-2.569	III no disk
55	CrA-Main					-2.59	-2.59	-2.542				-2.542	III no disk
56	CrA-North												–
57	CrA-Main	-2.567	-2.478	-2.753	-2.672	-2.497	-2.497	-2.489	-2.478	-2.631	-2.674	-2.636	III no disk
58	CrA-Main					-2.332	-2.332	-2.407				-2.407	III thin disk
59	CrA-North					-2.362	-2.362	-2.301				-2.301	III thin disk
60	CrA-Main					-2.355	-2.355	-2.34				-2.34	III thin disk
61	CrA-North					-2.326	-2.326	-2.288				-2.288	III thin disk
62	CrA-North					-2.666	-2.666	-2.608				-2.608	III no disk
63	CrA-Main					-2.789	-2.519	-2.769				-2.578	III no disk
64	CrA-North					-2.247	-2.247	-2.271				-2.271	III thin disk
65	CrA-Main	-2.938	-2.59			-2.613	-2.613	-2.536	-2.59			-2.598	III no disk
66	CrA-North					-2.736	-2.736	-2.736				-2.736	III no disk
67	CrA-North					-1.217	-1.217	-1.508		-1.102	-0.847	-1.102	II
68	Scorpio-Sting					-2.702	-2.702	-2.622				-2.622	III no disk
69	CrA-North					-2.539	-2.539	-2.468				-2.468	III thin disk
70	CrA-North					-2.645	-2.645	-2.604				-2.604	III no disk
71	CrA-North												–
72	CrA-Main												–
73	CrA-North					-2.651	-2.651	-2.561				-2.561	III no disk
74	CrA-North					-2.6	-2.6	-2.558				-2.558	III no disk
75	CrA-North					-2.563	-2.563	-2.516				-2.516	III no disk
76	CrA-North					-1.112	-0.719	-1.293				-0.919	II
77	CrA-Main					-2.463	-2.463	-2.416				-2.416	III thin disk
78	CrA-North					-2.098	-2.098	-2.129				-2.129	III thin disk
79	CrA-North					-2.113	-2.113	-2.27				-2.27	III thin disk
80	CrA-Main	-2.46	-2.188			-2.508	-2.508	-2.344	-2.188			-2.345	III thin disk
81	CrA-North					-2.308	-2.308	-2.332				-2.332	III thin disk
82	CrA-North					-2.711	-2.711	-2.67				-2.67	III no disk
83	Scorpio-Sting					-2.535	-2.535	-2.495				-2.495	III thin disk
84	CrA-North					-2.57	-2.57	-2.495				-2.495	III thin disk
85	CrA-North					-2.644	-2.644	-2.544				-2.544	III no disk
86	CrA-North					-2.684	-2.684	-2.647				-2.647	III no disk
87	CrA-Main					-2.442	-2.442	-2.428				-2.428	III thin disk
88	CrA-Main					-2.643	-2.643	-2.614				-2.614	III no disk
89	CrA-North					-2.779	-2.779	-2.516				-2.516	III no disk
90	CrA-Main					-0.121	-0.239	-0.419				-0.402	II
91	CrA-Main					-2.631	-2.587	-2.655				-2.611	III no disk
92	–					-1.535	-1.535	-1.816				-1.816	R
93	CrA-North					-2.447	-2.447	-2.446				-2.446	III thin disk
94	CrA-North					-2.235	-2.235	-2.276				-2.276	III thin disk
95	CrA-North					-2.635	-2.635	-2.609				-2.609	III no disk
96	CrA-Main	-2.039	-1.86	-2.183	-2.075	-2.071	-2.071	-1.979	-1.86	-2.063	-2.132	-2.075	III thin disk
97	Scorpio-Sting					-2.407	-2.407	-2.446				-2.446	III thin disk
98	CrA-North					-2.367	-2.367	-2.223				-2.223	III thin disk
99	CrA-North					-1.859	-1.859	-2.085				-2.085	III thin disk
100	CrA-North					-2.645	-2.645	-2.523				-2.523	III no disk
101	CrA-North												–
102	Scorpio-Sting												–
103	CrA-North												–
104	CrA-North												–
105	CrA-North					-2.638	-2.638	-2.638				-2.638	III no disk
106	Scorpio-Sting					-2.606	-2.606	-2.261				-2.261	III thin disk
107	CrA-Main	-1.159	-1.45	-0.582	-0.839	-0.946	-0.683	-1.217	-1.45	-0.858	-0.626	-0.794	II
108	CrA-Main					-2.61	-2.61	-2.613		-2.761	-2.8	-2.77	III no disk
109	CrA-Main					-2.61	-2.61	-2.566				-2.566	III no disk
110	CrA-Main	-2.68	-2.511	-2.888	-2.769	-2.899	-2.899	-2.773	-2.511	-2.785	-2.851	-2.795	III no disk
111	CrA-Main					-2.691	-2.691	-2.682		-2.784	-2.817	-2.784	III no disk

Continued on next page

TableA.2 – continued from previous page

ID	cluster	α_{IRAC}	α_{KI}	α_{IM}	α_{KIM}	α_{W3}	α_{WISE}	α_{KW3}	α_{KW4}	α_{KW3M}	α_{W3M}	α_{KIWM}	Class
112	CrA-North					-2.653	-2.653	-2.6				-2.6	III no disk
113	CrA-Main					-2.598	-2.598	-2.601				-2.601	III no disk
114	CrA-Main					-2.65	-2.65	-2.552				-2.552	III no disk
115	CrA-North					-1.101	-0.892	-1.409		-1.333	-1.158	-1.201	II
116	CrA-North					-2.546	-2.546	-2.47				-2.47	III thin disk
117	CrA-Main					-2.571	-2.571	-2.536				-2.536	III no disk
118	CrA-Main					-2.162	-2.162	-2.245				-2.245	III thin disk
119	CrA-North					-2.445	-2.445	-2.414				-2.414	III thin disk
120	CrA-North					-1.181	-1.27	-1.408				-1.394	II
121	CrA-North					-2.726	-2.726	-2.727				-2.727	III no disk
122	CrA-Main	-1.856	-1.892	-1.213	-1.384	-1.495	-1.212	-1.647	-1.892	-1.386	-1.239	-1.318	II
123	Scorpio-Sting					-2.705	-2.705	-2.632				-2.632	III no disk
124	CrA-North					-2.612	-2.612	-2.575				-2.575	III no disk
125	CrA-North					-2.665	-2.665	-2.592				-2.592	III no disk
126	CrA-North					-2.659	-2.659	-2.577				-2.577	III no disk
127	CrA-Main					-0.635	-0.242	-0.878		-0.495	-0.27	-0.408	II
128	CrA-North					-2.725	-2.725	-2.658				-2.658	III no disk
129	CrA-North					-2.658	-2.658	-2.566				-2.566	III no disk
130	CrA-North												–
131	CrA-North					-2.693	-2.693	-2.575				-2.575	III no disk
132	CrA-North					-2.413	-2.413	-2.511				-2.511	III no disk
133	CrA-North					-2.542	-2.542	-2.516				-2.516	III no disk
134	CrA-North					-2.935	-2.935	-2.802				-2.802	III no disk
135	CrA-North					-2.63	-2.63	-2.589				-2.589	III no disk
136	CrA-North					-2.557	-2.557	-2.521				-2.521	III no disk
137	CrA-Main					-2.569	-2.569	-2.53				-2.53	III no disk
138	CrA-North					-2.685	-2.469	-2.706				-2.529	III no disk
139	CrA-North					-2.687	-2.687	-2.672				-2.672	III no disk
140	CrA-North					-2.387	-2.387	-2.356				-2.356	III thin disk
141	Scorpio-Sting					-2.442	-1.989	-2.491				-2.119	III thin disk
142	CrA-Main					-2.665	-2.665	-2.636				-2.636	III no disk
143	CrA-North					-2.27	-2.27	-2.233				-2.233	III thin disk
144	CrA-North					-1.135	-1.135	-1.295				-1.295	II
145	CrA-Main					-2.642	-2.642	-2.566				-2.566	III no disk
146	CrA-Main					-2.661	-2.661	-2.585				-2.585	III no disk
147	CrA-Main					-2.606	-2.606	-2.556				-2.556	III no disk
148	CrA-Main					-2.552	-2.552	-2.507				-2.507	III no disk
149	CrA-North					-2.104	-2.104	-2.344				-2.344	III thin disk
150	CrA-North					-2.762	-2.84	-2.743		-2.803	-2.829	-2.82	III no disk
151	CrA-North					-2.224	-2.224	-2.113				-2.113	III thin disk
152	CrA-Main	-2.026	-2.321	-0.298	-0.837	-1.589	-0.594	-1.789	-2.321	-0.975	-0.655	-0.727	II
153	CrA-Main	-1.415	-1.167	-0.969	-1.049	-1.211	-0.749	-1.221	-1.167	-1.07	-1.025	-0.916	II
154	CrA-North					-2.626	-2.626	-2.588				-2.588	III no disk
155	CrA-Main					-2.65	-2.65	-2.65				-2.65	III no disk
156	CrA-Main					-2.634	-2.634	-2.584				-2.584	III no disk
157	CrA-Main	-1.108	-1.352	-1.101	-1.202	-1.131	-1.018	-1.341	-1.352	-1.192	-1.047	-1.147	II
158	CrA-Main	-1.455	-1.502	-1.059	-1.174	-1.672	-1.672	-1.679	-1.502	-1.261	-1.145	-1.275	II
159	CrA-North					-2.279	-2.279	-2.225				-2.225	III thin disk
160	CrA-North					-2.598	-2.598	-2.552				-2.552	III no disk
161	CrA-Main					-2.66	-2.66	-2.586				-2.586	III no disk
162	CrA-Main					-2.57	-2.57	-2.517		-2.736	-2.822	-2.736	III no disk
163	CrA-Main	-0.687	-1.17	-1.023	-1.106	-0.762	-0.646	-1.061	-1.17	-1.012	-0.849	-0.912	II
164	CrA-North					-2.682	-2.682	-2.61				-2.61	III no disk
165	CrA-Main											0.287	flat
166	CrA-Main					-2.412	-2.412	-2.221				-2.213	III thin disk
167	CrA-Main					-2.785	-2.822	-2.755				-2.795	III no disk
168	CrA-North					-2.666	-2.666	-2.644				-2.644	III no disk
169	CrA-Main					-2.445	-2.445	-2.419				-2.419	III thin disk
170	CrA-Main	-1.051	-1.167	-0.791	-0.901	-1.05	-0.786	-1.143	-1.167	-0.928	-0.823	-0.863	II
171	CrA-Main	-2.613	-2.439			-2.326	-1.425	-2.208	-2.439			-1.596	II
172	CrA-Main	-1.182	-1.478	-1.334	-1.417	-1.365	-1.353	-1.493	-1.478	-1.43	-1.349	-1.399	II

Continued on next page

TableA.2 – continued from previous page

ID	cluster	α_{IRAC}	α_{KI}	α_{IM}	α_{KIM}	α_{W3}	α_{WISE}	α_{KW3}	α_{KW4}	α_{KW3M}	α_{W3M}	α_{KIWM}	Class
173	CrA-Main					-2.597	-2.597	-2.602				-2.602	III no disk
174	CrA-North					-2.601	-2.601	-2.548				-2.548	III no disk
175	CrA-Main					-2.694	-2.694	-2.637				-2.637	III no disk
176	CrA-Main	-1.995	-1.979	-2.063	-2.041				-1.979			-2.041	III thin disk
177	CrA-North					-2.61	-2.61	-2.567				-2.567	III no disk
178	CrA-Main					-2.56	-2.56	-2.54				-2.54	III no disk
179	CrA-Main					-2.448	-2.448	-2.415		-1.722	-1.55	-1.736	III thin disk
180	CrA-Main					-2.652	-2.652	-2.624				-2.624	III no disk
181	CrA-North					-2.559	-2.559	-2.478				-2.478	III thin disk
182	CrA-Main					-2.299	-1.369	-2.294		-1.531	-1.326	-1.394	II
183	CrA-North					-0.93	-0.939	-1.2				-1.107	II
184	CrA-Main					-2.546	-2.546	-2.529				-2.529	III no disk
185	CrA-North					-2.669	-2.669	-2.607				-2.607	III no disk
186	CrA-North					-2.66	-2.66	-2.35				-2.35	III thin disk
187	CrA-Main					-2.159	-2.159	-2.026				-2.026	III thin disk
188	CrA-Main	-2.603	-2.503	-2.794	-2.707	-2.613	-2.613	-2.581	-2.503	-2.682	-2.725	-2.688	III no disk
189	CrA-Main					0.509	0.9	-0.253				0.334	I
190	CrA-Main	-2.389	-2.326	-1.984	-2.057	-2.223	-2.223	-2.274	-2.326	-2.068	-1.987	-2.09	III thin disk
191	CrA-Main					-2.316	-1.511	-2.417				-1.751	III thin disk
192	CrA-Main					-2.717	-2.717	-2.654		-2.789	-2.856	-2.785	III no disk
193	CrA-North					-2.668	-2.668	-2.619				-2.619	III no disk
194	CrA-Main												–
195	CrA-North					-2.78	-2.827	-2.723				-2.781	III no disk
196	CrA-Main	-2.244	-2.565	-1.332	-1.683	-1.732	-1.12	-2.154	-2.565	-1.749	-1.314	-1.515	II
197	CrA-North					-0.952	-0.534	-1.141				-0.745	II
198	–					-1.115	-0.968	-1.277		-1.151	-1.035	-1.096	R
199	CrA-North					-1.166	-1.033	-1.389				-1.203	II
200	CrA-Main					-2.725	-2.725	-2.711				-2.711	III no disk
201	Scorpio-Sting												–
202	CrA-Main	-2.525	-2.512	-2.778	-2.711	-2.653	-2.653	-2.588	-2.512	-2.709	-2.774	-2.7	III no disk
203	CrA-Main	-2.704	-2.521				-0.322	-2.777	-2.521			-1.135	II
204	CrA-North					-2.407	-2.407	-2.358				-2.358	III thin disk
205	CrA-Main	-0.391	-0.336	-0.987	-0.693	-0.642	-0.805	-0.56	-0.336	-0.695	-0.774	-0.744	II
206	CrA-Main					-2.669	-2.669	-2.616				-2.616	III no disk
207	Scorpio-Sting					-2.706	-2.706	-2.601				-2.601	III no disk
208	CrA-Main					-1.504	-1.276	-1.458				-1.297	II
209	CrA-North					-2.32	-2.32	-2.43				-2.43	III thin disk
210	CrA-Main					-2.646	-2.646	-2.572				-2.572	III no disk
211	–	-0.495	-2.265	0.023	-1.067				-2.265			-1.067	G
212	CrA-North					-2.465	-2.465	-2.402				-2.402	III thin disk
213	CrA-Main					-2.686	-2.686	-2.614				-2.614	III no disk
214	CrA-Main	-2.625	-2.619	-2.811	-2.764	-2.754	-2.754	-2.697	-2.619	-2.77	-2.818	-2.762	III no disk
215	CrA-North					-2.224	-2.224	-2.147				-2.147	III thin disk
216	CrA-Main	-2.676	-2.241	-1.875	-2.024				-2.241			-2.024	III thin disk
217	CrA-North					-2.607	-2.607	-2.549				-2.549	III no disk
218	CrA-Main	-1.493	-1.153	-1.484	-1.348	-1.701	-1.515	-1.478	-1.153	-1.391	-1.479	-1.428	II
219	CrA-Main	-2.548	-2.252	-2.548	-2.252	-2.404	-2.404	-2.308	-2.252	-2.308	-2.404	-2.333	III thin disk
220	CrA-North					-2.614	-2.614	-2.616				-2.616	III no disk
221	CrA-Main	-2.273	-2.302	-1.117	-1.409	-2.322	-1.434	-2.332	-2.302	-1.563	-1.35	-1.443	II
222	CrA-North					-2.738	-2.695	-2.73				-2.699	III no disk
223	CrA-Main	-1.04	-0.863	-1.21	-1.097	-1.257	-1.176	-1.099	-0.863	-1.121	-1.206	-1.131	II
224	CrA-North					-2.531	-2.531	-2.504				-2.504	III no disk
225	CrA-North												–
226	CrA-North					-2.133	-2.133	-2.302				-2.302	III thin disk
227	CrA-Main					-2.654	-2.654	-2.619		-2.721	-2.766	-2.731	III no disk
228	CrA-North					-2.761	-2.761	-2.726				-2.726	III no disk
229	CrA-Main	-0.962	-0.642	-0.643	-0.591	-0.774	-0.454	-0.67	-0.642	-0.592	-0.623	-0.53	II
230	CrA-North					-2.224	-2.224	-2.26				-2.26	III thin disk
231	CrA-North					-2.474	-2.474	-2.428				-2.428	III thin disk
232	CrA-Main					-2.557	-2.557	-2.517				-2.517	III no disk
233	CrA-Main	-0.584	-0.335	-0.402	-0.345	-0.166	-0.1	-0.285	-0.335	-0.263	-0.198	-0.263	flat

Continued on next page

TableA.2 – continued from previous page

ID	cluster	α_{IRAC}	α_{KI}	α_{IM}	α_{KIM}	α_{W3}	α_{WISE}	α_{KW3}	α_{KW4}	α_{KW3M}	α_{W3M}	α_{KIWM}	Class
234	CrA-North					-2.616	-2.616	-2.566				-2.566	III no disk
235	CrA-North					-2.618	-2.618	-2.547				-2.547	III no disk
236	CrA-North					-2.744	-2.774	-2.723		-2.813	-2.848	-2.797	III no disk
237	CrA-Main	-2.472	-2.343	-2.859	-2.713	-2.522	-2.522	-2.435	-2.343	-2.676	-2.785	-2.674	III no disk
238	CrA-North					-2.48	-2.48	-2.446				-2.446	III thin disk
239	CrA-North					-2.431	-2.431	-2.414				-2.414	III thin disk
240	CrA-North												–
241	CrA-North					-2.663	-2.663	-2.596				-2.596	III no disk
242	CrA-North					-2.043	-2.043	-2.186				-2.186	III thin disk
243	CrA-Main	1.557	1.974	0.51	0.933	0.631	0.631	1.23	1.974	0.964	0.536	0.89	I
244	Scorpio-Sting					-2.679	-2.679	-2.548				-2.548	III no disk
245	CrA-Main					-2.069	-2.069	-2.158				-2.355	III thin disk
246	Scorpio-Sting					-2.818	-2.818	-2.682				-2.682	III no disk
247	–					1.216	1.216	1.142				1.209	G
248	CrA-Main									0.384		0.586	I
249	CrA-North					-2.13	-2.13	-2.13				-2.13	III thin disk
250	CrA-Main					-1.838	-1.838	-1.802				-1.802	III thin disk
251	CrA-Main											0.083	flat
252	CrA-Main	-1.372	-1.554	-1.103	-1.242	-1.236	-1.236	-1.325	-1.554	-1.254	-1.19	-1.241	II
253	CrA-Main					-1.905	-1.905	-1.944				-2.024	III thin disk
254	CrA-Main	1.46	1.508	0.124	0.468	0.692	0.624	0.818	1.508	0.496	0.346	0.514	I
255	CrA-Main	0.62	0.479			1.263	1.263	0.566	0.479			0.513	I
256	CrA-Main											-0.168	flat
257	CrA-North					-2.488	-2.488	-2.439				-2.439	III thin disk
258	CrA-North					-2.148	-2.148	-2.165				-2.165	III thin disk
259	CrA-Main	-1.072	-1.244	-0.988	-1.078	-0.907	-0.109	-0.947	-1.244	-1.07	-1.083	-0.609	II
260	CrA-North					-2.751	-2.751	-2.625				-2.625	III no disk
261	CrA-Main					-1.191	-1.191	-1.37		-1.029	-0.848	-1.029	II
262	CrA-North					-1.404	-1.404	-1.563				-1.563	II
263	CrA-North					-1.453	-1.453	-1.526				-1.526	II
264	–					0.363	0.406	-0.053				0.134	G
265	CrA-Main					-1.065	-0.807	-1.324				-1.027	II
266	Scorpio-Sting					-2.518	-2.518	-2.482				-2.482	III thin disk
267	CrA-Main	-1.661	-1.602	-1.445	-1.474	-1.705	-1.705	-1.716	-1.602	-1.502	-1.438	-1.52	II
268	CrA-Main					-1.812	0.027	-1.772				-0.275	flat
269	CrA-Main					-2.866	-2.866	-2.441				-2.441	III thin disk
270	CrA-North					-2.046	-2.046	-2.225				-2.225	III thin disk
271	CrA-Main											0.697	I
272	CrA-Main	-1.399	-0.12	0.492	0.552				-0.12			0.552	I
273	CrA-Main					-2.32	-2.32	-2.361				-2.361	III thin disk
274	CrA-Main	-0.056	0.152	-0.281	-0.142				0.152			-0.142	flat
275	CrA-Main					-2.253	-2.253	-2.357				-2.357	III thin disk
276	CrA-Main					-0.668	-0.244	-1.091				-0.579	II
277	CrA-North												–
278	CrA-Main	1.194	0.862			0.417	0.417	0.608	0.862			0.841	I
279	CrA-North					-2.156	-2.156	-2.203				-2.203	III thin disk
280	CrA-Main					-0.896	-0.896	-1.322		-1.322	-0.896	-1.274	II
281	–	-1.448	-1.951			-0.709	-0.01	-1.039	-1.951			-0.371	G
282	CrA-Main					-1.967	-1.967	-2.232				-2.232	III thin disk
283	CrA-Main					1.485	1.485	1.997				1.879	I
284	–					-0.137	-0.114	-0.605		-0.561	-0.315	-0.467	G
285	–	3.814	2.434	1.086	1.188	1.551	1.247	1.275	2.434	1.104	1.195	1.147	G
286	CrA-Main	-0.873	-0.758	-0.816	-0.786	-0.75	0.549	-0.859	-0.758	-0.761	-0.68	-0.185	flat
287	CrA-Main					-1.296	-1.296	-0.988				-0.988	II
288	–	-2.389	-2.469	0.434	-0.282				-2.469			-0.282	G
289	CrA-Main					-2.043	-2.043	-2.14				-2.14	III thin disk
290	CrA-North					-2.205	-1.807	-2.239				-1.916	III thin disk
291	CrA-Main	-2.595	-2.321			-2.046	-2.046	-2.101	-2.321			-2.311	III thin disk
292	CrA-North					-2.613	-2.613	-2.606				-2.606	III no disk
293	CrA-Main					-2.235	-2.235	-1.848				-1.848	III thin disk
294	CrA-North					-2.121	-2.121	-2.171				-2.171	III thin disk

Continued on next page

TableA.2 – continued from previous page

ID	cluster	α_{IRAC}	α_{KI}	α_{IM}	α_{KIM}	α_{W3}	α_{WISE}	α_{KW3}	α_{KW4}	α_{KW3M}	α_{W3M}	α_{KIWM}	Class
295	CrA-Main	0.577	0.395	0.229	0.24				0.395			0.24	flat
296	CrA-Main					0.732	0.732	0.422		0.188	0.157	0.164	flat
297	CrA-Main					0.311	1.591	0.7				1.556	I
298	CrA-Main					0.104	0.343	-0.298		0.004	0.286	0.085	flat
299	CrA-Main												–
300	CrA-Main	0.922	0.771	0.204	0.317	0.404	0.404	0.367	0.771	0.318	0.323	0.336	I
301	CrA-Main	0.132	0.878	-0.24	0.152	-0.098	0.398	0.246	0.878	0.167	-0.026	0.243	flat
302	CrA-Main					-1.18	-0.928	-1.421		-1.265	-1.103	-1.139	II
303	CrA-Main							0.323				0.756	I
304	CrA-Main					-1.923	-1.923	-1.979				-1.979	III thin disk
305	–					1.914	1.914	2.246				0.582	HH
306	CrA-North					-2.002	-2.002	-2.11				-2.11	III thin disk
307	CrA-North					-2.62	-2.62	-2.559				-2.559	III no disk
308	CrA-Main					-2.06	-2.06	-2.146				-2.146	III thin disk
309	CrA-Main												–
310	CrA-Main					-1.297	-1.297	-1.492		-1.246	-1.082	-1.242	II
311	CrA-Main					-2.253	-2.253	-2.231				-2.231	III thin disk
312	CrA-North					-0.67	-0.582	-0.975				-0.793	II
313	CrA-North												–
314	CrA-North					-2.13	-2.13	-2.189				-2.189	III thin disk
315	–					-2.228	-2.228	-2.283				-2.283	R
316	CrA-North					-2.586	-2.586	-2.577				-2.577	III no disk
317	CrA-Main	0.042	0.161	0.374	0.342	0.464	0.464	0.231	0.161	0.381	0.42	0.349	I
318	CrA-Main					-2.008	-2.008	-2.155				-2.155	III thin disk
319	CrA-Main	-1.635	-1.586	-1.383	-1.424	-2.266	-2.266	-1.413	-1.586	-1.686	-2.185	-1.607	III thin disk
320	CrA-Main	-1.774	-0.094			2.343	2.343	1.625	-0.094			-0.019	flat
321	CrA-Main					-1.348	-1.348	-1.257		-1.241	-1.282	-1.241	II
322	CrA-North					-2.06	-2.06	-2.2				-2.2	III thin disk
323	CrA-North					-2.043	-2.043	-2.245				-2.245	III thin disk
324	CrA-North					-2.156	-2.156	-2.216				-2.216	III thin disk
325	CrA-Main											-0.597	II
326	CrA-Main												–
327	CrA-North					-1.002	-0.714	-1.343				-0.992	II
328	CrA-North					-1.14	-1.14	-1.369				-1.369	II
329	CrA-Main					-2.04	-2.04	-2.123				-2.123	III thin disk
330	CrA-North					-2.171	-2.171	-2.158				-2.158	III thin disk
331	CrA-Main											-0.975	II
332	CrA-North					-1.31	-0.78	-1.417		-1.024	-0.864	-0.908	II
333	CrA-Main	-2.261	-1.535	0.922	-0.157				-1.535			-0.157	flat
334	CrA-Main	0.223	0.469	0.1	0.229				0.469			0.229	flat
335	CrA-North					-2.588	-2.588	-2.591				-2.591	III no disk
336	CrA-North					-1.303	-0.735	-1.463				-0.961	II
337	Scorpio-Sting					-2.639	-2.639	-2.612				-2.612	III no disk
338	CrA-Main					-2.154	-2.154	-2.241				-2.241	III thin disk
339	CrA-North					-2.594	-2.594	-2.548				-2.548	III no disk
340	CrA-North					-2.089	-2.089	-2.026				-2.026	III thin disk
341	CrA-Main	-0.754	-0.121	-0.793	-0.527	-0.685	-0.097	-0.359	-0.121	-0.513	-0.718	-0.318	II
342	CrA-North					-2.121	-2.121	-2.229				-2.229	III thin disk
343	CrA-Main					-0.978	-0.978	-1.412				-1.412	II
344	CrA-North					-2.13	-2.13	-2.126				-2.126	III thin disk
345	CrA-North					-1.408	-1.408	-1.443				-1.443	II
346	CrA-Main	-2.442	-2.016			-1.503	-1.503	-1.651	-2.016			-1.996	III thin disk
347	CrA-Main	-1.095	-1.187	-0.944	-1.018	-1.165	-1.165	-1.268	-1.187	-1.039	-0.925	-1.047	II
348	–					0.917	1.096	0.341				0.694	G
349	CrA-North					-2.634	-2.634	-2.569				-2.569	III no disk
350	CrA-Main	1.008	0.866	0.481	0.551	0.7	0.7	0.809	0.866	0.5	0.436	0.547	I
351	CrA-North					-2.232	-2.232	-2.101				-2.101	III thin disk
352	CrA-Main					2.419	2.419	1.771				0.176	flat
353	–					0.534	0.653	0.797		0.631	0.454	0.677	G
354	CrA-North					-2.282	-2.282	-2.291				-2.291	III thin disk
355	CrA-Main	0.228	0.614	0.411	0.523	0.345	0.503	0.518	0.614	0.522	0.436	0.518	I

Continued on next page

TableA.2 – continued from previous page

ID	cluster	α_{IRAC}	α_{KI}	α_{IM}	α_{KIM}	α_{W3}	α_{WISE}	α_{KW3}	α_{KW4}	α_{KW3M}	α_{W3M}	α_{KIWM}	Class
356	CrA-Main	0.081		-0.414								-0.414	II
357	CrA-North					-2.758	-2.758	-2.611				-2.611	III no disk
358	CrA-Main	-0.24		-0.421								-0.421	II
359	CrA-Main					0.388	0.987	-0.236				0.881	I
360	CrA-North					-1.76	-1.408	-1.874				-1.557	II
361	CrA-North					-2.731	-2.731	-2.656				-2.656	III no disk
362	CrA-Main	1.665	-0.747				-0.273	0.562	-0.747			0.624	I
363	CrA-Main												–
364	CrA-North					-1.879	-1.879	-1.894				-1.894	III thin disk
365	CrA-North					-2.636	-2.636	-2.577				-2.577	III no disk
366	CrA-North					-1.281	-0.927	-1.293				-1.012	II
367	CrA-Main	7.738										7.738	I
368	CrA-Main	-0.279		1.928								1.928	I
369	CrA-North					-2.645	-2.645					-2.645	III no disk
370	CrA-North												–
371	CrA-North												–
372	CrA-North												–
373	CrA-Main	-0.057		-0.284								-0.284	flat
374	CrA-Main	-2.129		-2.612								-2.612	III no disk
375	CrA-Main	-2.669		-2.912								-2.912	III no disk
376	CrA-North					-2.741	-2.741	-2.68				-2.68	III no disk
377	CrA-Main	0.598		0.419								0.419	I
378	CrA-Main	-1.0		-0.413								-0.413	II
379	CrA-Main	-1.0		-0.375								-0.375	II
380	CrA-Main	3.449		1.965								1.965	I
381	CrA-Main	-1.256		-1.212								-1.212	II
382	CrA-Main	-2.0		-1.334								-1.334	II
383	CrA-Main	-1.0		-0.883								-0.883	II
384	CrA-Main	-0.551										-0.551	II
385	CrA-North					-2.008	-2.008	-2.054				-2.054	III thin disk
386	CrA-Main	4.114		0.715								0.715	I
387	CrA-Main	0.69		0.171								0.171	flat
388	CrA-Main	5.941										5.941	I
389	CrA-Main	-1.289		-1.003								-1.003	II
390	CrA-Main	-1.632		-1.382								-1.382	II
391	CrA-Main											0.012	flat
392	CrA-North					-2.722	-2.722	-2.708				-2.708	III no disk
393	CrA-Main	3.958		1.437								1.437	I
394	Scorpio-Sting					-2.774	-2.774	-2.684				-2.684	III no disk
395	CrA-Main	-0.807		-0.651								-0.651	II
396	CrA-Main	-1.489		-1.058								-1.058	II
397	CrA-Main	-2.648		-1.121								-1.121	II
398	Scorpio-Sting					-2.662	-2.662					-2.662	III no disk
399	CrA-North												–
400	CrA-North												–
401	CrA-North					-2.547	-2.547	-2.485				-2.485	III thin disk
402	CrA-Main					-0.745	-0.09					-0.09	flat
403	CrA-Main												–
404	CrA-North					-2.672	-2.672	-2.634				-2.634	III no disk
405	CrA-Main					-2.159	-2.159					-2.159	III thin disk
406	CrA-Main	-2.637	-2.899	-2.617	-2.728				-2.899			-2.728	III no disk
407	CrA-North					-2.133	-2.133	-2.208				-2.208	III thin disk
408	CrA-North					-2.476	-2.476	-2.444				-2.444	III thin disk
409	CrA-Main											-0.162	flat
410	CrA-North					-2.2	-2.2	-1.996				-1.996	III thin disk
411	CrA-Main					-2.672	-2.672					-2.672	III no disk
412	CrA-Main	1.611		0.686		0.832	1.192				0.675	0.951	I
413	–	-1.75		-0.318								-0.318	HH
414	CrA-Main	-0.975	-0.855				-0.044	-0.616	-0.855			-0.498	II
415	CrA-Main												–
416	CrA-Main							3.061				3.061	I

Continued on next page

TableA.2 – continued from previous page

ID	cluster	α_{IRAC}	α_{KI}	α_{IM}	α_{KIM}	α_{W3}	α_{WISE}	α_{KW3}	α_{KW4}	α_{KW3M}	α_{W3M}	α_{KIWM}	Class
417	CrA-Main	1.741	1.098	1.408	1.228				1.098			1.228	I
418	CrA-Main												–
419	Scorpio-Sting					-2.852	-2.852	-2.689				-2.689	III no disk
420	CrA-Main												–
421	CrA-North					-2.535	-2.535	-2.447				-2.447	III thin disk
422	CrA-North					-2.559	-2.559	-2.51				-2.51	III no disk
423	Scorpio-Sting												–
424	CrA-North					-2.652	-2.652	-2.587				-2.587	III no disk
425	CrA-North					-2.713	-2.713	-2.658				-2.658	III no disk
426	CrA-North					-2.572	-2.572	-2.527				-2.527	III no disk
427	CrA-North												–
428	CrA-North					-2.454	-2.454	-2.443				-2.443	III thin disk
429	Scorpio-Sting					-2.483	-2.483	-2.428				-2.428	III thin disk
430	CrA-North					-2.658	-2.658	-2.622				-2.622	III no disk
431	CrA-North					-2.724	-2.724	-2.697				-2.697	III no disk
432	CrA-North					-2.553	-2.553	-2.538				-2.538	III no disk
433	CrA-North					-2.363	-2.363	-2.364				-2.364	III thin disk
434	Scorpio-Sting					-2.317	-2.317	-2.359				-2.359	III thin disk
435	CrA-North					-2.715	-2.715	-2.691				-2.691	III no disk
436	CrA-North												–
437	CrA-North					-2.715	-2.412	-2.682				-2.457	III thin disk
438	CrA-North					-2.555	-2.555	-2.54				-2.54	III no disk
439	CrA-North					-2.148	-2.148	-2.12				-2.12	III thin disk
440	CrA-North												–
441	CrA-North					-2.469	-2.469	-2.33				-2.33	III thin disk
442	CrA-North												–
443	CrA-North												–
444	CrA-North					-2.259	-2.259	-2.174				-2.174	III thin disk
445	CrA-North					-2.825	-2.825	-2.749				-2.749	III no disk
446	CrA-North					-2.692	-2.692	-2.673				-2.673	III no disk
447	Scorpio-Sting												–
448	CrA-North					-2.229	-2.229	-2.229				-2.229	III thin disk
449	CrA-North					-2.513	-2.513	-2.466				-2.466	III thin disk
450	CrA-North					-2.553	-2.553	-2.511				-2.511	III no disk
451	CrA-North					-2.32	-2.32	-2.239				-2.239	III thin disk
452	CrA-North					-2.25	-2.25	-2.328				-2.328	III thin disk
453	CrA-North					-2.048	-2.048	-2.188				-2.188	III thin disk
454	CrA-North					-2.206	-2.206	-2.307				-2.307	III thin disk
455	CrA-North					-2.585	-2.585	-2.494				-2.494	III thin disk
456	CrA-North					-2.802	-2.802	-2.765				-2.765	III no disk
457	CrA-North					-2.75	-2.75	-2.664				-2.664	III no disk
458	CrA-North					-0.945	-0.671	-1.249				-0.923	II
459	CrA-North					-2.612	-2.612	-2.596				-2.596	III no disk
460	CrA-North					-2.547	-2.547	-2.52				-2.52	III no disk
461	CrA-North					-2.313	-2.313	-2.292				-2.292	III thin disk
462	Scorpio-Sting					-2.72	-2.72	-2.7				-2.7	III no disk
463	Scorpio-Sting												–
464	CrA-North					-2.61	-2.61	-2.565				-2.565	III no disk
465	CrA-North					-2.247	-2.247	-2.318				-2.318	III thin disk
466	CrA-North					-2.025	-2.025	-1.995				-1.995	III thin disk
467	CrA-North					-2.649	-2.649	-2.634				-2.634	III no disk
468	CrA-North					-2.712	-2.712	-2.759		-2.772	-2.752	-2.772	III no disk
469	CrA-North					-2.607	-2.607	-2.585				-2.585	III no disk
470	CrA-North												–
471	CrA-North					-2.218	-2.218	-2.295				-2.295	III thin disk
472	Scorpio-Sting												–
473	CrA-North					-2.624	-2.624	-2.544				-2.544	III no disk
474	CrA-North					-2.533	-2.533	-2.49				-2.49	III thin disk
475	CrA-North												–
476	Scorpio-Sting												–
477	CrA-North					-2.156	-2.156	-2.211				-2.211	III thin disk

Continued on next page

TableA.2 – continued from previous page

ID	cluster	α_{IRAC}	α_{KI}	α_{IM}	α_{KIM}	α_{W3}	α_{WISE}	α_{KW3}	α_{KW4}	α_{KW3M}	α_{W3M}	α_{KIWM}	Class
478	CrA-North					-2.197	-2.197	-2.219				-2.219	III thin disk
479	CrA-North					-2.572	-2.572	-2.544				-2.544	III no disk
480	CrA-North					-2.127	-2.127	-2.127				-2.127	III thin disk
481	CrA-North					-2.107	-2.107	-2.122				-2.122	III thin disk
482	CrA-Main					-0.167	0.059	-0.167				0.059	flat
483	CrA-North												–
484	CrA-North					-2.595	-2.595	-2.562				-2.562	III no disk
485	CrA-North					-2.218	-2.218	-2.279				-2.279	III thin disk
486	CrA-North												–
487	CrA-North					-2.675	-2.675	-2.629				-2.629	III no disk
488	Scorpio-Sting												–
489	CrA-North					-1.872	-1.552	-1.96				-1.677	III thin disk
490	CrA-Main					-2.634	-2.634	-2.629				-2.629	III no disk
491	CrA-North					-2.543	-2.543	-2.454				-2.454	III thin disk
492	CrA-North					-2.752	-2.752	-2.678				-2.678	III no disk
493	CrA-North					-1.137	-1.137	-1.334				-1.334	II
494	CrA-North					-2.066	-2.066	-2.178				-2.178	III thin disk
495	Scorpio-Sting					-2.237	-2.237	-2.261				-2.261	III thin disk
496	CrA-North					-2.652	-2.652	-2.62				-2.62	III no disk
497	CrA-North					-2.616	-2.616	-2.594				-2.594	III no disk
498	CrA-North					-2.221	-2.221	-2.324				-2.324	III thin disk
499	Scorpio-Sting					-1.506	-1.506	-1.606				-1.606	III thin disk
500	Scorpio-Sting					-2.043	-2.043	-2.254				-2.254	III thin disk
501	CrA-North					-2.684	-2.684	-2.682				-2.682	III no disk
502	CrA-North					-2.726	-2.726	-2.68				-2.68	III no disk
503	CrA-North					-2.314	-2.314	-1.992				-1.992	III thin disk
504	CrA-North					-2.79	-2.79	-2.664				-2.664	III no disk
505	CrA-North					-3.142	-2.908	-2.915		-2.979	-3.11	-2.898	III no disk
506	CrA-North					-2.6	-2.6	-2.553				-2.553	III no disk
507	CrA-Main	0.012	1.683	-0.136	0.74	0.382	0.597	0.973	1.683	0.62	0.228	0.695	I
508	CrA-North					-2.614	-2.614	-2.556				-2.556	III no disk
509	CrA-North					-2.121	-2.121	-2.278				-2.278	III thin disk
510	Scorpio-Sting					-2.891	-2.891	-2.792				-2.792	III no disk
511	CrA-North					-2.74	-2.74	-2.723				-2.723	III no disk
512	CrA-North					-2.51	-2.141	-2.549				-2.246	III thin disk
513	CrA-North					-2.468	-2.468	-2.462				-2.462	III thin disk
514	CrA-North					-2.685	-2.685	-2.637				-2.637	III no disk
515	CrA-North					-2.749	-2.749	-2.704				-2.704	III no disk
516	CrA-North					-2.711	-2.711	-2.648				-2.648	III no disk
517	Scorpio-Sting					-2.487	-2.487	-2.429				-2.429	III thin disk
518	Scorpio-Sting					-2.789	-2.789	-2.724				-2.724	III no disk
519	CrA-North					-1.602	-1.602	-1.846				-1.846	III thin disk
520	CrA-North					-1.621	-1.621	-1.661				-1.661	III thin disk
521	CrA-North					-2.65	-2.65	-2.598				-2.598	III no disk
522	CrA-North					-2.662	-2.662	-2.636				-2.636	III no disk
523	CrA-North												–
524	CrA-North					-2.063	-2.063	-2.181				-2.181	III thin disk
525	CrA-North												–
526	CrA-North					-2.574	-2.574	-2.555				-2.555	III no disk
527	CrA-North					-2.544	-2.544	-2.566				-2.566	III no disk
528	CrA-North												–
529	CrA-North					-2.63	-2.63	-2.59				-2.59	III no disk
530	CrA-North					-2.404	-2.404	-2.333				-2.333	III thin disk
531	CrA-North					-2.483	-2.483	-2.454				-2.454	III thin disk
532	CrA-North					-2.545	-2.545	-2.427				-2.427	III thin disk
533	CrA-North					-2.717	-2.717	-2.678				-2.678	III no disk
534	CrA-North					-2.2	-2.2	-2.243				-2.243	III thin disk
535	CrA-North					-2.36	-2.36	-2.324				-2.324	III thin disk
536	CrA-North												–
537	CrA-North					-2.572	-2.572	-2.515				-2.515	III no disk
538	CrA-North					-2.533	-2.533	-2.483				-2.483	III thin disk

Continued on next page

TableA.2 – continued from previous page

ID	cluster	α_{IRAC}	α_{KI}	α_{IM}	α_{KIM}	α_{W3}	α_{WISE}	α_{KW3}	α_{KW4}	α_{KW3M}	α_{W3M}	α_{KIWM}	Class
539	CrA-North					-2.25	-2.25	-2.279				-2.279	III thin disk
540	CrA-Main					-2.691	-2.691	-2.66				-2.66	III no disk
541	Scorpio-Sting					-2.688	-2.688	-2.676				-2.676	III no disk
542	CrA-North					-2.266	-2.266	-2.283				-2.283	III thin disk
543	CrA-North					-1.487	-1.487	-1.59				-1.59	II
544	CrA-North					-2.743	-2.743	-2.701				-2.701	III no disk
545	CrA-North					-2.762	-2.768	-2.743				-2.754	III no disk
546	CrA-North					-2.355	-2.355	-2.337				-2.337	III thin disk
547	CrA-North					-2.693	-2.693	-2.652		-2.766	-2.818	-2.766	III no disk
548	CrA-Main					-2.578	-2.578	-2.536				-2.536	III no disk
549	CrA-Main	1.045	0.711				0.136	0.741	0.711			0.687	I
550	CrA-North					-2.65	-2.65	-2.593				-2.593	III no disk
551	CrA-North					-2.186	-2.186	-2.244				-2.244	III thin disk
552	CrA-Main					-2.568	-2.568	-2.497				-2.497	III thin disk
553	CrA-North					-2.694	-2.694	-2.686				-2.686	III no disk
554	CrA-North					-2.369	-2.369	-2.319				-2.319	III thin disk
555	CrA-North					-2.679	-2.679	-2.653				-2.653	III no disk
556	CrA-North					-2.618	-2.618	-2.57				-2.57	III no disk
557	CrA-North					-2.148	-2.148	-2.196				-2.196	III thin disk
558	Scorpio-Sting					-2.636	-2.404	-2.644				-2.46	III thin disk
559	CrA-North					-2.485	-2.162	-2.547				-2.272	III thin disk
560	CrA-North					-2.183	-2.183	-2.211				-2.211	III thin disk
561	CrA-Main	-0.575	-0.956	-0.219	-0.563	0.726	0.818	0.347	-0.956	-0.305	-0.292	0.092	flat
562	CrA-North					-2.662	-2.662	-2.619				-2.619	III no disk
563	CrA-Main					-0.461	-0.133	-0.729				-0.374	II
564	CrA-North					-2.678	-2.678	-2.616				-2.616	III no disk
565	CrA-North					-1.58	-1.58	-1.66				-1.66	III thin disk
566	CrA-Main					-1.446	-0.942	-1.645				-1.178	II
567	CrA-North					-1.741	-1.471	-1.644				-1.468	II
568	CrA-Main	-2.512	-2.453	-2.861	-2.752	-2.489	-2.489	-2.448	-2.453	-2.707	-2.797	-2.699	III no disk
569	CrA-North					-2.235	-2.235	-2.354				-2.354	III thin disk
570	CrA-North												–
571	CrA-Main	-2.58	-2.528	-2.914	-2.812				-2.528			-2.812	III no disk

Appendix B

Flux conversion and equivalencies

Since the photometric data from different surveys is provided in different units, certain conversions are necessary in order to use them in different analysis, such as CMDs, CCDs or SEDs. Depending on whether we want to use color-magnitude and color-color diagrams, or spectral energy distributions, we need to convert the photometric measurements between flux densities (commonly given in Jy) and brightness (given in mag).

For instance the *Spitzer enhanced imaging products* (SEIP) provide flux measurements in mJy, whereas the *2MASS* survey provides brightness in magnitudes for the individual sources. In order to combine these two data products in a color-magnitude diagram, the flux measurements from *Spitzer* need to be converted into magnitudes. The conversion from Flux to magnitude is done using the following relation:

$$m = -2.5 \log_{10} \left(\frac{F}{F_{\mathrm{zp}}} \right) \tag{B.1}$$

Where F_{zp} is the zero magnitude flux in the selected filter. Meaning, that a source of brightness 0 mag in the selected passband has a certain flux F_{zp} which is different for the individual filters. In reverse, to get fluxes from magnitudes the following equation is used.

$$F = F_{\mathrm{zp}} 10^{(-0.4\, m)} \tag{B.2}$$

The individual zero magnitude fluxes for the different filters used in this study, including the wavelengths they are located at, are listed Table 1.2.

The flux density F_ν is given in dependence of the frequency ν of the electromagnetic wave. In some cases the flux density F_λ can also be given in dependence on the wavelength λ of the electromagnetic wave. To convert between the two, the following equations show the equivalencies in detail. We begin with the definition of a Jansky, to see which SI units need to be converted.

$$1\,\mathrm{Jy} = 1 \times 10^{-23} \frac{\mathrm{erg}}{\mathrm{s\,Hz\,cm^2}} \tag{B.3}$$

We then make use of the following identity:

$$\int F_\lambda d\lambda = \int F_\nu d\nu \tag{B.4}$$

By differentiating both sides of the equation above, we are left with the following:

$$F_\lambda d\lambda = F_\nu d\nu$$

Therefore, we can now convert F_ν to F_λ as follows:

$$F_\lambda = F_\nu \frac{d\nu}{d\lambda} \tag{B.5}$$

Introducing ν as a function of wavelength leads to:

$$\nu(\lambda) = \frac{c}{\lambda} \tag{B.6}$$

$$\frac{d\nu(\lambda)}{d\lambda} = -\frac{c}{\lambda^2} \tag{B.7}$$

$$= -2.997\,924\,58 \times 10^8 \frac{\mathrm{m}}{\mathrm{s}} \frac{1}{\mathrm{\mu m}^2} \tag{B.8}$$

Finally with with the correct conversions from $\mathrm{m\,s^{-1}}$ to $\mathrm{\mu m\,s^{-1}}$ for the speed of light, we get a conversion factor that needs to be multiplied with F_ν in order to get F_λ. Formally the derivative in Equation B.7 produces a negative sign which is omitted as it is not a physical solution, but rather indicates that there is an inverse relationship between wavelength and frequency. Meaning that with increasing frequency, the wavelength gets shorter.

$$\begin{aligned} F_\lambda &= F_\nu * 10^{-23} \frac{\mathrm{erg}}{\mathrm{s\,Hz\,cm^2}} * 2.997\,924\,58 \times 10^{14} \frac{\mathrm{\mu m}}{\mathrm{s}} \frac{1}{\mathrm{\mu m}^2} \\ &= F_\nu * 2.997\,924\,58 \times 10^{-9} \frac{\mathrm{Hz\,erg}}{\mathrm{s\,Hz\,cm^2\,\mu m}} \\ &= F_\nu * 2.997\,924\,58 \times 10^{-9} \frac{\mathrm{erg}}{\mathrm{s\,cm^2\,\mu m}} \end{aligned} \tag{B.9}$$

Appendix C

SExtractor quality control flags supplement

The list below is copied from the *SExtractor* (Bertin & Arnouts 1996) documentation webpage[1] and sums up what each bit stands for.

n=0 Bit value 1: aperture photometry is likely to be biased by neighboring sources or by more that 10 % of bad pixels in any aperture.

n=1 Bit value 2: The object has been deblended.

n=2 Bit value 4: At least one object pixel is saturated.

n=3 Bit value 8: The isophotal footprint of the detected object is truncated (too close to an image boundary).

n=4 Bit value 16: At least one photometric aperture is incomplete or corrupted (hitting buffer or memory limits).

n=5 Bit value 32: The isophotal footprint of the detected object is incomplete or corrupted (hitting buffer or memory limits).

n=6 Bit value 64: A memory overflow occurred during deblending.

n=7 Bit value 128: A memory overflow occurred during extraction.

Therefore, a SExtractor flag with value of less than four means, that only sources whose photometry has been influenced minimally by nearby sources or bad pixels, and deblended stars are acceptable for *VISIONS*. The nebulosity filter takes into account the measurement of several apertures of different radii, as well the signal to noise ratio to determine if the source is a true point source or not. Further details on these quality cuts will be given in the *VISIONS* survey overview (Meingast S. et al. in preparation), and may differ slightly from what is used for this study since I use early data products. Finally, as the *VISIONS* quality flag excludes bright sources due to saturation, a cross match with *2MASS* is performed in order to compensate for the loss of these bright stars in *VISIONS*.

[1] `https://sextractor.readthedocs.io/en/latest/Flagging.html`

Acknowledgements

With this thesis finally done I would like to thank all those who supported me over the course of this project. First and foremost I would like to thank my supervisor, Josefa Großschedl, who with her expertise and experience helped me enormously with a topic I was largely unfamiliar with at the beginning of this project. Without her this thesis would certainly not have come to a satisfying end. I especially hold in high regards her critical mind by which she questioned every bit of this thesis, which pushed me to improve this thesis to the point it is now.

Furthermore, it has been a privilege to work with the exceptional dataset of the *VISIONS* survey, and I would like to thank the *VISIONS* team in Vienna, led by Stefan Meingast, who supplied me with the source catalogs and high resolution images from this ambitious project.

I was also able to use partial yet unpublished data from Sebastian Ratzenböck, who selected YSOs using Gaia data by applying machine learning techniques from the verb+SigMA+ code which was developed by him, and I would like to thank him for allowing me to use the unpublished catalog for Corona Australis.

This work made use of Topcat[2] and Aladin[3]. In addition to that, I made extensive use of the `astropy`[4] python package and the astropy affiliate packages `astroquery`[5], and `mocpy`[6]. All plots and diagrams which were made by myself used the python plotting library `matplotlib`[7]

Finally, last but not least, I would like to thank my cat whose moral support was unparalleled.

[2] http://www.star.bristol.ac.uk/~mbt/topcat/

[3] "Aladin sky atlas" developed at CDS, Strasbourg Observatory, France. https://aladin.u-strasbg.fr/

[4] https://www.astropy.org/

[5] https://astroquery.readthedocs.io/en/latest/

[6] https://cds-astro.github.io/mocpy/stubs/mocpy.MOC.html

[7] https://matplotlib.org/